



TECHNISCHE UNIVERSITÄT MÜNCHEN

TUM School of Engineering and Design

A General Framework for Modelling the Microstructure and Water Retention Behaviour of Soils with Heterogeneous Pore Structure

Wei Yan

Vollständiger Abdruck der von der TUM School of Engineering and Design der Technischen Universität München zur Erlangung des akademischen Grades eines

Doktors der Ingenieurwissenschaften (Dr.-Ing.)

genehmigten Dissertation.

Vorsitz: Prof. Dr. Daniel Straub

Prüfer*innen der Dissertation:

1. Prof. Dr.-Ing. Roberto Cudmani
2. Prof. Dr.-Ing. Wei Wu
3. Prof. Dr.-Ing. Alexander Scheuermann

Die Dissertation wurde am 27.09.2022 bei der Technischen Universität München eingereicht und durch die TUM School of Engineering and Design am 11.02.2023 angenommen.

Declaration of Authorship

I hereby declare that except where specific reference is made to the work of others, the contents of this dissertation are original and have not been submitted in whole or in part for consideration for any other degree or qualification in this, or any other university. This dissertation is my own work and contains nothing which is the outcome of work done in collaboration with others, except as specified in the text and Acknowledgements.

Wei Yan

Zusammenfassung

In der klassischen Bodenmechanik wird Boden als homogenes poröses Material idealisiert. Es wird angenommen, dass seine Porengröße einer unimodalen Verteilungsfunktion folgt. Die in geotechnischen Anwendungen anzutreffenden Böden sind jedoch selten homogen, sondern durch eine heterogene Mikrostruktur gekennzeichnet, z.B. verdichtete Böden (z. B. in Straßendämmen), weitgestufte Böden (z. B. Dichtungsmaterial in der Deponie für radioaktive Stoffe) und Oberböden in der Natur. Die Saugspannungs-Wassergehalts-Beziehung (SWCC) dieser Böden, die den Zusammenhang zwischen Saugspannung und Wassergehalt beschreibt, weist ebenfalls eine ausgeprägte multimodale Charakteristik auf, da es stark mit der Porenstruktur zusammenhängt. Die SWCC nimmt eine bedeutende Rolle bei der Beschreibung von hydro-mechanisch gekoppelten Fragestellungen in ungesättigten Böden ein, da wichtige hydraulische und mechanische Bodeneigenschaften, wie effektive Spannung, Scherfestigkeit, Kompressionsverhalten, Schubmodul und ungesättigte hydraulische Leitfähigkeit von der Saugspannung bzw. dem Wassergehalt abhängig sind. Für unimodale Böden wurden zahlreiche empirische und semiempirische Ansätze zur Beschreibung der bodenmechanischen Eigenschaften auf Basis der SWCC entwickelt. Für Böden mit heterogener Porenstruktur können diese Beziehungen mit den für unimodale Böden entwickelten Ansätzen nichtzutreffend beschrieben werden. Daher ist ein umfassendes Verständnis und eine zutreffende Beschreibung der Porengrößenverteilung (PSD) und der SWCC von multimodalen Böden für Standsicherheits- und Verformungsbetrachtungen, bei denen der ungesättigte Zustand der Böden einen maßgeblichen Einfluss hat, erforderlich. Bisher fehlt in der Literatur noch ein allgemeines (d. h., die Modalitätszahl kann eine beliebige ganze Zahl sein) Konzept zur Quantifizierung der heterogenen Porenstruktur und der daraus resultierenden komplexen Saugspannungs-Wassergehalts-Beziehung von multimodalen Böden.

Der erste Teil dieser Arbeit zielt darauf ab, ein allgemeines Porengrößenverteilungsmodell zu entwickeln, welches es ermöglicht, Böden mit heterogener Struktur zu beschreiben. Basierend auf einer mathematischen Definition des Porenradius r in einem porösen Medium wird eine probabilistische PSD-Funktion vorgeschlagen. Die Parameter im Modell haben dabei eine eindeutige physikalische Bedeutung. Das vorgeschlagene Modell wird anhand einer Reihe von PSD-Messungen an verschiedenen Böden validiert, die von verdichteten Tonen bis hin zu weitgestuften grobkörnigen Böden reichen. Die Ergebnisse des Modells zeigen eine starke Übereinstimmung zwischen den rechnerisch bestimmten Kurven und den gemessenen PSD-Daten. Die Entwicklung der Mikrostruktur von tonigen Böden entlang verschiedener hydromechanischer Belastungspfade wurde ebenfalls analysiert.

Der zweite Teil der Arbeit widmet sich der Erstellung eines SWCC-Modells, um die Beziehung zwischen Wassergehalt und Saugspannung für einen multimodalen Boden zu simulieren. Die vorgeschlagene kontinuierliche Gleichung besitzt eine einfache mathematische Form. Basierend auf den Formmerkmalen der SWCC, die in einem doppelt logarithmischen Diagramm dargestellt sind, wurde ein einfaches Verfahren zur Parameterkalibrierung entwickelt. Die Einzigartigkeit des Parametersatzes bietet die Möglichkeit, das vorgeschlagene Modell zu verbessern, indem die Parameter mit Bodeneigenschaften (z. B. Dichte) und Zustandsparametern (z. B. mittlerer Druck) korreliert werden. Um das Modell zu validieren, wurde eine Reihe von SWCC-Messungen aus verschiedenen Böden mit den angepassten Kurven verglichen. Es wurde dabei eine gute Übereinstimmung zwischen den Messungen und den angepassten Kurven festgestellt.

Herkömmliche experimentelle Methoden zur SWCC-Messung sind zeitaufwändig und teuer. Im dritten Teil der Arbeit wird eine Methode zur Prognose der SWCCs direkt aus Porengrößenverteilungsdaten formuliert. Die

Bodenmikrostruktur wird dabei durch zwei unabhängige Zustandsvariablen quantifiziert: eine für das Gesamtvolumen (Porenzahl e) und die andere für die Porengrößenverteilung (ein neuer mikrostruktureller Zustandsparameter Ω). Eine einzigartige PSD-Fläche verbindet die SWCC und die Mikrostrukturentwicklung mit der Saugspannung während des Be- und Entwässerungsprozesses. Das Modell wurde validiert, indem die SWCCs von vier verschiedenen Böden prognostiziert wurden, inklusive einem gering kompressiblen schluffigen Sand und drei kompressiblen tonigen Böden. Die entwickelte SWCC-Funktion in geschlossener Form erleichtert die Implementierung des Modells für praktische Anwendungen.

In dieser Arbeit bildet das vorgeschlagene PSD-Modell und die entwickelten SWCC-Modelle die Grundlage, um die Mikrostruktur in Böden mit heterogenen Porenstrukturen zu analysieren und die damit verbundene SWCC zutreffend zu beschreiben. Es wird erwartet, dass das vorgeschlagene Konzept in konstitutive Modelle zur Beschreibung der Eigenschaften von multimodalen Böden (z. B. ungesättigte hydraulische Leitfähigkeit und effektive Spannungsparameter) integriert wird.

Abstract

In classical soil mechanics, soil is idealized as a homogenous porous material, and its pore size is assumed to obey a unimodal distribution function. However, many soils encountered in geotechnical and geo-environmental engineering applications are rarely homogenous but are characterised by a heterogeneous (or multimodal) microstructure, e.g., the compacted soils as construction material in the road embankment, gap-graded soils as sealing material in nuclear waste repository and topsoil in nature. The water retention behaviour (or soil water characteristic curve, SWCC) of these soils, which describes the relationship between soil suction and water content, also exhibits a distinguishing multimodal characteristic, as it is strongly related to the pore structure. In unsaturated soil mechanics, SWCC plays a crucial role in the hydro-mechanical coupling of unsaturated soils, since important hydraulic and mechanical soil properties, such as the effective stress, shear strength, compression index, yielding stress, shear modulus and unsaturated hydraulic conductivity are often related to suction or water content. For unimodal soils, numerous empirical and semi-empirical expressions have been developed to predict these unsaturated soil properties based on SWCC. However, for soils with a heterogeneous pore structure, these relationships may differ from those deduced for unimodal soils. For instance, a bimodal SWCC, resulting from a bimodal pore structure, may cause the bimodality in permeability function. Therefore, a comprehensive understanding and precise description for the pore structure and SWCC of multimodal soils is necessary for the safety- and stability-assessment of the geotechnical and geo-environmental facilities in the vadose zone. So far, a general (i.e., the modality number can be any positive integer) framework to quantify the heterogeneous pore structure and the consequent complex water retention behaviour of multimodal soils is missing in literature.

The first part of this thesis aims to develop a general pore size distribution model to describe the heterogeneous soil pore structure. Based on a mathematical definition of pore radius r in a porous medium, a probabilistic pore size distribution expression is proposed. The parameters in the model possess a clear physical meaning. The proposed model is validated using a set of pore size distribution (PSD) measurements from different soils, ranging from compacted clayey soils to gap-graded soils, yielding a strong consistency between the fitted curves and the measured PSD data. The microstructure evolution of clayey soils along different hydro-mechanical loading paths is analysed.

The second part of the thesis is devoted to advancing a SWCC model to precisely simulate the relationship between water content and soil suction for a multimodal soil. The proposed continuous equation possesses a simple mathematical form. A convenient parameter calibration method has been developed based on the shape features of the SWCC presented in double logarithmic diagram. The uniqueness of the parameter set provides the possibility to improve the proposed model by correlating the parameters to soil properties (e.g., density) and state parameters (e.g., mean pressure). To validate the model, a set of SWCC measurements from different soils are compared to the fitted curves. A good agreement is observed between them.

Traditional experimental techniques for SWCC measurement are time-consuming and expensive. In the third part of the thesis, a method to predict the water retention behaviour directly from pore size distribution data is developed. Soil microstructure is quantified by two independent state variables: void ratio e for the overall volume and a new microstructural state parameter Ω for the pore size distribution. A unique PSD-surface links the water retention curve and the microstructure evolution with suction during wetting and drying process. The model is validated by predicting the water retention curves of four different soil types, including a low compressible silty

sand and three compressible clayey soils. The closed-form water retention expression facilitates the implementation of the model in practical applications.

In this thesis, the proposed PSD model, the empirical and predictive SWCC models establish a general framework to quantify the evolving microstructure and the related water retention behaviour of soils with heterogeneous pore structure. The framework is applicable for all soil types. The proposed framework can be incorporated in thermal, hydraulic and mechanical constitutive models of multimodal soils, e.g., to define unsaturated hydraulic and thermal conductivity and effective stress variables.

Acknowledgements

This thesis is the result of my work carried out at Zentrum Geotechnik of Technical University of Munich (TUM). First of all, I would like to express my great gratitude to my supervisor Prof. Roberto Cudmani for his continuous support and clear guidance during my PhD study and offering me the opportunity to work in a warm and motivated team. The same gratitude goes to the members of my PhD committee, Prof. Dr. Wei Wu and Prof. Dr. Alexander Scheuermann, for reviewing and evaluating this thesis. I am deeply thankful to Prof. Dr. Daniel Straub as the chairman of the examination committee. Furthermore, I would like to acknowledge Dr. Emanuel Birle for the fruitful discussions and valuable advice. I sincerely appreciate his constructive comments and effort on revising the thesis. I extend my sincere thanks to Dr. Angerer Ludwig, who supervised my master thesis, supported me with his professional knowledge, and encouraged me to continue the research in the field of unsaturated soils. I also would like to thank my dear colleague Alexander Wiendl, with whom I shared the office and from whom I learned a lot of interesting Bavarian language. I am grateful for his help in revising German documents and useful tips for daily life in Munich. My special thanks also go to the colleagues in our institute: Friedrich Levin, Andy Klinger, Eren Matthews, Joshua Schorr, Ulrich Schindler, Belinda Bock, and many more, for the productive discussions and their selfless help. I would also like to express my appreciation to Chinese Scholarship Council for financially supporting my PhD study. My heartfelt thanks goes to my dear friends, Yan Gu, Qingcheng Zhang, Kun Wang, Jian Xu and Shengjuan Li, for their encouragement, support and company during my stay in Munich. Last but not least, I want to give my deepest gratitude to my parents, grandparents and younger sister, for their endless love and unconditional support throughout the challenging PhD journey.

List of Abbreviations

THMC	thermo-hydro-chemo-mechanical
PSD	pore size distribution
SWCC	soil water characteristic curve
WRC	water retention curve
ULS	ultimate limit state
SLS	serviceability limit state
GA	gas adsorption
MIP	mercury intrusion porosimetry
BCM	Brooks and Corey model
VGM	van Genuchten model
FXM	Fredlund and Xing model
D-CMVGM	discrete – continuous multimodal van Genuchten model
DMVGM	discrete multimodal van Genuchten model
CMVGM	continuous multimodal van Genuchten model
MNRM	modality number reduction method

List of Symbols

P_{Hg}	mercury pressure
T_{Hg}	surface tension of mercury
θ_{Hg}	the contact angle between mercury and soil particle surface
r	entrance pore radius
e_{cum}	intruded void ratio
n_{cum}	intruded porosity
V_{cum}	normalized pore volume in one-gram dry soil
$f(r)$	pore size density curve
e_0	initial void ratio of the soil sample
N^*	number of data points from MIP tests
$\omega(r)$	dimensionless pore size density curve
w_L	liquid limit
w_p	plastic limit
ρ_s	particle density
w_{opt}	optimum water content of standard proctor test
ρ_{opt}	optimum dry density of standard proctor test
C_U	uniformity coefficient
ρ_d	initial dry density
s_0	initial suction
V_{max}^*	maximum normalized pore volume in one-gram dry soil
N	modality number
S	specific surface area
e_{Hg}	mercury intrusion volume in terms of void ratio
M	mol/L
S_e	effective degree of saturation
ϕ_i	weighting factor
s	matric suction
u_a	pore-air pressure
u_w	pore-water pressure
s_{ae}	air entry suction
s_{res}	residual suction
s_{max}	maximum suction
S_r	degree of saturation
$S_{r,res}$	residual degree of saturation
$S_{r,max}$	maximum degree of saturation
$s_{ae,1}$	interaggregate air entry suction
$s_{ae,2}$	intraaggregate air entry suction

s_j	delimiting suction
$S_{r,j}$	degree of saturation at the delimiting point
$S_{r,1}$	degree of saturation of interaggregate porosity
$S_{r,2}$	degree of saturation of intraaggregate porosity
R_1	volumetric fraction of interaggregate porosity
R_2	volumetric fraction of intraaggregate porosity
T	surface tension of water
θ	contact angle between soil solid surface and water
ξ	dummy variable of integration for pore radius
$\delta(x)$	Dirac delta function
m_i	unitless pore size spectrum number of a sub-porosity
r_i^f	reference pore radius of a sub-porosity
R_i	volumetric fraction of a sub-porosity
r_{max}	maximum pore radius
V_{res}	permanent saturated void volume
V_{dry}	permanent dry void volume
V_{unsat}	unsaturated void volume
$K_{max,i}$	maximum slope of i^{th} sub-curve in the double logarithmic plot
$R_{i,eff}$	effective volumetric fraction of i^{th} sub-curve
Ω	microstructural state parameter
σ_{ij}^{net}	net stress tensor
p_0^*	pre-consolidation pressure at saturated state
β_{ink}	scaling factor for “ink-bottle” effect
β_θ	parameter for the different contact angles between wetting and drying

List of Figures

Fig. 2.1. MIP test data for a sand-clay mixture (70% sand + 30% clay) a) cumulative mercury intrusion curve b) pore size density curve (data from Juang and Holtz (1986b)).....	5
Fig. 2.2. MIP test data for fine-grained and coarse-grained soils a) cumulative mercury intrusion curves of Lias clay b) pore size density curves of Lias clay soils (data from Birle (2011)) c) cumulative mercury intrusion curves of Ottawa sand b) pore size density curves of Ottawa sand (data from Juang and Holtz (1986b))	7
Fig. 2.3. MIP test data for a sand-bentonite mixture (80% quartz sand + 20% MX80 bentonite) after compaction a) cumulative mercury intrusion curve b) pore size density curve (data from Manca et al. (2016)).....	8
Fig. 2.4. Influence of compaction on soil microstructure a) pore size density curves for FEBEX bentonite (data from Lloret et al. (2003)) b) pore size density curves for a sand clay mixture (data from Li and Zhang (2009)).	10
Fig. 2.5. Influence of suction on soil microstructure a) microstructural evolution of unsaturated compacted London clay during wetting under a constant vertical load (data from Monroy et al. (2010)) b) microstructural evolution of an unsaturated compacted sand bentonite mixture during wetting under isochoric condition (data from Manca et al. (2016))	10
Fig. 2.6. Influence of pore water salinity on microstructure evolution of sand bentonite mixture during hydration (initial dry density $\rho_d = 1.5 \text{ g/cm}^3$) a) cumulative curves of as-compacted samples b) pore size density curves of as-compacted samples c) cumulative curves of saturated samples d) pore size density curves of saturated samples (data from Manca et al. (2016))	11
Fig. 3.1. Schematic illustration for water retention behaviour of unimodal soils a) a typical soil water characteristic curve for desiccation b) hydraulic hysteresis	15
Fig. 3.2. Bimodal SWCC induced by bimodal pore structure a) bimodal pore size distribution of SW-SM with gravel in the saturated and completely dry states (data from Zhao et al. (2013)) b) SWCC measurement of SW-SM with gravel c) bimodal pore size distribution of compacted Guilin lateritic soil at high ($S_r = 0.89$) and low ($S_r = 0.12$) water content d) bimodal main wetting and drying curves of compacted Guilin lateritic soil (data from Cai et al. (2020))	18
Fig. 4.1. Definition of pore radius according to Scheidegger (2020).....	24
Fig. 4.2. Schematic for pore size distribution curves of a) an idealised porosity as a single spherical pore in representative elementary volume (REV) b) an idealised porosity as a set of individual spherical pores in REV c) a unimodal porosity d) a multimodal porosity (Figure adapted from Yan and Cudmani (2022a), copyright © 2022 Elsevier. Reprinted with permission).....	25
Fig. 4.3. Schematic of the soil composition with N-modal pore structure (Figure from Yan et al. (2021a)).....	27
Fig. 4.4. a) interpretation for water retention curves and PSD curves by a unique surface in the $r - s - F (= S_e)$ space b) water retention curves in the conventional $\log s - S_e$ plane c) PSD curves in the $\log r - F$ plane (Figure from Yan and Cudmani (2022b)).....	29

Table of contents

Declaration of Authorship.....	i
Zusammenfassung.....	iii
Abstract.....	v
Acknowledgements.....	vii
List of Abbreviations.....	viii
List of Symbols.....	ix
List of Figures.....	xi
Table of contents.....	xiii
1. Introduction.....	1
1.1. Motivation and objectives.....	1
1.2. Outline.....	2
2. Basics of multimodal soil microstructure.....	4
2.1. Introduction.....	4
2.2. Literature review.....	4
2.2.1. Experimental techniques and basics of soil pore structure.....	4
2.2.2. Microstructural evolution.....	9
2.2.3. Existing multimodal PSD models.....	13
2.3. Summary.....	13
3. Basics of multimodal water retention behaviour.....	15
3.1. Introduction.....	15
3.2. Literature review.....	17
3.2.1. Water retention behaviour of soils with heterogeneous pore structure.....	17
3.2.2. Predicting multimodal water retention curve from PSD data.....	21
3.3. Summary.....	23
4. Methodology.....	24
4.1. Modelling multimodal pore size distribution.....	24
4.2. Modelling multimodal soil water characteristic curves.....	27
4.3. Predicting multimodal water retention behaviour based on pore size distribution data.....	28
5. Summaries of publications.....	31

5.1.	Paper I: A general analytical expression for pore size distribution based on probability theory.....	31
5.1.1.	Summary of the publication	31
5.1.2.	Individual contributions of the candidate	31
5.2.	Paper II: A new framework to determine general multimodal soil water characteristic curves	32
5.2.1.	Summary of the publication	32
5.2.2.	Individual contributions of the candidate	32
5.3.	Paper III: A novel framework for predicting water retention behaviour based on pore size distribution data of multimodal unsaturated soils.....	33
5.3.1.	Summary of the publication	33
5.3.2.	Individual contributions of the candidate	33
6.	Conclusions and outlook.....	34
	References.....	37
	List of Publications	42
	Appendix – original journal papers.....	43
	Paper I – A general analytical expression for pore size distribution based on probability theory.....	43
	Paper II – A new framework to determine general multimodal soil water characteristic curves.....	44
	Paper III – A novel framework for predicting water retention behaviour based on pore size distribution data of multimodal unsaturated soils.....	45

1. Introduction

1.1. Motivation and objectives

In conventional soil mechanics, soil is idealized as a porous material with homogeneous fabric. The void space is characterised by the state variable void ratio e (the ratio of the void volume to solid volume) or porosity n (the ratio of the void volume to total volume). However, many soils encountered in practical geotechnical, geo-environmental and agricultural engineering applications possess a heterogeneous fabric and pore structure (Carminati et al., 2008).

In clayey soils compacted at dry side of optimum water content, particle aggregation leads to a bimodal pore structure consisting of two sub-porosities, i.e., the interaggregate porosity (or macro-porosity) between the aggregates and the intra-aggregate porosity (micro-porosity) within the aggregates (Cai et al., 2020, Birle, 2011, Romero et al., 1999, Diamond, 1970). This bimodal pore structure is different from the matrix type fabric (i.e., a unimodal porosity) in the reconstituted sample of the same soil. The discrepancies in the microstructure of the same soil cause a remarkable difference in the macroscopic hydro-mechanical behaviour, such as the water retention properties (Cai et al., 2020, Vanapalli et al., 1999, Birle, 2011), the unsaturated hydraulic conductivity, the apparent pre-consolidation stress (Koliji et al., 2010), the unsaturated shear strength (Chowdhury and Azam, 2016, Della Vecchia et al., 2013, Zhai et al., 2019), the effective stress (Alonso et al., 2010) and the swelling pressure (Manca et al., 2016), among others.

In nuclear waste repositories, bentonite-enriched soils, e.g., sand-bentonite mixtures, are often utilized as an engineering barrier and backfilling material to delay the migration of nuclides due to their low water permeability and swelling potential (Watanabe and Yokoyama, 2021, Nagra, 2008). In these soils, three distinguishing pore families can be identified, including the pore space between sand grains and bentonite aggregates (interaggregate porosity), the voids between individual clay particles within aggregates (intraaggregate porosity) and the planar void space between the clay layers (i.e., smectite sheets) within clay particles (interlayer porosity). Numerous experimental studies have testified that the overall soil pore structure can significantly change upon thermo-hydro-chemo-mechanical (THMC) loadings (Abed and Sołowski, 2017, Manca et al., 2016, Wang et al., 2014). For instance, during hydration, water molecules enter the planar interlayer voids, resulting in an increase in the distance between the smectite sheets and overall expansion of the bentonite aggregates. This swelling behaviour of bentonite reduces the water permeability and alters the macroscopic hydro-mechanical behaviour of the material. Therefore, a good understating of the microstructure and its evolution along THMC loading paths of these soils is crucial for the safety assessment of the nuclear waste repositories. So far, a large amount of pore size distribution (PSD) data has been experimentally determined and is currently available in the literature, while a general PSD model to quantify the multimodal pore structure is still missing, which limits the incorporation of the microstructure effect in the hydraulic and constitutive modelling of soils with heterogeneous pore structure (Koliji et al., 2010, Della Vecchia et al., 2013).

The soil water characteristic curve (SWCC), also known as the water retention curve (WRC), is a constitutive law that describes the relationship between soil suction and water content, expressed in terms of gravity water content w (the ratio of water mass to solid mass), volumetric water content θ (the ratio of water volume to total soil volume), water ratio e_w (the ratio of water volume to solid volume), or degree of saturation S_r (the ratio of

water volume to void volume). SWCC plays a key role in geotechnical and geo-environmental applications in the unsaturated zone, as many important soil properties are closely related to the water retention behaviour (Fredlund and Rahardjo, 1993). For instance, unsaturated hydraulic conductivity is a function of soil suction or water content. The direct measurement of this parameter in laboratory is especially time-consuming and costly (Van Genuchten, 1980, Leong and Rahardjo, 1997a). Therefore, numerous analytical expressions from the more easily measured SWCC and the saturated permeability coefficient have been developed to estimate the unsaturated hydraulic conductivity at any suction level or water content, e.g., Burdine (1953), Mualem (1976) and Fredlund et al. (1994), among others. The knowledge of SWCC is hence necessary to quantify the water distribution and to simulate the multiphase fluid flow and the material transportation in unsaturated soils (Lu, 2016).

SWCC also significantly influences the mechanical parameters of unsaturated soils such as the effective stress parameter (Bishop, 1959, Khalili and Khabbaz, 1998, Khalili et al., 2004, Lu et al., 2010, Alonso et al., 2010), the shear strength (Gao et al., 2020, Zhai et al., 2019, Vanapalli et al., 1996, Sheng et al., 2011) and the compression index (Zhou et al., 2012), which are often dependent on the soil suction or the water content. For this reason, SWCC is required for the ultimate limit state (ULS) and serviceability limit state (SLS) analysis of the geotechnical engineering infrastructure based on unsaturated soils, for example, the slope stability analysis of the earthwork embankments that lie above the groundwater level (Angerer, 2020, Zhang et al., 2014).

The heterogeneous pore structure of the soil causes a multimodality in its water retention behaviour. On the one hand, the conventional unimodal SWCC expressions are unable to describe the soil suction – water content relationship precisely for these soils. On the other hand, the relationships between the SWCC and the hydro-mechanical properties deduced from unimodal soils may fail in bimodal or multimodal soils. For these reasons, a general multimodal SWCC model is needed not only for assessing the dependency of hydraulic and mechanical properties on suction and water content, but also for the hydraulic and constitutive modelling to solve the boundary value problems of heterogeneous soils in geotechnical and geo-environmental engineering applications (e.g., stability and water flow analyses for the embankments and dams in vadose zone).

The objectives of the study are divided into three parts: (I) Developing a general multimodal pore size distribution model based on probability theory to quantify the soil pore structure and characterise its evolution along hydro-mechanical loading paths; (II) Developing an empirical SWCC model with an efficient and convenient parameter calibration approach to describe the soil suction – water content relationship of soils with heterogeneous microstructure; (III) Establishing a framework to predict the water retention behaviour of multimodal soils based on PSD measurement, considering the effects of volume change and the associated microstructure change during SWCC testing. By combining the proposed empirical and predictive SWCC models as well as the PSD model, a novel approach is developed in this thesis to quantify the soil suction, water content, and microstructure for the multimodal deformable soils in a unique framework.

1.2. Outline

This thesis is structured as follows: chapter 1 describes the motivation and objectives of the thesis. Chapter 2 introduces the experimental techniques for PSD measurement and presents the state-of-the-art experimental results for the microstructural evolution along mechanical, hydraulic and chemical loading paths. Chapter 3 reviews the basics of water retention behaviour and the relationship between SWCC and PSD. Chapter 4 describes the methodology for developing the SWCC and PSD models for multimodal soils. Chapter 5 summarises three

publications, including the development of the general multimodal PSD model based on probabilistic concept (Paper I), the empirical multimodal SWCC model with a convenient and efficient parameter calibration method (Paper II), and the predictive SWCC model based on the pore size distribution data of deformable multimodal soils (Paper III). Chapter 6 draws conclusions and proposes an outlook on further development and implementation of the proposed framework.

2. Basics of multimodal soil microstructure

2.1. Introduction

Porous material is widespread in industry (e.g., activated carbons, concrete, and ceramic), in the natural environment (e.g., wood, soils, and rocks), and even in biological tissues (e.g., human bones) (Yan and Cudmani, 2022a). The pore structure dominates the physical and chemical properties of porous material. For instance, experimental studies have shown that the in-situ strength of concrete depends significantly on its pore size characteristics and porosity (Kumar and Bhattacharjee, 2003). In this section, the focus is on the features of soil pore structure and the characteristics of the microstructural evolution along hydro-mechanical loading paths.

The soil microstructure characterised by the pore size distribution (PSD) has been widely investigated over the past decades, as it plays an essential role in the macroscopic hydro-mechanical behaviour of unsaturated soils, e.g., effective stress (Alonso et al., 2010), shear strength (Ng et al., 2020), compressibility (Mun and McCartney, 2015), swelling behaviour (Lloret et al., 2003), gas and liquid permeabilities (Mualem, 1976, Juang and Holtz, 1986a, Garcia-Bengochea, 1978) and material transport properties. Soil microstructural information is of great interest to geotechnical, geo-environmental, agricultural and mining engineers as it is very relevant to the practical applications in these engineering fields. For example, the microstructure of barrier soils (e.g., sand-bentonite mixtures or compacted bentonite) used as the sealing material in the nuclear waste containment structure, dominates the gas and liquid permeabilities of the material and evolves remarkably along hydro-mechanical, chemical and thermal paths (Manca et al., 2016, Lloret and Villar, 2007). In order to simulate the enrichment and migration of methane in the coalbed, the pore size distribution of coal has been extensively studied for the understating of multiphase flow in mining engineering (Xiong et al., 2020, Liu et al., 2020, Zhang et al., 2020). The pore structure of the soils and rocks encountered in these engineering fields is heterogeneous. Although a large number of PSD data (discontinuous data points) have been determined over the past few decades, a closed-form PSD expression, which facilitates the implementation of PSD information in constitutive and numerical modelling for these engineering applications, is still lacking.

2.2. Literature review

2.2.1. Experimental techniques and basics of soil pore structure

To date, a variety of testing techniques have been developed to measure the soil pore structure, which can be divided into two categories: image analysis and indirect approach (Xiong et al., 2020). The imaging technique includes, among others, scanning electron microscopy (SEM) (Romero et al., 1999, Cui et al., 2002, Manca et al., 2016, Cai et al., 2020, Collins and McGown, 1974), environmental scanning electron microscopy (ESEM) (Romero et al., 2011, MUSSO et al., 2013, Villar and Lloret, 2001, Sun et al., 2019), X-ray computed tomography (Gebrenegus et al., 2006) and nuclear magnetic resonance imaging (Wang and Ni, 2003, Sørland et al., 2007, Benavides et al., 2020). On the one hand, in order to obtain high-resolution photomicrographs, imaging techniques usually require sophisticated experimental facilities and hence are expensive. On the other hand, imaging techniques solely provide qualitative microstructural information of the limited observation area of the soil sample.

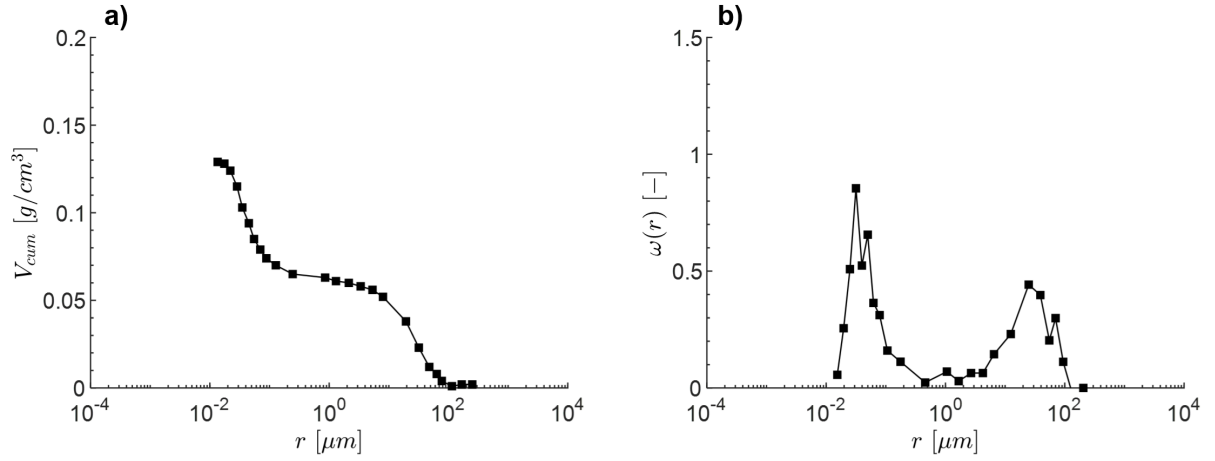


Fig. 2.1. MIP test data for a sand-clay mixture (70% sand + 30% clay) a) cumulative mercury intrusion curve b) pore size density curve (data from Juang and Holtz (1986b))

The indirect approach includes, among others, gas adsorption (GA) method (e.g., carbon dioxide adsorption and nitrogen adsorption) and mercury intrusion porosimetry (MIP) tests. Since the 1970s (e.g., Diamond (1970), Diamond (1971), Ahmed et al. (1974)), MIP tests, which are relatively less expensive, have been widely used in geotechnical and geo-environmental engineering to determine the pore size distribution data of soils and rocks. A small piece of specimen of a dried sample is placed in the penetrometer where a vacuum is applied to allow mercury to fill the chamber. Afterwards, the mercury pressure is incrementally raised, and mercury penetrates the voids from the larger to the smaller (Monroy et al., 2010). The volume of mercury intruded into the specimen and the corresponding pressure in mercury are continuously recorded. The relationship between the applied mercury pressure P_{Hg} and the entrance pore radius r can be expressed by the Washburn equation (Washburn, 1921):

$$P_{Hg} = -\frac{2T_{Hg} \cos \theta_{Hg}}{r} \quad (2.1)$$

Here, T_{Hg} ($= 0.484$ N/m at 25°C) denotes the surface tension of mercury and θ_{Hg} ($\approx 140^\circ$) represents the contact angle between mercury and soil particle surface. Equation (2.1) indicates that mercury, as a non-wetting fluid, cannot enter the cylindrical capillary channel of radius r unless a pressure P_{Hg} is applied. Converting the mercury pressure to the entrance pore radius via Eq. (2.1), MIP test data is conventionally presented in the plane of cumulative pore volume versus the entrance pore radius, referred to as the cumulative intrusion curve.

The cumulative intrusion curve from the MIP test can be expressed in terms of intruded void ratio e_{cum} (Romero et al., 2011, MUSSO et al., 2013, Monroy et al., 2010), intruded porosity n_{cum} (Birle, 2011), the normalized void ratio e_{cum}/e_{max} (e_{max} = maximum intruded void ratio, i.e., the initial void ratio of the sample before MIP test) (Juang and Holtz, 1986a) or the normalized pore volume in one gram dry soil V_{cum} (in cm^3/g , $V_{cum} = e_{cum}/\rho_s$, ρ_s = soil particle density) (Li and Zhang, 2009, Romero et al., 1999, Juang and Holtz, 1986b). Fig. 2.1a shows a cumulative mercury intrusion curve in terms of $V_{cum}(r)$ for a sand-clay mixture (70% sand + 30% clay).

Another useful information attained from the MIP test is the pore size density data $f(r)$ (i.e., the first derivative of the cumulative curve). When the pore radius is expressed in an arithmetic scale, the density data yields

$$\begin{cases} f(r_j) = -\frac{V_{cum}^i - V_{cum}^{i-1}}{r^i - r^{i-1}} \cdot \frac{\rho_s}{e_0} & i = 2, 3, \dots, N^* \\ r_j = \frac{r^i + r^{i-1}}{2} \end{cases} \quad (2.2)$$

Here, e_0 is the initial void ratio of the soil sample, and N^* denotes the data points number of the MIP tests. According to Juang and Holtz (1986a), as the investigated soil pore radius usually covers several orders of magnitude, it is more convenient to express the pore radius in a logarithmic scale. Then the density data can be presented in a dimensionless $\omega(r)$ form (Angerer, 2020, Juang and Holtz, 1986a):

$$\begin{cases} \omega(r_j) = -\frac{V_{cum}^i - V_{cum}^{i-1}}{\log(r^i/r^{i-1})} \cdot \frac{\rho_s}{e_0} & i = 2, 3, \dots, N^* \\ r_j = \sqrt{r^i \cdot r^{i-1}} \end{cases} \quad (2.3)$$

Fig. 2.1b demonstrates a pore size density curve in terms of $\omega(r)$ determined by the MIP test for the sand-clay mixture.

In conventional soil mechanics, the change of the void space is usually characterised by the volumetric state parameters, while the explicit morphological information of the void space, for example the change of the pore size distribution, is rarely considered. To better understand the hydro-mechanical behaviour of soil in saturated and unsaturated states, numerous studies have been undertaken to investigate the microstructure of different soil types. The experimental results have shown that the soil pore structure is heterogeneous in nature and can be unimodal, bimodal and even multimodal (i.e., more than two sub-porosities).

It is well known that clayey soils display a matrix-type structure when compacted on the wet side of optimum water content and a granular aggregate-type structure when compacted on the dry side of optimum water content (Delage and Lefebvre, 1984). The void space between the aggregates is denoted as interaggregate (or macro) porosity, and that within aggregates is denoted as intraaggregate (or micro) porosity. The “double structure” (Alonso et al., 1987) of compacted clayey soils was first reported in the pioneering work of Diamond (1970) and Barden and Sides (1970), and then confirmed in different clayey soils by other research, e.g., Sridharan et al. (1971) (kaolinite clay), Delage and Lefebvre (1984) (Champlain clay), Romero et al. (1999) (Boom Clay), Birle (2011) (Lias clay), Monroy et al. (2010) (London clay), MUSSO et al. (2013) (FEBEX bentonite), and Wang et al. (2014) (MX-80 bentonite), among others. Fig. 2.2 shows the PSD data determined by MIP tests conducted on two samples (Pm1 and Pm8) of Lias clay (liquid limit $w_L = 46.5\%$, plastic limit $w_p = 19.5\%$, particle density $\rho_s = 2.78 \text{ g/cm}^3$, standard proctor optimum water content $w_{opt} = 20.8\%$). The sample Pm1 was compacted on the dry side of the optimum water content (compaction water content $w = 16\%$) and the sample Pm8 on the wet side of the optimum water content ($w = 23.2\%$). The mercury intrusion curves in terms of V_{cum} and the dimensionless pore size density curves are shown in Fig. 2.2a and 2.2b, respectively. In the sample Pm8, the single pore family possesses a dominant pore radius of 63 nm. The pore structure of the sample Pm1 exhibits a distinct bimodal characteristic. The interaggregate porosity is characterised by a dominant pore radius of 6 μm , which is much larger than that in the intraaggregate regime of 30 nm (see Fig. 2.2b).

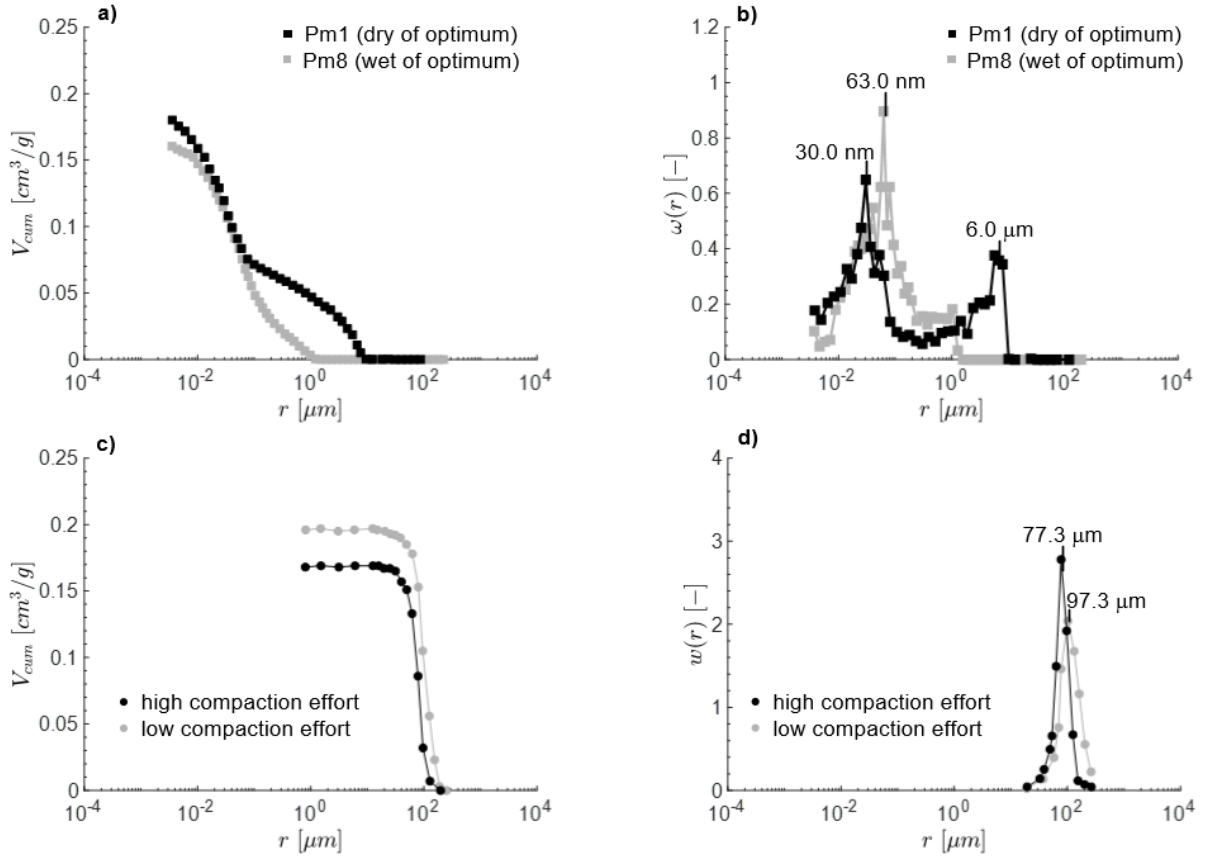


Fig. 2.2. MIP test data for fine-grained and coarse-grained soils a) cumulative mercury intrusion curves of Lias clay b) pore size density curves of Lias clay soils (data from Birle (2011)) c) cumulative mercury intrusion curves of Ottawa sand b) pore size density curves of Ottawa sand (data from Juang and Holtz (1986b))

A similar microstructural phenomenon was also found in compacted silts. Delage et al. (1996) observed two sub-porosities in the Jossigny silt ($w_L = 37.0\%$, $w_p = 19.0\%$, $\rho_s = 2.78$ g/cm³, $w_{opt} = 18.0\%$) samples compacted at dry of optimum and a matrix type microstructure in the samples compacted at wet of optimum. Recently, Ying et al. (2021) investigated the microstructure of a compacted sandy silt ($w_L = 29.0\%$, $w_p = 19.0\%$, $\rho_s = 2.71$ g/cm³, $w_{opt} = 17.0\%$) by means of MIP tests and ESEM micrographs. They reported that a granular aggregate structure with bimodal pore size distribution was well developed in the samples compacted at optimum water content and the dry side of optimum water content. These results revealed the fact that sample preparation conditions (e.g., compaction water content) can significantly influence the pore structure of fine-grained soils.

The pore size distribution of compacted coarse-grained soils is relatively simple and uniform. Juang and Holtz (1986b) performed MIP tests on two compacted samples of Ottawa sand (poorly graded clean quartz sand, $d_{10}/d_{30}/d_{60}/d_{100} = 0.30/0.40/0.60/0.80$ mm) with different initial dry densities, 1.62 g/cm³ (for the loose sample) and 1.72 g/cm³ (for the dense sample). The mercury intrusion curves and the dimensionless pore size density curves are demonstrated in Fig. 2.2c and 2.2d, respectively. Both samples show a remarkable unimodal characteristic. Compared to the compacted Lias clay samples, the pore size distribution of Ottawa sand, on the one hand, covers a narrower range from about 20 μm to 300 μm (see Fig. 2.2d). On the other hand, the dominant pore sizes of both samples (77.3 μm for the dense sample and 97.3 μm for the loose sample) are much larger than those of the inter- (= 6 μm) and intra-aggregate porosities (= 30 nm) in sample Pm1 of Lias clay. It is also noted that the peak value of the density curve at the dominant pore radius in Ottawa sand (between 2.0 to 3.0) is much higher than that in the inter- and intra-aggregate pore regime in Lias clay (between 0.4 to 1.0). All of these features in the

soil microstructure could be attributed to the uniformity of the grain size distribution and the relatively large mean grain size of Ottawa sand. As a poorly graded clean quartz sand, the uniformity coefficient $C_U (= d_{60} / d_{10})$ of Ottawa sand is equal to 2.0.

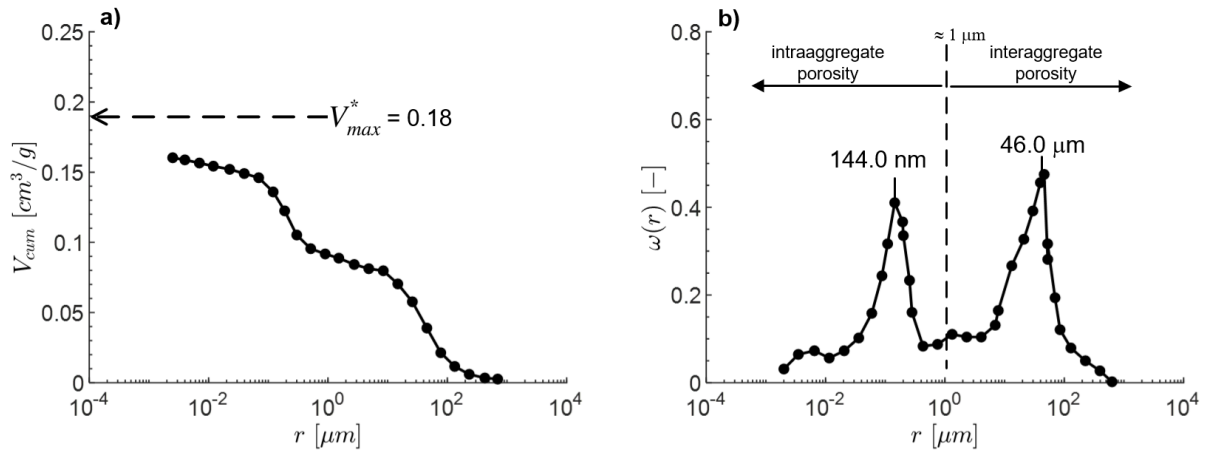


Fig. 2.3. MIP test data for a sand-bentonite mixture (80% quartz sand + 20% MX80 bentonite) after compaction a) cumulative mercury intrusion curve b) pore size density curve (data from Manca et al. (2016))

The pore structure of gap-graded soils or mixed soils is of great interest to geotechnical and geo-environmental engineers. For example, sand-clay mixtures have been widely used as a self-sealing material for engineering barriers in deep geological nuclear waste repositories due to their low liquid and gas conductivity and swelling potential (Nagra, 2008, Manca et al., 2016). Knowledge of the microstructure of sand-clay mixtures is necessary to understand their macroscopic hydro-mechanical behaviour, which plays an essential role in evaluating the performance of the engineering barriers and the safety assessment of the overall repository (Wang et al., 2013). Manca et al. (2016) analysed the evolving microstructure of a sand-bentonite mixture (i.e., a mixture of 80% quartz sand and 20% MX-80 bentonite, $\rho_s = 2.67 \text{ g/cm}^3$) under hydro-chemo-mechanical loadings by means of SEM photomicrograph and MIP tests. The mercury intrusion curves and the pore size density curves determined on an as-compacted sample (initial dry density $\rho_d = 1.8 \text{ g/cm}^3$, initial suction $s_0 = 280 \text{ kPa}$) are shown in Fig. 2.3a and 2.3b, respectively. As can be seen, the pore structure demonstrates a clear bimodal characteristic. The pore radius of $1 \mu\text{m}$ is approximated as the delimiting value to distinguish the inter- and intra-aggregate porosities. The interaggregate porosity presents the pore family between the clay aggregates and sand grains, and the intra-aggregate porosity corresponds to the void space within clay aggregates. The intra-aggregate dominant pore radius is equal to 144 nm , which is close to that of the compacted Lias clay (see Fig. 2.2b). The interaggregate dominant pore radius is equal to $46 \mu\text{m}$, which is greater than that of the Lias clay and close to that of the Ottawa sand.

In Fig. 2.3a, one sees that the maximum intruded mercury volume ($\approx 0.16 \text{ g/cm}^3$) does not reach the total void volume of the sample ($V_{max}^* = e_0 / \rho_s = 0.18 \text{ g/cm}^3$). Manca et al. (2016) ascribed the gap to the planar inter-layer void space between the smectite sheets within the clay platelets. During hydration, due to the invasion of water molecules, the distance between the smectite sheets varies from a minimum of 0.3 nm to a maximum of 1.2 nm , which is far lower than the minimum detectable pore size of mercury intrusion porosimetry ($= 4 \text{ nm}$) (Manca et al., 2016). The increase of the inter-layer pores results in the expanding of the aggregates, and hence is directly related to the macroscopic swelling behaviour and the “self-sealing” ability of the soil. For this reason, the existence of the inter-layer porosity cannot be neglected for the bentonite-enriched soils, although they are

undetectable in MIP tests. Thus, three pore families exist in the sand-bentonite mixture, namely the interaggregate, the intra-aggregate and the inter-layer porosities. The interaction of the sub-porosities, which significantly evolves along hydro-chemo-mechanical loading paths, leads to a complex microstructural behaviour of the soil.

By analysing the MIP data of fine-grained, coarse-grained and gap-graded soils, following primary conclusions can be drawn on the basics of soil microstructure:

- The maximum or mean pore radius of the soil is closely related to the grain size distribution. In general, the dominant pore radius of a coarse-grained soil is larger than that of a fine-grained soil with a single pore mode (e.g., reconstituted sample or the sample compacted at wet of optimum) and the inter- and intra-aggregate porosities of a fine-grained soil with a bimodal pore mode (e.g., the sample compacted at dry of optimum).
- The microstructures of the soils encountered in geotechnical and geo-environmental engineering applications are heterogeneous. On the one hand, the modality number N is a varying integer: the microstructure can exhibit unimodal ($N = 1$, e.g., Ottawa sand, and Lias-clay compacted at wet side), bimodal ($N = 2$, e.g., Lias-clay compacted at dry side) and even multimodal ($N \geq 3$, e.g., sand-bentonite mixture) characteristics. On the other hand, the pore size can range from one to several orders of magnitude. For example, the pore size of Ottawa sand ranges from $20 \mu\text{m}$ to $300 \mu\text{m}$, while that of the sand-bentonite mixture ranges from $0.002 \mu\text{m}$ to $500 \mu\text{m}$.
- The maximum frequency of the density curve at the dominant pore radius is highly related to the uniformity of the grain size distribution, e.g., the poorly graded Ottawa sand possesses the highest peak value of the density curve at the dominant pore radius.

2.2.2. Microstructural evolution

In recent years, particular attention has been paid to the microstructural evolution induced by mechanical, hydraulic and chemical loadings. In this section, the influence of compaction effort, hydration and water salinity on the soil pore structure is discussed.

In general, an increase in the compaction effort or the consolidation pressure on a single pore mode soil results in a decrease in its dominant pore size (or mean pore size), accompanying a reduction in the overall void volume. For instance, the dominant pore radius of Ottawa sand decreases from $97.3 \mu\text{m}$ to $77.3 \mu\text{m}$ due to the increased compaction effort. Correspondingly, the pore size density curve shifts along the abscissa, as shown in Fig. 2.2d. In addition, the shape of the pore size density curve remains unchanged as it is related to the soil grain size distribution, which is not affected by mechanical loading without the occurrence of particle breakage.

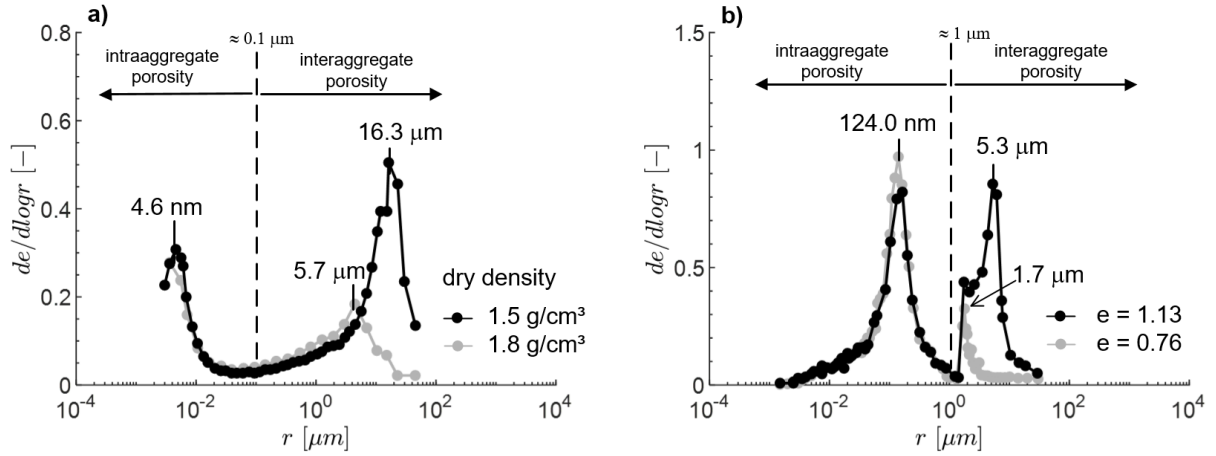


Fig. 2.4. Influence of compaction on soil microstructure a) pore size density curves for FEBEX bentonite (data from Lloret et al. (2003)) b) pore size density curves for a sand clay mixture (data from Li and Zhang (2009))

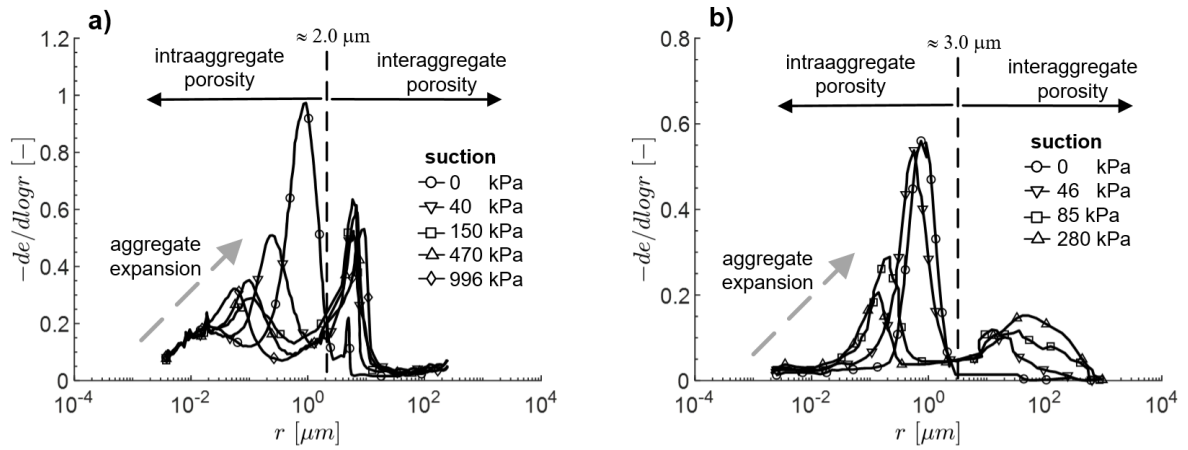


Fig. 2.5. Influence of suction on soil microstructure a) microstructural evolution of unsaturated compacted London clay during wetting under a constant vertical load (data from Monroy et al. (2010)) b) microstructural evolution of an unsaturated compacted sand bentonite mixture during wetting under isochoric condition (data from Manca et al. (2016))

In bimodal soils, numerous experimental studies have shown that both the volume and the mean pore radius of the interaggregate porosity decrease with increasing compaction effort or consolidation pressure, while the intra-aggregate pore structure remains almost unaffected. Lloret et al. (2003) investigated the influence of compaction effort on the bimodal microstructure of FEBEX bentonite ($w_L = 102 \pm 4 \%$, $w_p = 53 \pm 3 \%$, $\rho_s = 2.70 \text{ g/cm}^3$, montmorillonite content $> 90\%$, specific surface area $S = 32 \pm 3 \text{ m}^2/\text{g}$). MIP tests were carried out on two samples compacted to very different dry densities, i.e., 1.5 g/cm^3 and 1.8 g/cm^3 . The pore size density curves in terms of $-de_{Hg}/d \log r$ (e_{Hg} represents the mercury intrusion volume in terms of void ratio) are demonstrated in Fig. 2.4a, showing a remarkable bimodal characteristic. A delimiting pore radius to distinguish the inter- and intra-aggregate porosity is approximated at about $0.1 \mu\text{m}$. From Fig. 2.4a one sees that the interaggregate pore volume (i.e., the area under the interaggregate sub-curve) remarkably decreases with increasing compaction effort and dry density. Simultaneously, the interaggregate dominant pore radius decreases from $16.3 \mu\text{m}$ to $5.7 \mu\text{m}$. In contrast, the intra-aggregate porosity is not affected. Both the intra-aggregate pore volume and the dominant pore radius ($= 4.6 \text{ nm}$) remain constant.

Li and Zhang (2009) reported a similar characteristic in the microstructural evolution of a lean clay with sand ($w_L = 47.0\%$, $w_p = 32.0\%$, $\rho_s = 2.64\text{ g/cm}^3$, $w_{opt} = 20.5\%$) during compaction, as shown in Fig. 2.4b. MIP tests were carried out on a loose ($e_0 = 0.76$) and a dense sample ($e_0 = 1.13$), and both samples demonstrate a clear bimodal pore size distribution due to the existence of aggregates formed by the fine contents. A delimiting pore radius of about $1\ \mu\text{m}$ is estimated to separate the inter- and intra-aggregate parts. Again, the reduction of the overall volume during compaction is attributed to the decrease of the interaggregate porosity, while the intra-aggregate pore volume remains unchanged. The interaggregate dominant pore radius decreases from $5.3\ \mu\text{m}$ to $1.7\ \mu\text{m}$ as the interaggregate pore volume decreases. These observations in FEBEX bentonite and the lean clay with sand imply that in bimodal soils the compaction procedure (at dry side of proctor optimum) solely causes the rearrangement of the sand grains and clay aggregates with a constant intra-aggregate porosity. The interaggregate void space progressively reduces with increasing compaction effort, leading to a decrease in the interaggregate dominant pore radius.

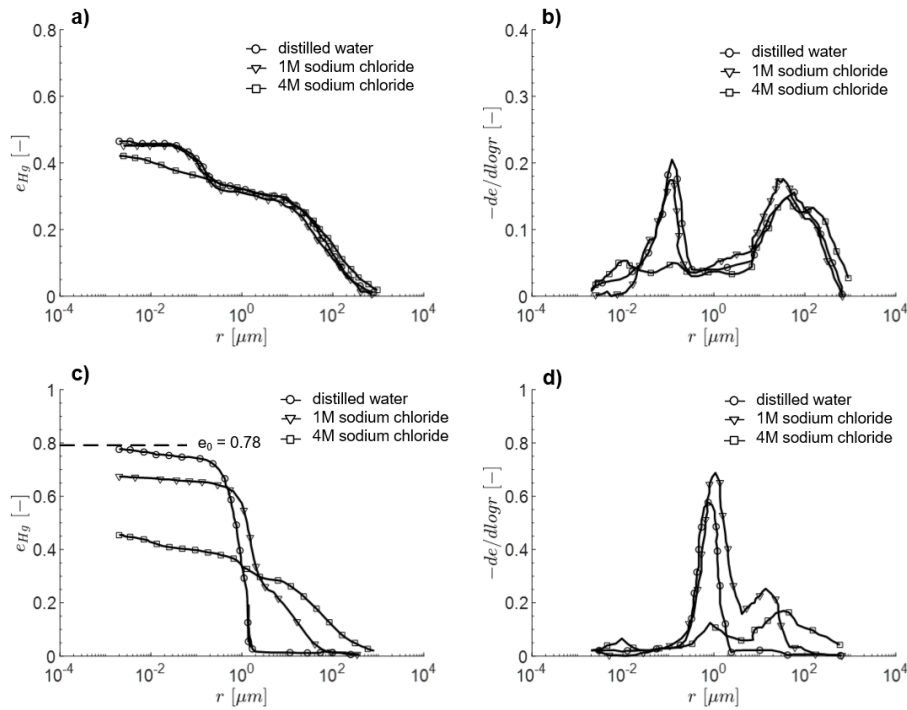


Fig. 2.6. Influence of pore water salinity on microstructure evolution of sand bentonite mixture during hydration (initial dry density $\rho_d = 1.5\text{ g/cm}^3$) a) cumulative curves of as-compacted samples b) pore size density curves of as-compacted samples c) cumulative curves of saturated samples d) pore size density curves of saturated samples (data from Manca et al. (2016))

The soil microstructure also alters strongly with hydraulic loading. Fig. 2.5a reveals the evolving pore structure of compacted London clay ($w_L = 83.0\%$, $w_p = 29.0\%$, $\rho_s = 2.70\text{ g/cm}^3$) during a wetting process (data from Monroy et al. (2010)). The soil shows a typical bimodal pore structure at the as-compacted state with an initial suction of 996 kPa. A delimiting pore radius of $2.0\ \mu\text{m}$ is approximated for distinguishing the inter- and intra-aggregate porosity. The compacted sample was then progressively wetted to different suction levels, i.e., 470 kPa, 150 kPa, 40 kPa and 0 kPa (saturated state) under a constant vertical stress of 7 kPa (i.e., free swelling condition). The soil microstructure at each suction level was measured by MIP tests, and the pore size density curves are presented in Fig. 2.5a. As can be seen, the intra-aggregate pore volume increases with decreasing suction, which could be attributed to the expansion of aggregates. It is also noted that the interaggregate pore volume is almost

constant in the suction regime from 996 kPa to 40 kPa and decreases dramatically with decreasing suction from 40 kPa to 0 kPa. In the saturated state, the interaggregate pores almost vanish, and the pore size distribution turns into a unimodal pattern, meaning that the modality number N decreases from two to one along the wetting path.

The sand-bentonite mixture used as the “self-sealing” material in the nuclear waste disposals, usually undergoes hydraulic, thermal and chemical loadings (e.g., water salinity) due to the surrounding hydro-geological environment, resulting in a complex evolution of microstructure. Manca et al. (2016) investigated the microstructural evolution of a compacted sand-bentonite mixture (80% quartz sand + 20% MX-80 bentonite, $\rho_s = 2.67 \text{ g/cm}^3$) along a wetting path under isochoric condition. The as-compacted sample was then progressively wetted from an initial suction level at 280 kPa to 85 kPa, 40 kPa and 0 kPa in a constant volume cell. Fig. 2.5b shows the MIP test data at various suction levels, and a delimiting pore radius of $3.0 \mu\text{m}$. Similar to London clay, the aggregates in the soil expand during the wetting process. This leads to an increase in the intra-aggregate void space, whilst the interaggregate pore volume decreases due to the isochoric condition. In the saturated state, the interaggregate pore mode vanishes because the macro voids formed by sand grains are fully filled with clay particles, resulting in a unimodal pore size distribution.

In nuclear waste storage applications, saline water from the supporting concrete structure or the host rock can inhibit the “sealing ability” (i.e., the expansion of bentonite) of the sand-bentonite mixture and consequently affect its liquid and gas conductivity. Therefore, the influence of the water salinity on the soil microstructure evolution is especially concerned. Fig. 2.6a and 2.6b show the MIP data of the as-compacted samples of sand-bentonite mixture prepared with different types of pore fluids, namely distilled water, 1M sodium chloride (i.e., NaCl solution at 1 mol/L concentration) and 4M sodium chloride. It is found out that the cumulative PSD curves and the density curves for the samples prepared with distilled water and 1M sodium chloride are almost identical. This means that the soil pore structure is not affected by the water salinity at low concentrations of 0 to 1 mol/L. However, as the water salinity increases from 1 mol/L to 4 mol/L, the total pore volume as well as the intra-aggregate porosity degrades, whilst the interaggregate pore volume is slightly affected. This observation reveals the fact that saline water with high concentration significantly inhibits the initial swelling of aggregates during the mixture preparation (Manca et al., 2016).

Fig. 2.6c and 2.6d demonstrate the cumulative and density curves of the saturated samples (wetted from as-compacted state under isochoric condition) at different sodium chloride concentrations. In comparison with Fig. 2.6a and 2.6b, respectively, the influence of the water salinity on the microstructural evolution during wetting is assessed. For the sample hydrated with distilled water, the maximum mercury intrusion volume is close to the total void volume of the soil (the dashed line in Fig. 2.6c). This phenomenon implies a complete swelling of the bentonite assemblage and a subsequent splitting of the smectite sheets, resulting in the vanishing of inter-aggregate and inter-layer porosities. Eventually, a monomodal porosity at the intra-aggregate scale is formed, which can be fully detected in MIP tests. For the sample hydrated with saline water at 1 mol/L concentration, there is a distinguishing gap between the total mercury intrusion volume and the total void volume of the soil. The interaggregate porosity is preserved when the sample is wetted from the as-compacted state to the fully saturated state. A similar pore structure is also shown in the sample hydrated with saline water at 4 mol/L concentration. Based on these experimental results, it can be concluded that the water salinity retards the swelling of the bentonite at both the intra-aggregate and the interlayer levels.

2.2.3. Existing multimodal PSD models

From the experimental evidence in the previous sections, one sees that soil pore size distribution can cover several orders of magnitude and vary from a unimodal mode (e.g., granular soils) to a bimodal (e.g., compacted clayey soils) or even a multimodal mode (e.g., sand-bentonite mixture). In deformable soils, the pore structure alters remarkably along mechanical, hydraulic and chemical loading paths. Therefore, a general multimodal pore size distribution model is needed to quantify the heterogeneous pore structure and capture the essential features of the microstructural evolution.

Ross and Smettem (1993) proposed that a multimodal pore size distribution expression could be derived from a multimodal soil water characteristic curve model, which is a superposition of several unimodal sub-curves (Yan and Cudmani, 2022a):

$$f(s) = \sum_{i=1}^N \phi_i \frac{dS_{e,i}(s)}{ds} \quad (2.4)$$

Here, $S_{e,i}(s)$ represents the SWCC (in terms of effective degree of saturation) dominated by a sub-porosity and ϕ_i is the weighing factor fulfilling the condition:

$$\sum_{i=1}^N \phi_i = 1 \quad (2.5)$$

where N is the modality number. Experimental results in the literature, e.g., Monroy et al. (2010), Zhai et al. (2020b) and Cai et al. (2020), have shown that the microstructure of deformable soils highly depends on suction and hence can alter significantly during the SWCC testing. This means that the PSD-curve derived from a SWCC measurement is not representative of a rigid soil pore structure (Yan and Cudmani, 2022a). Additionally, the Ross and Smettem model is incapable of accounting for the changes in microstructure during hydro-mechanical-chemical loadings. A further modification is also difficult since the parameters of the model are fitting parameters and cannot be determined independently from one another.

2.3. Summary

The soil microstructure is a fundamental property dominating the essential features in the hydro-mechanical behaviour of fully and partially saturated soils, which is necessary in various practical applications in geotechnical, geo-environmental, mining and agricultural engineering. In the past decades, MIP tests have been widely used to determine the pore size distribution of different kinds of soils, varying from a simple general soil to a complex mixture of fine-grained and coarse-grained soils.

In general, the soil pore size distribution covers a wide range with several orders of magnitudes and consists of several sub-porosities, for instance, interlayer, intra-aggregate and interaggregate porosity. The multimodal soil pore structure significantly evolves when the soil is subjected to mechanical (e.g., compaction, consolidation, shearing), hydraulic (e.g., wetting and drying cycles), chemical (e.g., different salt concentration in pore water) or even thermal loadings (Houhou et al., 2021). The microstructure evolution is characterised by the changes in the volume, maximum and dominant pore radius, the maximum frequency (i.e., the peak value of the density curve at

the dominant pore radius) of each sub-porosity as well as the modality number of the overall pore size distribution. Although a large amount of soil pore size distribution data has been experimentally determined in the past decades, a general multimodal pore size distribution model that is capable of precisely describing the soil pore size distribution is still missing. To solve this problem, a general multimodal PSD framework was developed in Paper I (Yan and Cudmani, 2022a), which is summarised in section 5.1.

3. Basics of multimodal water retention behaviour

3.1. Introduction

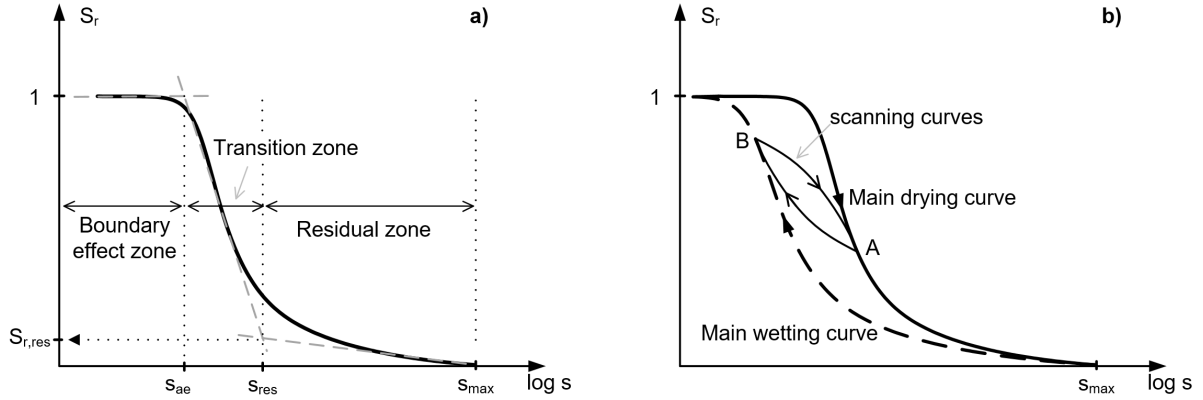


Fig. 3.1. Schematic illustration for water retention behaviour of unimodal soils a) a typical soil water characteristic curve for desiccation b) hydraulic hysteresis

The soil water characteristic curve (SWCC) is a mathematical function describing the water content held by the soil at a given suction level (Abed and Sołowski, 2021). SWCC plays a key role in practical applications of unsaturated soils, as many important hydraulic and mechanical properties such as the unsaturated hydraulic conductivity (Leong and Rahardjo, 1997a, Fredlund et al., 1994, Rahimi et al., 2015, Zhai et al., 2017) and the shear strength (Lin et al., 2022, Vanapalli et al., 1996, Zhai et al., 2019, Sheng et al., 2011), are closely related to the suction or the water content of the soil. Thus, SWCC is one of the most fundamental hydraulic characteristics of the soil (Assouline et al., 1998).

Fig. 3.1a schematically shows a typical SWCC for desiccation in terms of the degree of saturation S_r . The matric suction s , defined as the difference between pore-air pressure and pore-water pressure ($s = u_a - u_w$, where u_a and u_w represent the pore-air and pore-water pressure, respectively), is traditionally expressed in a logarithmic scale. Three special suction values, i.e., the air entry suction s_{ae} , the residual suction s_{res} and the maximum suction s_{max} , can be identified based on the graphical properties of SWCC (Vanapalli et al., 1999). The air entry suction s_{ae} represents the suction value required to desiccate the largest pore in the soil, also referred to as the “bubbling pressure” (Brooks and Corey, 1964). For a given SWCC, the air entry suction s_{ae} is conventionally identified as the suction value at the intersection between the tangent line of the constant slope part of the SWCC and the horizontal line at 100% saturation (see Fig. 3.1a). The maximum suction s_{max} represents the suction value at which the SWCC ends in a completely dry state (i.e., zero water content). Fredlund and Xing (1994) proposed a maximum suction of 1000 MPa for all soil types based on the thermodynamic consideration of Richards (1965). The residual suction s_{res} corresponds to the suction value from which the liquid phase becomes discontinuous (Vanapalli et al., 1999). A very large reduction in suction is required to remove the remaining water in the soil (Fredlund and Xing, 1994). However, this definition is ambiguous. To quantify the residual suction s_{res} of a given SWCC, Vanapalli et al. (1999) proposed to extend a second tangent line from the end part of the SWCC through the maximum suction (see Fig. 3.1a). Then the suction value and water content at the intersection of the two tangent lines are defined as the residual suction s_{res} and the residual degree of saturation $S_{r,res}$, respectively.

According to Vanapalli et al. (1999), the whole desiccation process can be divided into three stages, i.e., the boundary effect zone, the transition zone and the residual zone (see Fig. 3.1a). In the boundary effect zone (suction lower than air entry value), the soil remains fully saturated (i.e., $S_r = 1$), and all pores are filled with water. After the air entry suction is surpassed, the curve enters the transition zone (suction between air entry value and residual suction). In this stage, the water stored in the capillary channels is rapidly drained along with a strong reduction in the liquid phase connectivity as the suction increases. The desiccation process in the transition zone is dominated by the capillary effect (i.e., the presence of menisci) and hence strongly depends on the soil pore size distribution. The suction regime between the residual suction and the maximum suction is defined as the residual zone where the liquid phase becomes discontinuous and soil desiccation is controlled by adsorption effect. As shown in Fig. 3.1a, a large change in suction is needed to drain the water from the soil until maximum suction is reached at a completely dry state.

Fig. 3.1b schematically presents typical soil water characteristic curves in a wetting and drying cycle: one determined by drying a fully saturated sample (i.e., the main drying curve depicted in solid line) and the other by wetting a fully dry sample (i.e., the main wetting curve depicted in dashed line). It is not hard to find out that the soil water content is lower in the wetting curve than in the drying curve at a given suction level. This phenomenon is referred to as “hydraulic hysteresis”, which can be attributed to the following reasons: (I) The non-uniformity in the pore sizes of the connected capillary channels causes the so-called “ink-bottle effect” (Haines, 1930). (II) The drying contact angle is smaller than the wetting contact angle at the soil solid-pore water interface (Fredlund and Rahardjo, 1993). (III) Irreversible changes in pore size distribution and volumetric deformation during a wetting-drying cycle. If one re-saturates a sample from a hydraulic state at the main drying curve (e.g., point A in Fig. 3.1b), the subsequent suction-water content relationship for the rewetting follows a loop within the main wetting and drying curves and eventually lands on the main wetting curve (e.g., point B in Fig. 3.1b). A similar phenomenon can also be observed by re-desiccating a sample from a hydraulic state at the main wetting curve (e.g., the loop from point B to point A in Fig. 3.1b). These rewetting and redrying loops within the main wetting and drying boundaries are called “scanning curves”.

To facilitate the implementation of water retention behaviour in practical applications, SWCC is usually expressed as an equation. So far, numerous empirical models to simulate the unimodal soil water characteristic curve have been developed. Among them, the Brooks and Corey model (BCM) (Brooks and Corey, 1964), the van Genuchten model (VGM) (Van Genuchten, 1980) and the Fredlund and Xing model (FXM) (Fredlund and Xing, 1994) are most widely used. BCM (Brooks and Corey, 1964) is a piecewise SWCC function with two fitting parameters which can be expressed as

$$S_e(s) = \begin{cases} 1, & s \leq s_{ae} \\ \left(\frac{s}{s_{ae}}\right)^{-\lambda}, & s > s_{ae} \end{cases} \quad (3.1)$$

Here, λ is a fitting parameter related to the soil pore size distribution, s_{ae} represents the air entry suction and S_e is the effective degree of saturation defined as

$$S_e(s) = \frac{S_r(s) - S_{r,res}}{S_{r,max} - S_{r,res}} \quad (3.2)$$

where $S_{r,max}$ is the maximum degree of saturation at zero suction. Van Genuchten (1980) improved BCM and proposed a SWCC expression with three fitting parameters in a continuous form:

$$S_e(s) = [1 + (\alpha s)^n]^{-m} \quad (3.3)$$

Here, the parameter α represents the inverse of the air entry suction in the unit $[P^{-1}]$, n and m are two fitting parameters related to the soil pore size distribution. Later, Fredlund and Xing (1994) pointed out that VGM (Eq. (3.3)) curve drops to zero in a narrow suction range, and hence is not suitable to describe the suction-water content relationship at high suction regime (i.e., greater than residual suction). Moreover, the SWCC should end up in a completely dry state at the maximum suction. Based on these considerations, Fredlund and Xing (1994) suggested the following closed-form expression to describe the soil water retention behaviour:

$$S_e(s) = \left[1 - \frac{\ln(1 + s/S_{res})}{\ln(1 + s_{max}/S_{res})} \right] \{ \ln[e + (s/a)^n] \}^{-m} \quad (3.4)$$

Here, a is a fitting parameter related to the air entry suction, n is a fitting parameter reflecting the soil pore size distribution, and m is a fitting parameter dominating the asymmetry of the curve in the conventional $\log s - S_r$ plane. These unimodal SWCC models have been successfully applied to many geotechnical and geo-environmental problems, such as the simulation of water distribution or movement in the vadose zone (Lu, 2016). However, they are limited for simulating the water retention behaviour of the soils with heterogeneous pore structure, which is introduced in the following sections.

3.2. Literature review

3.2.1. Water retention behaviour of soils with heterogeneous pore structure

Experimental evidence in recent studies has shown that two or more independent sub-porosities (see section 2.2.1), resulting from fine particle aggregation or gap-graded grain size distribution, can exist in compacted fine-grained soils (Romero et al., 2011, Lloret and Villar, 2007), mixed soils (Juang and Holtz, 1986b, Burger and Shackelford, 2001b) and undisturbed natural soils (Othmer et al., 1991, Durner, 1994). As a result, the water retention curves of such soils show bimodal or even multimodal characteristics, which cannot be accurately described by the empirical unimodal SWCC models, e.g., BCM, VGM and FXM.

Fig. 3.2 demonstrates the multimodality in SWCCs resulting from the heterogeneous pore size distribution. Zhao et al. (2013) performed a comprehensive study on the bimodal hydraulic and shear behaviour of an unsaturated, well-graded sand with silt and gravel (SW-SM with gravel, fine content = 10%, $w_{opt} = 10\%$, $\rho_s = 2.64 \text{ g/cm}^3$). The samples tested were compacted to a target initial void ratio of 0.62 at a saturation degree of 39.8%. Mercury intrusion porosimetry tests were conducted to detect the soil pore structure. The pore size density data of a saturated sample and an oven-dried sample (first saturated before oven drying) are shown in Fig. 3.2a. One sees that the pore structure in the saturated state consists of two sub-porosities, one originating from the void space between the gravel and sand particles (interaggregate porosity, dominant pore radius is equal to $28 \mu\text{m}$), and the other from the void space within the aggregate of fines (intra-aggregate porosity, dominant pore radius is equal to

1.04 μm). A delimiting pore radius is identified at about 3.0 μm . From the pore size distribution curve of the oven-dried sample, it is observed that the bimodal characteristic of the microstructure remains unchanged during the drying process. However, the volume of the aggregates decreases from saturated to completely dry states, which is reflected by the remarkable reduction in area under the intra-aggregate sub-curve. Simultaneously, the intra-aggregate dominant pore radius decreases from 1.04 μm (in the saturated state) to 0.52 μm (in the completely dry state). In contrast, the area under the interaggregate sub-curve is nearly unchanged, and the interaggregate dominant pore radius increases slightly from 28 μm (in the saturated state) to 40 μm (in the completely dry state). This means that the interaggregate porosity within the skeleton of grain-to-grain contact is almost unaffected by oven drying.

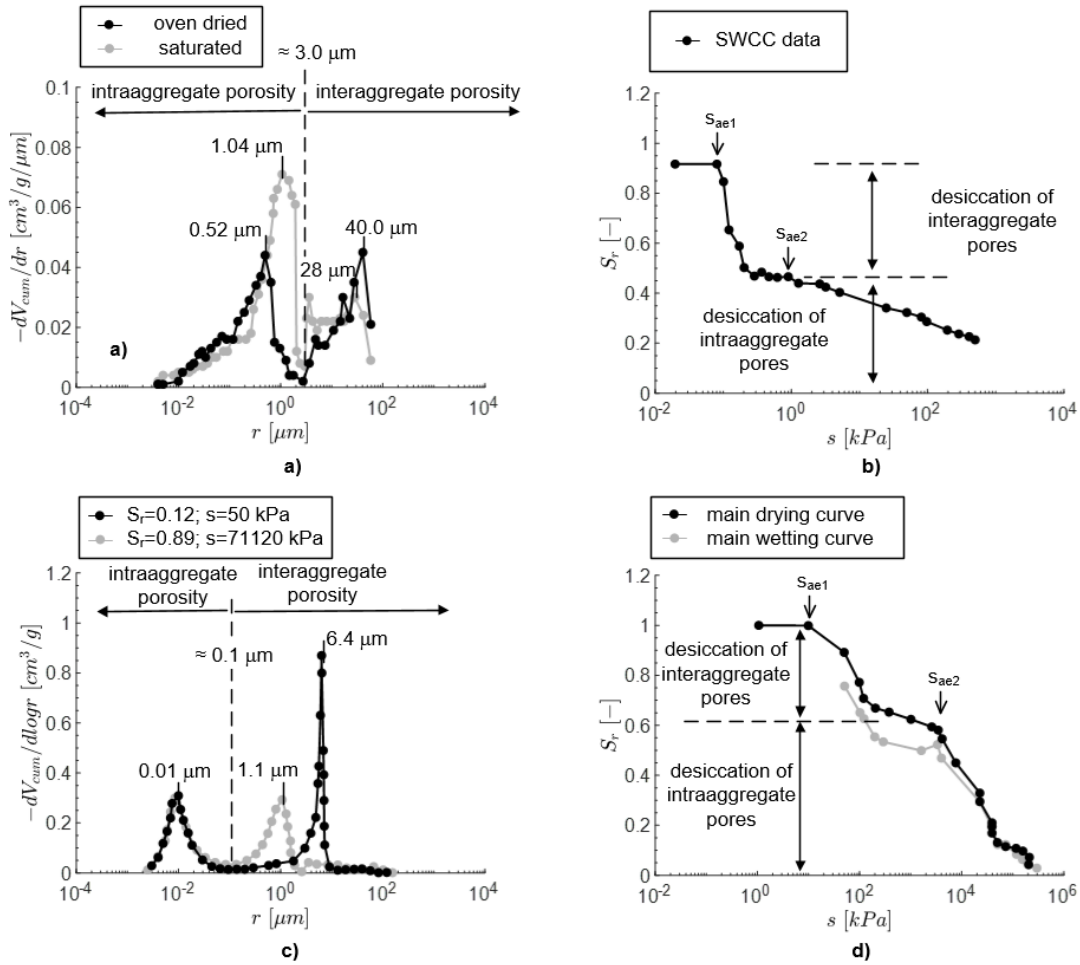


Fig. 3.2. Bimodal SWCC induced by bimodal pore structure a) bimodal pore size distribution of SW-SM with gravel in the saturated and completely dry states (data from Zhao et al. (2013)) b) SWCC measurement of SW-SM with gravel c) bimodal pore size distribution of compacted Guilin lateritic soil at high ($S_r = 0.89$) and low ($S_r = 0.12$) water content d) bimodal main wetting and drying curves of compacted Guilin lateritic soil (data from Cai et al. (2020))

As a result of the bimodal pore structure, the water retention behaviour shows distinct bimodal characteristics as shown in Fig. 3.2b. The SWCC measurement was performed on a sample that was saturated from the as-compacted state. The maximum degree of saturation ($S_{r,max} \approx 0.9$) of less than 1.0 at very low suction level ($s = 0.02 \text{ kPa}$) could be attributed to the entrapped air in the soil sample. After the imposed suction surpasses the interaggregate air entry value ($s_{ae1} \approx 0.08 \text{ kPa}$), the water stored in the interaggregate pores is first drained with

increasing suction. Due to the relatively uniform pore size distribution, the interaggregate porosity is fully drained in a narrow suction range. At this stage, the aggregates remain saturated because the current suction is lower than the air entry value of the intra-aggregate porosity ($s_{ae2} \approx 0.9$ kPa). Afterwards, the water retention curve enters a transition stage where the overall water content is almost constant as the intra-aggregate porosity remains saturated, as shown in Fig. 3.2b. The onset of the secondary reduction in the overall water content is observed at the air entry suction of the intra-aggregate porosity. The drainage of intra-aggregate pore water with increasing suction is apparently linear in the semilogarithmic plot. Moreover, we see that the drainage of the intra-aggregate is much slower than that of the interaggregate porosity (i.e., the slope of the curve is much smaller than that of the interaggregate porosity), which is ascribed to the relatively dispersed pore size distribution of the intra-aggregate porosity (see Fig. 3.2a).

Cai et al. (2020) investigated the bimodal water retention behaviour and the pore size distribution of compacted Guilin lateritic soil (high plastic clay, $w_L = 67.3\%$, $w_p = 38.1\%$, $w_{opt} = 26.0\%$, $\rho_s = 2.74$ g/cm³). The soil pore structure was measured by means of MIP tests. Fig. 3.2c demonstrates the pore size distributions of the compacted samples at high ($S_r = 0.89$, initial suction $s = 71120$ kPa) and low ($S_r = 0.12$, initial suction $s = 50$ kPa) water content, which exhibit a distinct bimodal characteristic. A delimiting pore radius of $0.1 \mu\text{m}$ is approximated to separate the intra- and inter-aggregate porosities. The intra-aggregate porosity possesses a dominant pore radius of $0.01 \mu\text{m}$ and remains almost unchanged when suction increases from 50 to 71120 kPa. In contrast, the interaggregate dominant pore radius increases from 1.1 to $6.4 \mu\text{m}$ with decreasing water content, indicating the presence of fissures in the compacted lateritic soil in a relatively dry state. Again, the bimodal soil microstructure causes a bimodal water retention behaviour, as shown in Fig. 3.2d. The pore water stored in the voids between clay aggregates is drained after surpassing the interaggregate air entry value ($s_{ae1} \approx 10$ kPa), whilst the intra-aggregate porosity remains saturated. Different from the observation in SW-SM with a gravel soil, the water content of the compacted lateritic soil decreases slightly with the suction in the transition stage, which corresponds to the overlapping of the pore size distributions of the inter- and intra-aggregate porosities. A rapid drainage of pore water from the clay aggregates is observed after the current suction surpasses the intra-aggregate air entry value ($s_{ae2} \approx 2.6 \times 10^3$ kPa). In addition, the main wetting curve shows a similar shape as the main drying curve with a distinct bimodal characteristic. Hydraulic hysteresis was also observed in compacted lateritic soils, i.e., the main wetting curve is not consistent with the main drying curve, especially in the range controlled by the interaggregate porosity and the transition stage (i.e., the suction range $s \leq 2.6 \times 10^3$ kPa, see Fig. 3.2d).

The experimental results in Fig. 3.2 reveal the fact that multimodal pore size distribution leads to a multimodality in the water retention behaviour. Conversely, the multimodality in the water retention behaviour indicates the presence of a multimodal pore size distribution in soil. On the one hand, the multimodal water retention behaviour cannot be accurately quantified by conventional unimodal expressions. On the other hand, the relationship between the SWCC and the hydro-mechanical properties (e.g., unsaturated hydraulic conductivity and shear strength) deduced from unimodal soils may be invalid for multimodal soils. Thus, a general multimodal SWCC expression is needed to precisely describe the water retention behaviour of soils with heterogeneous pore structure in the practical geotechnical and geo-environmental engineering applications.

To date, intensive efforts have been made to develop bimodal and multimodal SWCC equations to simulate the water retention behaviour of soils with heterogeneous pore structure, which can be categorized into three

groups: the piecewise form, the continuous form using the volumetric fraction approach, and the models using the unique parameter approach (Wijaya and Leong, 2016). Burger and Shackelford (2001a) proposed a piecewise bimodal SWCC expression using a delimiting point to separate the SWCC into a macro- and micro-sub-curve:

$$S_r = \begin{cases} S_{r,j} + (S_{r,max} - S_{r,j})S_{r,1}, & \text{for } s < s_j \\ S_{r,res} + (S_{r,j} - S_{r,res})S_{r,2}, & \text{for } s \geq s_j \end{cases} \quad (3.5)$$

Here, s_j and $S_{r,j}$ represent the suction and degree of saturation of the delimiting point, respectively. $S_{r,1}$ and $S_{r,2}$ are the local degree of saturation in the macro- and microporosity described by a unimodal SWCC equation.

It is noted that the discontinuity feature of the bimodal SWCC equation in piecewise form is inconvenient for numerical applications and the incorporation into a constitutive modelling. Therefore, continuous equations for bimodal soils were advanced using a “volumetric fraction approach” (Coppola, 2000, Dexter et al., 2008, Durner, 1994, Othmer et al., 1991, Ross and Smettem, 1993), regarding the overall soil pore structure as the superposition of the micro- and macro-sub-porosity:

$$S_r = (S_{r,max} - S_{r,res})(R_1 S_{r,1} + R_2 S_{r,2}) + S_{r,res} \quad (3.6)$$

Here, R_1 and R_2 represent the volumetric fractions of the micro- and macro-sub-porosity, respectively, which fulfil the condition $R_1 + R_2 = 1$. For instance, Othmer et al. (1991) developed a continuous bimodal SWCC function based on the SWCC data obtained from undisturbed soil samples. It was reported that the accuracy of predicting undisturbed soil unsaturated permeability (measured in field) was significantly improved compared to using a unimodal SWCC function. Durner (1994) proposed a bimodal SWCC expression constructed by a linear superposition of two van Genuchten-type sub-curves (i.e., substituting VGM into $S_{r,1}$ and $S_{r,2}$ of Eq. (3.6)). However, the model parameters should be considered as curve shape coefficients with no physical meaning. To calibrate the model parameters, the bimodal function is fitted to SWCC data using a specific best-fitting procedure, which requires a proper initial approximation of the parameters and appropriate constraint conditions beforehand. The difficulties in determining the parameters of the bimodal SWCC models developed under the “volumetric fraction approach” have two reasons: (I) A larger number of parameters have to be calibrated simultaneously by a single best-fitting approach based on one SWCC data set, leading to convergence problems in the optimization process; (II) The values of the parameters may not be unique for an identical SWCC data set due to the intercorrelation between the parameters (Gitirana Jr and Fredlund, 2004, Wijaya and Leong, 2016, Satyanaga et al., 2013, Sillers et al., 2001).

Recently, to overcome the shortcomings of the volumetric fraction models and retain the SWCC equation in a continuous form, several bimodal SWCC models based on a “unique parameter approach” (i.e., relate the independent model parameters to shape features of SWCC) have been developed. For instance, Gitirana Jr and Fredlund (2004) advanced a bimodal model based on the parameters with a clear physical and graphical meaning. Only one additional curve-fitting parameter is required in their model. Wijaya and Leong (2016) presented an empirical bimodal SWCC model by considering the SWCC as an assemble of several linear segments. The Heaviside function was employed to smooth the junctions of the linear segments. All model parameters could be determined directly based on the graphical properties of SWCC. Although the SWCC models in the unique parameter approach framework facilitate the parameter calibration procedure and ensure a unique parameter set,

they usually require a relatively complex mathematical form involving a large number of model parameters. Further details of the existing bimodal and multimodal SWCC models, developed in piecewise form, continuous form and unique parameter approach, was presented in Yan et al. (2021a) (Paper II, see Appendix).

A continuous SWCC equation with a simple mathematical form and a convenient parameter calibration method, which is able to precisely simulate the water retention behaviour for the heterogeneous pore structure soils encountered in many geotechnical and geo-environmental applications, is still missing in the literature. Such a general multimodal SWCC model was proposed in Yan et al. (2021a).

3.2.2. Predicting multimodal water retention curve from PSD data

Conventional experimental techniques to measure the SWCC are expensive and time-consuming, especially for fine-grained soils (Aubertin et al., 2003, Prapaharan et al., 1985). In the absence of a SWCC measurement, predictive models are needed to describe the water retention behaviour and other associated hydraulic properties (e.g., unsaturated hydraulic conductivity). In the past decades, numerous predictive SWCC models have been advanced based on other, more easily obtained soil properties, e.g., grain-size distribution and bulk density, which are referred to as ‘‘Pedo-transfer functions’’ (Arya and Paris, 1981, Gupta and Larson, 1979, Scheinost et al., 1997, Vereecken et al., 1989, Aubertin et al., 2003, Li et al., 2014, Zhai et al., 2020a). However, the influence of the heterogeneous pore structure on soil water retention behaviour was not considered in most Pedo-transfer functions, leading to remarkable discrepancies between the predicted and measured SWCCs. For example, Cai et al. (2020) reported that the SWCC measured on a compacted Guilin lateritic soil displays a distinct bimodality, while that of a reconstituted sample shows a unimodal characteristic. The different water retention behaviour of the same soil can be ascribed to the different pore structures formed in the sample preparation procedure, i.e., a bimodal porosity in the compacted sample and a matrix-type porosity in the reconstituted sample. This means that the water retention behaviour is directly related to the soil pore structure, but not to material constants (Birle, 2011). Compared to conventional SWCC measurement methods, experimental techniques to detect the pore size distribution, e.g., MIP test, are relatively simple and fast (Prapaharan et al., 1985).

For a given MIP test data set (P_{Hg}^i, V_{cum}^i), a SWCC can be deduced by applying Kelvin’s capillary law (Prapaharan et al., 1985, Romero et al., 1999, Sun and Cui, 2020, Zhai et al., 2020b):

$$r = \frac{C}{s} = \frac{2T \cos \theta}{s} \quad (3.7)$$

Here, C is a constant equal to $2T \cos \theta$, where T is the surface tension of water (0.072 N/m at 25 °C) and θ is the contact angle between soil and water ($\theta \approx 0^\circ$ for desiccation) (Fredlund and Rahardjo, 1993, Lu and Likos, 2004). From Eqs. (2.1) and (3.7), the SWCC ($s_{MIP}^i, s_{r,MIP}^i$) can be derived directly from the MIP data (P_{Hg}^i, V_{cum}^i) (Prapaharan et al., 1985):

$$s_{MIP}^i = -\frac{T \cos \theta}{T_{Hg} \cos \theta_{Hg}} P_{Hg}^i \quad (3.8)$$

and

$$S_{r,MIP}^i = 1 - \frac{V_{cum}^i}{e_0/\rho_s} \quad (3.9)$$

It is noted that the contact angle between mercury and the soil is greater than 90° . The intrusion of mercury is hence similar to the ejection of water from soil, indicating that the SWCC derived from Eqs. (3.8) and (3.9) corresponds to the drying curve (Prapaharan et al., 1985). Furthermore, the derived SWCC is a discrete representation with a limited number of data points, and hence is inconvenient for practical applications.

To acquire a continuous SWCC from PSD, the soil pore structure is conventionally assumed as a bundle of capillary tubes with circular cross section. For a rigid soil pore structure (i.e., no volume change and microstructure evolution during SWCC testing), the closed-form SWCC equation in terms of effective degree of saturation S_e gives (Fredlund and Xing, 1994, Zhang and Chen, 2005)

$$S_e(s) = \int_0^{r=C/s} f(\xi) d\xi \quad (3.10)$$

Here, ξ is a dummy variable of integration for pore radius, and $f(\xi)$ represents the soil pore size density function. Eq. (3.10) means that for a given suction level s , the capillary channels whose radius is equal to or smaller than r ($= C/s$) are filled with water. The approach in Eq. (3.10), where a SWCC equation is directly derived from the pore size distribution function based on Kelvin's capillary law, is referred to as the "direct transformation method" (Yan et al., 2021b). In the last decades, unimodal SWCC equations have been inferred based on Eq. (3.10). Kosugi (1994) proposed a unimodal SWCC expression using a lognormal distribution law for $f(\xi)$. The parameters of the derived SWCC model possess clear physical meanings. Fredlund and Xing (1994) substituted an empirical unimodal pore size distribution function in $f(\xi)$ to derive a unimodal SWCC equation.

However, the assumption of a rigid monomodal pore structure during SWCC testing in Eq. (3.10) is not adequate for deformable soils, e.g., clayey soils. Experimental results in the literature have shown that both the overall soil volume and the pore size distribution evolve significantly along the wetting and drying paths (see section 2.2.2). Recently, different approaches have been developed to derive the water retention curve directly from pore size distribution data. For example, Simms and Yanful (2002) developed a pore-network model based on suction-induced pore shrinkage and pore trapping from the PSD curves. Lately, Della Vecchia et al. (2015) derived the water retention curve for compacted Boom clay from a bimodal pore size distribution expression, using an empirical correlation between aggregate porosity and current water content based on the activity of clay fractions. However, the microstructure of the soils encountered in geotechnical and geo-environmental engineering applications can consist of several independent sub-porosities. So far, a predictive SWCC model based on PSD data for a general multimodal soil (i.e., the modality number can be arbitrary positive integer) is still lacking in the literature.

For the most general case, it is necessary to modify the approach in Eq. (3.10) to derive SWCC from the PSD measurement, which needs to take into account the multimodality of the pore structure, the changes in the overall volume and the microstructure evolution during wetting and drying cycles. Paper III (Yan and Cudmani, 2022b) advanced a novel and comprehensive framework to predict the water retention behaviour of multimodal deformable soils based on the pore size distribution (PSD) measurements.

3.3. Summary

The soil water retention curve plays a key role in geotechnical and geo-environmental applications in unsaturated zone as it significantly influences the hydro-mechanical behaviour of unsaturated soils. The heterogeneous pore structure causes a distinct multimodal characteristic of the water retention behaviour, which cannot be accurately described by conventional empirical unimodal SWCC models. Moreover, the dependencies of important hydraulic and mechanical properties (e.g., unsaturated hydraulic conductivity and shear strength) on SWCC of a multimodal soil may differ from those derived from a unimodal pore structure. For instance, a bimodal PSD in soil and the consequent bimodal SWCC result in the bimodality of the permeability function (Li et al., 2014). Thus, a general multimodal SWCC model is required to accurately simulate the complex water retention behaviour of soils with heterogeneous microstructure. To overcome the shortcomings of the existing bimodal and multimodal SWCC equations, a general N-modal continuous SWCC function was developed in Yan et al. (2021a) (Paper II, see Appendix).

To calibrate the model parameters, empirical SWCC equations are usually fitted to SWCC data. Thus, they can only be implemented in practical applications if the SWCC data is available in the suction range of interest. However, the process of SWCC measurement is tedious, expensive and time-consuming, especially for fine-grained soils due to their low permeability. In the absence of SWCC data, a predictive model based on other, more easily determined soil properties would be useful. In Yan and Cudmani (2022b) (Paper III, see Appendix), we developed a predictive model to estimate water retention curves based on pore size distribution data.

4. Methodology

4.1. Modelling multimodal pore size distribution

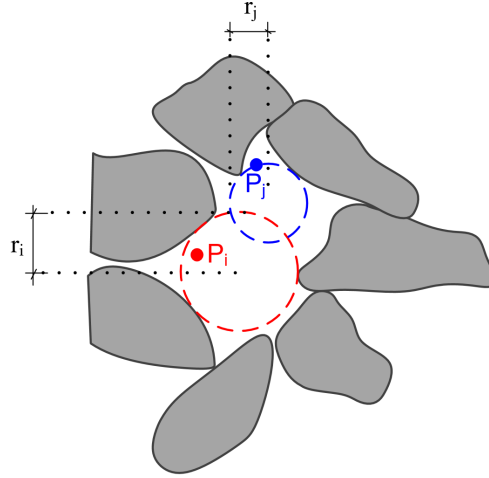


Fig. 4.1. Definition of pore radius according to Scheidegger (2020)

In most soils encountered in geotechnical and geo-environmental engineering applications, the soil microstructure is generally heterogeneous and can consist of several sub-porosities, resulting from irregular pore shapes, various pore sizes of widely varying magnitudes, gap-graded grain size distribution, and aggregation of fines. To develop a general multimodal PSD model, a probabilistic distribution of pore sizes based on the concept of Scheidegger (2020), i.e., a mathematical definition of the pore radius r in a porous medium, is assumed. The pore radius r denoted to a point in pore space is defined as the radius of the maximum sphere containing that point in pore space (i.e., the sphere cannot touch the solid particle) (Yan and Cudmani, 2022a). It is worth noting that the point does not have to be centred on the maximum sphere. Fig. 4.1 demonstrates an example of the definition of the pore radius under the Scheidegger's framework. One sees that the point P_i lies within its maximum sphere and the point P_j locates exactly on the boundary of its maximum sphere. The pore radius (r_i) denoted to point P_i is much larger than the pore radius (r_j) of point P_j . This indicates that the pore radius r is a non-negative random variable depending on the position of the point in the pore space (Yan and Cudmani, 2022a). Based on the probabilistic concept, the pore size density function must hold the following condition:

$$\int_0^{+\infty} f(r) dr = 1 \quad (4.1)$$

The microstructure of an idealised porous medium, represented by a representative elementary volume (REV) with a spherical pore in the centre, is demonstrated in Fig. 4.2a. In Scheidegger's framework, the pore radius denoted to each point within the pore space is r_1 , and hence the pore size density function $f(r)$ gives (Yan and Cudmani, 2022a)

$$f(r) = \delta(r - r_1) \quad (4.2)$$

where $\delta(x)$ is the Dirac delta function defined on the non-negative domain:

$$\delta(x) = \begin{cases} +\infty, & x = 0 \\ 0, & x \neq 0 \end{cases} \quad (4.3)$$

and

$$\int_0^{+\infty} \delta(x) dx = 1 \quad (4.4)$$

If the pore space in a REV is an assembly of N individual isolated spherical pores (see Fig. 4.2b), the pore size density function $f(r)$ yields

$$f(r) = \sum_{i=1}^N R_i \delta(r - r_i) \quad (4.5)$$

Here, r_i is the radius of the i^{th} spherical pore, and R_i represents the volumetric fraction of each spherical pore fulfilling the following condition:

$$\sum_{i=1}^N R_i = 1 \quad (4.6)$$

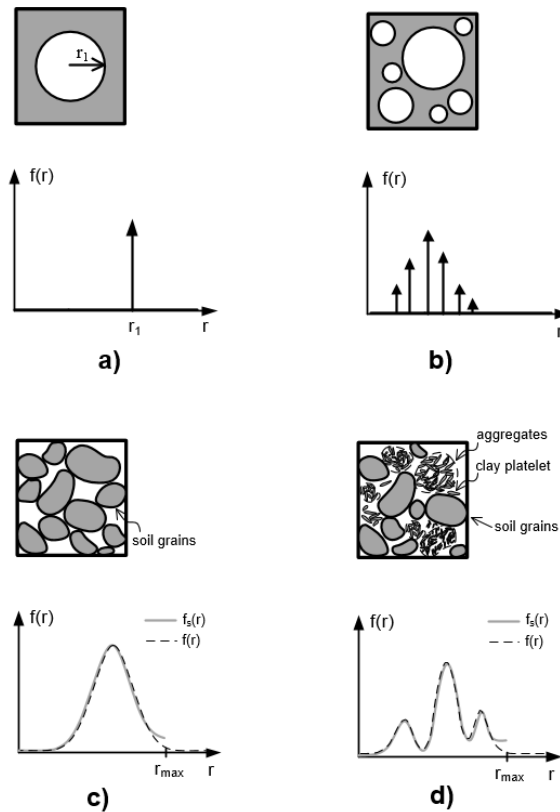


Fig. 4.2. Schematic for pore size distribution curves of a) an idealised porosity as a single spherical pore in representative elementary volume (REV) b) an idealised porosity as a set of individual spherical pores in REV c) a unimodal porosity d) a multimodal porosity (Figure adapted from Yan and Cudmani (2022a), copyright © 2022 Elsevier. Reprinted with permission)

Applying Scheidegger's concept to a unimodal soil, the pore size density function is a continuous expression fulfilling the condition of Eq. (4.1) (see Fig. 4.2c). An appropriate unimodal PSD-function $f(r)$ is proposed (derived from the van Genuchten model (Van Genuchten, 1980)):

$$f(r) = \frac{m(r^f/r)^{\frac{1}{1-m}}}{r(1-m) \left[1 + (r^f/r)^{\frac{1}{1-m}} \right]^{m+1}} \quad (4.7)$$

where m ($0 < m < 1$) is the unitless pore size spectrum number, and r^f represents a reference pore radius proportional to the maximal pore radius r_{max} (i.e., $r^f \propto r_{max}$) (Yan and Cudmani, 2022a). When presenting the pore radius r on a logarithmic scale (Juang and Holtz, 1986a), the condition in Eq. (4.1) could be expressed equivalently as

$$\int_0^{+\infty} \omega(r) d \log r = 1 \quad (4.8)$$

and the dimensionless pore size density function $\omega(r)$ gives

$$\omega(r) = \frac{(\ln 10)m_i(r_i^f/r)^{\frac{1}{1-m_i}}}{(1-m_i) \left[1 + (r_i^f/r)^{\frac{1}{1-m_i}} \right]^{m_i+1}} \quad (4.9)$$

Applying Scheidegger's concept to a multimodal soil (see Fig. 4.2d) and quantifying each sub-porosity with the unimodal pore size density function, we obtain a general multimodal pore size distribution function

$$f(r) = \sum_{i=1}^N R_i \frac{m_i(r_i^f/r)^{\frac{1}{1-m_i}}}{r(1-m_i) \left[1 + (r_i^f/r)^{\frac{1}{1-m_i}} \right]^{m_i+1}} \quad (4.10)$$

and the dimensionless PSD expression

$$\omega(r) = \sum_{i=1}^N R_i \frac{(\ln 10)m_i(r_i^f/r)^{\frac{1}{1-m_i}}}{(1-m_i) \left[1 + (r_i^f/r)^{\frac{1}{1-m_i}} \right]^{m_i+1}} \quad (4.11)$$

Here, R_i , m_i and r_i^f are the volumetric fraction, unitless pore size spectrum number, and reference pore radius of each sub-porosity, respectively. In MIP tests, since the larger pores are intruded first, the mercury intrusion curve corresponds to the complementary cumulative function and hence gives (in terms of V_{cum})

$$V_{cum}(r) = \frac{e_0}{\rho_s} \left\{ 1 - \sum_{i=1}^N R_i \left[1 + \left(\frac{r_i^f}{r} \right)^{\frac{1}{1-m_i}} \right]^{-m_i} \right\} \quad (4.12)$$

To validate the multimodal PSD model (Eq. (4.11)), the PSD curves (determined by MIP tests) of soils with a heterogeneous pore structure, including Boom clay (Romero et al., 1999), MX80 bentonite (Wang et al., 2014) and a sand-clay mixture (Juang and Holtz, 1986b), were simulated. The model parameters were determined by fitting the multimodal PSD expression to pore size distribution data measured in MIP tests. A good agreement between the reproduced PSD curves and the measurements was observed.

4.2. Modelling multimodal soil water characteristic curves

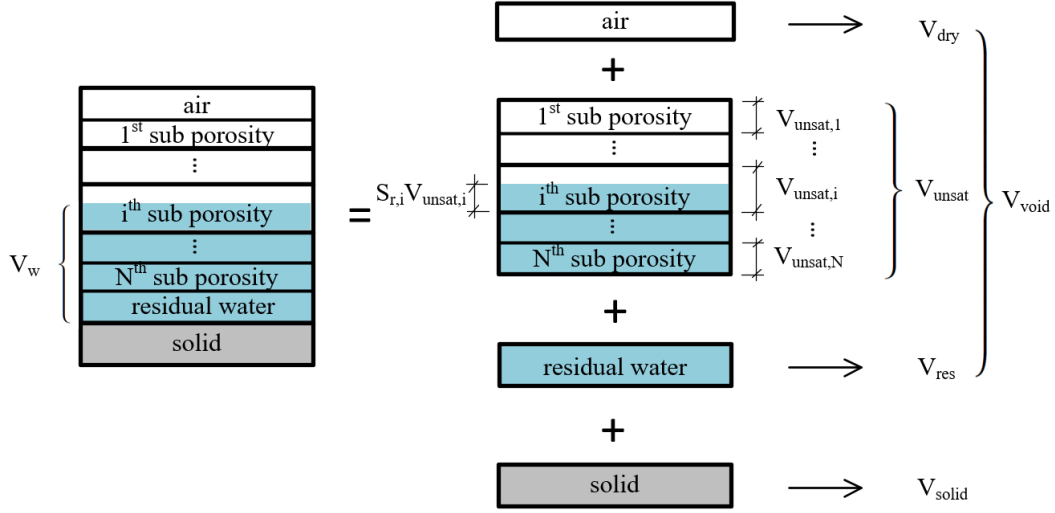


Fig. 4.3. Schematic of the soil composition with N-modal pore structure (Figure from Yan et al. (2021a))

To simulate the water retention behaviour of multimodal soils, a new SWCC model, referred to as the “discrete-continuous multimodal van Genuchten model” (D-CMVGM), was advanced.

In a multimodal soil, the whole pore space consists of three parts, the permanently saturated part V_{res} (volume of adsorbed water), the permanently dry part V_{dry} (volume of isolated pores), and the unsaturated part V_{unsat} , as schematically shown in Fig. 4.3. The void volume V_{unsat} is regarded as an assembly of N sub-porosities. For such a N -modal soil, its SWCC can be divided into N sub-curves using $N-1$ delimiting suctions s_i ($i = 2, \dots, N$). The desiccation process of the i^{th} sub-porosity corresponds to a suction range $[s_i, s_{i+1})$, where $s_1 = 0$ and $s_{N+1} = +\infty$. This means that for an imposed suction $s \in [s_i, s_{i+1})$, the first to the $(i-1)^{\text{th}}$ sub-porosities are completely dry, and the $(i+1)^{\text{th}}$ to the N^{th} sub-porosities are fully saturated (Yan et al., 2021a). The discrete bimodal SWCC model by Burger and Shackelford (2001a) is extended to a multimodal case

$$S_r = (S_{r,max} - S_{r,res}) \left\{ \left(1 - \sum_1^i R_i \right) + R_i \left[1 + (\alpha_i s)^{\frac{1}{1-m_i}} \right]^{-m_i} \right\} + S_{r,res} \text{ for } s \in [s_i, s_{i+1}) \quad (4.13)$$

Here, R_i represents the volumetric fraction, α_i and m_i are the van Genuchten model parameters of the i^{th} sub-porosity. The discontinuous multimodal SWCC function in Eq. (4.13) is named as the “discrete multimodal van Genuchten model” (DMVGM).

To obtain a continuous multimodal SWCC equation, the whole pore space of the soil is regarded as a superposition of several overlapping sub-porosities (Ross and Smettem, 1993). Using the van Genuchten model to quantify the water retention curve of each sub-porosity, a continuous N -modal SWCC equation yields (Yan et al., 2021a):

$$S_r = (S_{r,max} - S_{r,res}) \sum_1^N R_i \left[1 + (\alpha_i s)^{\frac{1}{1-m_i}} \right]^{-m_i} + S_{r,res} \quad (4.14)$$

which is named as the “continuous multimodal van Genuchten model” (CMVGM). The continuous feature of CMVGM facilitates its implementation in numerical modelling and practical applications. However, problems arise in parameter calibration in CMVGM. Since the model parameters (a total of $3N+2$ parameters) are strongly intercorrelated, on the one hand, parameter determination using solely the least square fitting approach can lead to convergence problems and inefficiency of the optimization process (Wijaya and Leong, 2016). On the other hand, a unique set of parameters may not exist (Satyanaga et al., 2013, Leong and Rahardjo, 1997b, Sillers et al., 2001).

To solve the problems in CMVGM, the parameters in DMVGM (except for the delimiting suction) are adopted in CMVGM to describe a continuous multimodal SWCC. This novel method, which takes advantage of both DMVGM (convenient parameter determination method) and CMVGM (simple and continuous mathematical function), is named as the D-CMVGM framework.

A convenient parameter calibration approach for D-CMVGM framework was developed and summarised in Yan et al. (2021a) (Paper II). The model was validated using nine bimodal and three trimodal water retention curves of different soils varying from clayey soils to artificial soil mixtures. The fitted curves show very good agreement with the measured SWCC data.

4.3. Predicting multimodal water retention behaviour based on pore size distribution data

To predict the water retention behaviour of multimodal deformable soils directly from their pore size distribution data, the full picture of the soil microstructure is quantified by the void ratio (for the overall void volume) and a new microstructural state parameter Ω (for pore size distribution) defined as

$$\Omega = \Omega_k = \{R_1, r_1^f, m_1, \dots, R_N, r_N^f, m_N\} \quad (4.15)$$

where R_i , m_i and r_i^f are the parameters of the general multimodal PSD model proposed by Yan and Cudmani (2022a) (Paper II). To characterise the microstructure evolution along hydro-mechanical loading paths, the microstructural state parameter Ω is assumed to be suction-, stress- and loading-history- dependent

$$\Omega = \Omega_k(\sigma_{ij}^{net}, p_0^*, s) \quad (4.16)$$

Here, σ_{ij}^{net} is the net stress tensor, and p_0^* represents the pre-consolidation pressure at saturated state. Considering that SWCCs are traditionally measured under zero or very low net stress, it is reasonable to assume that the pre-consolidation pressure p_0^* is unaffected by suction during SWCC testing (i.e., no wetting-collapse phenomenon). Thus Eq. (4.16) degrades to

$$\Omega = \Omega_k(s) \quad (4.17)$$

Substituting the suction-dependent multimodal PSD function in Eq. (3.10), the drying branch of the water retention curve in terms of the effective degree of saturation gives

$$S_e^d(s) = \int_0^{2T \cos \theta_d / s} f(\Omega_k(s), r) dr = F\left(\Omega_k(s), \frac{C_d}{s}\right) \quad (4.18)$$

where θ_d is the soil-water contact angle during drying and C_d is a constant equal to $2T \cos \theta_d$.

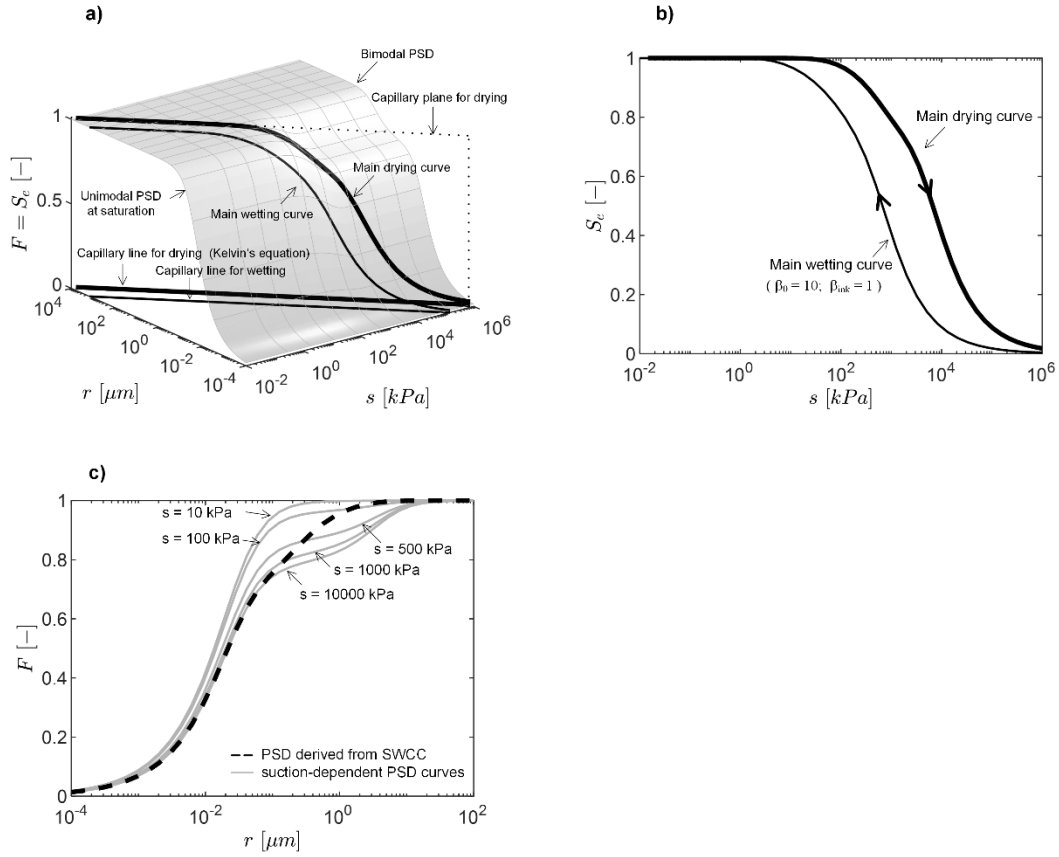


Fig. 4.4. a) interpretation for water retention curves and PSD curves by a unique surface in the $r - s - F (= S_c)$ space b) water retention curves in the conventional $\log s - S_c$ plane c) PSD curves in the $\log r - F$ plane (Figure from Yan and Cudmani (2022b))

To account for the hysteresis effect, two additional parameters β_{ink} and β_θ are introduced in the wetting process. The parameter β_{ink} ($0 < \beta_{ink} \leq 1$) is a scaling factor to take the ‘‘ink-bottle effect’’ into account. The parameter β_θ reflects the effect of different contact angles in the wetting and drying processes, which is defined as

$$\beta_\theta = \frac{\cos \theta_d}{\cos \theta_w} \geq 1 \quad (4.19)$$

where θ_w is the soil-water contact angle during wetting. Assuming reversible microstructure evolution in wetting and drying cycles, the wetting branch of the water retention curve yields

$$S_e^w = \beta_{ink} \int_0^{2T \cos \theta_w / s} f(\Omega_k(s), r) dr = \beta_{ink} F \left(\Omega_k(s), \frac{\beta_\theta C_d}{s} \right) \quad (4.20)$$

Considering the residual state of the soil (i.e., $S_r \rightarrow S_r^{res}$ as $s \rightarrow +\infty$), the SWCC model in terms of degree of saturation gives

$$S_r(s) = \begin{cases} (1 - S_r^{res})F\left(\Omega_k(s), \frac{C_d}{s}\right) + S_r^{res}, & \text{for drying} \\ (1 - S_r^{res})\beta_{ink}F\left(\Omega_k(s), \frac{\beta_\theta C_d}{s}\right) + S_r^{res}, & \text{for wetting} \end{cases} \quad (4.21)$$

and in terms of gravity water content yields

$$w(s) = \begin{cases} \frac{e_d(s)}{G_s} \left[(1 - S_r^{res})F\left(\Omega_k(s), \frac{C_d}{s}\right) + S_r^{res} \right], & \text{for drying} \\ \frac{e_w(s)}{G_s} \left[(1 - S_r^{res})\beta_{ink}F\left(\Omega_k(s), \frac{\beta_\theta C_d}{s}\right) + S_r^{res} \right], & \text{for wetting} \end{cases} \quad (4.22)$$

Here, $e_d(s)$ and $e_w(s)$ represent the shrinkage and swelling curves, respectively. The proposed model (Eqs. (4.21) and (4.22)) quantifies the relationship between the multimodal water retention behaviour and the pore structure of multimodal deformable soils, in which the overall volume change (characterised by the void ratio e) and the microstructural evolution (characterised by the state parameter Ω) during SWCC testing have been taken into account.

The key idea of the proposed method is to characterise the unique PSD-surface by the microstructural parameter Ω in $r - s - F (= S_e)$ space, which represents the reversible microstructure evolution during drying and wetting. Fig. 4.4a demonstrates an example of a PSD-surface. The PSD curve varies from a unimodal mode in the saturation state (i.e., the cumulative PSD curve at $s = 1 \times 10^{-2}$ kPa) to a distinct bimodal mode in the completely dry state (i.e., the cumulative PSD curve at $s = 1 \times 10^6$ kPa). Kelvin's capillary law (Eq. (3.7)) for wetting and drying is presented by two lines in the $\log r - \log s$ plane. Then the water retention curves can be visualized as the cross-sections between the PSD-surface and the capillary planes (Fig. 4.4a). Projecting the cross-sections onto the $\log s - S_e$ plane gives the conventional main drying and main wetting curves in terms of the effective degree of saturation (see Fig. 4.4b). In Fig. 4.4c, the projection of the drying cross-section onto the $\log r - F$ plane is equivalent to the PSD curve derived from the main drying curve, which crosses the PSD curves at different suction levels determined by the microstructure parameter Ω . This implies that for deformable soils, the pore size distribution derived from their macroscopic SWCC is not representative of the microscopic pore structure dominated by the current soil suction.

To calibrate the model, a set of PSD curves at different suction levels is needed to track the microstructure evolution of deformable soils during SWCC testing. The proposed model was validated using SWCC measurements and PSD data of four different soils, including Silty Sand (Angerer, 2020), Lateritic soil (Cai et al., 2020), Sandy Loam (Cuisinier and Laloui, 2004) and London Clay (Monroy et al., 2010). The predicted SWCCs are in good consistency with the measurements.

5. Summaries of publications

Three relevant publications are briefly summarised in this section.

5.1. Paper I: A general analytical expression for pore size distribution based on probability theory

Yan, W., & Cudmani, R. (2022). A general analytical expression for pore size distribution based on probability theory. Engineering Geology, 297. doi:10.1016/j.enggeo.2021.106501

5.1.1. Summary of the publication

A precise description of the pore size distribution of soils and rocks is essential for understanding the fundamental features of the thermo-hydro-mechanical behaviour of unsaturated soils and for geotechnical, geo-environmental and geological engineering applications. A large amount of PSD-data of soils is currently available in the literature, while a general expression to simulate these PSD curves is still lacking. In this paper, we proposed a multimodal PSD model (i.e., the modality number can be any positive integer) based on the probability theory. The mathematical definition of the pore radius in a porous material according to Scheidegger (2020) was adopted, and the pore radius r was regarded as a non-negative random variable. The PSD expression for a multimodal soil was obtained by a linear superposition of several sub-curves derived from van Genuchten model. The model was validated with MIP test data sets from three different soils, i.e., compacted Boom clay (bimodal PSD, data from Romero et al. (1999)), MX80 bentonite (trimodal PSD, data from Wang et al. (2014)) and a sand-clay mixture (unimodal and bimodal PSDs, data from Juang and Holtz (1986b)). A good agreement between the reproduced PSD curves and the measurements was observed. The parameters in the proposed multimodal PSD expression have clear physical meanings, enabling a modification of the model by relating the PSD-parameters to other soil properties. The model was extended to predict the relationship between water content, soil suction and dry density of Boom clay after compaction and the time-dependent microstructure evolution of MX80 bentonite after saturation under isochoric conditions. In addition, the influence of the fine content on the overall microstructure of the sand-clay mixture was analysed. The proposed general framework is a powerful tool to precisely quantify the heterogeneous soil microstructure. It can be further incorporated into the existing permeability functions, effective stress parameter formulation as well as constitutive and hydraulic models of unsaturated soils. Besides soils, the proposed pore size distribution model can also be applied to simulate the pore structure of other porous and granular materials, since the underlying physics are the same for all (Yan and Cudmani, 2022a).

5.1.2. Individual contributions of the candidate

The article *Yan and Cudmani (2022a)* (Paper I) was published in the international peer-reviewed journal *Engineering Geology*. Contributions to this article by first author *Wei Yan* include concept and method development, programming and coding, data and results analysis, model validation, and original manuscript writing.

5.2. Paper II: A new framework to determine general multimodal soil water characteristic curves

Yan, W., Birle, E., & Cudmani, R. (2021). A new framework to determine general multimodal soil water characteristic curves. Acta Geotechnica, 16(10), 3187-3208. doi:10.1007/s11440-021-01245-2

5.2.1. Summary of the publication

The soil water retention curve is a fundamental soil property as it strongly influences the hydro-mechanical behaviour of unsaturated soils. Numerous empirical unimodal and bimodal SWCC equations have been developed over the last decades and successfully applied in practical applications in the vadose zone. However, soils encountered in modern geotechnical and geo-environmental engineering applications can possess a heterogeneous pore structure (more than two sub-porosities), which causes multimodal water retention behaviour. So far, a general multimodal SWCC model is missing in the literature. The prediction of the hydraulic and mechanical properties of such soils in the unsaturated state is still challenging. In this paper, a new SWCC model (D-CMVGM) was advanced to simulate the general water retention behaviour of multimodal soils. Based on the graphical properties of the SWCC in the double logarithmic diagram, a convenient parameter calibration method was advanced, ensuring the stability of the best-fitting procedure. The proposed model was validated using a set of bimodal and three trimodal water retention curves of different soils varying from clayey soils to artificial soil mixtures. A good agreement between the measured SWCC data and the reproduced curves was observed. The major advantages of the proposed model over the existing bimodal and multimodal SWCC models are summarised below:

- The proposed model is able to quantify the multimodal SWCC very accurately and possesses a simple mathematical function.
- The modality number can be any positive integer, and hence the SWCC equation is capable of simulating the water retention behaviour of all soil types.
- The parameter calibration method is simple and convenient. Most parameters can be determined graphically (R_i and m_i). Only one curve fitting procedure is required, which is rapid and stable thanks to the previously determined parameters.
- The proposed parameter calibration approach ensures unique values in the parameters.
- A modality number reduction method (MNRM) was developed to minimize the modality number N and the number of parameters by presenting the SWCC data in a double logarithmic plot.
- The parameters possess clear physical meanings and can be determined individually, allowing further improvement by correlating the parameters to other soil properties or state parameters.

5.2.2. Individual contributions of the candidate

The article *Yan and Cudmani (2022a)* (Paper II) was published in the international peer-reviewed journal *Acta geotechnica*. Contributions to this article by first author *Wei Yan* include concept and method development, programming and coding, data and results analysis, model validation, and original manuscript writing.

5.3. Paper III: A novel framework for predicting water retention behaviour based on pore size distribution data of multimodal unsaturated soils

Yan, W., & Cudmani, R. (2022). A novel framework for predicting water retention behaviour based on pore size distribution data of multimodal unsaturated soils. submitted to Acta geotechnica.

5.3.1. Summary of the publication

When using empirical SWCC models, e.g., VGM and FXM, the water retention data in the suction range of interest are required to determine the model parameters via a best-fitting procedure. However, current experimental methods for SWCC measurements are time-consuming and tedious. This problem is even more acute in multimodal soils, since SWCC data over the full suction range is necessary to identify the modality number and the water retention behaviour characteristics of all sub-porosities. The existing “direct transformation method” (Fredlund and Xing, 1994, Kosugi, 1996, Prapaharan et al., 1985), which predicts SWCC directly from a single unimodal PSD data set using Kelvin’s equation, assumes a rigid unimodal pore structure and ignores the multimodality of pore structure and the evolving microstructure during SWCC testing for deformable soils. To address these shortcomings, a new predictive multimodal SWCC model based on the probabilistic PSD model was developed (Yan and Cudmani (2022b)). The relationship between the microscopic evolving PSD curves and the macroscopic SWCC was interpreted by a unique PSD-surface characterised by the microstructural parameter Ω in $r - s - F (= S_e)$ space, and a reversible microstructure evolution during drying and wetting was assumed. The model was validated by predicting the water retention curves of four different soils based on their PSD data at different suction levels (i.e., Silty Sand (Angerer, 2020), Lateritic soil (Cai et al., 2020), Sandy Loam (Cuisinier and Laloui, 2004) and London Clay (Monroy et al., 2010)). The predicted SWCCs show a good agreement with the measurements. For practical unsaturated soil applications, conventional SWCC measurements are time-consuming and tedious, especially for deformable fine-grained soils due to their low permeability. The proposed framework provides a feasible approach to predict the water retention behaviour of all soil types based on their PSD data. The determination of PSD, for example by means of MIP tests, can be accomplished much faster than conventional SWCC measurements (Prapaharan et al., 1985). For non-deformable soils (e.g., gravel and sand), only one PSD data set is sufficient. For deformable soils, a set of PSD curves at different suction levels is needed to track the microstructure evolution during SWCC testing.

5.3.2. Individual contributions of the candidate

The article (Paper III) has been submitted to the international peer-reviewed journal *Acta geotechnica* (under review). Contributions to this article by first author *Wei Yan* include concept and method development, programming and coding, data and results analysis, model validation, and original manuscript writing.

6. Conclusions and outlook

In classical soil mechanics, the soil is usually idealized as a homogenous porous material. However, many soils encountered in geotechnical and geo-environmental engineering applications are rarely homogenous, but are characterised by a heterogeneous microstructure (Carminati et al., 2008). For example, top-soils in nature, gap-graded soils and compacted soils possess a bimodal or even multimodal pore structure. A complex interaction exists between the soil hydro-mechanical behaviour and its microstructure. In addition, Experimental studies have shown that hydraulic and mechanical loadings cause significant changes in the soil pore structure. Conversely, the PSD strongly influences the hydraulic and mechanical properties of soils, e.g., the effective stress parameter, the unsaturated shear strength, the water retention behaviour and the unsaturated hydraulic conductivity. Therefore, a general framework for quantifying the heterogeneous microstructure is necessary for a better understanding of the hydro-mechanical behaviour of these soils, as required for the design of geotechnical and geo-environmental structures.

In Yan and Cudmani (2022a) (Paper I), a general analytical expression for the multimodal pore size distribution is developed based on probability theory. The parameters in the proposed model have a clear physical meaning, allowing the model to be modified to characterise the evolving microstructure of the soils subjected to hydraulic and mechanical loadings (e.g., compaction, consolidation, wetting and drying cycles). The model was validated using the PSD data of different soils varying from compacted clayey soils to mixed soils. The simulated PSD curves show strong consistency with measurements. It is shown that the pore size spectrum number m_i remains unchanged along mechanical (e.g., compaction) and hydraulic loading (e.g., desiccation and hydration) paths. In contrast, the volumetric fraction R_i and the reference pore radius r_i^f vary remarkably with density and suction. This important finding provides new insights into the dependencies of other hydraulic and mechanical properties (e.g., water retention behaviour) on the soil microstructure. In principle, the PSD model is capable of describing the pore structure of arbitrary porous and granular materials, since the underlying physical and statistical concepts are the same.

The multimodal pore structure causes multimodality in soil water retention behaviour. Conventional unimodal SWCC equations (e.g., BCM, VGM and FXM) are unable to accurately describe multimodal SWCCs. Furthermore, the dependencies of the soil hydro-mechanical properties on its water retention behaviour can be different in soils with heterogeneous pore structure than in unimodal soils. In Yan et al. (2021a) (Paper II), an empirical SWCC model (D-CMGVM) was developed, which is a powerful tool to precisely describe a general multimodal water retention curve (the modality number N can be any positive integer). Compared to the existing multimodal SWCC models, the proposed continuous SWCC equation possesses a relatively simple mathematical form. A convenient and efficient parameter calibration approach has also been developed based on the linearization of SWCC presented in the double logarithmic plot. The unique values in the parameters facilitate the implementation of the model in practical applications and further improvement by correlating the parameters with other soil properties or state parameters.

In the absence of SWCC data, the water retention behaviour can be predicted from other soil properties, for example, pore size distribution. In Yan and Cudmani (2022b) (Paper III), we proposed a novel framework to predict the multimodal water retention curve for deformable soils from their PSD measurements. The full picture

of the soil pore structure is characterised by a volumetric state variable e and a new microstructural state variable Ω from the multimodal PSD model of Yan and Cudmani (2022a) (Paper I). Assuming reversible microstructural behaviour, a unique PSD surface for wetting and drying in the $r - s - F (= S_e)$ space is derived based on PSD curves at different suction levels. Then water retention curves are acquired from the cross-section of the PSD surface and the plane of Kelvin's capillary law. The framework quantitatively describes the relationship between the macroscopic water retention behaviour and the microscopic evolving microstructure for a general multimodal deformable soil. It was validated using SWCC measurements from a variety of soils. The predicted water retention curves from PSD data are in good agreement with the measurements. The proposed model, on the one hand, provides new insights into the incorporation of SWCC into other unsaturated soil property formulations. On the other hand, it offers a feasible approach to predict the water retention behaviour of all soil types, providing an alternative to the time-consuming and expensive direct SWCC measurements.

The proposed PSD model as well as the empirical and predictive SWCC models are applicable for all soil types. These models establish a general framework to analyse the evolving microstructure and precisely describe the related water retention behaviour for the soils with heterogeneous pore structure. Nonetheless, the proposed framework can be further improved, and subsequent research is summarised below.

- The general multimodal PSD model is developed based on probability theory. Besides soils, it can also be utilized to quantify the pore structure of the other porous and granular materials, for example, concrete (Fujikura and Oshita, 2011), coal (Zhang et al., 2020, Liu et al., 2020), and rocks (Burdine et al., 1950), among others.
- In the predictive SWCC model, a reversible microstructure evolution during wetting and drying cycles is assumed. Further experimental evidence is needed to check the validity range of the assumption.
- Irreversible changes in the soil pore structure can take place due to the plastic deformation resulting from hydro-mechanical loading (e.g., wetting collapse process). New techniques and experimental results are still missing in the literature to explore the relationship between the soil microstructure and a general hydraulic and mechanical state (e.g., net stress, suction and loading history).
- In Paper III, the water retention curves are predicted based on the PSD data determined by MIP tests. In principle, the proposed framework is still valid using the PSD data obtained from more advanced experimental techniques, reducing the cost and experimental time.
- The proposed framework can be incorporated into the effective stress formulation (Alonso et al., 2010) and the constitutive modelling (Koliji et al., 2010) of unsaturated aggregated soils, where both the multimodal water retention behaviour and the microstructure evolution along hydro-mechanical loading paths should be taken into account.
- The pore structure in compacted fine-grained soils (e.g., London Clay (Monroy et al., 2010)) exhibits a unimodal characteristic (a matrix-type pore structure) in the saturated state and a distinct bimodal characteristic at high suction levels (an aggregated-type pore structure). The dependencies of the unsaturated shear strength and the failure mechanism on the microstructure evolution should be further investigated. For example, the shear strength of a matrix-type fabric at low suction level is mobilised by the friction between the particles of fines, and that of a distinct aggregate fabric at high suction level is provoked by the friction between aggregates of fines. Experimental results for the microstructure-based

unsaturated shear strength and failure mechanism at a moderate suction level are still lacking in the literature.

- In conventional permeability functions, a rigid pore structure is assumed, and hence a constant PSD is deduced from the water retention curve. For multimodal deformable soils, both the overall volume and the microstructure alter remarkably during SWCC testing. Thus, a new relationship between the permeability function and the macroscopic SWCC as well as the microscopic evolution in the pore structure can be further investigated.

References

- Abed, A. A. & Sołowski, W. T. (2017) A study on how to couple thermo-hydro-mechanical behaviour of unsaturated soils: Physical equations, numerical implementation and examples. *Computers and Geotechnics* **92**:132-155, 10.1016/j.compgeo.2017.07.021.
- Abed, A. A. & Sołowski, W. T. (2021) Estimation of water retention behaviour of bentonite based on mineralogy and mercury intrusion porosimetry tests. *Géotechnique* **71(6)**:494-508
- Ahmed, S., Lovell, C. W. & Diamond, S. (1974) Pore Sizes and Strength of Compacted Clay. *Journal of the Geotechnical Engineering Division* **100(4)**:407-425, doi:10.1061/AJGEB6.0000035.
- Alonso, E., Gens, A. & Hight, D. (1987) General report. Special problem soils. In *Proceedings of the 9th European Conference on soil mechanics and foundation engineering, Dublin.*, vol. 3, pp. 1087-1146.
- Alonso, E. E., Pereira, J. M., Vaunat, J. & Olivella, S. (2010) A microstructurally based effective stress for unsaturated soils. *Géotechnique* **60(12)**:913-925, 10.1680/geot.8.P.002.
- Angerer, L. (2020) Experimental evaluation of the suction-induced effective stress and the shear strength of as-compacted silty sands.) Technische Universität München.
- Arya, L. M. & Paris, J. F. (1981) A physicoempirical model to predict the soil moisture characteristic from particle-size distribution and bulk density data. *Soil Science Society of America Journal* **45(6)**:1023-1030
- Assouline, S., Tessier, D. & Bruand, A. (1998) A conceptual model of the soil water retention curve. *Water resources research* **34(2)**:223-231
- Aubertin, M., Mbonimpa, M., Bussière, B. & Chapuis, R. P. (2003) A model to predict the water retention curve from basic geotechnical properties. *Canadian Geotechnical Journal* **40(6)**:1104-1122, 10.1139/t03-054.
- Barden, L. & Sides, G. R. (1970) Engineering Behavior and Structure of Compacted Clay. *Journal of the Soil Mechanics and Foundations Division* **96(4)**:1171-1200, 10.1061/JSFEAQ.0001434.
- Benavides, F., Leiderman, R., Souza, A., Carneiro, G. & Bagueira De Vasconcellos Azeredo, R. (2020) Pore size distribution from NMR and image based methods: A comparative study. *Journal of Petroleum Science and Engineering* **184**:106321, <https://doi.org/10.1016/j.petrol.2019.106321>.
- Birle, E. (2011) Geohydraulische Eigenschaften verdichteter Tone unter besonderer Berücksichtigung des ungesättigten Zustandes.) Technische Universität München.
- Bishop, A. W. (1959) The principle of effective stress. *Teknisk ukeblad* **39**:859-863
- Brooks, R. & Corey, T. (1964) Hydraulic properties of porous media. *Hydrology Papers, Colorado State University* **24**:37
- Burdine, N. (1953) Relative permeability calculations from pore size distribution data. *Journal of Petroleum Technology* **5(03)**:71-78
- Burdine, N., Gournay, L. & Reichertz, P. (1950) Pore size distribution of petroleum reservoir rocks. *Journal of Petroleum Technology* **2(07)**:195-204
- Burger, C. A. & Shackelford, C. D. (2001a) Evaluating dual porosity of pelletized diatomaceous earth using bimodal soil-water characteristic curve functions. *Canadian Geotechnical Journal* **38(1)**:53-66
- Burger, C. A. & Shackelford, C. D. (2001b) Soil-water characteristic curves and dual porosity of sand–diatomaceous earth mixtures. *Journal of Geotechnical and Geoenvironmental Engineering* **127(9)**:790-800
- Cai, G., Zhou, A., Liu, Y., Xu, R. & Zhao, C. (2020) Soil water retention behavior and microstructure evolution of lateritic soil in the suction range of 0–286.7 MPa. *Acta Geotechnica* **15(12)**:3327-3341
- Carminati, A., Kaestner, A., Lehmann, P. & Flühler, H. (2008) Unsaturated water flow across soil aggregate contacts. *Advances in Water Resources* **31(9)**:1221-1232, <https://doi.org/10.1016/j.advwatres.2008.01.008>.
- Chowdhury, R. H. & Azam, S. (2016) Unsaturated shear strength properties of a compacted expansive soil from Regina, Canada. *Innovative Infrastructure Solutions* **1(1)**, 10.1007/s41062-016-0047-2.
- Collins, K. & McGown, A. (1974) The form and function of microfabric features in a variety of natural soils. *Géotechnique* **24(2)**:223-254, 10.1680/geot.1974.24.2.223.
- Coppola, A. (2000) Unimodal and bimodal descriptions of hydraulic properties for aggregated soils. *Soil Science Society of America Journal* **64(4)**:1252-1262
- Cui, Y., Loiseau, C. & Delage, P. (2002) Microstructure changes of a confined swelling soil due to suction. In *Unsaturated Soils: Proceedings of the Third International Conference on Unsaturated Soils, UNSAT 2002, 10-13 March 2002, Recife, Brazil.*) CRC Press, vol. 2, pp. 593.
- Cuisinier, O. & Laloui, L. (2004) Fabric evolution during hydromechanical loading of a compacted silt. *International Journal for numerical and analytical methods in geomechanics* **28(6)**:483-499, <https://doi.org/10.1002/nag.348>.
- Delage, P., Audiguier, M., Cui, Y.-J. & Howat, M. D. (1996) Microstructure of a compacted silt. *Canadian Geotechnical Journal* **33(1)**:150-158

- Delage, P. & Lefebvre, G. (1984) Study of the structure of a sensitive Champlain clay and of its evolution during consolidation. *Canadian Geotechnical Journal* **21(1)**:21-35
- Della Vecchia, G., Diudonné, A.-C., Jommi, C. & Charlier, R. (2015) Accounting for evolving pore size distribution in water retention models for compacted clays. *International Journal for numerical and analytical methods in geomechanics* **39(7)**:702-723, 10.1002/nag.2326.
- Della Vecchia, G., Jommi, C. & Romero, E. (2013) A fully coupled elastic-plastic hydromechanical model for compacted soils accounting for clay activity. *International Journal for numerical and analytical methods in geomechanics* **37(5)**:503-535, 10.1002/nag.1116.
- Dexter, A. R., Czyż, E. A., Richard, G. & Reszkowska, A. (2008) A user-friendly water retention function that takes account of the textural and structural pore spaces in soil. *Geoderma* **143(3-4)**:243-253, 10.1016/j.geoderma.2007.11.010.
- Diamond, S. (1970) Pore size distributions in clays. *Clays and Clay Minerals* **18(1)**:7-23
- Diamond, S. (1971) Microstructure and Pore Structure of Impact-Compacted Clays. *Clays and Clay Minerals* **19(4)**:239-249, 10.1346/ccmn.1971.0190405.
- Durner, W. (1994) Hydraulic conductivity estimation for soils with heterogeneous pore structure. *Water resources research* **30(2)**:211-223
- Fredlund, D., Xing, A. & Huang, S. (1994) Predicting the permeability function for unsaturated soils using the soil-water characteristic curve. *Canadian Geotechnical Journal* **31(4)**:533-546
- Fredlund, D. G. & Rahardjo, H. (1993) *Soil mechanics for unsaturated soils*. John Wiley & Sons.
- Fredlund, D. G. & Xing, A. (1994) Equations for the soil-water characteristic curve. *Canadian Geotechnical Journal* **31(4)**:521-532
- Fujikura, Y. & Oshita, H. (2011) Pore structure model of hydrates comprising various cements and SCMs based on changes in particle size of constituent phases. *Journal of Advanced Concrete Technology* **9(2)**:133-147
- Gao, Y., Sun, D. A., Zhou, A. & Li, J. (2020) Predicting Shear Strength of Unsaturated Soils over Wide Suction Range. *International journal of Geomechanics* **20(2)**:04019175, doi:10.1061/(ASCE)GM.1943-5622.0001555.
- Garcia-Bengochea, I. (1978) The relation between permeability and pore size distribution of compacted clayey silts: Interim report
- Gebrenergus, T., Tuller, M. & Muhuthan, B. (2006) The application of X-ray computed tomography for characterisation of surface crack networks in bentonite-sand mixtures. In *Advances in X-ray tomography for geomaterials.* ISTE Ltd London, UK, pp. UK-212.
- Gitirana Jr, G. & Fredlund, D. G. (2004) Soil-water characteristic curve equation with independent properties. *Journal of Geotechnical and Geoenvironmental Engineering* **130(2)**:209-212
- Gupta, S. & Larson, W. (1979) Estimating soil water retention characteristics from particle size distribution, organic matter percent, and bulk density. *Water resources research* **15(6)**:1633-1635
- Haines, W. B. (1930) Studies in the physical properties of soil. V. The hysteresis effect in capillary properties, and the modes of moisture distribution associated therewith. *The Journal of Agricultural Science* **20(1)**:97-116
- Houhou, R., Sutman, M., Sadek, S. & Laloui, L. (2021) Microstructure observations in compacted clays subjected to thermal loading. *Engineering Geology* **287**:105928, <https://doi.org/10.1016/j.enggeo.2020.105928>.
- Juang, C. & Holtz, R. (1986a) A probabilistic permeability model and the pore size density function. *International Journal for numerical and analytical methods in geomechanics* **10(5)**:543-553
- Juang, C. & Holtz, R. D. (1986b) Fabric, pore size distribution, and permeability of sandy soils. *Journal of geotechnical engineering* **112(9)**:855-868
- Khalili, N., Geiser, F. & Blight, G. (2004) Effective stress in unsaturated soils: Review with new evidence. *International journal of Geomechanics* **4(2)**:115-126
- Khalili, N. & Khabbaz, M. (1998) A unique relationship for χ for the determination of the shear strength of unsaturated soils. *Géotechnique* **48(5)**:681-687
- Koliji, A., Laloui, L. & Vulliet, L. (2010) Constitutive modeling of unsaturated aggregated soils. *International Journal for numerical and analytical methods in geomechanics* **34(17)**:1846-1876, 10.1002/nag.888.
- Kosugi, K. I. (1994) Three-parameter lognormal distribution model for soil water retention. *Water resources research* **30(4)**:891-901
- Kosugi, K. I. (1996) Lognormal distribution model for unsaturated soil hydraulic properties. *Water resources research* **32(9)**:2697-2703
- Kumar, R. & Bhattacharjee, B. (2003) Porosity, pore size distribution and in situ strength of concrete. *Cement and Concrete Research* **33(1)**:155-164, [https://doi.org/10.1016/S0008-8846\(02\)00942-0](https://doi.org/10.1016/S0008-8846(02)00942-0).
- Leong, E. C. & Rahardjo, H. (1997a) Permeability functions for unsaturated soils. *Journal of Geotechnical and Geoenvironmental Engineering* **123(12)**:1118-1126

- Leong, E. C. & Rahardjo, H. (1997b) Review of soil-water characteristic curve equations. *Journal of Geotechnical and Geoenvironmental Engineering* **123(12)**:1106-1117
- Li, X., Li, J. H. & Zhang, L. M. (2014) Predicting bimodal soil–water characteristic curves and permeability functions using physically based parameters. *Computers and Geotechnics* **57**:85-96, <https://doi.org/10.1016/j.compgeo.2014.01.004>.
- Li, X. & Zhang, L. M. (2009) Characterization of dual-structure pore-size distribution of soil. *Canadian Geotechnical Journal* **46(2)**:129-141, 10.1139/t08-110.
- Lin, Z., Qian, J. & Shi, Z. (2022) Estimation of the unsaturated shear strength of expansive soils in relation to capillary water-retention curve. *Computers and Geotechnics* **146**, 10.1016/j.compgeo.2022.104735.
- Liu, L.-L., Cui, Z.-H., Wang, J.-J., Xia, Z.-H., Duan, L.-J., Yang, Y., Li, M. & Li, T. (2020) Pore size distribution characteristics of high rank coal with various grain sizes. *ACS omega* **5(31)**:19785-19795
- Lloret, A. & Villar, M. V. (2007) Advances on the knowledge of the thermo-hydro-mechanical behaviour of heavily compacted “FEBEX” bentonite. *Physics and Chemistry of the Earth, Parts A/B/C* **32(8-14)**:701-715, 10.1016/j.pce.2006.03.002.
- Lloret, A., Villar, M. V., Sánchez, M., Gens, A., Pintado, X. & Alonso, E. E. (2003) Mechanical behaviour of heavily compacted bentonite under high suction changes. *Géotechnique* **53(1)**:27-40, 10.1680/geot.2003.53.1.27.
- Lu, N. (2016) Generalized soil water retention equation for adsorption and capillarity. *Journal of Geotechnical and Geoenvironmental Engineering* **142(10)**:04016051
- Lu, N., Godt, J. W. & Wu, D. T. (2010) A closed-form equation for effective stress in unsaturated soil. *Water resources research* **46(5)**, <https://doi.org/10.1029/2009WR008646>.
- Lu, N. & Likos, W. J. (2004) *Unsaturated soil mechanics*. Wiley.
- Manca, D., Ferrari, A. & Laloui, L. (2016) Fabric evolution and the related swelling behaviour of a sand/bentonite mixture upon hydro-chemo-mechanical loadings. *Géotechnique* **66(1)**:41-57, 10.1680/jgeot.15.P.073.
- Monroy, R., Zdravkovic, L. & Ridley, A. (2010) Evolution of microstructure in compacted London Clay during wetting and loading. *Géotechnique* **60(2)**:105-119, 10.1680/geot.8.P.125.
- Mualem, Y. (1976) A new model for predicting the hydraulic conductivity of unsaturated porous media. *Water resources research* **12(3)**:513-522
- Mun, W. & McCartney, J. S. (2015) Compression mechanisms of unsaturated clay under high stresses. *Canadian Geotechnical Journal* **52(12)**:2099-2112
- Musso, G., Romero, E. & Vecchia, G. D. (2013) Double-structure effects on the chemo-hydro-mechanical behaviour of a compacted active clay. *Géotechnique* **63(3)**:206-220, 10.1680/geot.SIP13.P.011.
- Nagra (2008) *Effects of post-disposal gas generation in a repository for low- and intermediate-level waste sited in the Opalinus Clay of Northern Switzerland Technical report--08-07*. Switzerland, Report 1015-2636, pp. 175.
- Ng, C. W. W., Sadeghi, H., Jafarzadeh, F., Sadeghi, M., Zhou, C. & Baghbanrezvan, S. (2020) Effect of microstructure on shear strength and dilatancy of unsaturated loess at high suctions. *Canadian Geotechnical Journal* **57(2)**:221-235, 10.1139/cgj-2018-0592.
- Othmer, H., Diekkrüger, B. & Kutilek, M. (1991) Bimodal porosity and unsaturated hydraulic conductivity. *Soil Science* **152(3)**:139-150
- Prapaharan, S., Altschaeffl, A. G. & Dempsey, B. J. (1985) Moisture Curve of Compacted Clay: Mercury Intrusion Method. *Journal of geotechnical engineering* **111(9)**:1139-1143, doi:10.1061/(ASCE)0733-9410(1985)111:9(1139).
- Rahimi, A., Rahardjo, H. & Leong, E.-C. (2015) Effect of range of soil–water characteristic curve measurements on estimation of permeability function. *Engineering Geology* **185**:96-104, 10.1016/j.enggeo.2014.11.017.
- Richards, B. (1965) *Measurement of free energy of soil moisture by the psychrometric technique, using thermistors*.
- Romero, E., Della Vecchia, G. & Jommi, C. (2011) An insight into the water retention properties of compacted clayey soils. *Géotechnique* **61(4)**:313-328
- Romero, E., Gens, A. & Lloret, A. (1999) Water permeability, water retention and microstructure of unsaturated compacted Boom clay. *Engineering Geology* **54(1-2)**:117-127
- Ross, P. J. & Smettem, K. R. (1993) Describing soil hydraulic properties with sums of simple functions. *Soil Science Society of America Journal* **57(1)**:26-29
- Satyanaga, A., Rahardjo, H., Leong, E.-C. & Wang, J.-Y. (2013) Water characteristic curve of soil with bimodal grain-size distribution. *Computers and Geotechnics* **48**:51-61
- Scheidegger, A. E. (2020) *The physics of flow through porous media*. University of Toronto press.
- Scheinost, A., Sinowski, W. & Auerswald, K. (1997) Regionalization of soil water retention curves in a highly variable soilscape, I. Developing a new pedotransfer function. *Geoderma* **78(3)**:129-143
- Sheng, D., Zhou, A. & Fredlund, D. G. (2011) Shear strength criteria for unsaturated soils. *Geotechnical and Geological Engineering* **29(2)**:145-159

- Sillers, W. S., Fredlund, D. G. & Zakerzaheh, N. (2001) Mathematical attributes of some soil–water characteristic curve models. *Geotechnical & Geological Engineering* **19(3)**:243-283, 10.1023/A:1013109728218.
- Simms, P. & Yanful, E. (2002) Predicting soil–Water characteristic curves of compacted plastic soils from measured pore-size distributions. *Géotechnique* **52(4)**:269-278
- Sørland, G., Djurhuus, K., Widerøe, H., Lien, J. & Skauge, A. (2007) ABSOLUTE PORE SIZE DISTRIBUTIONS FROM NMR. *Diffusion Fundamentals* **5**:4.1-4.15
- Sridharan, A., Altschaeffl, A. G. & Diamond, S. (1971) Pore Size Distribution Studies. *Journal of the Soil Mechanics and Foundations Division* **97(5)**:771-787, 10.1061/JSFEAQ.0001595.
- Sun, H., Mašin, D., Najser, J., Neděla, V. & Navrátilová, E. (2019) Bentonite microstructure and saturation evolution in wetting–drying cycles evaluated using ESEM, MIP and WRC measurements. *Géotechnique* **69(8)**:713-726
- Sun, W.-J. & Cui, Y.-J. (2020) Determining the soil-water retention curve using mercury intrusion porosimetry test in consideration of soil volume change. *Journal of Rock Mechanics and Geotechnical Engineering* **12(5)**:1070-1079, 10.1016/j.jrmge.2019.12.022.
- Van Genuchten, M. T. (1980) A closed-form equation for predicting the hydraulic conductivity of unsaturated soils. *Soil Science Society of America Journal* **44(5)**:892-898
- Vanapalli, S. K., Fredlund, D. G. & Pufahl, D. E. (1996) The relationship between the soil-water characteristic curve and the unsaturated shear strength of a compacted glacial till. *Geotechnical Testing Journal* **19(3)**:259-268
- Vanapalli, S. K., Fredlund, D. G. & Pufahl, D. E. (1999) The influence of soil structure and stress history on the soil–water characteristics of a compacted till. *Géotechnique* **49(2)**:143-159, 10.1680/geot.1999.49.2.143.
- Vereecken, H., Maes, J., Feyen, J. & Darius, P. (1989) Estimating the soil moisture retention characteristic from texture, bulk density, and carbon content. *Soil Science* **148(6)**:389-403
- Villar, M. & Lloret, A. (2001) Variation of the intrinsic permeability of expansive clays upon saturation. *Clay science for engineering*:259-266
- Wang, Q., Cui, Y.-J., Minh Tang, A., Xiang-Ling, L. & Wei-Min, Y. (2014) Time- and density-dependent microstructure features of compacted bentonite. *Soils and Foundations* **54(4)**:657-666, 10.1016/j.sandf.2014.06.021.
- Wang, Q., Tang, A. M., Cui, Y.-J., Barnichon, J.-D. & Ye, W.-M. (2013) Investigation of the hydro-mechanical behaviour of compacted bentonite/sand mixture based on the BExM model. *Computers and Geotechnics* **54**:46-52, 10.1016/j.compgeo.2013.05.011.
- Wang, X. & Ni, Q. (2003) Determination of cortical bone porosity and pore size distribution using a low field pulsed NMR approach. *Journal of Orthopaedic Research* **21(2)**:312-319
- Washburn, E. W. (1921) Note on a method of determining the distribution of pore sizes in a porous material. *Proceedings of the National Academy of Sciences of the United States of America* **7(4)**:115
- Watanabe, Y. & Yokoyama, S. (2021) Self-sealing behavior of compacted bentonite–sand mixtures containing technological voids. *Geomechanics for Energy and the Environment* **25**, 10.1016/j.gete.2020.100213.
- Wijaya, M. & Leong, E. (2016) Equation for unimodal and bimodal soil–water characteristic curves. *Soils and Foundations* **56(2)**:291-300
- Xiong, Q., Li, K., Yang, D., Yu, H., Pan, Z. & Song, Y. (2020) Characterizing coal pore space by gas adsorption, mercury intrusion, FIB–SEM and μ -CT. *Environmental Earth Sciences* **79(10)**, 10.1007/s12665-020-08950-3.
- Yan, W., Birle, E. & Cudmani, R. (2021a) A new framework to determine general multimodal soil water characteristic curves. *Acta Geotechnica* **16(10)**:3187-3208, 10.1007/s11440-021-01245-2.
- Yan, W., Birle, E. & Cudmani, R. (2021b) A simple approach for predicting soil water characteristic curve of clayey soils using pore size distribution data. In *MATEC Web of Conferences*.) EDP Sciences, vol. 337, pp. 02012.
- Yan, W. & Cudmani, R. (2022a) A general analytical expression for pore size distribution based on probability theory. *Engineering Geology* **297**, 10.1016/j.enggeo.2021.106501.
- Yan, W. & Cudmani, R. (2022b) A novel framework for predicting water retention behaviour based on pore size distribution data of multimodal unsaturated soils. *submitted to Acta geotechnica*
- Ying, Z., Cui, Y.-J., Benahmed, N. & Duc, M. (2021) Drying effect on the microstructure of compacted salted silt. *Géotechnique*:1-9, 10.1680/jgeot.20.P.319.
- Zhai, Q., Rahardjo, H., Satyanaga, A. & Dai, G. (2019) Estimation of unsaturated shear strength from soil–water characteristic curve. *Acta Geotechnica* **14(6)**:1977-1990, 10.1007/s11440-019-00785-y.
- Zhai, Q., Rahardjo, H., Satyanaga, A. & Dai, G. (2020a) Estimation of the soil-water characteristic curve from the grain size distribution of coarse-grained soils. *Engineering Geology* **267**, 10.1016/j.enggeo.2020.105502.

- Zhai, Q., Rahardjo, H., Satyanaga, A., Dai, G. & Zhuang, Y. (2020b) Framework to estimate the soil-water characteristic curve for soils with different void ratios. *Bulletin of Engineering Geology and the Environment* **79(8)**:4399-4409, 10.1007/s10064-020-01825-8.
- Zhai, Q., Rahardjo, H., Satyanaga, A. & Priono (2017) Effect of bimodal soil-water characteristic curve on the estimation of permeability function. *Engineering Geology* **230**:142-151, 10.1016/j.enggeo.2017.09.025.
- Zhang, L. & Chen, Q. (2005) Predicting bimodal soil–water characteristic curves. *Journal of Geotechnical and Geoenvironmental Engineering* **131(5)**:666-670
- Zhang, L., Fredlund, D. G., Fredlund, M. D. & Wilson, G. W. (2014) Modeling the unsaturated soil zone in slope stability analysis. *Canadian Geotechnical Journal* **51(12)**:1384-1398
- Zhang, Z., Qin, Y., Yi, T., You, Z. & Yang, Z. (2020) Pore structure characteristics of coal and their geological controlling factors in eastern Yunnan and western Guizhou, China. *ACS omega* **5(31)**:19565-19578
- Zhao, H., Zhang, L. & Fredlund, D. (2013) Bimodal shear-strength behavior of unsaturated coarse-grained soils. *Journal of Geotechnical and Geoenvironmental Engineering* **139(12)**:2070-2081
- Zhou, A.-N., Sheng, D., Sloan, S. W. & Gens, A. (2012) Interpretation of unsaturated soil behaviour in the stress–saturation space, I: volume change and water retention behaviour. *Computers and Geotechnics* **43**:178-187

List of Publications

Journal Papers

- Yan, W. & Cudmani, R. (2022a) A general analytical expression for pore size distribution based on probability theory. *Engineering Geology* **297**, 10.1016/j.enggeo.2021.106501. (Paper I)
- Yan, W., Birle, E. & Cudmani, R. (2021a) A new framework to determine general multimodal soil water characteristic curves. *Acta Geotechnica* **16(10)**:3187-3208, 10.1007/s11440-021-01245-2. (Paper II)
- Yan, W. & Cudmani, R. (2022b) A novel framework for predicting water retention behaviour based on pore size distribution data of multimodal unsaturated soils. submitted to *Acta geotechnica* (under review) (Paper III)
- Cudmani, R., Yan, W. & Schindler (2022), U. A constitutive model for the simulation of temperature-, stress- and rate-dependent behaviour of frozen granular soils. *Géotechnique* **0(0)**:1-13, 10.1680/jgeot.21.00012.

Conference Papers

- Yan, W., Birle, E. & Cudmani, R. (2021b) A simple approach for predicting soil water characteristic curve of clayey soils using pore size distribution data. In *MATEC Web of Conferences*. EDP Sciences, vol. 337, pp. 02012.
- Cudmani, R., Sun, J. & Yan, W. (2018) A Constitutive Model for Frozen Granular Soils. In *Proceedings of China-Europe Conference on Geotechnical Engineering.*) Springer, pp. 1345-1349.

Appendix – original journal papers

Paper I – A general analytical expression for pore size distribution based on probability theory

Yan, W. & Cudmani, R. (2022a) A general analytical expression for pore size distribution based on probability theory. *Engineering Geology* **297**, 10.1016/j.enggeo.2021.106501.

1 **A general analytical expression for pore size distribution based on**
2 **probability theory**

3 Author 1:

- 4 • Wei Yan* (given name: Wei / Family name: Yan)
- 5 • Department of Civil, Geo and Environmental Engineering, Technical University of Munich, Franz-
6 Langering-Straße 10, 81245 Munich, Germany
- 7 • E-Mail: wei.yan@tum.de
- 8 • ORCID number: 0000-0001-7008-966X

9 Author 2:

- 10 • Roberto Cudmani (given name: Roberto / Family name: Cudmani)
- 11 • Department of Civil, Geo and Environmental Engineering, Technical University of Munich, Franz-
12 Langering-Straße 10, 81245 Munich, Germany
- 13 • E-Mail: roberto.cudmani@tum.de

14

15

16 *Corresponding author: Wei Yan (E-Mail: wei.yan@tum.de, Franz-Langering-Straße 10, 81245 Munich,
17 Technical University of Munich, Munich, Germany)

18

19 **Abstract**

20 The pore structure of soils and rocks plays a crucial role in geotechnical, geo-environmental and geological
21 engineering, as it dominates the hydro-mechanical behaviour, gas- and liquid-permeability as well as material
22 transport property of soils and rocks. A large amount of pore size distribution (PSD) data of porous materials have
23 been experimentally determined in the past decades and are currently available in the literature. However, a general
24 expression to parameterize these PSD curves is still missing. In this study, a general multimodal PSD model is
25 developed based on the probability theory, which is a strong tool to quantify the complex soil microstructure
26 precisely. The parameters in the model possess a clear physical meaning. The model is validated by reproducing
27 the PSD curves of two clays and a sand-clay mixture having a complex pore structure. The parameterized PSD
28 curves demonstrate a strong consistency with the measurements. In addition, the model is applied to predict the
29 PSD evolution under hydro-mechanical processes (e.g., compaction, saturation- swelling-process), the water
30 content – soil suction – dry density relationship of Boom clay after compaction and the time-dependent PSD
31 evolution of MX80 Bentonite. Beside soils, the proposed general multimodal PSD relationship can describe the
32 pore structure of any other porous and granular material, as all the underlying physics is the same for all of them.
33 The proposed model can be incorporated into the existing effective stress parameter formulation, permeability
34 models and constitutive models of unsaturated multimodal soils.

35 **Keywords**

36 Pore size distribution; multimodal; unsaturated soil; microstructure; probability; porous material

37 **1. Introduction**

38 Porous materials exist widely in natural environment (e.g., soils and rocks), industry (e.g., concrete, ceramic and
39 membrane) and biological tissues (e.g., human bone (Wang and Ni 2003)). A precise description of pore size
40 distribution (PSD) of porous materials is essential for understanding the fundamental features of their thermo-
41 hydro-mechanical behaviour and for their applications in various engineering fields. For instance, comprehensive
42 information of the microstructure of bentonites under different thermo-mechanical conditions is required for its
43 applications in high-level radioactive waste repositories (e.g., as sealing materials) (Lloret and Villar 2007); the
44 properties of the pore structure in petroleum reservoir rocks are significant in petroleum industry for a better
45 interpretation of the flow process in the porous matrix (Burdine et al. 1950); the pore size distribution of human
46 bone has been investigated to assess the age - influence on the bone pore structure (Wang and Ni 2003).

47 Especially, the pore size distribution of soils and rocks plays a crucial role in the geotechnical, geo-
48 environmental, geological and mining engineering applications, since it dominates the gas- and liquid-permeability
49 as well as material transport property of soils and rocks (Burdine et al. 1950; Juang and Holtz 1986a; Mualem
50 1976). For geologic carbon sequestration, the pore size distribution of storage rock is used to predict the capillary
51 pressure-saturation relationship, model the multiphase fluid flow and estimate the storage capacity (Cheng et al.
52 2017; Liu et al. 2013). In jet grouting approach, soil microstructural information (e.g., the maximum and mean
53 pore radius) is needed to approximate the applying pressure of cement and the grouted soil geometry. In mining
54 engineering, the coal pore structure is pivotal for the simulation of the enrichment and migration of methane in
55 coalbed (Cai et al. 2020; Zhang et al. 2020). Therefore, a general analytical pore size distribution expression, for
56 describing soil and rock microstructure precisely, is necessary to improve the techniques in these engineering
57 applications.

58 Numerous PSD models have been developed to describe unimodal microstructure of soils (e.g., pure sand). In
59 the simplest case, soil pore size is usually assumed to obey Gaussian distribution (Milligan and Adams 1954),
60 lognormal distribution (Kosugi 1996) or empirical unimodal distributions (Brutsaert 1966; Fredlund and Xing
61 1994). However, these unimodal models are incapable of precisely describing the pore structure of fine-grained
62 soils with complex pore structure (e.g., clayey soils compacted at the dry side with interaggregate and
63 intraaggregate porosities (Alonso et al. 1987; Delage and Lefebvre 1984)). In the past decades, the bimodal
64 microstructure of compacted clayey soils has been confirmed by a large number of research works by means of
65 mercury intrusion porosimetry (MIP) as well as scanning electron microscope (SEM) (Birle 2011; Burton et al.
66 2014; Diamond 1970, 1971; Gao et al. 2019; Griffiths and Joshi 1989; Monroy et al. 2010; Romero et al. 1999;
67 Sun et al. 2019). Similar bimodal pore structures have also been detected in gap-graded soils (Angerer 2020;
68 Satyanaga et al. 2013) and artificial mixture of fine-grained and coarse-grained soils (Juang and Holtz 1986b).
69 Based on the experimental evidence, a number of bimodal models have been developed to describe the “dual-
70 structure” of soils (Jensen et al. 2019; Li et al. 2014a; Li and Zhang 2009; Ross and Smettem 1993). For example,
71 Li and Zhang (2009) proposed a bimodal PSD model by regarding the bimodal pore size distribution as a
72 superposition of two lognormal distributions. Afterwards, Li et al. (2014b) extended this model by integrating an
73 examination of the density dependency of PSDs for clayey soils into this model.

74 Recently, several research works have shown that the soil porosity can be more complex than bimodal. Wang
75 et al. (2014) observed that the microstructure of compacted MX80 bentonite consists of four sub porosities during
76 a hydration process. Similarly, Prikryl and Weishauptová (2010) also observed four pore categories in a bentonite-
77 sand mixture through adsorption technique and MIP tests. Except for soils, the pore structures of other porous
78 materials, e.g., shale (Liu et al. 2019) and cement-based materials (Fujikura and Oshita 2011; Zhu et al. 2019), are
79 even more complex. These experimental results indicate that a general multimodal pore size distribution model,
80 in which the number of sub porosity counts as a varying integer, is required to describe the complex pore structures
81 of porous materials.

82 So far, the attempts to find an analytical expression to describe the general multimodal pore size distribution
83 for porous materials, including different soil types, have been unsuccessful. Durner (1994) pointed out that a
84 multimodal pore structure could be regarded as an assemblage of several sub porosities. Ross and Smettem (1993)
85 proposed an analytical expression for a multimodal PSD by superposition of several unimodal PSD functions.
86 However, the parameters in their model are fitting parameters without physical meaning. As a result, further
87 modifications of the model, which are necessary to account for the variations in pore structure along mechanical
88 and hydraulic paths, are difficult.

89 In summary, a general multimodal pore size distribution model able to simulate experimental PSD for different
90 porous materials available in the literature is still missing. The main goals of this contribution are to develop and
91 validate a general multimodal PSD model for porous materials based on the probability theory and show its
92 application to the analysis of the PSD evolution along hydro-mechanical paths. Providing the quantitative analysis
93 of soil microstructure, the proposed PSD model can be incorporated to existing permeability models (Childs and
94 Collis-George 1950; Juang and Holtz 1986a; Kosugi 1996) and constitutive models (Alonso et al. 2013; Gens and
95 Alonso 1992) or used to assess the effective stress parameter of unsaturated multimodal soils (Alonso et al. 2010).

96 **2. Theoretical basis for a multimodal PSD model**

97 **2.1. Definition of pore radius and pore size density function**

98 The complex pore structure in a porous material (e.g., soils) results from the irregular shapes and various sizes of
 99 pores, which can be interconnected (accessible from outside) or isolated (not accessible from outside). To develop
 100 our multimodal PSD model, a probabilistic distribution of the pore sizes based on the concept of Scheidegger
 101 (2020) and Juang and Holtz (1986a) is assumed.

102 Scheidegger (2020) introduced a mathematical definition of pore radius r in a porous medium. In a
 103 representative elementary volume (REV), the pore radius r denoted to a point of the pore space is defined as the
 104 radius of the maximum sphere containing this point within the pore space (i.e., the sphere cannot touch the solid
 105 particle, and the point can locate at any position in the sphere). In this framework, the pore radius r is a non-
 106 negative random variable depending on the position of the point in the pore space. Thus, the term $f(r)dr$, where
 107 $f(r)$ represents the pore size density function, describes the occurrence probability of a sphere with a radius $r \rightarrow$
 108 $r + dr$ in a porous medium. Based on probabilistic concept, following condition must be hold:

$$\int_0^{+\infty} f(r) dr = 1. \tag{1}$$

109 **2.1.1. Idealized case: isolated spherical void space in soil**

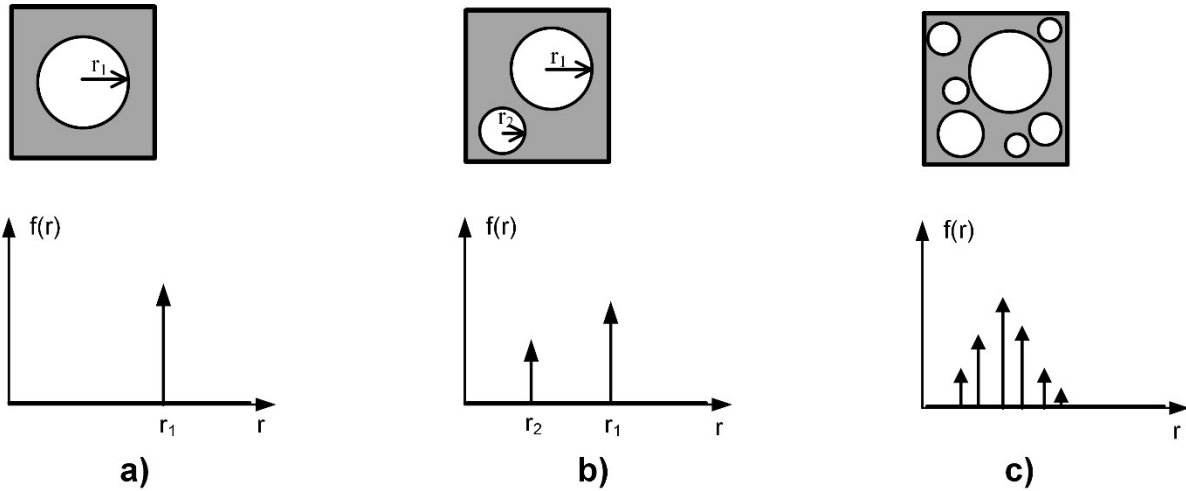


Fig. 1. Schematic representation of pore size density functions for idealized cases

110 Fig. 1a illustrates the microstructure of a porous medium, which is represented by a REV with a spherical pore
 111 in the centre (i.e., an idealized case). The radius of the sphere is denoted with r_1 . According to Scheidegger's
 112 definition, the pore radius denoted to each point within the pore space is r_1 . Thus, the pore size density function
 113 $f(r)$ can be expressed as

$$f(r) = \delta(r - r_1), \tag{2}$$

114 where $\delta(x)$ is Dirac delta function defined as

$$\delta(x) = \begin{cases} +\infty, & x = 0 \\ 0, & x \neq 0 \end{cases} \tag{3}$$

115 and

$$\int_{-\infty}^{+\infty} \delta(x) dx = 1. \quad (4)$$

116 Considering the non-negative nature of pore radius, Eq. (4) can be rewritten as

$$\int_0^{+\infty} \delta(x) dx = 1. \quad (5)$$

117 From Eqs. (3) – (5), it can be easily shown that the pore size density function $f(r)$ defined in Eq. (2) fulfils the
118 condition in Eq. (1).

119 When the pore space in an REV consists of N individual isolated spherical pores, as shown in Fig. 1b and 1c,
120 the pore size density function $f(r)$ can be expressed as:

$$f(r) = \sum_{i=1}^N R_i \delta(r - r_i), \quad (6)$$

121 where R_i and r_i represent the volumetric fraction and the radius of the i^{th} spherical pore, respectively. The
122 volumetric fractions R_i must fulfil the following condition:

$$\sum_{i=1}^N R_i = 1. \quad (7)$$

123 A schematical illustration of the pore size density functions $f(r)$ for a REV with two and more isolated spherical
124 pores are shown in Fig. 1b and 1c, respectively.

125

126 **2.1.2. Realistic cases: interconnected irregular void space in soils**

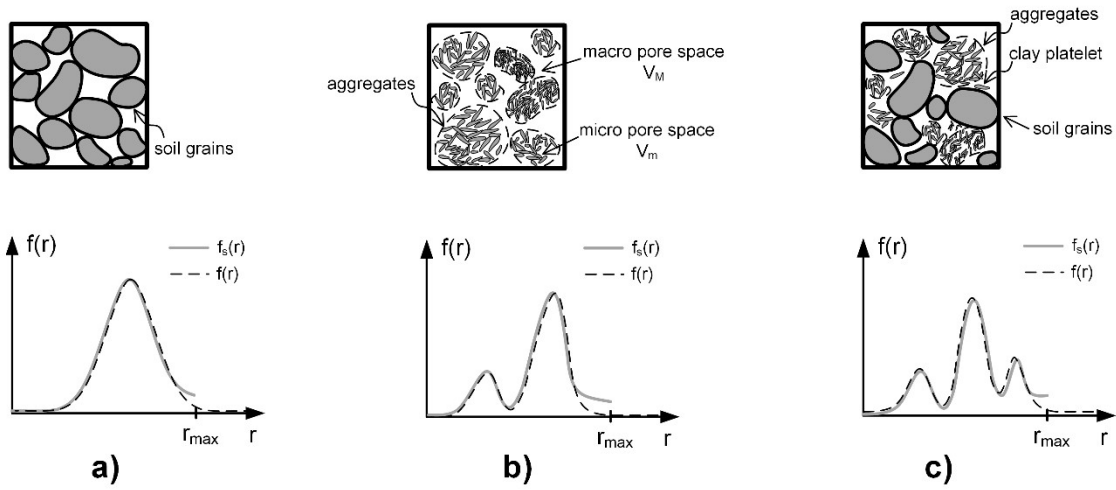


Fig. 2. Schematic representation of pore size density functions for different soil types

127 The pore structure of a soil consists of interconnected and isolated pores with irregular shapes and different sizes.
 128 Applying Scheidegger's definition for soil void space, the pore radius r is a nonnegative continuous random
 129 variable, and the pore size density function $f(r)$ is a nonnegative continuous function (Juang and Holtz 1986a).
 130 Considering that there must be a maximal spherical pore in the void space, we have:

$$\int_0^{r_{max}} f_S(r) dr = 1 \quad (8)$$

131 and

$$f_S(r) \geq 0, \forall r \in (0, r_{max}]. \quad (9)$$

132 Herein, $f_S(r)$ is the pore size density function of soils under Scheidegger's framework, and r_{max} represents the
 133 radius of the maximal spherical pore. Noting that $r = 0$ means the point locates on the particle – void interface,
 134 $f_S(r)$ is defined on the domain $r \in (0, r_{max}]$. Since all the points within the maximal spherical pore are denoted
 135 with r_{max} , we acquire following inequality:

$$\lim_{\Delta r \rightarrow 0} \left(\int_{r_{max}-\Delta r}^{r_{max}} f_S(r) dr \right) = \frac{V_{(r=r_{max})}}{V_{tot}} > 0. \quad (10)$$

136 Herein, Δr is an infinitesimal positive value, $V_{(r=r_{max})}$ represents the volume of the maximal spherical pore, and
 137 V_{tot} is the total void volume of REV. From Eq.(10) we have

$$f_S(r_{max}) > 0. \quad (11)$$

138 In Fig. 2a, the pore size density function $f_S(r)$ of a typical granular soil (e.g., pure sand) under Scheidegger's
 139 framework is schematically shown. It is noted that the domain of the function $f_S(r)$ contains r_{max} . On one hand,
 140 it is difficult to determine r_{max} accurately by means of existing experimental techniques. On the other hand, r_{max}
 141 is a variable depending on the other soil state parameters (e.g., the stress state, soil suction and void ratio). For the
 142 convenience of practical applications, the pore size density function can be extended on the entire pore radius
 143 domain $r \in (0, +\infty)$ by

$$f^*(r) = \begin{cases} f_S(r), & r \in (0, r_{max}] \\ 0, & r \in (r_{max}, +\infty) \end{cases} \quad (12)$$

144 From Eq. (11) and (12) we obtain

$$\lim_{r \rightarrow r_{max}^-} f^*(r) = f_S(r_{max}) > \lim_{r \rightarrow r_{max}^+} f^*(r) = 0, \quad (13)$$

145 which indicates a point of discontinuity at $r = r_{max}$. Without loss of generality, we assume that the volume of the
 146 maximum sphere $V_{(r=r_{max})}$ is an infinitesimal of higher order than the total void volume V_{tot} . That means,
 147 $f_S(r_{max})$ is sufficient close to zero. Therefore, it is reasonable to find a continuous function $f(r)$ to approximate
 148 $f^*(r)$, if following conditions are fulfilled:

$$\lim_{r \rightarrow +\infty} f(r) = 0 \text{ and } \int_0^{+\infty} f(r) dr = 1. \quad (14)$$

149 A comparison between $f_S(r)$ and $f(r)$ for typical granular soils with unimodal pore structure is schematically
 150 shown in Fig. 2a. The area under both curves is equal to one. Considering the conditions expressed in Eqs. (14),
 151 an appropriate unimodal pore size density function $f(r)$ derived from van Genuchten model (Van Genuchten
 152 1980) is proposed:

$$f(r) = \frac{m(r^f/r)^{\frac{1}{1-m}}}{r(1-m) \left[1 + (r^f/r)^{\frac{1}{1-m}} \right]^{m+1}} \quad (15)$$

153 Herein, m ($0 < m < 1$) is the unitless pore size spectrum number, and r^f ($r^f > 0$) is a reference pore radius
 154 related to the maximal pore radius r_{max} (i.e., $r^f \propto r_{max}$).

155 2.2. Developing a general multimodal PSD model

156 In Fig. 2b, a bimodal soil pore structure (e.g., for clayey soils compacted at the dry side (Romero et al. 1999)) is
 157 schematically shown. The total pore volume V_{tot} is divided into a macro (V_M) and micro (V_m) part by the boundary
 158 surface of aggregates (dashed lines). Applying Scheidegger's concept in the micro and macro pore spaces and
 159 repeating the process from Eq. (8) to Eq. (15), we obtain the pore size density functions $f_m(r)$ (for micro porosity)
 160 and $f_M(r)$ (for macro porosity). Considering that both $f_m(r)$ and $f_M(r)$ are defined on the entire pore radius
 161 domain $r \in (0, +\infty)$, the overall pore size density function $f(r)$ for the bimodal soil is obtained by supposition
 162 of $f_m(r)$ and $f_M(r)$:

$$f(r) = \frac{V_M}{V_{tot}} f_M(r) + \frac{V_m}{V_{tot}} f_m(r) = R_M f_M(r) + R_m f_m(r), \quad (16)$$

163 where R_M and R_m represent the volumetric fraction of macro- and micro-porosity, respectively. Similarly,
 164 repeating the process from Eq. (8) to Eq. (15) for each sub porosity of a multimodal soil, the overall multimodal
 165 pore size density function gives

$$f(r) = \sum_{i=1}^N R_i f_i(r) \quad (17)$$

166 where N is an integer representing the modality number, and R_i is the volumetric fraction of each sub porosity.
 167 Rewriting Eq. (15), the probability density function of the i^{th} porosity $f_i(r)$ can be expressed as

$$f_i(r) = \frac{m_i (r_i^f / r)^{\frac{1}{1-m_i}}}{r(1-m_i) \left[1 + (r_i^f / r)^{\frac{1}{1-m_i}} \right]^{m_i+1}} \quad (18)$$

168 where m_i ($0 < m_i < 1$) and r_i^f ($r_i^f > 0$) are the unitless pore size spectrum number and the reference pore radius
 169 of i^{th} sub porosity, respectively. Substituting Eq. (18) in Eq. (17), a general N-modal PSD function yields

$$f(r) = \sum_{i=1}^N R_i \frac{m_i (r_i^f / r)^{\frac{1}{1-m_i}}}{r(1-m_i) \left[1 + (r_i^f / r)^{\frac{1}{1-m_i}} \right]^{m_i+1}} \quad (19)$$

170 The schema in Fig. 2c demonstrates an example of a tri-modal soil consisting of soil grains, aggregates and free
 171 fine-grain particles.

172 2.3. A dimensionless multimodal PSD model

173 It is noted that $f(r)$ is in the unit of L^{-1} (inverse of length). Juang and Holtz (1986a) proposed to express the
 174 pores size density function in a dimensionless form by presenting the pore radius r in logarithmic scale. Then, Eq.
 175 (1) can be equivalently expressed as

$$\int_0^{+\infty} \omega(r) d \log r = 1. \quad (20)$$

176 Herein, $\omega(r)$ is defined as the dimensionless pore size density function. Comparing Eq. (20) and Eq. (1), we obtain
 177 the simple relationship between $f(r)$ and $\omega(r)$:

$$\omega(r) = (\ln 10) r f(r). \quad (21)$$

178 Substituting Eq. (19) in Eq. (21) gives:

$$\omega(r) = \sum_{i=1}^N R_i \omega_i(r) = \sum_{i=1}^N R_i \frac{(\ln 10) m_i (r_i^f / r)^{\frac{1}{1-m_i}}}{(1-m_i) \left[1 + (r_i^f / r)^{\frac{1}{1-m_i}} \right]^{m_i+1}}, \quad (22)$$

179 where $\omega_i(r)$ represents the dimensionless pore size density function of each sub porosity. In this paper, the pore
 180 radius r is presented in a logarithmic scale, and the dimensionless form $\omega(r)$ is used to describe the pore size
 181 density curves in the following sections.

182 Using the dimensionless form $\omega(r)$, the cumulative pore size distribution curve of a multimodal soil can be
 183 described by:

$$F(r) = \int_0^r \omega(r) d \log r = \sum_{i=1}^N R_i \left[1 + \left(\frac{r_i^f}{r} \right)^{\frac{1}{1-m_i}} \right]^{-m_i} \quad (23)$$

184 and the complementary cumulative curve yields

$$F_c(r) = \int_r^{+\infty} \omega(r) d \log r = 1 - \sum_{i=1}^N R_i \left[1 + \left(\frac{r_i^f}{r} \right)^{\frac{1}{1-m_i}} \right]^{-m_i} \quad (24)$$

185 Let us employ a simple mathematical transformation:

$$s^* = \frac{1}{r} \in (0, +\infty) \quad (25)$$

186 where s^* is a variable representing the inverse of pore radius r . Substituting Eq. (25) in Eq. (23), we obtain

$$F(s^*) = \sum_{i=1}^N R_i \left[1 + (r_i^f s^*)^{\frac{1}{1-m_i}} \right]^{-m_i}. \quad (26)$$

187 Eq. (26) is useful in the parameter determination procedure, which will be introduced in the following section.

188

189 **3. Parametric study**

190 **3.1. Physical and graphical meanings of the parameters**

191 In this section, a parametric study is conducted to show graphically the physical meanings of the parameters of the
 192 proposed multimodal PSD model [Eq. (22)]. Fig. 3a shows $\omega_i(r)$ curves with a fixed r_i^f ($r_i^f = 1 \mu m$) and various
 193 m_i , which indicates that the pore size spectrum parameter m_i determines the shape of $\omega_i(r)$ and affects the
 194 maximum value of $\omega_i(r)$ and its location. As can be seen, the sub pore size density curve $\omega_i(r)$ becomes flatter
 195 with decreasing m_i . From a physical point of view, the smaller the m_i , the more disperse the pore radius (in the
 196 logarithmic scale) is. On the contrary, m_i tends to one for the pore size density curve of a REV with N individual
 197 spherical pores (see Fig. 1c), i.e., Eq. (19) degrades to Eq. (6).

198 Fig. 3b demonstrates the $\omega_i(r)$ curves with different r_i^f and a fixed m_i ($m_i = 0.5$). As can be seen, the
 199 parameter r_i^f shifts the sub pore size density curves horizontally. Let us define the pore radius at the peak of $\omega_i(r)$
 200 curve as the mean pore radius $r_{i,mean}$ and that at the onset point of the bell-shape as the maximal pore radius $r_{i,max}$.
 201 It can be shown that the scaling factor of $r_{i,max}$ and $r_{i,mean}$ coincides with that of r_i^f (in this case the scaling factor
 202 is equal to 10). Thus, the “translation”-effect suggests that r_i^f is a parameter proportional to the maximal pore
 203 radius $r_{i,max}$ and the mean pore radius $r_{i,mean}$ of the sub porosity (i.e., $r_i^f \propto r_{i,max} \propto r_{i,mean}$).

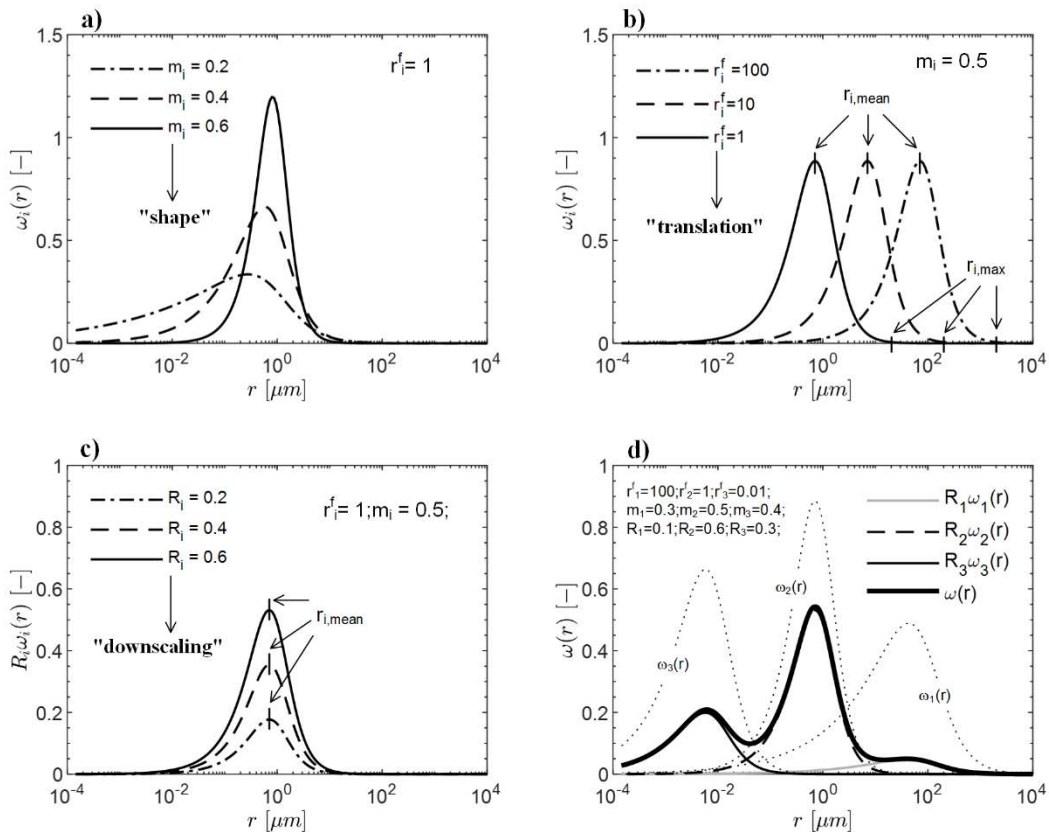


Fig. 3. Parametric study of the proposed model a) influence of parameter m_i b) influence of parameter r_i^f c) influence of parameter R_i d) graphical interpretation of a tri-modal PSD curve

204 Fig. 3c shows the impact of the volumetric fraction R_i on the PSD curve. With fixed values of r_i^f and m_i
 205 ($r_i^f = 1 \mu m$, $m_i = 0.5$), the peak value at $r_{i,mean}$ is “downscaled” as $\omega_i(r)$ multiplied by R_i , while the “location”
 206 (i.e., the value of $r_{i,mean}$) and “shape” of the $\omega_i(r)$ curve are not affected.

207 In Fig. 3d, an example of a tri-modal PSD curve with a given parameter set is illustrated. The dot-point-curves
 208 represent the PSD of sub porosities. The overall tri-modal PSD curve is acquired by a linear combination of the
 209 sub curves with the coefficients R_i , which is presented by the bold solid curve.

210 Summarizing, the parameters in the proposed multimodal PSD model possess clear physical meanings: m_i
 211 dominates the dispersion of the pore radius of a sub porosity and the shape of $\omega_i(r)$ curve; r_i^f reflects the maximal
 212 pore radius of a sub porosity and control the position of the maximum value of $\omega_i(r)$; R_i are the volumetric
 213 fractions of sub porosities and the coefficients of the linear superposition to obtain the overall pore size density
 214 curve $\omega(r)$.

215 3.2. Parameter calibration procedure for the multimodal PSD model

216 The proposed N-modal PSD model includes 3N parameters. A general and convenient parameter calibration
 217 method is required for the application of the model.

218 Pore size distribution data are usually expressed as a cumulative pore size distribution curve in terms of $V_{cum}^*(r)$
 219 (in the unit of [cm³/g]), which represents the pore volume normalised by soil dry weight (Delage et al. 1996;
 220 Delage and Lefebvre 1984; Diamond 1970, 1971; Juang and Holtz 1986b; Li and Zhang 2009). For a sample with
 221 void ratio e_0 , the maximal normalized pore volume V_{max}^* in 1-gram dry soil yields:

$$V_{max}^* = \frac{e_0}{\rho_s} \quad (27)$$

222 where ρ_s is the soil particle density. A data point $(r_j, V_{cum,j}^*)$ can be directly transformed to a data point (s_j^*, F_j)
 223 by

$$\begin{cases} s_j^* = \frac{1}{r_j} \\ F_j = 1 - \frac{V_{cum,j}^*}{V_{max}^*} \end{cases} \quad (28)$$

224 Then, by using Eq. (26) to fit the experimental data points in the $s^* - F$ plane, the 3N parameters of the model
 225 can be determined. A general and efficient parameter determination procedure for Eq. (26), by which R_i and m_i
 226 (2N parameters) are graphically determined, and r_i^f (N parameters) are obtained by solely one curve-fitting
 227 procedure, has been presented in Yan et al. (2021).

228

229 **4. Applications**

230 **4.1. Microstructural evolution during compaction**

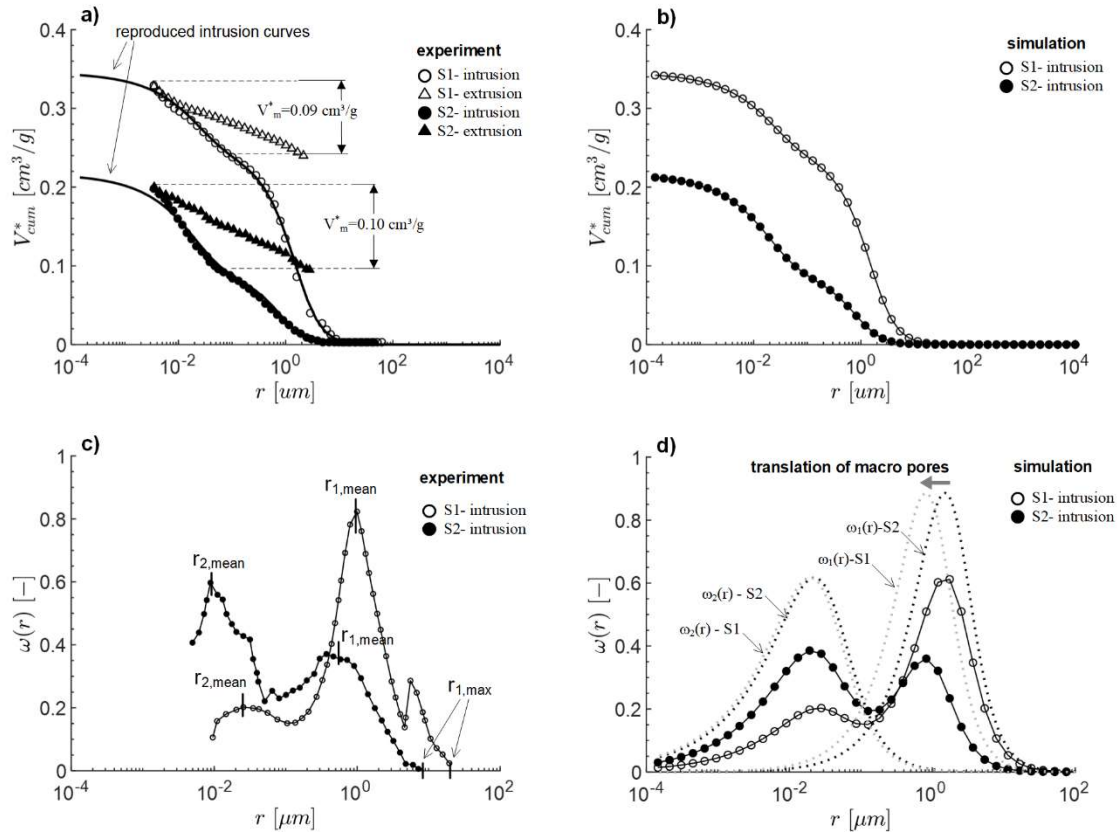


Fig. 4. Parameterization of the microstructure of compacted Boom clay: a) measured mercury intrusion and extrusion curves of samples S1 (1.40 g/cm³) and S2 (1.72 g/cm³) b) reproduced mercury intrusion curves c) measured pore size density curves d) reproduced pore size density curves [data adapted from Romero et al. (1999)]

231

Reference/soil	Sample	r_1^f	m_1	R_1	r_2^f	m_2	R_2	V_m^*
Romero et al. (1999) Boom clay	S1	2.42	0.50	0.70	0.041	0.38	0.30	0.11
	S2	1.15	0.46	0.40	0.036	0.38	0.60	0.13

232 **Table 1: parameters of the proposed PSD model and calculated intraaggregate pore volume of the samples**

233 Romero et al. (1999) analysed the microstructure of compacted Boom clay (liquid limit $w_L = 56\%$, plastic limit
 234 $w_p = 29\%$, particle density $\rho_s = 2.7$ g/cm³ (Romero et al. 2011)) by means of mercury intrusion/extrusion tests. Two
 235 samples were statically compacted at a constant water content of 15% to different dry densities, 1.40 g/cm³ (i.e.,
 236 $e_0 = 0.93$, denoted as sample S1) and 1.72 g/cm³ (i.e., $e_0 = 0.58$, denoted as sample S2). The measured intrusion
 237 curves are limited in a range of apparent pore radius from 0.0035 μm to 67.5 μm due to the limitation of the
 238 experimental apparatus, as shown in Fig. 4a. Following the mercury intrusion, mercury extrusion tests were
 239 conducted by releasing the mercury pressure. The mercury volume out from the soil in extrusion cycle corresponds
 240 to intraaggregate pore volume, while the entrapped mercury volume indicates the volume of interaggregate
 241 porosity ((Delage and Lefebvre 1984; Romero et al. 1999)). Fig. 4c demonstrates the $\omega(r)$ curves, which show a
 242 distinct bimodal pore structure.

243 From Eqs. (24) and (27), a cumulative pore size distribution curve of a multimodal soil measured in MIP tests
 244 can be expressed as:

$$V_{cum}^*(r) = \frac{e_0}{\rho_s} \left\{ 1 - \sum_{i=1}^N R_i \left[1 + \left(\frac{r_i^f}{r} \right)^{\frac{1}{1-m_i}} \right]^{-m_i} \right\}. \quad (29)$$

245 To parameterize the microstructure of compacted Boom clay, a bimodal model ($N = 2$) is adopted, and the
 246 parameters for both samples are given in Table 1.

247 Based on the results of mercury intrusion and extrusion tests, Romero 1999 concluded that the intraaggregate
 248 pore volume was almost unchanged during compaction and the volume change was attributed to the reduction in
 249 the interaggregate pore volume. This finding was later supported by other experimental results (e.g., Burton et al.
 250 (2014); Gao et al. (2019); Li and Zhang (2009)). Under the proposed PSD framework, this essential feature of the
 251 microstructural evolution during compaction can be interpreted by a parametric study of the model.

252 For the intraaggregate porosity, the pore size spectrum parameter m_2 and the reference pore size r_2^f are almost
 253 unchanged as compaction effort increased (see Table 1). That means, the intraaggregate pore structure $\omega_2(r)$ are
 254 not affected during compaction, as shown in Fig. 4d. The increase of peak value of the overall pore size density
 255 curve $\omega(r)$ at $r_{2,mean}$ is attributed to the increase in the volumetric fraction R_2 (i.e., a reduced “downscaling”
 256 effect).

257 For the interaggregate porosity, the reference pore size r_1^f decreases (i.e., the maximal pore radius of
 258 interaggregate porosity decreases) and the pore size spectrum parameter m_1 is unchanged, resulting in the
 259 translation of $\omega_1(r)$ curve along the abscissa (see Fig. 4d). Considering that the aggregates are stable, this
 260 phenomenon can be interpreted by the rearrangement of the aggregates and hence a reduction in the interaggregate
 261 pore volume during compaction. A similar microstructural behaviour (i.e., translation of pore size density curve
 262 with an unchanged shape) has also been observed in granular soils during compaction (Juang and Lovell 1986),
 263 which indicates that the aggregates of compacted clayey soils behaves like solid particles during compaction.

264 Fig. 4b and 4d demonstrate the parameterized cumulative curves and the pore size density curves, respectively.
 265 For a better comparison, the reproduced cumulative curves have also been plotted in Fig. 4a, which demonstrate a
 266 strong consistency with the measurements. In addition, the intraaggregate pore volume is calculated by
 267 $V_m^* = R_2 e_0 / \rho_s$, as given in Table 1. The calculated intraaggregate pore volumes of both samples are slightly
 268 higher than that determined by mercury extrusion tests (see Fig. 4a), because mercury intrusion and extrusion
 269 porosimetry could not detect the pores smaller than $0.0035 \mu\text{m}$ due to the apparatus limitation.

270

271 **4.2. Modelling the water content – soil suction – dry density relationship during compaction**

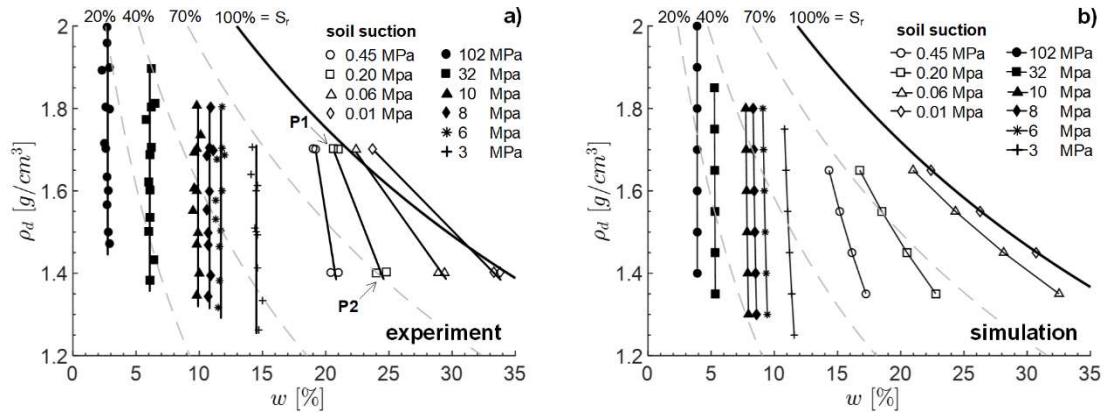


Fig. 5. water content – soil suction – dry density relationship of Boom clay during compaction a) experimental measurements b) prediction of the proposed model [data adapted from Romero et al. (1999)]

272

Reference/soil	r_1^f	m_1	r_2^f	m_2	e_{tot}^m	w_{res}
Romero et al. (1999)	[μm]	[-]	[μm]	[-]	[-]	[%]
Boom clay	1.79	0.48	0.39	0.38	0.32	2.5

273 **Table 2: parameters for modelling the water content – soil suction – dry density relationship**

274 To investigate the water content – soil suction – dry density relationship, Romero et al. (1999) statically compacted
 275 Boom clay samples with different water contents to different dry densities. The experimental results are shown in
 276 Fig. 5a.

277 For the samples compacted at relatively low water content ($< 15\%$), the soil suction did not change regardless
 278 of the density after compaction. That means, the suction – water content relationship is density-independent (see
 279 the vertical contours in Fig. 5a). The reason is that solely intraaggregate pores contain water, and the interaggregate
 280 pores are almost dry. The compaction process induces the rearrangement of aggregates to reach a higher overall
 281 dry density, whereas the intraaggregate pore structure remains almost unchanged. Consequently, the overall degree
 282 of saturation increases due to the reduction in dry density, but the suction, which is controlled by the local degree
 283 of saturation of the intraaggregate porosity, remains unchanged.

284 For the samples compacted at relatively high water content ($> 20\%$), the aggregates are almost saturated. The
 285 suction level is determined by both compaction water content and the target density after compaction, which
 286 influences the interaggregate pore structure. With the same compaction water content, the higher the target density,
 287 the higher the local degree of saturation in the interaggregate porosity and hence the lower the suction. In
 288 other words, a sample compacted to a loose state must have higher water content to achieve a given suction than
 289 the sample compacted to a dense state (see the points P1 (dense state) and P2 (loose state) in Fig. 5a). This results
 290 in the inclined contours with constant suction in the water content – dry density plane.

291 Based on these analysis, the proposed multimodal PSD model (bimodal, $N = 2$) is extended to simulate the
 292 water content – soil suction – dry density relationship of Boom clay during compaction. The soil void space is
 293 regarded as a bundle of capillary tubes, and the capillary law is used to determine a corresponding pore radius r at
 294 a given suction level by (Fredlund and Xing 1994):

$$r = (2T_s \cos \varphi) / s \quad (30)$$

295 where T_s is the surface tension of air-water interface ($T_s = 0.072$ N/m at 25 °C) and φ is the soil-water contact
 296 angle ($\varphi \approx 0$) (Lu and Likos 2004). That means, the pores whose radius are smaller than the value determined by
 297 Eq. (30) are saturated at a given suction level s .

298 Since the aggregates are stable during compaction, the constant total intraaggregate pore volume is denoted as
 299 e_{tot}^m . In addition, a constant residual water content w_{res} is assumed to account for the adsorptive water. Its pore
 300 space is expressed as:

$$e_{res} = \frac{\rho_s}{\rho_w} w_{res} = G_s w_{res} \quad (31)$$

301 where ρ_s is soil particle density, ρ_w represents the density of water, and G_s is the soil specific gravity ($G_s = 2.70$
 302 for Boom clay). Since the adsorbed water appears as a thin film surround the soil particle (Lu and Likos 2004), its
 303 occupying pore space can be reasonably regarded as a part of intraaggregate porosity. Then, the volume of capillary
 304 pores within intraaggregate porosity (e_{cap}^m) gives:

$$e_{cap}^m = e_{tot}^m - e_{res}, \quad (32)$$

305 and its microstructural feature is characterized by the intraaggregate PSD parameters r_2^f and m_2 . Similarly, the
 306 total volume of interaggregate porosity is regarded as capillary pores (e^M), which gives:

$$e^M = \frac{\rho_s}{\rho_d} - 1 - e_{tot}^m, \quad (33)$$

307 where ρ_d is the dry density of the soil, and its microstructural feature is characterized by the interaggregate PSD
 308 parameters r_1^f and m_1 . In general, the parameter r_1^f is density- or stress-dependent, resulting in the density- or
 309 stress-dependency of suction-water content relationship (Gallipoli et al. 2003; Hu et al. 2013; Vanapalli et al.
 310 1996). Nevertheless, a constant r_1^f is assumed in the model for the sake of simplicity. For the PSD parameters r_1^f ,
 311 m_1 , r_2^f and m_2 as well as the total intraaggregate pore volume e_{tot}^m , a mean value of that determined from both
 312 samples (S1 and S2 samples) is adopted, which are given in Table 2.

313 Based on these assumptions, the water content – soil suction – dry density relationship yields:

$$w = (e^M F_M + e_{cap}^m F_m) \frac{1}{G_s} + w_{res} \quad (34)$$

314 where F_M and F_m are the cumulative PSD functions for interaggregate and intraaggregate porosity at a given
 315 suction level, respectively, which can be expressed by

$$\begin{cases} F_M = \int_0^{(2T_s \cos \varphi)/s} \omega_1(r) d \log r = \left[1 + \left(\frac{r_1^f}{2T_s \cos \varphi} s \right)^{\frac{1}{1-m_1}} \right]^{-m_1} \\ F_m = \int_0^{(2T_s \cos \varphi)/s} \omega_2(r) d \log r = \left[1 + \left(\frac{r_2^f}{2T_s \cos \varphi} s \right)^{\frac{1}{1-m_2}} \right]^{-m_2} \end{cases} \quad (35)$$

316 Substituting Eqs. (31) - (33) in Eq.(34), we obtain:

$$w(\rho_d, s) = \left(\frac{\rho_s}{\rho_d} - 1 - e_{tot}^m \right) \frac{F_M}{G_s} + (e_{tot}^m - G_s w_{res}) \frac{F_m}{G_s} + w_{res} \quad (36)$$

317 Herein, the water content at a very high suction $s = 102$ MPa is adopted as the residual water content (i.e.,
318 $w_{res} = 2.5\%$, see Fig. 5a). Eq. (36) gives the relationship between water content and dry density at a specific
319 suction level.

320 Fig. 5b demonstrates the water content – soil suction – dry density relationship predicted by Eq. (36) for the
321 compacted Boom clay, which shows a good agreement with the measurements. The vertical contours with constant
322 suctions in the relatively low water content range have been correctly predicted, despite the slight discrepancy
323 between the predicted and measured water content at a given suction level. The model also predicts inclined
324 contours with constant suction in the relatively low water content range. The predicted water content is slightly
325 lower than the measurement for a given suction and density, which might be attributed to disregarding the density-
326 dependence of the interaggregate reference pore radius. Another reason for the differences between the prediction
327 and the measurements is the influence of compaction water content on the soil microstructure, i.e., the
328 interaggregate and intraaggregate PSD parameters may vary with compaction water content (Both samples S1 and
329 S2 were compacted at a constant water content of 15%). Considering the made assumptions and simplifications
330 and the complexity of the density – water content – suction relationship of compacted Boom Clay, the agreement
331 between the experimental and predicted results is quite satisfactory.

332 It is also interesting to note that Eq. (36) indicates a density dependent constitutive relationship between gravity
333 water content and soil suction [i.e., soil water characteristic curve (SWCC)], although the volumetric deformation
334 during SWCC tests have not been considered. As can be seen, the soil dry density solely influences the first term
335 of Eq. (36). That means, for the compacted clayey soils with distinct bimodal porosity, only the part of SWCC
336 dominated by the interaggregate porosity is affected by the overall dry density, while that determined by
337 intraaggregate porosity as well as the adsorptive water remains unchanged. This finding is supported by
338 experimental evidence in recent studies, e.g., Cai et al. (2020), Angerer (2020) and Chen et al. (2019).
339

340 **4.3. Description of the pore structure of MX80 bentonite**

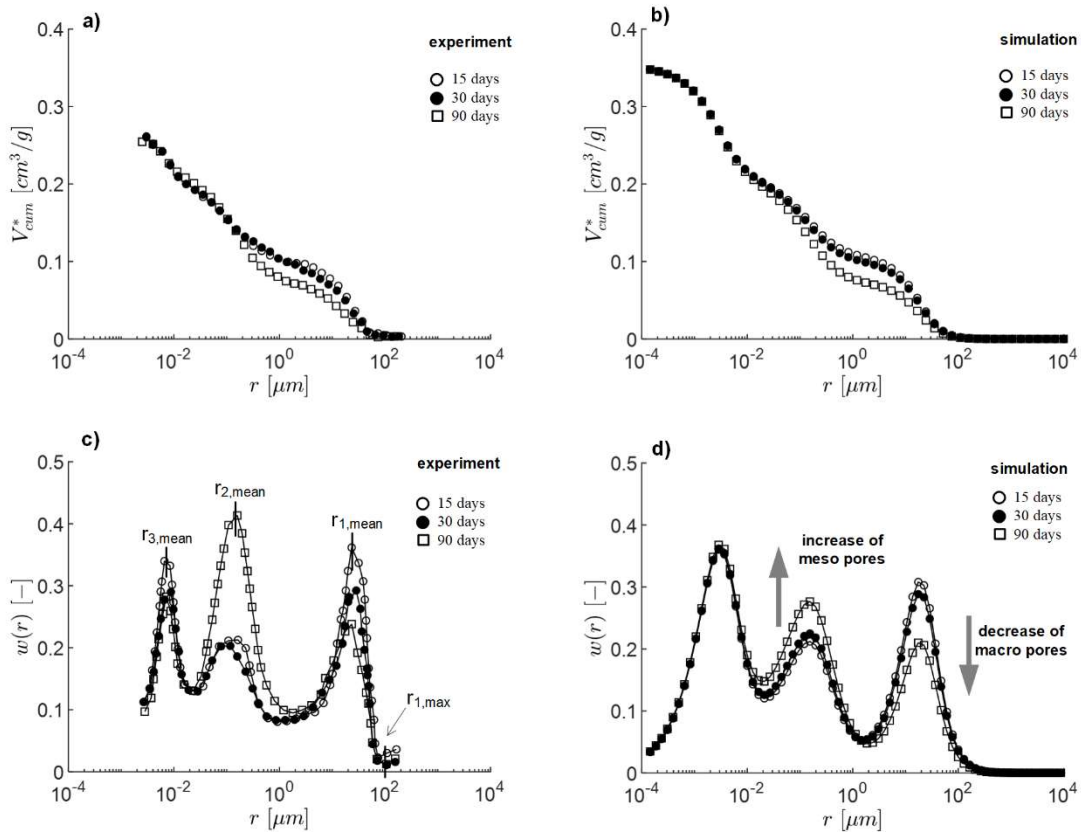


Fig. 6. The pore structure of MX80 bentonite at different hydration times: a) measured cumulative pore size distribution curves b) predicted cumulative pore size distribution curves c) measured pore size density curves d) predicted pore size density curves [data adapted from Wang et al. (2014)]

341

Reference/soil	Time after saturation	r_1^f	m_1	R_1	r_2^f	m_2	R_2	r_3^f	m_3	R_3
Wang et al. (2014) Bentonite MX80		[μm]	[-]	[-]	[μm]	[-]	[-]	[μm]	[-]	[-]
	T= 15 days	27.73	0.55	0.30	0.20	0.40	0.32	0.0044	0.50	0.38
	T= 30 days	25.16	0.55	0.28	0.25	0.40	0.34	0.0042	0.50	0.38
	T= 90 days	22.36	0.55	0.21	0.32	0.40	0.41	0.0038	0.50	0.38
	time-dependent model	25.10	0.55	-	0.26	0.40	-	0.0041	0.50	0.38

342 **Table 3: parameters of the tri-modal model**

343 Wang et al. (2014) investigated the pore structure evolution of compacted MX80 bentonite during wetting-swelling
 344 tests. The samples were hydrated in constant volume cells to control the target dry density (1.4 g/cm^3) after swelling.
 345 The soil pore structures were measured by MIP tests at different hydration-times (15, 30 and 90 days) after
 346 saturation, as shown in Fig. 6a (cumulative pore size distribution curves) and 6c (pore size density curves). Three
 347 sub porosities, i.e., micro porosity ($r < 0.04 \mu\text{m}$), meso porosity ($0.04 \mu\text{m} < r < 2 \mu\text{m}$) and macro porosity ($r > 2$
 348 μm), which varied during the hydration-time, were identified.

349 To account for the tri-modality in the soil pore structure, a tri-modal model ($N = 3$) is utilized to describe the
 350 PSD curves. Table 3 shows the parameters which are determined based on the cumulative curves. The changes in
 351 the pore structure over time can be analysed by a parametric study associated with a graphical analysis. On the one
 352 hand, the mean pore radius of each sub porosity is almost unchanged with time (see Fig. 6c), resulting in a constant
 353 value for the reference pore radius r_i^f (see Table 3). On the other hand, the shape of the individual sub porosity
 354 curves does not vary with time, which implies a constant pore spectrum number m_i . Therefore, the microstructure
 355 of each sub porosity (i.e., sub pore size distribution $\omega_i(r)$) does not change during swelling, and the changes in

356 the peak value of the overall $\omega(r)$ curve at $r_{1,mean}$ and $r_{2,mean}$ are caused by the variation of the volumetric
 357 fractions of macro and meso porosity. Based on our model, the microstructural evolution of the compacted MX80
 358 bentonite during swelling results only from the degradation of macro to meso pores, while the volume fraction and
 359 pore structure of micro porosity remain almost unchanged.

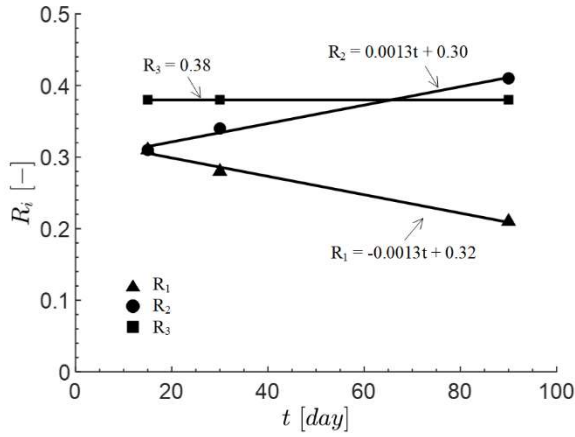


Fig. 7. Regression analysis for the volumetric fractions of sub porosities over time

360 In order to capture the time-effect on the microstructural evolution during swelling, the volumetric fractions of
 361 the sub porosities are plotted against time, as shown in Fig. 7. A simple linear relationship between R_1 and time t
 362 is determined by regression analysis:

$$R_1 = -0.0013t + 0.32 \quad (37)$$

363 Since R_3 is a constant ($R_3 = 0.38$), R_2 is solved from Eqs. (7) and (37):

$$R_2 = 0.0013t + 0.30 \quad (38)$$

364 Substituting Eqs. (37) and (38) in Eq. (22) (pore size density curve) and Eq. (29) (cumulative pore size distribution
 365 curve), we obtain a time-dependent PSD model for the compacted MX80 bentonite during the water equilibrium
 366 process, and the parameters are given in Table 3. Again, mean values are adopted for the constant microstructural
 367 parameters r_i^f and m_i .

368 The predicted cumulative curves and the tri-modal pore size density curves at hydration time 15, 30 and 90
 369 days are illustrated in Fig. 6b and 6d, respectively. Despite of the relatively large deviation of $\omega(r)$ in the meso
 370 pore range, the model predictions are in good agreement with the measurements. By considering the evolution of
 371 R_i , the decrease in the macro pore volume and increase in the meso pore volume can be realistically captured and
 372 the soil pore structure at any hydration time within the interval 15 to 90 days can be predicted by the tri-modal
 373 PSD model.

374

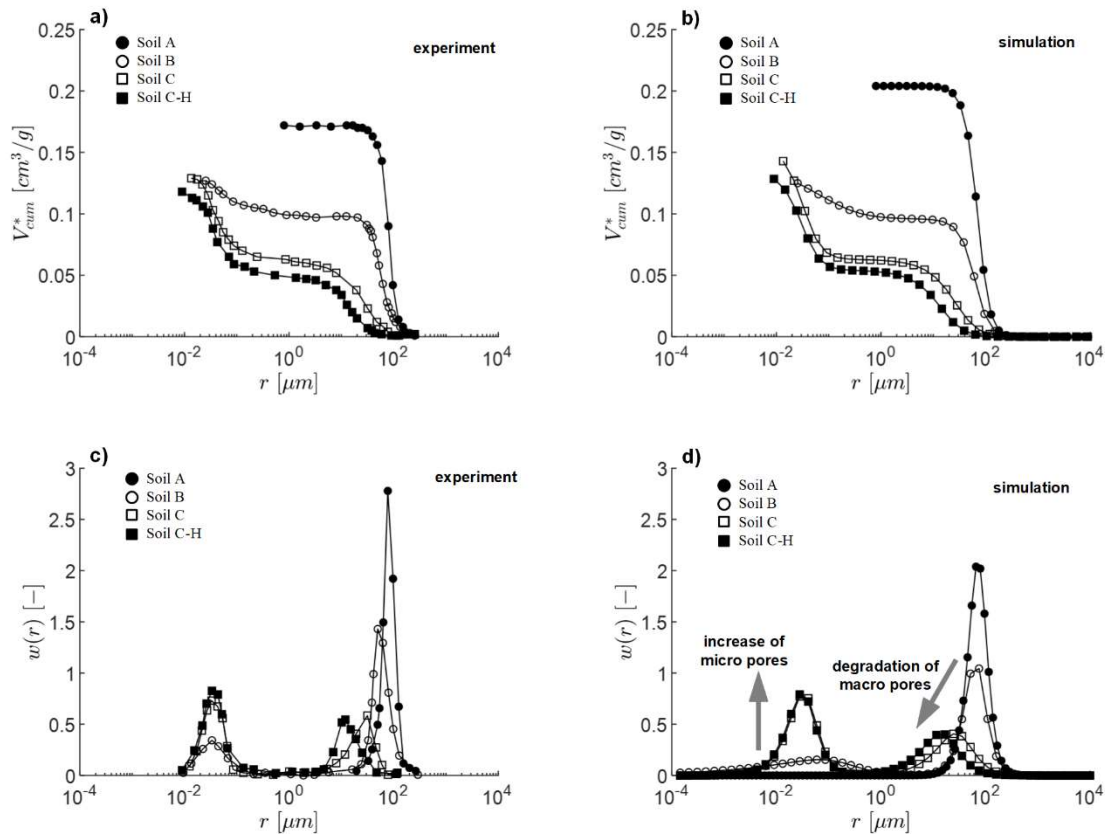


Fig. 8. Parameterization of the microstructure of pure sand and sand-clay mixtures: a) measured mercury intrusion curves b) reproduced mercury intrusion curves c) measured pore size density curves d) reproduced pore size density curves [data adapted from Juang and Holtz (1986b)]

376

Reference/soil type	soils	ρ_d / clay content	R_1	r_1^f	m_1	R_2	r_2^f	m_2
		[g/cm³] / [%]	[-]	[μm]	[-]	[-]	[μm]	[-]
Juang and Holtz (1986b) Sand - clay mixture	Soil A	1.72 / 0	1.00	76.32	0.75	-	-	-
	Soil B	1.88 / 10	0.62	69.05	0.71	0.38	0.190	0.25
	Soil C	1.87 / 30	0.40	35.37	0.55	0.60	0.039	0.63
	Soil C-H	1.95 / 30	0.40	18.59	0.55	0.60	0.037	0.63

377 **Table 4: parameters of the proposed PSD model for pure sand and sand – clay mixtures**

378 Juang and Holtz (1986b) investigated the microstructure of pure Ottawa sand and Ottawa sand – kaolinitic clay
 379 mixture (compacted at the dry of optimum) by means of mercury intrusion porosimetry. The detected cumulative
 380 pore volume curves and the pore size density curves of four different soils, i.e., soil A (pure sand), soil B (90%
 381 sand + 10% clay), soil C (70% sand + 30% clay) and soil C-H (70% sand + 30% clay), are presented in Fig. 8a
 382 and 8c, respectively. As can be seen, pure sand shows a unimodal microstructure, while sand-clay mixtures are
 383 characterized by a remarkable bimodal pore structure.

384 The modelled cumulative volume curves and pore size density curves for the experimental soils are shown in
 385 Fig. 8b and 8d, respectively, by which a unimodal model ($N = 1$) is adopted for soil A and a bimodal model ($N =$
 386 2) for soil B, C and C-H. The parameters in the models as well as the soil properties are given in Table 4. As shown
 387 in Fig. 8, the experimental PSD curves can be satisfactory modelled by the PSD model.

388 Moreover, the influence of fine content on the observed pore structure can be better understood based on our
 389 model. In soil A (pure Ottawa sand), a unimodal model is sufficient to describe the PSD curves, as only a macro

390 porosity exists in the soil at the density and water content adopted in the experiments. The pore size spectrum
391 number m_1 controls the shape of the $\omega(r)$ curve, and the parameter r_1^f is dominated by the maximal pore radius.

392 The microstructure of soil B might be regarded as a pore structure formed by a sand grain skeleton, in which a
393 small amount of clay aggregates and clay particles are filling a small part of the intergranular voids (macro pores).
394 Most of the macro pores remain unchanged due to the low clay content (10%). The clay affects the pore
395 microstructure structure twofold: i) the pore sizes of macro porosity become more dispersed; ii) a second sub-
396 porosity is formed. The former one induces a slightly reduction of the macro pore spectrum number m_1 in
397 comparison with soil A (see Table 4), and the latter one leads to the bimodality of the pore structure (i.e., an
398 increase in the modality number N). In addition, the maximal pore radius of the macro pore structure is almost
399 unchanged, as most macro pores between sand grains are only slightly affected by the clay. Therefore, the
400 interaggregate reference parameter r_1^f in soil B is rather close to that of soil A, as shown in Table. 4. It is also
401 interesting to note that the macro pore size spectrum number m_1 does not change during compaction- (Boom Clay)
402 and saturation-swelling-process (MX80 bentonite), while it changes from soil A to soil B, as the change in fine
403 content creates a new soil with a different pore structure.

404 In soil C, the macro pore structure formed by sand grains is dramatically “disturbed” due to the high clay
405 content (30%). Comparing with soil B, more clay aggregates penetrates the macro pores, which leads to a further
406 decrease in parameter m_1 . That means, the original macro pores between sand grains degrade to smaller pores
407 between sand grain – clay aggregates. Simultaneously, the decrease in the maximum macro pore radius leads to a
408 significant reduction in the macro reference pore size r_1^f . Because of different compaction water content and
409 energy (details in sample preparation method is given by Juang and Holtz (1986b)), the intraaggregate pore
410 structures in soil B and soil C are different, which is reflected in the different values of the parameters m_2 and r_2^f .
411 In addition, the peak value of the $\omega(r)$ curve in the micro pore range of soil C is higher than soil B, resulting from
412 a higher fine content and hence a larger intraaggregate volumetric fraction R_2 .

413 Soil C-H represents the sample of soil C compacted to a higher density in a modified proctor. The effects of
414 compaction effort (mechanical loading) on the pore structure the are shown by comparing the PSD curves of soil
415 C and soil C - H. As explained for Boom clay, the compaction effort solely causes a reduction in the maximum
416 pore size and the overall volume of interaggregate porosity (see the shifting of the interaggregate curve in Fig. 8d),
417 while the intraaggregate porosity is not affected.

418 5. Conclusion

419 Based on Scheidegger’s definition of pore radius and assuming a statistical distribution of pore sizes, a model has
420 been developed to describe a general multimodal pore structure of porous materials. Contrary to existing models,
421 the parameters of the proposed model have an unambiguous physical meaning. This enables further adaptations of
422 the model to describe the PSD evolution during hydro-mechanical paths (e.g., compaction- and saturation-
423 swelling-process).

424 To validate the model, the proposed multimodal PSD model has been used to describe the pore structure of
425 different soils, including Boom clay (bimodal PSD), MX80 bentonite (tri-modal PSD) and sand-clay mixtures with
426 different fine contents (unimodal and bimodal PSD). The comparison of experimental and simulated results

427 demonstrate the ability of the proposed multimodal approach to consistently simulate the pore structure of complex
428 porous materials. For Boom clay, the water content – soil suction – dry density relationship after compaction is
429 predicted by combining the capillarity theory and the multimodal PSD model. For MX80 bentonite, a semi-
430 empirical relationship has been derived based on the PSD model and the experimental data to predict the
431 microstructural evolution during swelling. For sand-clay mixtures, the influence of fine content on the pore
432 structure has been explained quantitatively and qualitatively.

433 The proposed general pore size distribution framework and the multimodal PSD expression appears to be a
434 powerful tool to realistically simulate the complex soil microstructure. Since the model is developed based on a
435 general probability theory, in principle, it can be used to describe the pore structure of arbitrary porous materials,
436 as long as the model assumptions are valid. By quantifying the microstructure of soils and rocks precisely, the
437 model could assist to improve the techniques in geotechnical, geo-environmental and geological applications. As
438 the mechanical (e.g., effective stress, shear strength, wetting-collapse behaviour) and hydraulic properties (e.g.,
439 water retention behaviour, permeability) of unsaturated soils are highly related to the pore structure, the model can
440 be incorporated into existing permeability and constitutive models, and employed to assess the effective stress
441 parameter, particularly for unsaturated multimodal soils.

442

443 **Acknowledgement**

444 The support of the China Scholarship Council (number 201608080128) is greatly acknowledged by the first
445 Author.

446 **Funding**

447 The research leading to these results received funding from China Scholarship Council under Grant Agreement
448 Number 201608080128.

449 **Conflicts of interest**

450 The authors have no conflicts of interest to declare that are relevant to the content of this article.

451 **Availability of data and material**

452 The data used to support the findings of this study are available from the corresponding author upon request.

453 **Code availability**

454 The code used to support the findings of this study are available from the corresponding author upon request

455 **References**

- 456 Alonso, E., Gens, A. & Hight, D. 1987. General report. Special problem soils. *Proceedings of the 9th European*
457 *Conference on soil mechanics and foundation engineering, Dublin*, 1087-1146.
- 458 Alonso, E.E., Pereira, J.-M., Vaunat, J. & Olivella, S. 2010. A microstructurally based effective stress for
459 unsaturated soils. *Géotechnique*, **60**, 913-925.
- 460 Alonso, E.E., Pinyol, N.M. & Gens, A. 2013. Compacted soil behaviour: initial state, structure and constitutive
461 modelling. *Géotechnique*, **63**, 463-478, doi: 10.1680/geot.11.P.134.
- 462 Angerer, L. 2020. *Experimental evaluation of the suction-induced effective stress and the shear strength of as-*
463 *compacted silty sands*, Technische Universität München.
- 464 Birle, E. 2011. *Geohydraulische Eigenschaften verdichteter Tone unter besonderer Berücksichtigung des*
465 *ungesättigten Zustandes*, Technische Universität München.
- 466 Brutsaert, W. 1966. Probability laws for pore-size distributions. *Soil Science*, **101**, 85-92.
- 467 Burdine, N., Gournay, L. & Reichertz, P. 1950. Pore size distribution of petroleum reservoir rocks. *Journal of*
468 *Petroleum Technology*, **2**, 195-204.
- 469 Burton, G., Sheng, D. & Campbell, C. 2014. Bimodal pore size distribution of a high-plasticity compacted clay.
470 *Geotechnique Letters*, **4**, 88-93.
- 471 Cai, G., Zhou, A., Liu, Y., Xu, R. & Zhao, C. 2020. Soil water retention behavior and microstructure evolution
472 of lateritic soil in the suction range of 0–286.7 MPa. *Acta Geotechnica*, **15**, 3327-3341.
- 473 Chen, R.-P., Liu, P., Liu, X.-M., Wang, P.-F. & Kang, X. 2019. Pore-scale model for estimating the bimodal
474 soil–water characteristic curve and hydraulic conductivity of compacted soils with different initial densities.
475 *Engineering Geology*, **260**, 105199.
- 476 Cheng, C.-L., Perfect, E., Yu, T.E. & Gragg, M.J. 2017. Impact of the capillary pressure-saturation pore-size
477 distribution parameter on geological carbon sequestration estimates. *Journal of Sustainable Mining*, **16**, 67-72.
- 478 Childs, E.C. & Collis-George, N. 1950. The permeability of porous materials. *Proceedings of the Royal Society*
479 *of London. Series A. Mathematical and Physical Sciences*, **201**, 392-405.
- 480 Delage, P., Audiguier, M., Cui, Y.-J. & Howat, M.D. 1996. Microstructure of a compacted silt. *Canadian*
481 *Geotechnical Journal*, **33**, 150-158.
- 482 Delage, P. & Lefebvre, G. 1984. Study of the structure of a sensitive Champlain clay and of its evolution during
483 consolidation. *Canadian Geotechnical Journal*, **21**, 21-35.
- 484 Diamond, S. 1970. Pore size distributions in clays. *Clays and Clay Minerals*, **18**, 7-23.
- 485 Diamond, S. 1971. Microstructure and Pore Structure of Impact-Compacted Clays. *Clays and Clay Minerals*, **19**,
486 239-249, doi: 10.1346/ccmn.1971.0190405.
- 487 Durner, W. 1994. Hydraulic conductivity estimation for soils with heterogeneous pore structure. *Water resources*
488 *research*, **30**, 211-223.
- 489 Fredlund, D.G. & Xing, A. 1994. Equations for the soil-water characteristic curve. *Canadian Geotechnical*
490 *Journal*, **31**, 521-532.
- 491 Fujikura, Y. & Oshita, H. 2011. Pore structure model of hydrates comprising various cements and SCMs based
492 on changes in particle size of constituent phases. *Journal of Advanced Concrete Technology*, **9**, 133-147.
- 493 Gallipoli, D., Wheeler, S. & Karstunen, M. 2003. Modelling the variation of degree of saturation in a deformable
494 unsaturated soil. *Géotechnique*, **53**, 105-112.

495 Gao, Y., Sun, D.a., Zhu, Z. & Xu, Y. 2019. Hydromechanical behavior of unsaturated soil with different initial
496 densities over a wide suction range. *Acta Geotechnica*, **14**, 417-428.

497 Gens, A. & Alonso, E. 1992. A framework for the behaviour of unsaturated expansive clays. *Canadian*
498 *Geotechnical Journal*, **29**, 1013-1032.

499 Griffiths, F. & Joshi, R. 1989. Change in pore size distribution due to consolidation of clays. *Géotechnique*, **39**,
500 159-167.

501 Hu, R., Chen, Y.-F., Liu, H.-H. & Zhou, C.-B. 2013. A water retention curve and unsaturated hydraulic
502 conductivity model for deformable soils: consideration of the change in pore-size distribution. *Géotechnique*, **63**,
503 1389-1405.

504 Jensen, J.L., Schjønning, P., Watts, C.W., Christensen, B.T. & Munkholm, L.J. 2019. Soil Water Retention: Uni-
505 Modal Models of Pore-Size Distribution Neglect Impacts of Soil Management. *Soil Science Society of America*
506 *Journal*, **83**, 18-26, doi: 10.2136/sssaj2018.06.0238.

507 Juang, C. & Holtz, R. 1986a. A probabilistic permeability model and the pore size density function. *International*
508 *Journal for numerical and analytical methods in geomechanics*, **10**, 543-553.

509 Juang, C. & Holtz, R.D. 1986b. Fabric, pore size distribution, and permeability of sandy soils. *Journal of*
510 *geotechnical engineering*, **112**, 855-868.

511 Juang, C. & Lovell, C. 1986. Measurement of Pore-Size Density Function in Sand. *Transportation Research*
512 *Record*.

513 Kosugi, K.i. 1996. Lognormal distribution model for unsaturated soil hydraulic properties. *Water resources*
514 *research*, **32**, 2697-2703.

515 Li, X., Li, J. & Zhang, L. 2014a. Predicting bimodal soil–water characteristic curves and permeability functions
516 using physically based parameters. *Computers and Geotechnics*, **57**, 85-96.

517 Li, X., Zhang, L.-M. & Wu, L.-Z. 2014b. A framework for unifying soil fabric, suction, void ratio, and water
518 content during the dehydration process. *Soil Science Society of America Journal*, **78**, 387-399.

519 Li, X. & Zhang, L.M. 2009. Characterization of dual-structure pore-size distribution of soil. *Canadian*
520 *Geotechnical Journal*, **46**, 129-141, doi: 10.1139/t08-110.

521 Liu, K., Ostadhassan, M. & Cai, J. 2019. Characterizing Pore Size Distributions of Shale. *Petrophysical*
522 *Characterization and Fluids Transport in Unconventional Reservoirs*. Elsevier, 3-20.

523 Liu, Y., Wang, H., Shen, Z. & Song, Y. 2013. Estimation of CO₂ storage capacity in porous media by using X-
524 ray micro-CT. *Energy Procedia*, **37**, 5201-5208.

525 Lloret, A. & Villar, M.V. 2007. Advances on the knowledge of the thermo-hydro-mechanical behaviour of
526 heavily compacted “FEBEX” bentonite. *Physics and Chemistry of the Earth, Parts A/B/C*, **32**, 701-715, doi:
527 10.1016/j.pce.2006.03.002.

528 Lu, N. & Likos, W.J. 2004. *Unsaturated soil mechanics*. Wiley.

529 Milligan, W. & Adams, C. 1954. An analytical expression for cumulative pore volumes and pore size
530 distributions. *The Journal of Physical Chemistry*, **58**, 891-893.

531 Monroy, R., Zdravkovic, L. & Ridley, A. 2010. Evolution of microstructure in compacted London Clay during
532 wetting and loading. *Géotechnique*, **60**, 105-119, doi: 10.1680/geot.8.P.125.

533 Mualem, Y. 1976. A new model for predicting the hydraulic conductivity of unsaturated porous media. *Water*
534 *resources research*, **12**, 513-522.

535 Prikryl, R. & Weishauptová, Z. 2010. Hierarchical porosity of bentonite-based buffer and its modification due to
536 increased temperature and hydration. *Applied Clay Science*, **47**, 163-170.

537 Romero, E., DELLA VECCHIA, G. & Jommi, C. 2011. An insight into the water retention properties of
538 compacted clayey soils. *Géotechnique*, **61**, 313-328.

539 Romero, E., Gens, A. & Lloret, A. 1999. Water permeability, water retention and microstructure of unsaturated
540 compacted Boom clay. *Engineering Geology*, **54**, 117-127.

541 Ross, P.J. & Smettem, K.R. 1993. Describing soil hydraulic properties with sums of simple functions. *Soil*
542 *Science Society of America Journal*, **57**, 26-29.

543 Satyanaga, A., Rahardjo, H., Leong, E.-C. & Wang, J.-Y. 2013. Water characteristic curve of soil with bimodal
544 grain-size distribution. *Computers and Geotechnics*, **48**, 51-61.

545 Scheidegger, A.E. 2020. *The physics of flow through porous media*. University of Toronto press.

546 Sun, H., Mašin, D., Najser, J., Neděla, V. & Navrátilová, E. 2019. Bentonite microstructure and saturation
547 evolution in wetting–drying cycles evaluated using ESEM, MIP and WRC measurements. *Géotechnique*, **69**,
548 713-726.

549 Van Genuchten, M.T. 1980. A closed-form equation for predicting the hydraulic conductivity of unsaturated
550 soils 1. *Soil Science Society of America Journal*, **44**, 892-898.

551 Vanapalli, S.K., Fredlund, D.G. & Pufahl, D.E. 1996. The relationship between the soil-water characteristic
552 curve and the unsaturated shear strength of a compacted glacial till. *Geotechnical Testing Journal*, **19**, 259-268.

553 Wang, Q., Cui, Y.-J., Minh Tang, A., Xiang-Ling, L. & Wei-Min, Y. 2014. Time- and density-dependent
554 microstructure features of compacted bentonite. *Soils and Foundations*, **54**, 657-666, doi:
555 10.1016/j.sandf.2014.06.021.

556 Wang, X. & Ni, Q. 2003. Determination of cortical bone porosity and pore size distribution using a low field
557 pulsed NMR approach. *Journal of Orthopaedic Research*, **21**, 312-319.
558 Yan, W., Birle, E. & Cudmani, R. 2021. A new framework to determine general multimodal soil water
559 characteristic curves. *Acta Geotechnica*, 1-22.
560 Zhang, Z., Qin, Y., Yi, T., You, Z. & Yang, Z. 2020. Pore structure characteristics of coal and their geological
561 controlling factors in eastern Yunnan and western Guizhou, China. *ACS omega*, **5**, 19565-19578.
562 Zhu, J., Zhang, R., Zhang, Y. & He, F. 2019. The fractal characteristics of pore size distribution in cement-based
563 materials and its effect on gas permeability. *Scientific reports*, **9**, 1-12.

564

Paper II – A new framework to determine general multimodal soil water characteristic curves

Yan, W., Birle, E. & Cudmani, R. (2021a) A new framework to determine general multimodal soil water characteristic curves. *Acta Geotechnica* **16(10)**:3187-3208, 10.1007/s11440-021-01245-2.



A new framework to determine general multimodal soil water characteristic curves

Wei Yan¹ · Emanuel Birle¹ · Roberto Cudmani¹

Received: 10 September 2020 / Accepted: 29 May 2021
© The Author(s) 2021

Abstract

A soil water characteristic curve (SWCC) model named as discrete-continuous multimodal van Genuchten model with a convenient parameter calibration method is developed to describe the relationship between soil suction and the water content of a soil with complex pore structure. The modality number N of the SWCC in the proposed model can be any positive integer (the so-called multimodal or N -modal SWCC). A unique set of parameters is determined by combining curve fitting and a graphical method based on the shape features of the SWCC in the $\log s$ – $\log S_e$ plane. In addition, a modality number reduction method is proposed to minimize the number of parameters and simplify the form of SWCC function. The proposed model is validated using a set of bimodal and trimodal SWCC measurements from different soils, which yield a strong consistency between the fitted curves and the measured SWCC data. The uniqueness in the set of parameters provides the possibility to further improve the proposed model by correlating the parameters to soil properties and state parameters.

Keywords Bimodal · Discrete-continuous multimodal van Genuchten model · Multimodal · Parameter calibration · Soil water characteristic curve · Unsaturated soil

1 Introduction

The soil water characteristic curve (SWCC) describes the relationship between soil suction and water content (e.g., volumetric water content θ , gravity water content w or degree of saturation S_r) of a soil. In unsaturated soil mechanics, SWCC predominates the hydro-mechanical coupling of unsaturated soils [14, 25, 39], since mechanical properties like the shear modulus, compression index, and yielding stress are often related to suction [1, 3, 31, 38, 45] or degree of saturation [27, 50, 51]. Additionally, soil properties, which are time-consuming to determine, like the unsaturated hydraulic conductivity and pore size distribution, can be derived from SWCC [2, 16, 26, 33]. Thus, a precise description for SWCC of soils is significant for

geotechnical and geo-environmental engineering, soil science as well as agriculture engineering.

A number of empirical models have been developed to reproduce the unimodal SWCC, for example, Brooks and Corey Model (BCM) [6], van Genuchten Model (VGM) [16], as well as Fredlund and Xing Model (FXM) [13]. Parameters of these models are usually obtained by best-fitting SWCC data or obtained indirectly from soil properties by using the so-called pedotransfer functions [5, 19, 22, 36, 42, 43].

In recent studies, two or more pore series, resulting from the gap-graded grain size distribution or the aggregation of fine particles, have been widely observed in undisturbed soils [28], mixed soils [7, 8, 35] and compacted fine-grained soils [10, 32]. The SWCC of such soils can thus be bimodal or even multimodal, which cannot be appropriately described by unimodal SWCC models. Therefore, a set of bimodal SWCC models, as a piecewise function [8, 40, 47] or a continuous function [9, 11, 12, 23, 28, 34, 46], have been developed for the soils with heterogeneous pore structure.

✉ Wei Yan
wei.yan@tum.de

¹ Department of Civil, Geo and Environmental Engineering, Technical University of Munich, Franz-Langinger-Str. 10, 81245 Munich, Germany

The first piecewise bimodal SWCC model was developed by Smettem, Kirkby [40], who introduced two independent closed-form analytical solutions to describe the macro- and microporosity of an aggregated loam. Afterward, Wilson et al. [47] extended the method to model the hydraulic properties of a soil with three pore families by using its SWCC data. Following the framework suggested by Smettem, Kirkby [40], Burger, Shackelford [8] proposed a piecewise function to describe the bimodal SWCC of a pelletized diatomaceous earth. In their work, bimodal SWCC was divided into a macro- and a micro-sub-curve using a chosen delimiting point, leading to a piecewise bimodal SWCC function as

$$S_r = \begin{cases} S_{r,j} + (S_{r,\max} - S_{r,j})S_{r,1}, & \text{for } s < s_j \\ S_{r,\text{res}} + (S_{r,j} - S_{r,\text{res}})S_{r,2}, & \text{for } s \geq s_j \end{cases} \quad (1)$$

where S_r represents the degree of saturation; $S_{r,\max}$ is the maximum degree of saturation; $S_{r,\text{res}}$ is the degree of saturation at residual state; s_j is the delimiting suction; $S_{r,j}$ is the degree of saturation at delimiting point; $S_{r,1}$ and $S_{r,2}$ represent the independent closed-form analytical solutions for the local degree of saturation in the macro- and microporosity, respectively, which can be described by a unimodal SWCC function (e.g., BCM, VGM or FXM). After choosing an appropriate delimiting point, the parameters are obtained by fitting the individual unimodal function for subporosity to their corresponding SWCC data. However, in spite of the convenience in the parameter calibration process, the discontinuity feature is not expected for the numerical applications and the incorporation into a constitutive modeling.

A general framework for a continuous bimodal SWCC was proposed by Ross, Smettem [34] using ‘volumetric fraction approach’ [21, 46]. The overall pore space of the soil is regarded as the superposition of two overlapping subporosities, i.e., the micro- and macroporosity, and the bimodal SWCC function in terms of effective degree of saturation S_e can be expressed as

$$S_e = R_1 S_{r,1} + R_2 S_{r,2} \quad \text{with } R_1 + R_2 = 1. \quad (2)$$

Herein, R_1 and R_2 represent the volumetric fraction of micro- and macroporosity, respectively; $S_{r,1}$ and $S_{r,2}$ represent the sub-SWCC curves for the macro- and microporosity, respectively, which can be described by a unimodal SWCC function. Based on this framework, a number of continuous bimodal SWCC model have been developed [9, 11, 12, 28, 34]. Details of these continuous bimodal SWCC models are summarized in Table 1. In comparison with the piecewise form, continuous bimodal SWCC model is more convenient for numerical and practical applications, but the parameters involved in these models are highly correlated, resulting in difficulties in the calibration process [18, 46]. Durner [12] pointed out that

the parameters should be regarded as curve shape coefficients instead of parameters with physical meanings. To best fit the parameters, a specific curve fitting procedure associated with a proper initial approximation of the parameters and appropriate constraint conditions are required. Nevertheless, identical SWCC may be reproduced by different sets of parameters [18, 46], due to the possible intercorrelations among the parameters.

To overcome the difficulties in parameter calibration, another type of continuous bimodal SWCC functions has been developed based on the independent parameters related to the SWCC shape features, referred to as ‘unique parameter approach’ [21, 46]. Gitirana and Fredlund [18] presented a bimodal model with the parameters determined with bending points from the shape of SWCC, which requires only one additional curve fitting parameter. Using a similar approach, Li et al. [23] proposed another empirical bimodal SWCC function that directly incorporates the suction and gravity water content of bending points of SWCC into the model. Wijaya and Leong [46] decomposed SWCCs into several linear segments and employed the Heaviside function to smooth the junctions of the linear segments. In this manner, all the parameters involved can be graphically determined without curve fitting procedure. Details of these models developed with the ‘unique parameter approach’ are summarized in Table 1. The major advantage of this type of bimodal SWCC model is the direct graphical determination of the parameters, which enables sensitivity analyses of SWCC parameters, making it possible to extend the SWCC model by relating the parameters to other soil properties and state parameters [18, 46]. However, this type of model usually requires a rather complex mathematical form for the SWCC function, as shown in Table 1.

For continuous bimodal SWCC, the simple volumetric fraction models show difficulty in parameter determination, while the unique parameter approach requires a rather complex SWCC function. This problem is more significant for multimodal SWCCs. Recent studies have reported that the pore structures in unsaturated fine-grained soils are more complex than to be represented by a bimodal pore size distribution [24, 30, 41, 44], resulting in multimodal SWCCs. To describe multimodal SWCCs, the existing bimodal SWCC models can be extended to N -modal SWCC functions. However, the parameter determination procedure is more complicated due to the significant increase in the number of parameters and the intercorrelations among them. So far, however, a general continuous N -modal SWCC model (‘general’ means that the modality number N can be any positive integer) is still lacking. The objective of this paper is to develop a N -modal SWCC model in a simple mathematical form with a convenient parameter calibration method.

Table 1 Comparison of the existing continuous multimodal SWCC functions and the proposed model

References	SWCCC function	Characteristics	Number of parameters	Developing approach/calibration method	Additional interpretation
Othmer et al. [28]	$\text{original: } \theta = \sum_{i=1}^2 \{ \theta_{r,i} + (\theta_{s,i} - \theta_{r,i}) [1 + (\alpha_i s)^{n_i}]^{-m_i} \}$ $\text{Let: } S_r = \frac{\theta}{n}; S_{r,\max} = \frac{\theta_{s,1} + \theta_{s,2}}{n}; S_{r,\text{res}} = \frac{\theta_{r,1} + \theta_{r,2}}{\theta_{s,1} + \theta_{s,2}};$ $R_1 = \frac{\theta_{s,1} - \theta_{r,1}}{\theta_{s,1} + \theta_{s,2}}; R_2 = \frac{\theta_{s,2} - \theta_{r,2}}{\theta_{s,1} + \theta_{s,2}}$ $\text{transformed: } S_r = S_{r,\text{res}} + (S_{r,\max} - S_{r,\text{res}}) \{ R_1 [1 + (\alpha_1 s)^{n_1}]^{-m_1} + R_2 [1 + (\alpha_2 s)^{n_2}]^{-m_2} \}$	Bimodal	10	Volumetric fraction approach/curve fitting procedure	n : porosity of the soil
Dumer [12]	$S_r = S_{r,\text{res}} + (S_{r,\max} - S_{r,\text{res}}) \{ R_1 [1 + (\alpha_1 s)^{n_1}]^{-m_1} + R_2 [1 + (\alpha_2 s)^{n_2}]^{-m_2} \}$	Bimodal	9	Volumetric fraction approach/curve fitting procedure	R_i : volumetric fraction α_i, n_i and m_i : van Genuchten model parameters
Coppola [9]	$S_r = S_{r,\text{res}} + (S_{r,\max} - S_{r,\text{res}}) [R_1 (1 + \alpha_1 s) \exp(-\alpha_1 s) + R_2 [1 + (\alpha_2 s)^{n_2}]^{-m_2}]$	Bimodal	7	Volumetric fraction approach/curve fitting procedure	α_i : the parameter for one-parameter model
Dexter et al. [11]	$\text{original: } w = A_0 + A_1 \exp(-\alpha_1 s) + A_2 \exp(-\alpha_2 s)$ $\text{Let: } W_{\max} = \frac{\rho_w e; S_r}{\rho_s W_{\max}};$ $S_{r,\max} = \frac{A_0 + A_1 + A_2}{W_{\max}}; S_{r,\text{res}} = \frac{A_0}{W_{\max}};$ $R_1 = \frac{A_1 e}{A_1 + A_2}; R_2 = \frac{A_2}{A_1 + A_2}$	Bimodal	5	Volumetric fraction approach/curve fitting procedure	ρ_w : density of water ρ_s : density of soil solid e : void ratio of the soil W_{\max} : maximum gravity water content of the soil

Table 1 (continued)

References	SWCCC function	Characteristics	Number of parameters	Developing approach/calibration method	Additional interpretation
Wijaya, Leong [46]	$\text{transformed: } S_r = S_{r, \text{res}} + (S_{r, \text{max}} - S_{r, \text{res}}) [R_1 \exp(-\alpha_1 s) + R_2 \exp(-\alpha_2 s)]$ $w = w_{\text{sat}} - m_1 (\log s - \log s_1) - \sum_{i=2}^5 R_i (m_i - m_{i-1})$ <p style="text-align: center;">With</p> $R_i = \frac{1}{2} (\log s - \log s_1) + \frac{1}{2c_i} \ln \left\{ \frac{\cosh[c_i (\log s - \log s_1)]}{\cosh[c_i (\log s_1 - \log s_1)]} \right\}$	Bimodal	15	Unique parameter approach/graphical determination	m_i : slope of linear segment i s_1 : the suction value at $w = w_{\text{sat}}$ s_i ($i \geq 2$): the suction value of the cross-point of segment i and segment $i + 1$ c_i ($i \geq 2$): the parameter controls the curvature of the transition range between segment i and segment $i + 1$
Li et al. [23]	$w = \frac{(0.75w_s - 3w_r) \sqrt{s_{a2}^2 / \log(s_r/s_{a2})}}{s^2 / \log(s_r/s_{a2}) + \sqrt{s_{a2}^2 / \log(s_r/s_{a2})}} + \frac{(0.25w_s - w_r) (4s_r)^{0.8}}{s^{0.8} + (4s_r)^{0.8}}$ $+ \frac{3w_r \sqrt{s_{a2}^2 / \log(s_r/s_{a2})}}{s^2 / \log(s_r/s_{a2}) + \sqrt{s_{a2}^2 / \log(s_r/s_{a2})}} + \frac{w_r (4s_r)^{0.8}}{s^{0.8} + (4s_r)^{0.8}}$	Bimodal	6	Unique parameter approach/graphical determination	w_s : saturated water content w_r : residual water content s_r : The residual suction for water stored in macro-pores s_a : the first air entry value s_{a2} : The air entry value for water stored in micro-pores s_i : the second residual suction
Gitirana Jr, Fredlund [18]	$S_r = \frac{S_1 - S_2}{1 + \left(\frac{s}{\sqrt{s_{\text{res1}} s_{\text{res2}}}}\right)^{d_1}} + \frac{S_2 - S_3}{1 + \left(\frac{s}{\sqrt{s_{\text{res1}} s_{\text{res2}}}}\right)^{d_2}} + \frac{S_3 - S_4}{1 + \left(\frac{s}{\sqrt{s_{\text{res1}} s_{\text{res2}}}}\right)^{d_3}} + S_4$ <p style="text-align: center;">With</p>	Bimodal	11	Unique parameter approach/graphical determination	Bimodal SWCC divided into five linear asymptotes. All the parameter can be determined by 6 characteristic points (0,1), ($s_{b1}, 1$), ($s_{\text{res1}}, S_{r, \text{res1}}$), ($s_{b2}, S_{r, \text{res2}}$), ($s_{\text{res2}}, S_{r, \text{res2}}$), (10 ⁶ , 0). Details

$$\sum_1^N R_i = 1. \quad (8)$$

The concept of Burger, Shackelford [8] for bimodal soils can be extended to establish the S_r - s relationship for a multimodal soil by assuming an idealized N -modal pore structure as following (see Fig. 2a). For a N -modal soil, we may introduce $N-1$ delimiting points s_i ($2 \leq i \leq N$) to divide the SWCC into N subcurves. One subcurve represents one subporosity. In addition, two additional 'delimiting' suctions $s_1 = 0$ and $s_{N+1} = \infty$ are employed for mathematical convenience. For an imposed suction $s \in [s_i, s_{i+1})$, it is assumed that the 1st to the $(i-1)$ th subporosity are completely desaturated, whereas the $(i+1)$ th to the N th subporosity are fully saturated. The i th subporosity is under desaturation process, and the water volume in the i th subporosity $V_{w,i}$ is expressed as

$$V_{w,i} = S_{r,i} V_{\text{unsat},i} \quad \text{for } s \in [s_i, s_{i+1}), \quad (9)$$

where $S_{r,i}$ represents the local degree of saturation of the i th subporosity and is described by a unimodal SWCC model (e.g., VGM). From Eqs. (3)–(9), the total water volume in the soil at a suction level $s \in [s_i, s_{i+1})$, can be expressed as

$$V_w = S_{r,i} V_{\text{unsat},i} + V_{\text{unsat}} - \sum_1^i V_{\text{unsat},i} + V_{\text{res}} \quad (10)$$

for $s \in [s_i, s_{i+1})$.

The degree of saturation gives

$$S_r = \frac{V_w}{V_{\text{void}}} = \left(S_{r,i} R_i + 1 - \sum_1^i R_i \right) \frac{V_{\text{unsat}}}{V_{\text{void}}} + \frac{V_{\text{res}}}{V_{\text{void}}} \quad (11)$$

for $s \in [s_i, s_{i+1})$.

Substituting Eqs. (4) and (5) into (11) gives

$$S_r = \left(S_{r,i} R_i + 1 - \sum_1^i R_i \right) (S_{r,\text{max}} - S_{r,\text{res}}) + S_{r,\text{res}} \quad (12)$$

for $s \in [s_i, s_{i+1})$.

From Eq. (12), it is not hard to find that SWCC in terms of the effective degree of saturation S_e can be expressed as

$$S_e = \left(1 - \sum_1^i R_i \right) + R_i S_{r,i} \quad \text{for } s \in [s_i, s_{i+1}) \quad (13)$$

In this paper, VGM (with the constraint $m + 1/n = 1$ suggested by Van Genuchten and Nielsen [17]) is adopted to describe $S_{r,i}$:

$$S_{r,i} = \left[1 + (\alpha_i s)^{\frac{1}{1-m_i}} \right]^{-m_i} \quad \text{for } s \in [s_i, s_{i+1}) \quad (14)$$

where α_i and m_i are the VGM parameters for the i th subporosity. From Eqs. (12)–(14), we get the degree of saturation of a N -modal soil in a piecewise form

$$S_r = (S_{r,\text{max}} - S_{r,\text{res}}) \left\{ \left(1 - \sum_1^i R_i \right) + R_i \left[1 + (\alpha_i s)^{\frac{1}{1-m_i}} \right]^{-m_i} \right\} + S_{r,\text{res}} \quad \text{for } s \in [s_i, s_{i+1}) \quad (15)$$

and the effective degree of saturation

$$S_e = \left(1 - \sum_1^i R_i \right) + R_i \left[1 + (\alpha_i s)^{\frac{1}{1-m_i}} \right]^{-m_i} \quad \text{for } s \in [s_i, s_{i+1}). \quad (16)$$

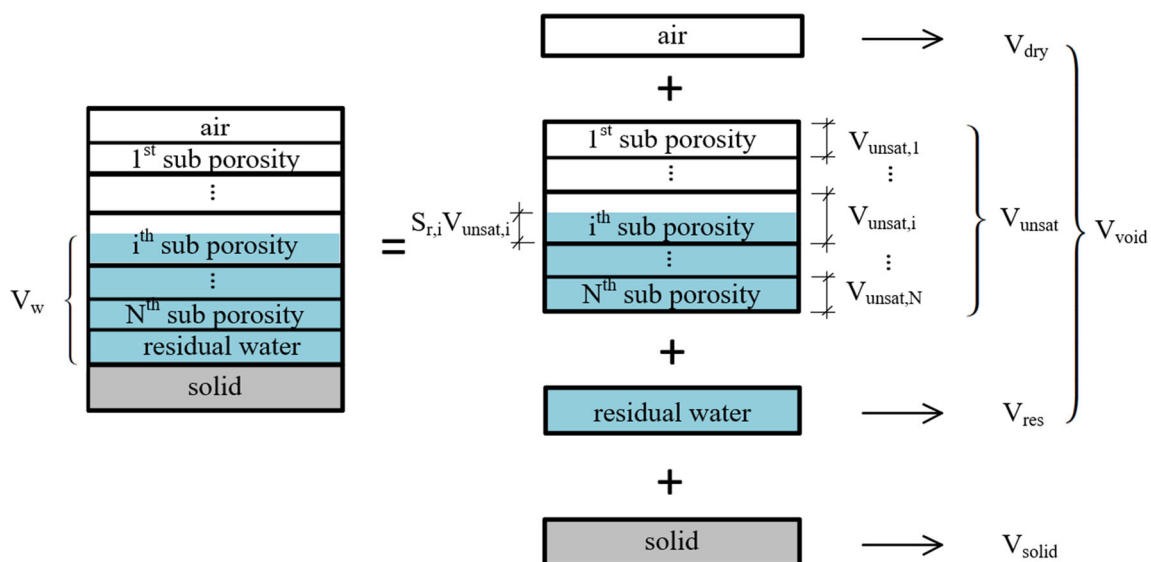


Fig. 1 Schematic of the soil composition with N -modal pore structure

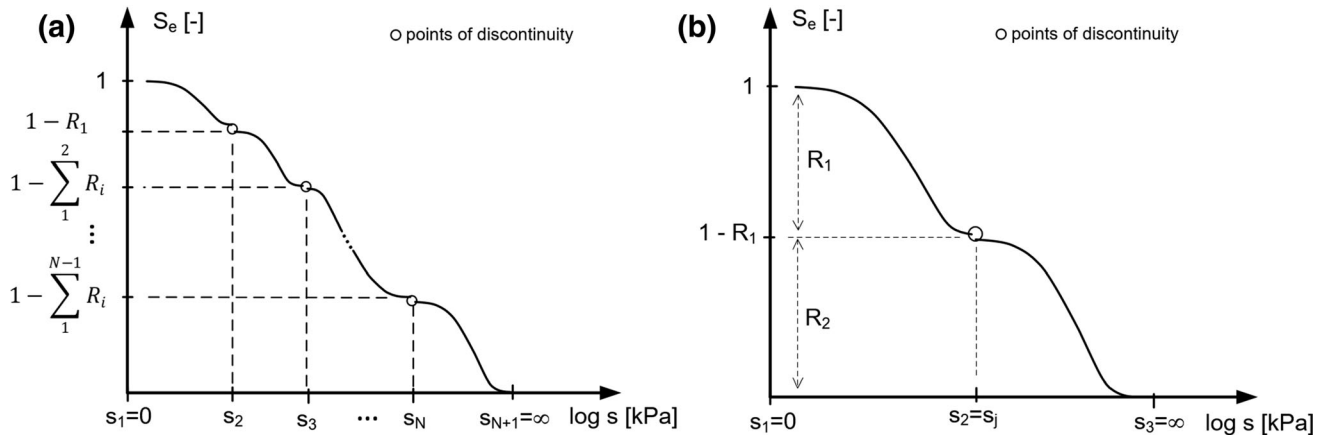


Fig. 2 **a** Schematic presentation of DMVGM for a N -modal soil, **b** schematic presentation of DMVGM for a bimodal soil ($N = 2$, equivalent to the bimodal model of Burger, Shackelford [8])

The piecewise SWCC function in Eq. (16) is named as discrete multimodal van Genuchten model (DMVGM). From the left limit of a delimiting point $s = s_i$

$$\lim_{s \rightarrow s_i^-} S_e = \left(1 - \sum_{i=1}^{i-1} R_i \right) + R_{i-1} \left[1 + (\alpha_{i-1} s_i)^{\frac{1}{1-m_{i-1}}} \right]^{-m_{i-1}} \quad (17)$$

and the right limit

$$\lim_{s \rightarrow s_i^+} S_e = \left(1 - \sum_{i=1}^i R_i \right) + R_i \left[1 + (\alpha_i s_i)^{\frac{1}{1-m_i}} \right]^{-m_i}, \quad (18)$$

we get the following inequality

$$\lim_{s \rightarrow s_i^-} S_e > \left(1 - \sum_{i=1}^{i-1} R_i \right) > \lim_{s \rightarrow s_i^+} S_e. \quad (19)$$

Therefore, DMVGM predicts a point of discontinuity at each delimiting points, as shown in Fig. 2a. For a bimodal soil ($s_1 = 0, s_2 = s_j, s_3 = \infty$), Eq. (16) degrades to

$$S_e = \begin{cases} R_2 + R_1 \left[1 + (\alpha_1 s)^{\frac{1}{1-m_1}} \right]^{-m_1}, & \text{for } s \in [0, s_j] \\ R_2 \left[1 + (\alpha_2 s)^{\frac{1}{1-m_2}} \right]^{-m_2}, & \text{for } s \in [s_j, \infty) \end{cases} \quad (20)$$

and the volumetric fraction of macro (R_1)- and micro (R_2)-porosity can be expressed as

$$R_1 = \frac{S_{r,\max} - S_{r,j}}{S_{r,\max} - S_{r,\text{res}}} \quad \text{and} \quad R_2 = \frac{S_{r,j} - S_{r,\text{res}}}{S_{r,\max} - S_{r,\text{res}}} \quad (21)$$

Substituting Eqs. (21) in (20), it is not hard to see that the Burger, Shackelford [8] bimodal model (using VGM to describe $S_{r,i}$) is equivalent to DMVGM with $N = 2$, as shown in Fig. 2b.

2.2 A continuous multimodal SWCC model—CMVGM

In order to derive a continuous multimodal SWCC model, the whole pore space of the soil is regarded as a superposition of a set of overlapping subporosities, each of which occupies a volumetric fraction R_i [12, 34, 48]. The continuous multimodal SWCC model in terms of effective degree of saturation S_e is obtained by extending the bimodal function (Eq. 2) as

$$S_e = \sum_{i=1}^N R_i S_{r,i} \quad (22)$$

where again N is the modality number, R_i is the volumetric fraction of each subporosity with $\sum_{i=1}^N R_i = 1$, and $S_{r,i}$ is the local degree of saturation of a subporosity. This general concept was first proposed by Ross and Smettem [34]. They pointed out that $S_{r,i}$ may be described by any unimodal SWCC model (e.g., BCM and VGM). For the aim of simplicity, $S_{r,i}$ is replaced by VGM (with the constraint $m + 1/n = 1$) in this study. A continuous N -modal SWCC model is then expressed as

$$S_e = \sum_{i=1}^N R_i \left[1 + (\alpha_i s)^{\frac{1}{1-m_i}} \right]^{-m_i}, \quad (23)$$

where again α_i and m_i are the VGM parameters for each subporosity. The SWCC function in Eq. (23) is named as continuous multimodal van Genuchten model (CMVGM).

3 Development of discrete-continuous multimodal Van Genuchten model (D-CMVGM)

In Sect. 2, two N -modal SWCC functions in piecewise form [DMVGM in Eq. (16)] and continuous form [CMVGM in Eq. (23)] are introduced. For practical applications of these models, convenient parameter calibration methods are required. In comparison with CMVGM, the parameter determination method for DMVGM is relatively simple due to the independence of the parameters for each subporosity, but the numerical implementation is inconvenient since DMVGM generates $N-1$ discontinuity points in the SWCC. Furthermore, the discontinuity feature is more significant with increasing modality number N . In contrast, CMVGM describes a continuous SWCC with convenient numerical implementation. However, including the $S_{r,\max}$ and $S_{r,\text{res}}$, the totally $3N + 2$ parameters can be hardly determined through solely a best fitting procedure due to the strong intercorrelation among the parameters.

Note that the CMVGM and DMVGM possess identical set of parameters except for the additional delimiting suctions s_i for DMVGM, it is possible to calibrate the common parameters in DMVGM and use CMVGM to describe a continuous multimodal SWCC. This framework, utilizing both advantages of DMVGM (convenient parameter determination method) and CMVGM (simple and continuous mathematical function), is named as D-CMVGM. The detailed properties in D-CMVGM are shown in Table 1. In this section, the feasibility of the D-CMVGM framework for bimodal SWCCs is validated in Sect. 3.1; the determination procedure for the modality number N , delimiting suctions for DMVGM, as well as the common $3N + 2$ parameters for DMVGM and CMVGM, is shown in Sect. 3.2; an example for reproducing a multimodal SWCC of a silty sand by D-CMVGM is demonstrated in Sect. 3.3; the development of a modality number reduction method (MNRM) is shown in Sect. 3.4.

3.1 Feasibility of D-CMVGM framework for bimodal SWCCs

The feasibility of D-CMVGM framework is validated by using CMVGM and DMVGM with identical parameters to simulate the same bimodal SWCCs, as shown in Fig. 3. Additionally, for DMVGM, the point at $S_e = R_2$ is chosen as the delimiting point. For the silty sand [49] in Fig. 3a with a relative high ratio of $\alpha_1/\alpha_2 = 77$ (distinct bimodal pore structure), DMVGM and CMVGM reproduce almost identical SWCC. For the undisturbed loams [28] in Fig. 3b, c with relative low ratios of $\alpha_1/\alpha_2 = 46$ and 24,

respectively, as well as the coarse sand [37] in Fig. 3d with an extreme low ratio of $\alpha_1/\alpha_2 = 3.6$, the SWCCs reproduced by CMVGM and DMVGM are in good agreement with a slight discrepancy near the delimiting point. In general, DMVGM and CMVGM with the same set of parameters reproduce almost identical bimodal SWCC despite a slight discrepancy in a small range near delimiting point. The more pronounced the bimodal feature is, the less remarkable is the discrepancy. This phenomenon revealed a crucial fact that the parameters in CMVGM can be obtained with DMVGM based on SWCC data. Substituting the determined parameters in CMVGM then gives a continuous SWCC over the entire suction range. In fact, the parameter set of CMVGM for a multimodal SWCC may be not unique [18, 46], which will be discussed in Sect. 5. The unique parameter set determined by DMVGM is regarded as one of the suitable parameter sets of CMVGM. This common parameter set of DMVGM and CMVGM can be conveniently determined in the proposed D-CMVGM framework, which is introduced in the following subsections.

3.2 Parameter calibration method for the D-CMVGM framework

3.2.1 Determination of S_{\max} and S_{res}

Under the framework of D-CMVGM, the effective degree of saturation S_e of a soil with complex pore structure is described by Eq. (23), while SWCC is usually represented in terms of gravity water content w , volumetric water content θ or degree of saturation S_r . Thus, a complete multimodal SWCC model can be generally expressed as

$$S = (S_{\max} - S_{\text{res}})S_e + S_{\text{res}} \quad (24)$$

where S is defined as general water content representing w , θ or S_r ; S_{\max} and S_{res} are the maximum and residual values of that general water content, respectively. The maximum value of the water content measured during SWCC tests is adopted for the parameter S_{\max} . The parameter S_{res} representing the residual water content at high suction range is set equal to zero. From Eq. (24), we obtain

$$S_e = \frac{S - S_{\text{res}}}{S_{\max} - S_{\text{res}}} \quad (25)$$

The SWCC data are then represented in terms of S_e by using Eq. (25) and replotted in the $\log s$ - $\log S_e$ plane to determine the other parameters.

3.2.2 Determination of N and R_i

Figure 4a shows a set of unimodal and multimodal SWCCs divided into several linear segments (slope not equal to

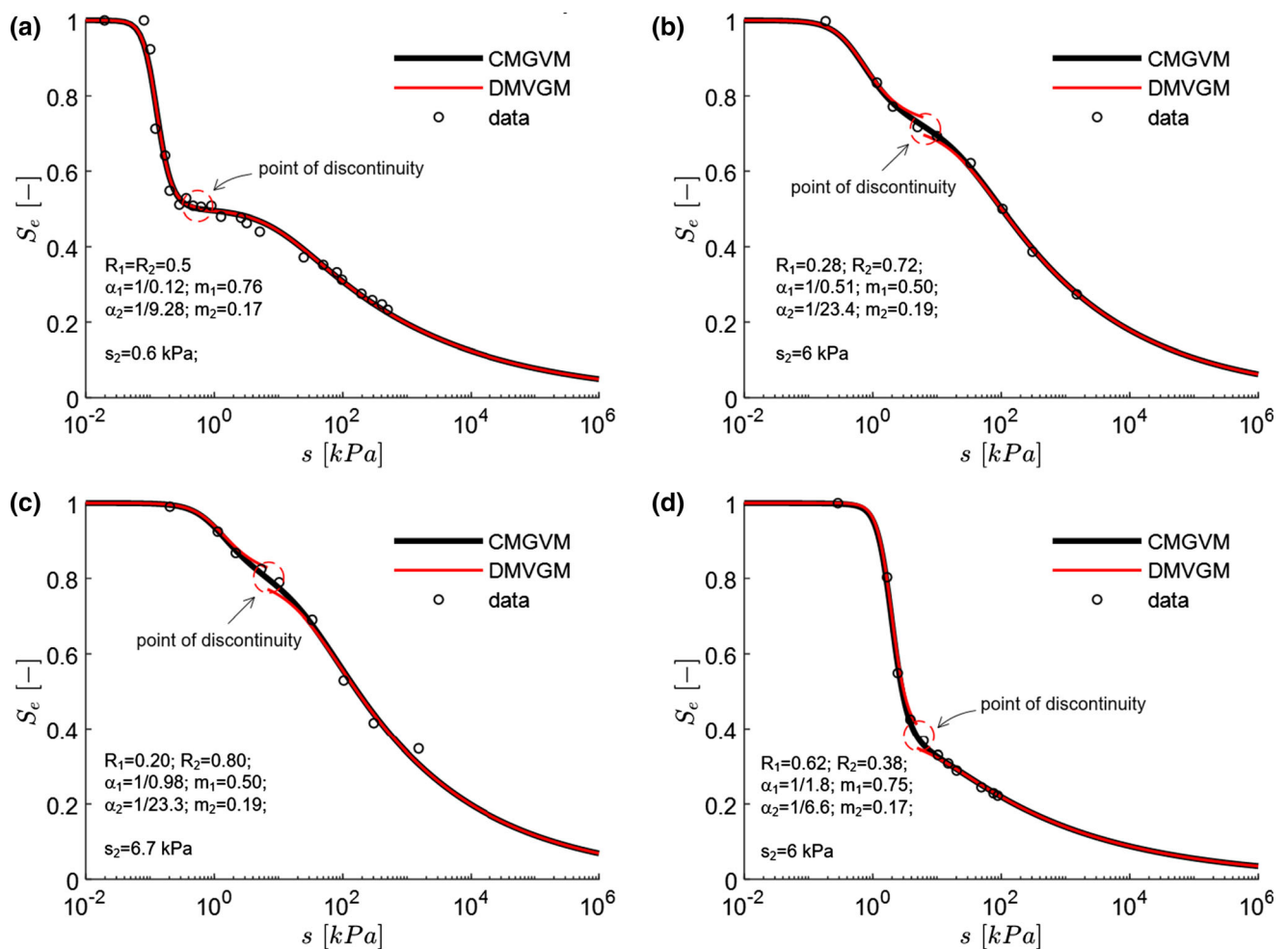


Fig. 3 Fitted bimodal SWCCs in terms of S_e by using DMVGM and CMVGM with identical parameters **a** SWCC of a silty sand with $S_{r,max} = 0.92$, $S_{r,res} = 0$, data from [49], **b** SWCC of undisturbed Neuenkirchen loam (at a depth of 15 m) with $w_{max} = 0.46$ (maximum gravity water content) and $w_{res} = 0$ (residual gravity water content), data from [28], **c** SWCC of undisturbed Neuenkirchen loam (at a depth of 60 m) with $w_{max} = 0.42$ and $w_{res} = 0$, data from [28], **d** SWCC of a coarse sand with $\theta_{max} = 0.32$ (maximum volumetric water content) and $\theta_{res} = 0$ (residual volumetric water content), data from [37]

zero) and horizontal segments in the $\log s$ – $\log S_e$ plane (In this paper, $\log X$ represents the base 10 logarithm of X). Under the framework of D-CMVGM, a linear segment in the $\log s$ – $\log S_e$ plane is regarded as a ‘subporosity’, i.e., the modality number N is identical with the number of the linear segments (horizontal segments occupy zero volumetric fraction). As shown in Fig. 4a, the SWCC of silty loam [6] is unimodal; the SWCCs of kaolin–sand mixture [35], coarse sand [37] and undisturbed loam [28] are bimodal. Particularly, the SWCC of silty sand with gravel [49] is trimodal. The first linear segment represents the macroporosity, and the third linear segment represents the microporosity within the aggregations of fine particles. The second ‘transition’ linear segment, which is determined by the pore space in the overlapping range of macro- and microporosity, can be regarded as an extra porosity, although it occupies a small volumetric fraction. A similar

finding has also been reported by Lloret and Villar [24]. They treated the microstructure of the heavily compacted ‘FEBEX’ bentonite as an assemblage of two distinguished porosities (macro- and microporosity) and an extra porosity in their overlapping range.

In the $\log s$ – $\log S_e$ plane, the cross-points of each adjacent linear segments and horizontal segments are chosen as delimiting points, and the volumetric fraction R_i for each ‘subporosity’ is graphically determined. Based on this concept, a general procedure to separate a N -modal SWCC into N linear segments in the $\log s$ – $\log S_e$ plane is demonstrated in Fig. 4b.

3.2.3 Determination of m and α for unimodal case ($N = 1$)

For the case of $N = 1$, both DMVGM and CMVGM degrade to VGM, which means that D-CMVGM with

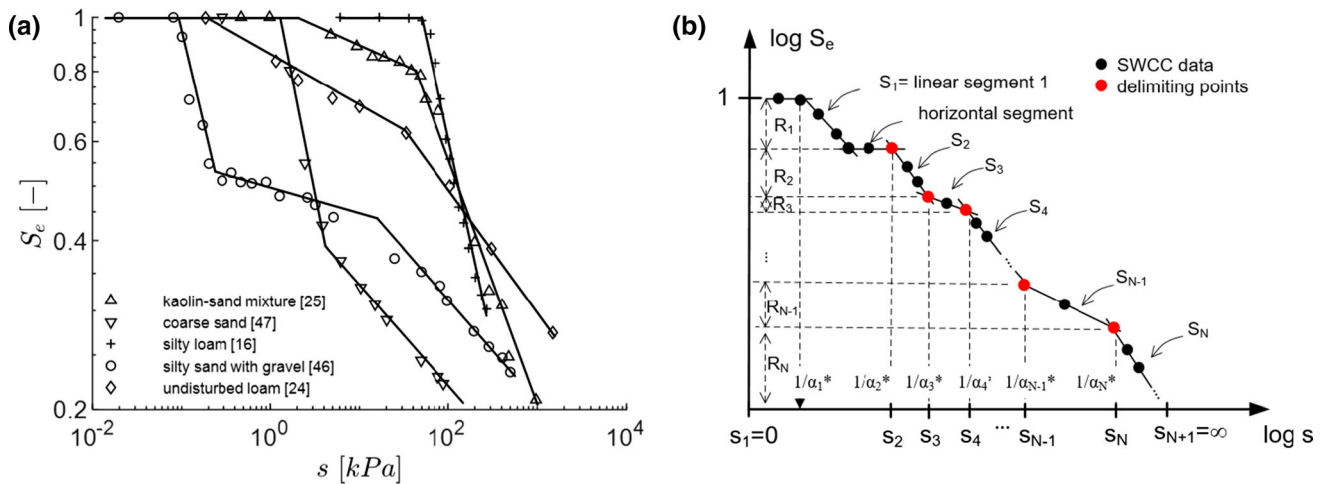


Fig. 4 **a** Presenting SWCCs of different soils in the logs– $\log S_e$ plane, **b** schematic representation of a general procedure for separating a N -modal SWCC into linear segments in the logs– $\log S_e$ plane

$N = 1$ is equivalent to VGM. The SWCC in terms of effective degree of saturation S_e is

$$S_e = \left[1 + (\alpha s)^{\frac{1}{1-m}} \right]^{-m}. \quad (26)$$

The slope k of the SWCC in the logs– $\log S_e$ plane is defined as

$$k = -\frac{d \log S_e}{d \log s} = -\frac{d S_e / S_e}{d s} s = \frac{m}{1-m} \frac{(\alpha s)^{\frac{1}{1-m}}}{1 + (\alpha s)^{\frac{1}{1-m}}} \quad (27)$$

From Eq. (27), it is not hard to see that the slope k monotonically increases with increasing suction. Thus, the maximum slope k_{\max} is reached, when suction tends to infinite:

$$k_{\max} = \lim_{s \rightarrow +\infty} \left(-\frac{d \log S_e}{d \log s} \right) = \frac{m}{1-m}. \quad (28)$$

Taking the logarithm of both sides of Eq. (26) gives

$$\log S_e = -\frac{m}{1-m} \log s - \frac{m}{1-m} \log \alpha - m \log \left[1 + (\alpha s)^{\frac{1}{1-m}} \right]. \quad (29)$$

When suction trends to infinite, the third term on the right-hand side of Eq. (29) vanishes, indicating a linear asymptote of VGM in the logs– $\log S_e$ plane as

$$\log S_e^* = -\frac{m}{1-m} \log s - \frac{m}{1-m} \log \alpha, \quad (30)$$

where S_e^* is the value of effective degree of saturation on the asymptote. When the soil is saturated, the suction value s_{ae} on the asymptote is solved from Eq. (30) by setting $S_e^* = 1$, which gives

$$s_{ae} = \frac{1}{\alpha}. \quad (31)$$

This suction s_{ae} is usually regarded as the air entry value of the soil. These features of VGM expressed in Eqs. (26)–(31) can also be found in [15, 20].

The evolution of VGM in the logs– $\log S_e$ plane is schematically demonstrated in Fig. 5a. When suction exceeds the air entry value, VGM rapidly trends to its asymptote and the slope k increases up to $m/(1-m)$. That means, for a unimodal SWCC, the linear asymptote can be approximated by using the measured SWCC data and the parameter m is back calculated as

$$m = \frac{k}{1+k} \quad (32)$$

where k is the slope of the approximated asymptote. The parameter α is the inverse of s_{ae} (Eq. 31), which can be graphically determined, as shown in Fig. 5a. An example is shown in Fig. 5b, the SWCC of a compacted silty sand (data from [29]) is accurately reproduced by VGM with the parameters determined by the proposed calibration method.

3.2.4 Determination of m_i and α_i for multimodal case ($N \geq 2$)

For the case of $N \geq 2$, the N -modal SWCC presented in the logs– $\log S_e$ plane is divided into N linear segments, as shown in Fig. 4. The parameters m_i and α_i are determined based on the slope and position of each linear segment. In DMVGM, the slope k_i of the i th subcurve in the $\log s$ – $\log S_e$ plane is defined as

$$k_i = -\frac{d \log S_e}{d \log s} = -\frac{d S_e / S_e}{d s} s \quad \text{for } s \in [s_i, s_{i+1}) \quad (33)$$

Taking the derivative with respect to s in Eq. (16) gives

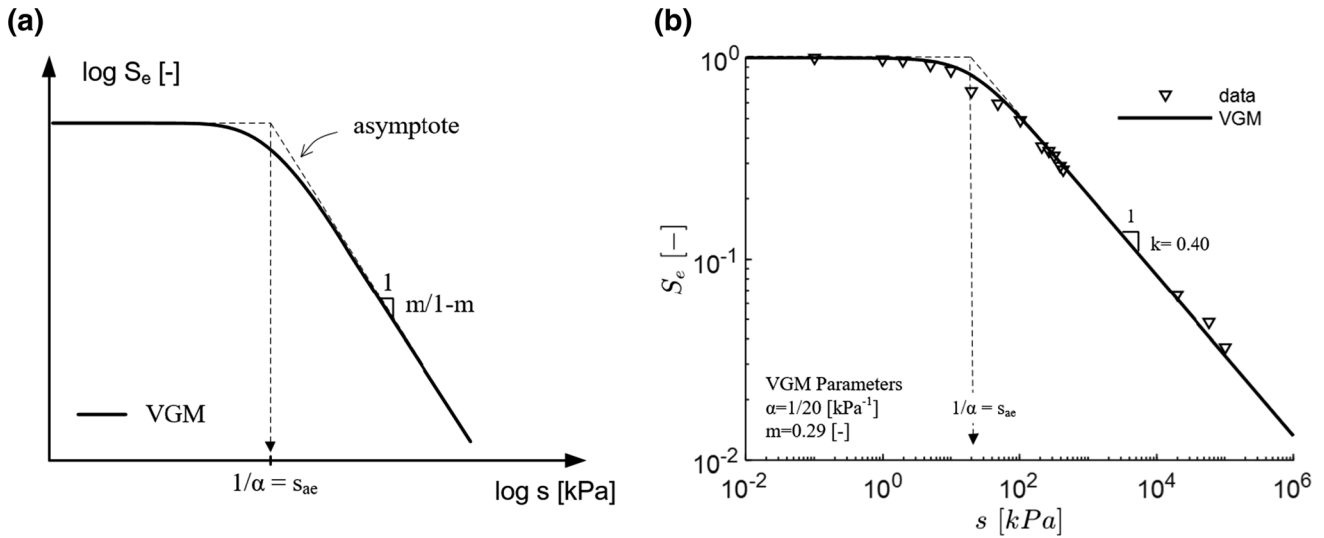


Fig. 5 a Schematic for the evolution of D-CMVGM with $N = 1$ (VGM) in the $\log s$ – $\log S_e$ plane, b fitted SWCC of a silty sand (data from [29]) by D-CMVGM with $N = 1$ (VGM)

$$\frac{dS_e}{ds} = -\frac{m_i}{1 - m_i} R_i \alpha_i^{\frac{1}{1-m_i}} s^{\frac{1}{1-m_i}-1} \left[1 + (\alpha_i s)^{\frac{1}{1-m_i}} \right]^{-m_i-1} \quad (34)$$

for $s \in [s_i, s_{i+1})$

Combining Eqs. (13), (14), (33) and (34), we obtain

$$k_i = \frac{m_i}{1 - m_i} \left(1 - S_{r,i}^{1/m_i} \right) \frac{R_i S_{r,i}}{\left(1 - \sum_1^i R_i \right) + R_i S_{r,i}} \quad (35)$$

for $s \in [s_i, s_{i+1})$

Details in the derivation of Eq. (35) are shown in Appendix A. Note that

$$1 - \sum_1^i R_i = \sum_1^N R_i - R_i, \quad (36)$$

Equation (35) may be rewritten as

$$k_i = \frac{m_i}{1 - m_i} \left(1 - S_{r,i}^{1/m_i} \right) \frac{R_i S_{r,i}}{\left(\sum_1^N R_i - R_i \right) + R_i S_{r,i}} \quad (37)$$

for $s \in [s_i, s_{i+1})$.

Let us define the effective volumetric fraction $R_{\text{eff},i}$ for the i th subporosity as

$$R_{\text{eff},i} = R_i / \sum_1^N R_i. \quad (38)$$

Substituting Eqs. (38) in (37) gives

$$k_i = \frac{m_i}{1 - m_i} \left(1 - S_{r,i}^{1/m_i} \right) \frac{R_{\text{eff},i} S_{r,i}}{\left(1 - R_{\text{eff},i} \right) + R_{\text{eff},i} S_{r,i}} \quad (39)$$

for $s \in [s_i, s_{i+1})$.

For the i th subporosity, it shall be noted that the parameters m_i and $R_{\text{eff},i}$ are two constants. The parameter m_i is characterized by the pore size distribution of the i th subporosity. That means, the slope k_i solely depends on the

local degree of saturation $S_{r,i}$ according to Eq. (39). As suction increases from s_i to s_{i+1} , $S_{r,i}$ gradually decreases from 1 (fully saturated i th subporosity) to 0 (fully desaturated i th subporosity). From mathematical point of view, Eq. (39) predicts a maximum for the slope k_i during the desaturation process. Furthermore, it is proved that the maximum slope $k_{i,\text{max}}$ exists for any combination of $R_{\text{eff},i}$ ($0 < R_{\text{eff},i} \leq 1$) and m_i ($0 < m_i < 1$) (see Appendix B). An example of the k_i evolutions for different combinations of m_i and $R_{\text{eff},i}$ is shown in Fig. 6a ($m_i = 0.8$) and b ($R_{\text{eff},i} = 0.8$). Thus, the maximum slope $k_{i,\text{max}}$ can be generally expressed as a function of m_i and $R_{\text{eff},i}$:

$$k_{i,\text{max}} = \max \left(-\frac{d \log S_e}{d \log s} \right) = f(m_i, R_{\text{eff},i}) \quad (40)$$

for $s \in [s_i, s_{i+1})$.

The analytical expression for the function $f(m_i, R_{\text{eff},i})$ is difficult to determine, but the evolution of $k_{i,\text{max}}$, depending on $R_{\text{eff},i}$ and m_i , can be numerically obtained according to Eq. (39), which are plotted in Fig. 7a (for $0 \leq k_{i,\text{max}} \leq 0.5$) and b (for $0.5 \leq k_{i,\text{max}} \leq 2.5$).

The mean slope $k_{i,\text{mean}}$, which is graphically determined from the i th linear segment in the $\log s$ – $\log S_e$ plane, is approximated by the maximum slope $k_{i,\text{max}}$ for each subporosity (such an approximation is proved to be adequate to describe the SWCC accurately, see the subsequent sections):

$$k_{i,\text{mean}} \approx k_{i,\text{max}} = f(m_i, R_{\text{eff},i}) \quad \text{for } s \in [s_i, s_{i+1}) \quad (41)$$

Consequently, m_i can be back calculated by Eq. (41) using the prior determined mean slope $k_{i,\text{mean}}$ and the effective volumetric fraction $R_{\text{eff},i}$ for each subporosity. Equivalently, the parameter m_i can be directly determined

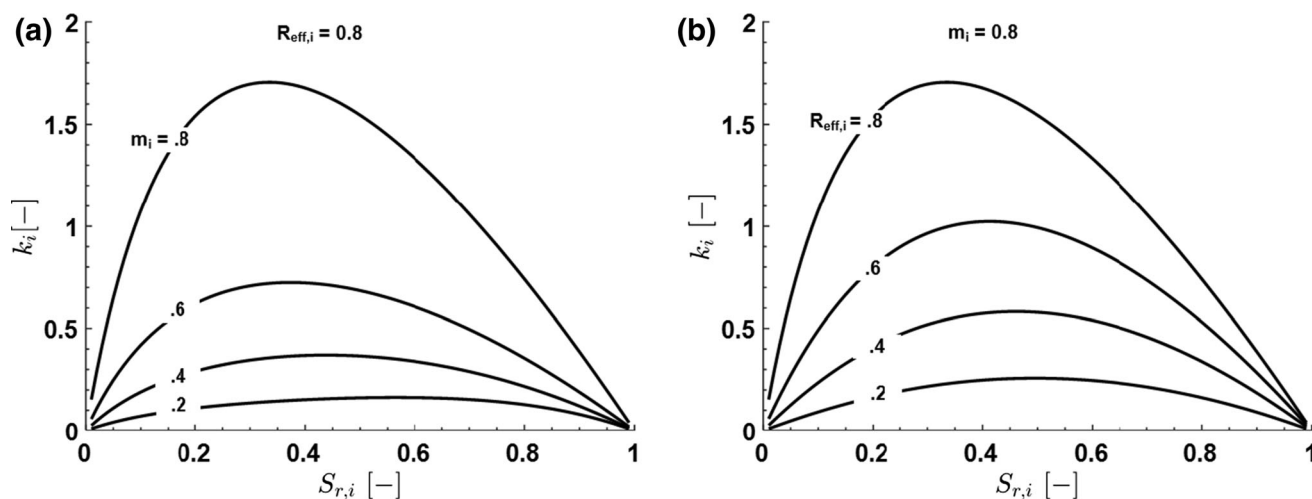


Fig. 6 The relationship between $R_{\text{eff},i}$, m_i and k_i **a** for $m_i = 0.8$ and **b** for $R_{\text{eff},i} = 0.8$

from Fig. 7a, b with graphically determined values of $k_{i,\text{mean}}$ and $R_{\text{eff},i}$.

In order to determine α_i , CMVGM with prior determined R_i and m_i is fitted to the overall SWCC data. As shown Fig. 4b, the initial approximation for α_1 (denoted as α_1^*) is regarded as the inverse of the suction of the point on the first linear segment by $S_e = 1$. For $i \geq 2$, the inverse of delimiting suctions is adopted as the initial approximation for α_i (denoted as α_i^*). It is worth to emphasize that such an approximation is already close to α_i . For this reason, the best fitting procedure is stable and converges rapidly. In this paper, the parameter α_i (in the unit of kPa^{-1}) is presented as the inverse of a suction value.

3.2.5 Summary for the parameterization of SWCCs by using the D-CMVGM framework

A general procedure to reproduce unimodal or multimodal SWCCs by using the D-CMVGM framework is summarized as following:

1. Determine S_{max} and S_{res} based on the measured SWCC data and calculate the effective degree of saturation S_e
2. Plot the SWCC data in the $\log s - \log S_e$ plane
3. Divide the SWCC data into N linear segments and determine the delimiting points
4. Calculate the volumetric fraction R_i and effective volumetric fraction $R_{\text{eff},i}$ of each subporosity
5. Measure the mean slope $k_{i,\text{mean}}$ of each linear segment
6. Determine the parameters m_i with prior determined $k_{i,\text{mean}}$ and $R_{\text{eff},i}$ from the diagram in Fig. 7.
7. Determine α_i^* from the SWCC in the $\log s - \log S_e$ plane. Adopt α_i^* as initial approximation for α_i . and fit CMVGM to all of the measured SWCC data with prior determined R_i and m_i .

8. Use CMVGM with the determined parameters to reproduce SWCC

For the case of $N = 1$, D-CMVGM is equivalent to VGM, and Eq. (40) degrades to Eq. (28), which corresponds to the curve for $R_{\text{eff},i} = 1$ in Fig. 7. The proposed parameter calibration method is automatically adapted to that for VGM, and hence the above described procedure is also valid for unimodal SWCCs.

3.3 Example of the reproduction of the SWCC for a silty sand with a trimodal function

The fitted SWCC of a silty sand (SW-SM with gravel according to [49]) by using D-CMVGM framework is demonstrated in Fig. 8. The maximum and residual degree of saturation $S_{r,\text{max}}$ and $S_{r,\text{res}}$ are set equal to 0.92 and 0, respectively (see Fig. 8a). Replotting the data in the $\log s - \log S_e$ plane, the SWCC shows a pronounced multimodal characterization. Dividing the SWCC into three linear segments (see Fig. 8b), denoted as S1, S2 and S3, respectively, a trimodal function ($N = 3$) is adopted to reproduce the SWCC. Setting the delimiting points at the two cross-points of the linear segments (see Fig. 8c), the volumetric fraction R_i of each subporosity is graphically determined ($R_1 = 0.47$; $R_2 = 0.07$; $R_3 = 0.46$) and the effective volumetric fraction $R_{\text{eff},i}$ is calculated ($R_{\text{eff},1} = 0.47$; $R_{\text{eff},2} = 0.13$; $R_{\text{eff},3} = 1.0$). Measuring the mean slope $k_{i,\text{mean}}$ of each linear segment ($k_{1,\text{mean}} = 0.62$; $k_{2,\text{mean}} = 0.04$; $k_{3,\text{mean}} = 0.19$), the parameters m_i are directly obtained from Fig. 7 ($m_1 = 0.78$; $m_2 = 0.42$; $m_3 = 0.17$, see Fig. 8d, e). Eventually, the α_i^* (initial approximation for α_i) are directly graphically determined, and the parameters α_i are obtained by fitting CMVGM to the overall SWCC data ($\alpha_1 = 1/0.12$; $\alpha_2 = 1/0.50$; $\alpha_3 = 1/15.5$). As shown in

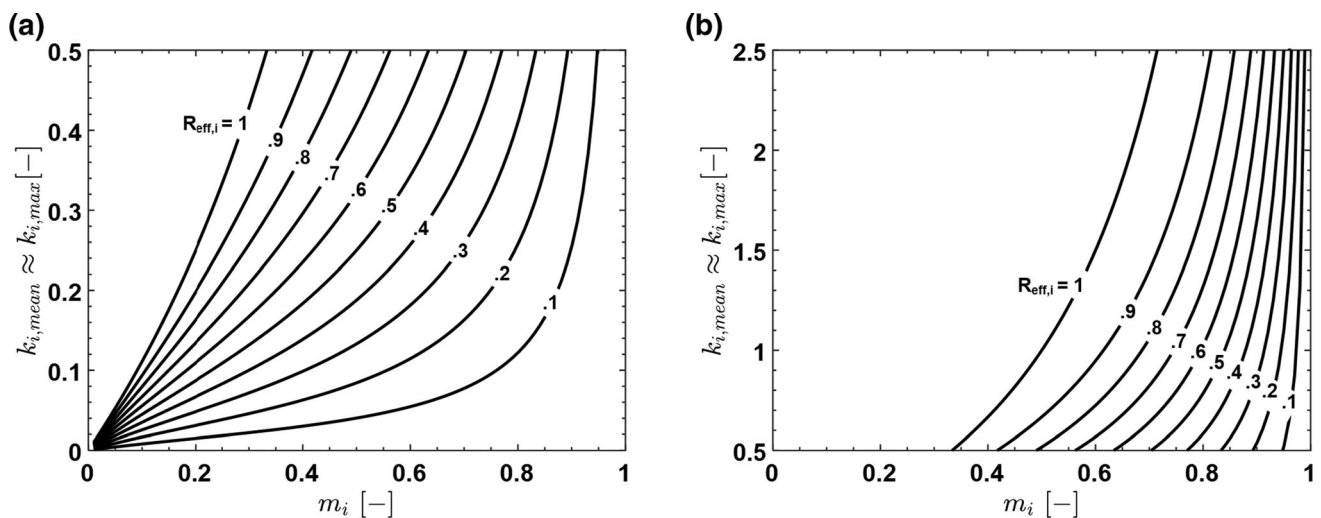


Fig. 7 The relationship between $R_{\text{eff},i}$, m_i and $k_{i,\text{max}}$ (numerically determined) for **a** $0 \leq k_{i,\text{max}} \leq 0.5$ and **b** $0.5 \leq k_{i,\text{max}} \leq 2.5$

Fig. 8f, the fitted curve is in good agreement with the SWCC data.

3.4 Modality number reduction method (MNRM) for D-CMVGM framework

In the previous subsections, the procedure of reproducing a multimodal SWCC by using D-CMVGM framework has been introduced. However, the modality number N can be further reduced by regarding the subporosity with relatively low volumetric fraction as the overlap of its adjacent subporosities. Such a subporosity is named as ‘transition subporosity’, and its linear segment is named as ‘transition segment (TS)’. In this study, the subporosity, whose volumetric fraction is lower than 0.1, is regarded as the transition subporosity. The middle point of a transition segment is chosen as a delimiting point to split the transition segment. By incorporating half of the volume into the former adjacent subporosity and the other half into the latter adjacent subporosity, the modality number is reduced (modality number coincides with the number of linear segments). This method is named as modality number reduction method (MNRM), which simplifies the form of SWCC function and reduces the number of unknown parameters. A schematic representation for dividing a N -modal SWCC into linear segments and transition segments in the $\log s$ – $\log S_e$ plane by using MNRM is shown in Fig. 9.

The procedure for reproducing the SWCC of a silty sand (SW–SM with gravel according to [49]) by using D-CMVGM framework incorporating MNRM is shown in Fig. 10. The second subporosity with a volumetric fraction of 0.07 is regarded as a transition subporosity and its linear segment as transition segment. The corresponding parameter calibration procedure is shown in Fig. 10. As can be

seen, the SWCC is precisely reproduced, while the SWCC function is simpler, and less parameters are required.

4 Applications of the D-CMVGM framework

4.1 Simulation of bimodal and trimodal SWCCs of mixed soils

In Fig. 11, the measured SWCCs of four mixed soils (S1–S4) from [35] are demonstrated. The four artificial soils were prepared by mixing coarse kaolin and Ottawa sand with different fines contents, and therefore they have different pore structures and different SWCCs. As shown in Fig. 11a, the SWCC of S1 can be regarded as an assembly of three linear segments. The second subporosity occupies a volumetric fraction of 0.08, which is less than 0.1. However, in order to validate the ability of the D-CMVGM to reproduce a trimodal SWCC and improve the accuracy of the curve fitting, this subporosity is not seen as a transition subporosity, and a trimodal function is used to reproduce the SWCC of S1. In Fig. 11b, the SWCC of S2 splits into four linear segments. As the second linear segment is almost horizontal (the volumetric fraction of second subporosity is close to zero), MNRM is applied, and the middle point of the second linear segment is chosen as a delimiting point. Therefore, a trimodal function is used to describe the SWCC of S2. The SWCCs of S3 and S4 splits into three linear segments, as shown in Fig. 11c, d, respectively. For the same reason as Fig. 11b, the second linear segments of both SWCCs are regarded as a transition segment, and delimiting points are set in the middle of the transition segments, i.e., a bimodal function is adequate to reproduce the SWCCs of S3 and S4.

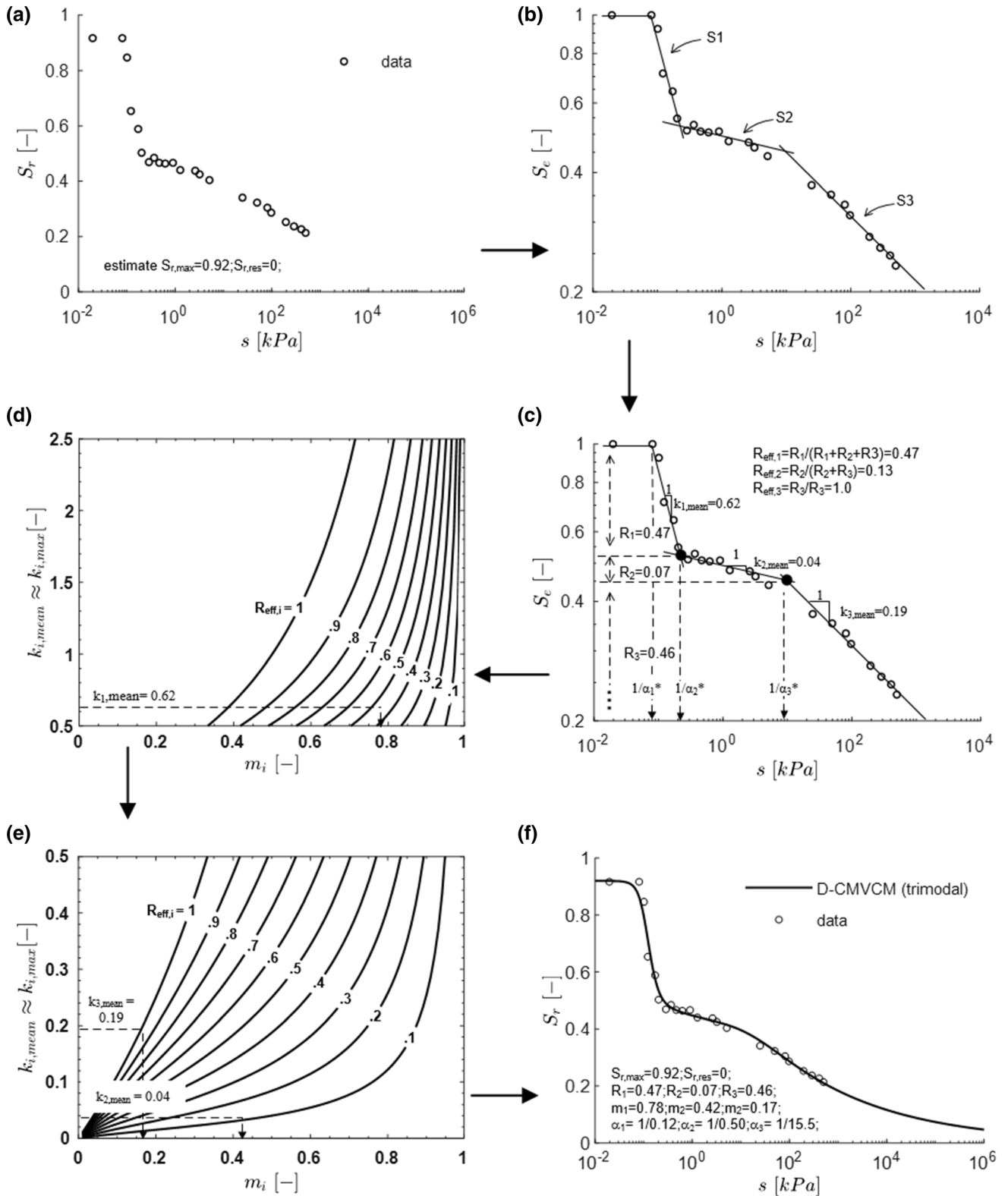


Fig. 8 A fitted multimodal SWCC of a silty sand from the D-CMVGM framework (data from [49])

The volumetric fraction R_i , the mean slope $k_{i,\text{mean}}$ as well as α_i^* (as the initial approximation of α_i) for each subporosity are presented in Fig. 11. The parameters for D-CMVGM framework as well as the θ_{max} and θ_{res} for each sample are listed in Table 2. Figure 12a, b demonstrate a good consistency between the fitted curves and the measured SWCCs.

4.2 Simulation of bimodal SWCCs of a silty sand

Angerer [4] prepared a set of reconstituted samples of low plasticity silty sand, which were statically compacted to different initial densities ($I_d = 0.5, 0.7$ and 0.9) at different water contents ($w = 3\%, 6\%$ and 10%). The fine content of the soil is 9.5% , including 1% clay and 8.5% silt. The SWCCs of the samples were measured over a wide suction range up to about 1×10^6 kPa by using both suction tensiometers (for suction lower than 1×10^3 kPa) and a chilled mirror hygrometer (for suction higher than 1×10^3 kPa). In this paper, only the SWCCs of the samples compacted at a medium density of $I_d = 0.7$ are presented and reproduced.

In Fig. 13a, the SWCC for the soil compacted at $w = 3\%$ is demonstrated in the $\log s$ – $\log S_e$ plane, which consists of two linear segments and a transition segment. A delimiting point is set in the middle of the transition segment according to MNRM. Therefore, a bimodal function is used to describe the SWCC. A similar approach is applied to the SWCCs for the samples compacted at $w = 6\%$ and $w = 10\%$ in Fig. 13b, c, respectively. The parameters of the three SWCCs are shown in Table 3. With the $S_{r,\text{max}}$ and $S_{r,\text{res}}$, the fitted SWCCs in terms of degree of saturation along with the SWCC data are presented in a conventional $\log s$ – S_r plane in Fig. 13d, by which a good

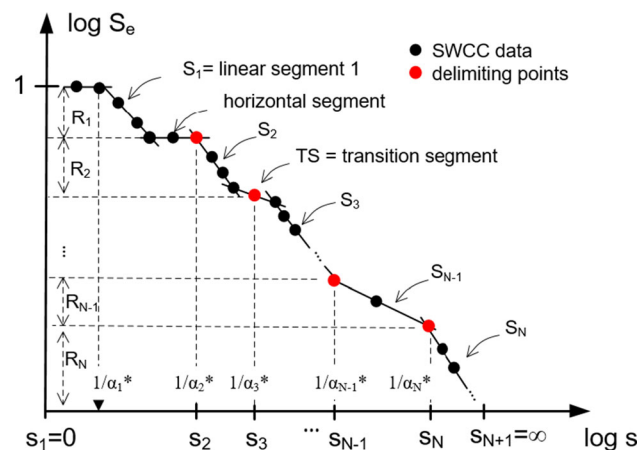


Fig. 9 Schematic representation of separating multimodal SWCC into linear segments and transition segments in the $\log s$ – $\log S_e$ plane by using MNRM

agreement between the fitted curves and measured SWCCs is shown.

In addition, the influence of the compaction water content on the SWCCs can be investigated from the variations of the parameters in Table 3. It is noted that the parameters R_1, R_2, α_1 and α_2 are affected, while the other parameters remain almost constant. When regression analysis is conducted and parameters R_1, R_2, α_1 and α_2 are related to compaction water content, the SWCC for the soil compacted at other water content can be estimated.

5 Discussion of the uniqueness of the set of parameters

As mentioned in Sect. 3, the parameters involved in CMVGM are highly correlated, and thus the use of the least square fitting approach for parameter determination might cause convergence problems in the optimization process [18, 46, 52]. Gitirana Jr and Fredlund [18] pointed out that a unique set of parameters may not exist, when the fitting parameters is not related to the shape features of curves. In this work, this issue is analyzed by reproducing the identical SWCC using CMVGM with two different set of parameters.

In Fig. 14a, the SWCC of a silty sand (SM with gravel according to [23]), presented in the $\log s$ – $\log S_e$ plane ($w_{\text{max}} = 0.176$ and $w_{\text{res}} = 0$), is approximated by three linear segments. Two delimiting points are set at the cross-points of the linear segments. The parameters determined for a trimodal SWCC function are referred to as ‘solution 1’. In order to find another set of parameters, a specific SWCC separation approach is introduced in Fig. 14b, where the second linear segment is regarded as a transition segment. One delimiting point is set in the middle of the transition segment, and the other delimiting point is used to divide the former first linear segment into two parts. Based on this specific separation approach, the determined parameters are referred to as ‘solution 2’. The parameters in both solutions are shown in Table 4.

The fitted SWCCs with both sets of parameters are demonstrated in Fig. 14c (in terms of effective degree of saturation S_e) and d (in terms of gravity water content w). Despite the different parameters, the two fitted curves are almost identical and consistent with the SWCC data, revealing a crucial fact that the set of parameters for CMVGM may be not unique for identical SWCC. Potentially causing the convergence problem and uncertainties in the curve fitting procedure, this shortcoming of CMVGM is overcome under the proposed D-CMVGM framework. A unique set of parameters can be determined with a predefined SWCC linearization and separation procedure in the $\log s$ – $\log S_e$ plane. This feature provides the possibility to

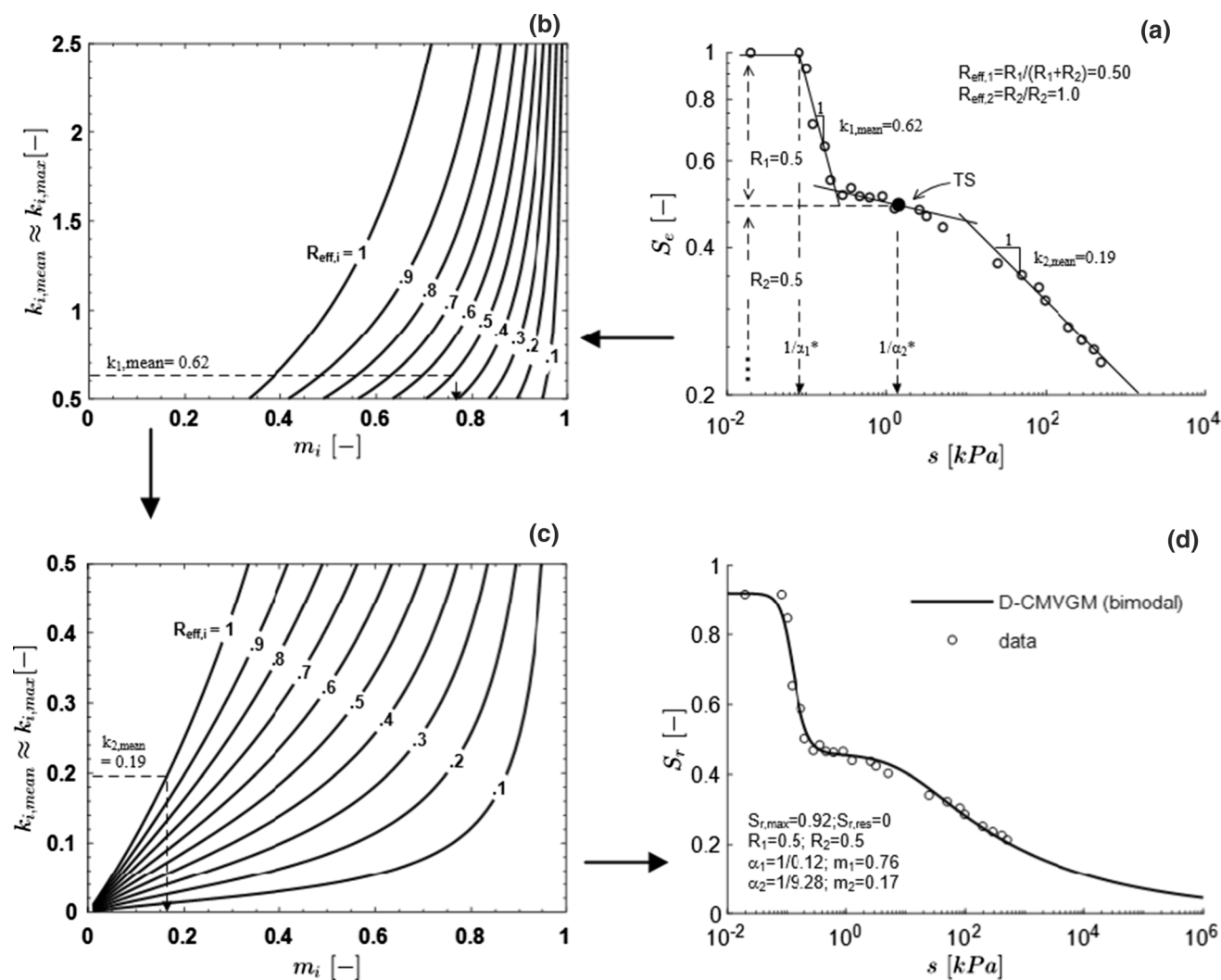


Fig. 10 A fitted multimodal SWCC of a silty sand from the D-CMVGM framework incorporated with MNRM (data from [49])

extend D-CMVGM by relating the parameters to soil properties or state parameters (for instance, compaction water content, see the example shown in Sect. 4.2).

6 Conclusion

A continuous N -modal SWCC model D-CMVGM with a convenient parameter calibration method is proposed, by which the modality number N can be any positive integer. The CMVGM provides a continuous function to describe the multimodal SWCC of the soils with heterogeneous pore structure. However, the determination of all the parameters solely with a curve fitting procedure leads to convergence problems and enhanced uncertainties, due to the non-

uniqueness in the parameters of CMVGM. This problem is overcome under the developed D-CMVGM framework. A unique set of parameters are conveniently determined by a prior SWCC linearization and separation procedure in the $\log s$ - $\log S_e$ plane. The modality number N corresponds to the number of linear segments of the SWCC presented in the $\log s$ - $\log S_e$ plane. In addition, MNRM is proposed to reduce the number of parameters and simplify the form of SWCC function. The parameters R_i and m_i can be graphically determined, and the parameters α_i are determined using a curve-fitting procedure with known parameters R_i and m_i . Eventually, the parameters are substituted into CMVGM to reproduce a continuous multimodal SWCC.

The mathematical form of D-CMVGM is relatively simple in comparison with other multimodal (bimodal)

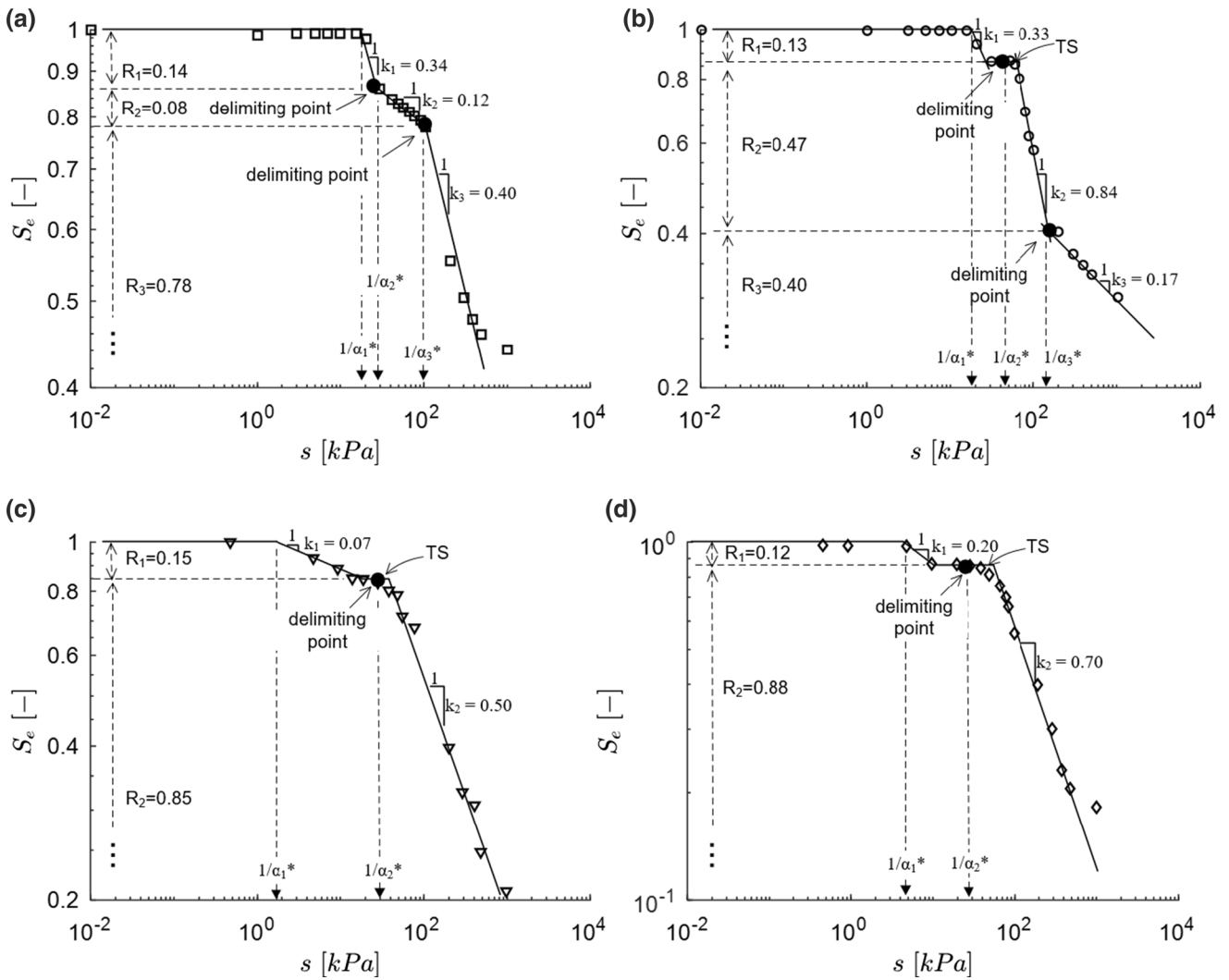


Fig. 11 Separation of the SWCCs of four sand–kaolin mixtures into linear segments in the $\log s$ – $\log S_e$ plane (data from [35]), **a** for soil S1, **b** for soil S2, **c** for soil S3, **d** for soil S4

Table 2 Parameters of D-CMVGM for soils S1–S4

	θ_{\max} [–]	θ_{res} [–]	α_1 [kPa ⁻¹]	m_1 [–]	R_1 [–]	α_2 [kPa ⁻¹]	m_2 [–]	R_2 [–]	α_3 [kPa ⁻¹]	m_3 [–]	R_3 [–]
S1	0.21	0	1/24	0.83	0.12	1/136	0.83	0.09	1/141	0.29	0.79
S2	0.32	0	1/20	0.82	0.13	1/87	0.86	0.47	1/316	0.17	0.40
S3	0.34	0	1/5.5	0.71	0.15	1/77	0.38	0.85	–	–	–
S4	0.31	0	1/5.7	0.71	0.12	1/103	0.43	0.88	–	–	–

SWCC model developed with unique parameter approach. In this work, a total of 9 bimodal SWCCs and 3 trimodal SWCCs from different soils are reproduced, and the fitted

curves show good consistency with the SWCC data. In addition, the D-CMVGM framework can be further

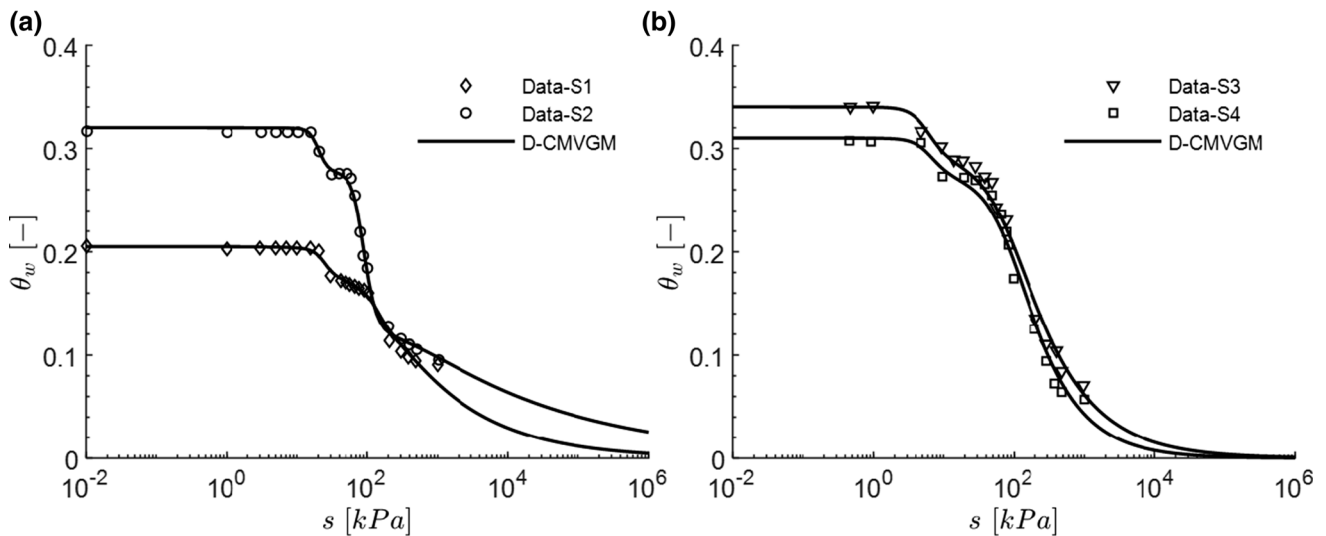


Fig. 12 Fitted SWCCs in terms of volumetric water content from the D-CMVGM framework (data from [35]) **a** for soils S1 and S2, **b** for soils S3 and S4

improved by correlating the parameters to other soil properties or state parameters.

Appendix

Appendix A: details in the derivation of Eq. (35)

Substituting Eqs. (34) in (33) gives

$$k_i = R_i \frac{m_i}{1 - m_i} \frac{\alpha_i^{-\frac{1}{m_i}} s^{\frac{1}{1-m_i}}}{\left[1 + (\alpha_i s)^{\frac{1}{1-m_i}}\right]^{-m_i-1}} \frac{1}{S_e} \quad (42)$$

for $s \in [s_i, s_{i+1})$.

Applying VGM for the i th subporosity (Eq. 14) to Eq. (42), we obtain

$$k_i = R_i \frac{m_i}{1 - m_i} \frac{(\alpha_i s)^{\frac{1}{1-m_i}} S_{r,i}}{1 + (\alpha_i s)^{\frac{1}{1-m_i}} S_e} \quad \text{for } s \in [s_i, s_{i+1}). \quad (43)$$

Substituting Eqs. (13) in (43), we have

$$k_i = \frac{m_i}{1 - m_i} \frac{(\alpha_i s)^{\frac{1}{1-m_i}} R_i S_{r,i}}{1 + (\alpha_i s)^{\frac{1}{1-m_i}} (1 - \sum_1^i R_i) + R_i S_{r,i}} \quad (44)$$

for $s \in [s_i, s_{i+1})$.

Rewrite Eq. (14) in the form

$$(\alpha_i s)^{\frac{1}{1-m_i}} = S_{r,i}^{-\frac{1}{m_i}} - 1 \quad \text{for } s \in [s_i, s_{i+1}), \quad (45)$$

and substituting Eqs. (45) in (44) gives Eq. (35).

Appendix B: proof for the existence of the maximum slope $k_{i,max}$

a) For the case $0 < R_{eff,i} < 1$ ($i < N$)

In Eq. (39), k_i is continuous on $S_{r,i} \in [0,1]$ and differentiable on $S_{r,i} \in (0,1)$. After the Lagrange's mean value theorem, there is a value ζ of $S_{r,i} \in (0,1)$ such that

$$\frac{dk_i}{dS_{r,i}}(S_{r,i} = \zeta) = \frac{k(1) - k(0)}{1 - 0} = 0, \quad (46)$$

Thus, the slope k_i at $S_{r,i} = \zeta$ is the maximum slope $k_{i,max}$.

b) For the case $R_{eff,i} = 1$ ($i = N$ or unimodal SWCC)

If $R_{eff,i} = 1$, Eq. (39) degrades to

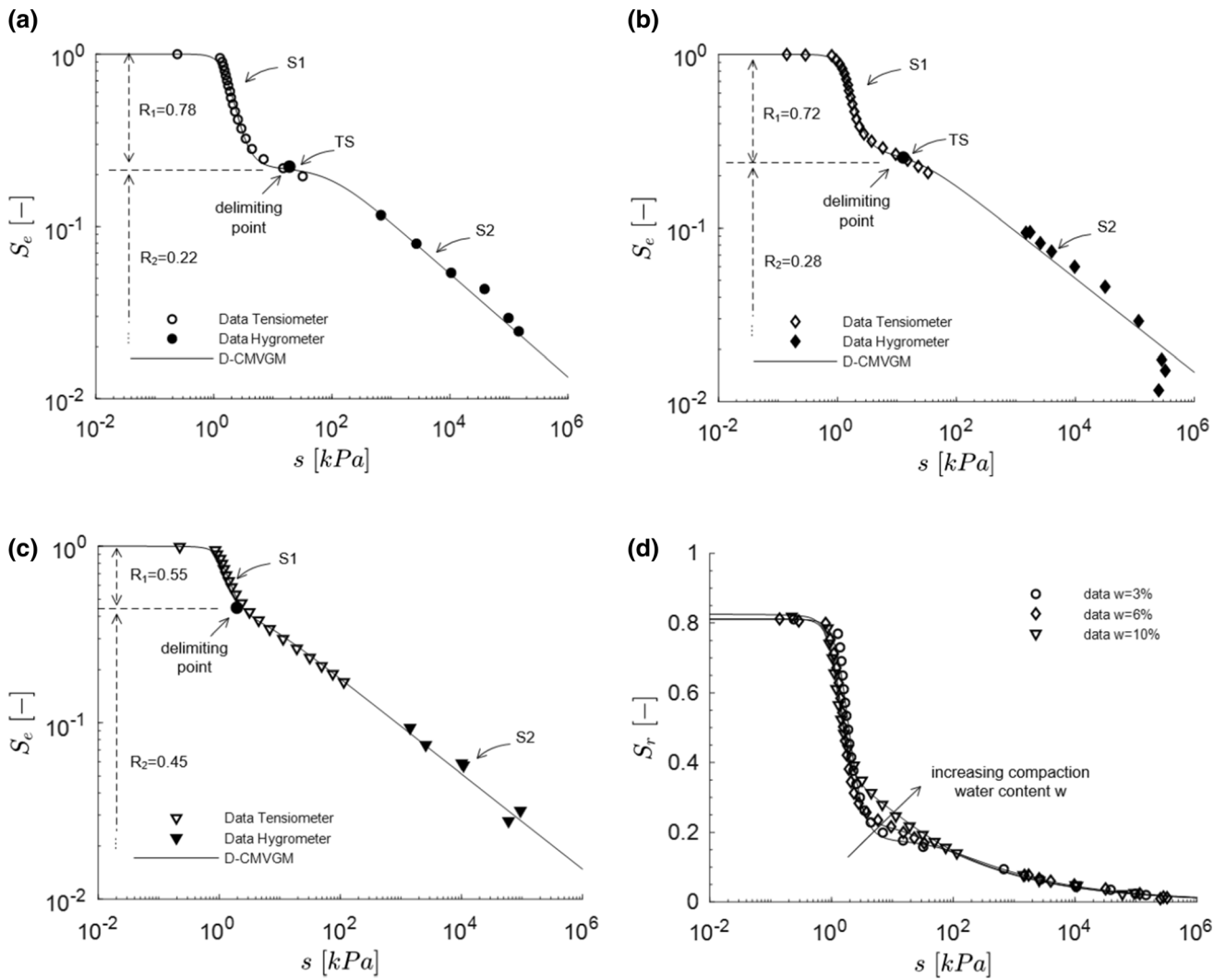


Fig. 13 **a** Separation of SWCC $w = 3\%$ into linear segments, **b** separation of SWCC $w = 6\%$ into linear segments, **c** separation of SWCC $w = 10\%$ into linear segments, **d** reproduction of the SWCCs of a medium dense silty sand compacted at different water contents (data from [4])

Table 3 Parameters of D-CMVGM for the compacted silty sand

	$S_{r,max}$ [-]	$S_{r,res}$ [-]	R_1 [-]	α_1 [kPa ⁻¹]	m_1 [-]	R_2 [-]	α_2 [kPa ⁻¹]	m_2 [-]
$w = 3\%$	0.81	0	0.78	1/1.7	0.75	0.22	1/87.9	0.21
$w = 6\%$	0.81	0	0.72	1/1.4	0.75	0.28	1/20.5	0.21
$w = 10\%$	0.82	0	0.55	1/1.2	0.78	0.45	1/2.7	0.21

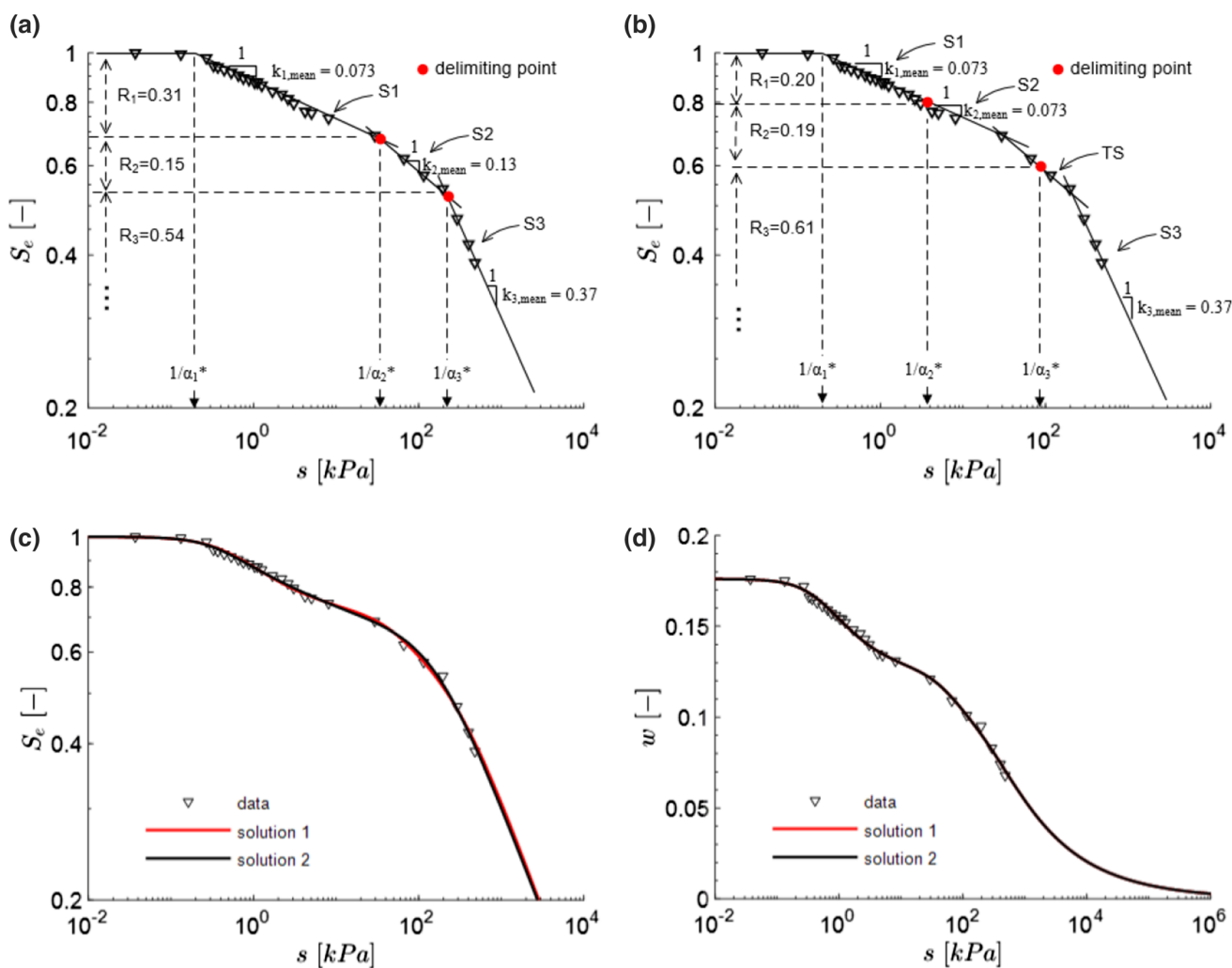


Fig. 14 **a** Separation of the SWCC into linear segments for solution 1, **b** separation of the SWCC into linear segments for solution 2, **c** fitted SWCCs of a silty sand in log s -log S_e plane, **d** fitted SWCCs of a silty sand in log s - w plane (data from [23])

Table 4 Two sets of parameters of trimodal CMVGM for the SWCC of a silty sand

	R_1 [-]	α_1 [kPa $^{-1}$]	m_1 [-]	R_2 [-]	α_2 [kPa $^{-1}$]	m_2 [-]	R_3 [-]	α_3 [kPa $^{-1}$]	m_3 [-]
Solution 1	0.31	1/0.51	0.38	0.15	1/51.7	0.50	0.54	1/276	0.30
Solution 2	0.20	1/0.40	0.45	0.19	1/2.0	0.23	0.61	1/159	0.30

$$k_i = \frac{m_i}{1 - m_i} \left(1 - S_{r,i}^{1/m_i} \right). \quad (47)$$

Thus, the slope at $S_{r,i} = 0$ is the maximum slope $k_{i,max}$.

Combining a) and b), the existence of the maximum slope $k_{i,max}$ for any combination of $m_i \in (0,1)$ and $R_{eff,i} \in (0,1]$ is proved.

Acknowledgements The support of the China Scholarship Council (Number 201608080128) is greatly acknowledged by the first Author.

Funding Open Access funding enabled and organized by Projekt DEAL. The research leading to these results received funding from China Scholarship Council under Grant Agreement Number 201608080128.

Availability of data and material The data used to support the findings of this study are available from the corresponding author upon request.

Code availability The code used to support the findings of this study are available from the corresponding author upon request.

Declarations

Conflict of interest The authors have no conflicts of interest to declare that are relevant to the content of this article.

Open Access This article is licensed under a Creative Commons Attribution 4.0 International License, which permits use, sharing, adaptation, distribution and reproduction in any medium or format, as long as you give appropriate credit to the original author(s) and the source, provide a link to the Creative Commons licence, and indicate if changes were made. The images or other third party material in this article are included in the article's Creative Commons licence, unless indicated otherwise in a credit line to the material. If material is not included in the article's Creative Commons licence and your intended use is not permitted by statutory regulation or exceeds the permitted use, you will need to obtain permission directly from the copyright holder. To view a copy of this licence, visit <http://creativecommons.org/licenses/by/4.0/>.

References

- Alonso EE, Gens A, Josa A (1990) A constitutive model for partially saturated soils. *Géotechnique* 40(3):405–430
- Alonso EE, Pinyol NM, Gens A (2013) Compacted soil behaviour: initial state, structure and constitutive modelling. *Géotechnique* 63(6):463–478. <https://doi.org/10.1680/geot.11.P.134>
- Alonso E, Vaunat J, Gens A (1999) Modelling the mechanical behaviour of expansive clays. *Eng Geol* 54(1–2):173–183
- Angerer L (2020) Experimental evaluation of the suction-induced effective stress and the shear strength of as-compacted silty sands. Technische Universität München
- Arya LM, Paris JF (1981) A physicoempirical model to predict the soil moisture characteristic from particle-size distribution and bulk density data. *Soil Sci Soc Am J* 45(6):1023–1030
- Brooks R, Corey T (1964) HYDRAU uc properties of porous media. *Hydrol Pap Colorado State Univ* 24:37
- Burger CA, Shackelford CD (2001) Soil-water characteristic curves and dual porosity of sand–diatomaceous earth mixtures. *J Geotech Geoenviron Eng* 127(9):790–800
- Burger CA, Shackelford CD (2001) Evaluating dual porosity of pelletized diatomaceous earth using bimodal soil-water characteristic curve functions. *Can Geotech J* 38(1):53–66
- Coppola A (2000) Unimodal and bimodal descriptions of hydraulic properties for aggregated soils. *Soil Sci Soc Am J* 64(4):1252–1262
- Delage P, Lefebvre G (1984) Study of the structure of a sensitive Champlain clay and of its evolution during consolidation. *Can Geotech J* 21(1):21–35
- Dexter AR, Czyż EA, Richard G, Reszkowska A (2008) A user-friendly water retention function that takes account of the textural and structural pore spaces in soil. *Geoderma* 143(3–4):243–253. <https://doi.org/10.1016/j.geoderma.2007.11.010>
- Durner W (1994) Hydraulic conductivity estimation for soils with heterogeneous pore structure. *Water Resour Res* 30(2):211–223
- Fredlund DG, Xing A (1994) Equations for the soil-water characteristic curve. *Can Geotech J* 31(4):521–532
- Fuentes W, Triantafyllidis T (2013) Hydro-mechanical hypoplastic models for unsaturated soils under isotropic stress conditions. *Comput Geotech* 51:72–82
- Gallipoli D (2012) A hysteretic soil-water retention model accounting for cyclic variations of suction and void ratio. *Géotechnique* 62(7):605–616
- Van Genuchten MT (1980) A closed-form equation for predicting the hydraulic conductivity of unsaturated soils 1. *Soil Sci Soc Am J* 44(5):892–898
- Van Genuchten MT, Nielsen D (1985) On describing and predicting the hydraulic properties. *Ann Geophys* 5:615–628
- Gitirana G Jr, Fredlund DG (2004) Soil-water characteristic curve equation with independent properties. *J Geotech Geoenviron Eng* 130(2):209–212
- Gupta S, Larson W (1979) Estimating soil water retention characteristics from particle size distribution, organic matter percent, and bulk density. *Water Resour Res* 15(6):1633–1635
- Hu R, Chen Y-F, Liu H-H, Zhou C-B (2013) A water retention curve and unsaturated hydraulic conductivity model for deformable soils: consideration of the change in pore-size distribution. *Géotechnique* 63(16):1389–1405
- Leong E-C (2019) Soil-water characteristic curves-determination, estimation and application. *Jap Geotech Soc Spec Publ* 7(2):21–30
- Leong EC, Rahardjo H, Tinjum JM, Benson CH, Blotz LR (1999) Soil-water characteristic curves for compacted clays. *J Geotech Geoenviron Eng* 125(7):629–630
- Li X, Li J, Zhang L (2014) Predicting bimodal soil–water characteristic curves and permeability functions using physically based parameters. *Comput Geotech* 57:85–96
- Lloret A, Villar MV (2007) Advances on the knowledge of the thermo-hydro-mechanical behaviour of heavily compacted “FEBEX” bentonite. *Phys Chem Earth Parts A/B/C* 32(8–14):701–715. <https://doi.org/10.1016/j.pce.2006.03.002>
- Mašín D (2013) Double structure hydromechanical coupling formalism and a model for unsaturated expansive clays. *Eng Geol* 165:73–88
- Mualem Y (1976) A new model for predicting the hydraulic conductivity of unsaturated porous media. *Water Resour Res* 12(3):513–522
- Mun W, McCartney JS (2015) Compression mechanisms of unsaturated clay under high stresses. *Can Geotech J* 52(12):2099–2112
- Othmer H, Diekkrüger B, Kutilek M (1991) Bimodal porosity and unsaturated hydraulic conductivity. *Soil Sci* 152(3):139–150
- Patil UD, Puppala AJ, Hoyos LR, Pedarla A (2017) Modeling critical-state shear strength behavior of compacted silty sand via suction-controlled triaxial testing. *Eng Geol* 231:21–33
- Příkryl R, Weishauptová Z (2010) Hierarchical porosity of bentonite-based buffer and its modification due to increased temperature and hydration. *Appl Clay Sci* 47(1–2):163–170
- Qian X, Gray DH, Woods RD (1993) Voids and granulometry: effects on shear modulus of unsaturated sands. *J Geotech Eng* 119(2):295–314
- Romero E, DELLA VECCHIA G, Jommi C, (2011) An insight into the water retention properties of compacted clayey soils. *Géotechnique* 61(4):313–328
- Romero E, Gens A, Lloret A (1999) Water permeability, water retention and microstructure of unsaturated compacted Boom clay. *Eng Geol* 54(1–2):117–127
- Ross PJ, Smettem KR (1993) Describing soil hydraulic properties with sums of simple functions. *Soil Sci Soc Am J* 57(1):26–29
- Satyanaga A, Rahardjo H, Leong E-C, Wang J-Y (2013) Water characteristic curve of soil with bimodal grain-size distribution. *Comput Geotech* 48:51–61
- Scheinost A, Sinowski W, Auerswald K (1997) Regionalization of soil water retention curves in a highly variable soilscape. I. Developing a new pedotransfer function. *Geoderma* 78(3):129–143
- Schnellmann R, Rahardjo H, Schneider HR (2013) Unsaturated shear strength of a silty sand. *Eng Geol* 162:88–96

38. Sheng D, Fredlund DG, Gens A (2008) A new modelling approach for unsaturated soils using independent stress variables. *Can Geotech J* 45(4):511–534
39. Sheng D, Zhou A-N (2011) Coupling hydraulic with mechanical models for unsaturated soils. *Can Geotech J* 48(5):826–840
40. Smettem K, Kirkby C (1990) Measuring the hydraulic properties of a stable aggregated soil. *J Hydrol* 117(1–4):1–13
41. Sun H, Mašín D, Najser J, Neděla V, Navrátilová E (2019) Fractal characteristics of pore structure of compacted bentonite studied by ESEM and MIP methods. *Acta Geotech*. <https://doi.org/10.1007/s11440-019-00857-z>
42. Tinjum JM, Benson CH, Blotz LR (1997) Soil-water characteristic curves for compacted clays. *J Geotech Geoenviron Eng* 123(11):1060–1069
43. Vereecken H, Maes J, Feyen J, Darius P (1989) Estimating the soil moisture retention characteristic from texture, bulk density, and carbon content. *Soil Sci* 148(6):389–403
44. Wang Q, Cui Y-J, Minh Tang A, Xiang-Ling L, Wei-Min Y (2014) Time- and density-dependent microstructure features of compacted bentonite. *Soils Found* 54(4):657–666. <https://doi.org/10.1016/j.sandf.2014.06.021>
45. Wheeler S, Sivakumar V (1995) An elasto-plastic critical state framework for unsaturated soil. *Géotechnique* 45(1):35–53
46. Wijaya M, Leong E (2016) Equation for unimodal and bimodal soil–water characteristic curves. *Soils Found* 56(2):291–300
47. Wilson G, Jardine P, Gwo J (1992) Modeling the hydraulic properties of a multiregion soil. *Soil Sci Soc Am J* 56(6):1731–1737
48. Zhang L, Chen Q (2005) Predicting bimodal soil-water characteristic curves. *J Geotech Geoenviron Eng* 131(5):666–670
49. Zhao H, Zhang L, Fredlund D (2013) Bimodal shear-strength behavior of unsaturated coarse-grained soils. *J Geotechn Geoenviron Eng* 139(12):2070–2081
50. Zhou A-N, Sheng D, Sloan SW, Gens A (2012) Interpretation of unsaturated soil behaviour in the stress–saturation space, I: volume change and water retention behaviour. *Comput Geotech* 43:178–187
51. Zhou A-N, Sheng D, Sloan SW, Gens A (2012) Interpretation of unsaturated soil behaviour in the stress–saturation space: II: constitutive relationships and validations. *Comput Geotech* 43:111–123
52. Zurmühl T, Durner W (1998) Determination of parameters for bimodal hydraulic functions by inverse modeling. *Soil Sci Soc Am J* 62(4):874–880

Publisher's Note Springer Nature remains neutral with regard to jurisdictional claims in published maps and institutional affiliations.

Paper III – A novel framework for predicting water retention behaviour based on pore size distribution data of multimodal unsaturated soils

Yan, W. & Cudmani, R. (2022b) A novel framework for predicting water retention behaviour based on pore size distribution data of multimodal unsaturated soils. submitted to *Acta geotechnica* (under review)

A novel framework for predicting water retention behaviour of multimodal unsaturated soils based on pore size distribution data

Author 1:

- Wei Yan* (given name: Wei / Family name: Yan)
- Department of Civil, Geo and Environmental Engineering, Technical University of Munich, Franz-Langering-Straße 10, 81245 Munich, Germany
- E-Mail: wei.yan@tum.de
- ORCID number: 0000-0001-7008-966X

Author 2:

- Roberto Cudmani (given name: Roberto / Family name: Cudmani)
- Department of Civil, Geo and Environmental Engineering, Technical University of Munich, Franz-Langering-Straße 10, 81245 Munich, Germany
- E-Mail: roberto.cudmani@tum.de

*Corresponding author: Wei Yan (E-Mail: wei.yan@tum.de, Franz-Langering-Straße 10, 81245 Munich, Technical University of Munich, Munich, Germany)

Abstract

The soil water characteristic curve (SWCC) strongly influences the hydro-mechanical properties of unsaturated soils and hence plays a decisive role in geotechnical and geo-environmental applications in vadose zone. This paper advances a novel framework to predict the water retention behaviour of multimodal deformable soils based on the pore size distribution (PSD) measurements, by which the dual effects of suction on the soil microstructure and volume during SWCC tests are considered. The full picture of soil microstructure is quantitatively described by void ratio (for the overall void volume) and a new microstructural state parameter (for pore size distribution) from a general multimodal PSD model. The relationship between the water retention curve and the pore size distribution measurement is interpreted by a unique PSD-surface, and a reversible microstructural behaviour is assumed during drying and wetting cycles. The model is validated by predicting the water retention curves of four different types of soils. A strong consistency between the measurement and prediction is observed. The closed-form water retention expression obtained directly from PSD measurements can be further incorporated into other unsaturated soil property formulations (e.g., unsaturated hydraulic conductivity and effective stress parameter) and facilitate the implementation of the model in particle applications.

Keywords

Soil microstructure; Water retention behaviour; Constitutive relations; Partial saturation; Pore size distribution

38 **1. Introduction**

39 The soil water characteristic curve (SWCC), defined as the relationship between the soil suction and water content
40 (gravity water content w , degree of saturation S_r or volumetric water content θ), is dominated by soil pore
41 structure. SWCC and soil microstructure play a decisive role in the unsaturated soil applications, as they
42 significantly influence the hydraulic (e.g., unsaturated permeability [1-3]) and mechanical properties (e.g., the
43 Bishop's effective stress parameter χ [4,5], shear strength [6], compressibility [7]) of unsaturated soils. However,
44 the experimental approaches to determine SWCC are tedious, expensive and time-consuming owing to the
45 relatively low hydraulic conductivity of unsaturated soils. For the practical applications, a number of empirical
46 curve-fitting models [8-10] and predictive models [11-13], relating the SWCC parameters to other soil properties
47 (the so-called pedotransfer functions), have been developed and successfully applied in geotechnical and geo-
48 environmental engineering applications in the vadose zone during the past decades.

49 Conventionally, the soil pore structure is regarded as a bundle of capillary tubes with circular cross section.
50 The pore radius of the capillary channel in the soil associated to a given suction level s is determined by Kelvin's
51 equation:

$$r = \frac{C}{s} = \frac{2T \cos \theta}{s} \quad (1)$$

52 Here, C is a constant equal to $2T \cos \theta$, T is the surface tension of water (0.072 N/m at 25 °C) and θ is the contact
53 angle between soil and water ($\theta \approx 0^\circ$ for desiccation) [14,15]. This means that the pores smaller than or equal to
54 this value r are filled with water at the given suction level s . Assuming that the pore structure remains constant
55 during the SWCC tests, the dependency of the water content (in terms of effective degree of saturation S_e) on the
56 soil suction s can be derived from the integration of pore size distribution function:

$$S_e(s) = \int_0^{r=C/s} f(\xi) d\xi \quad (2)$$

57 where ξ is a dummy variable of integration representing pore radius, and $f(\xi)$ is the pore size distribution (PSD)
58 function. The procedure in Eqs. (1) and (2), determining a SWCC directly from pore size distribution information,
59 is referred to as "direct transformation method" [16]. Inversely, soil pore size distribution can be derived from
60 SWCC under the constant pore structure assumption [17].

61 In the past decades, a number of empirical unimodal SWCC equations have been derived, assuming $f(\xi)$ obeys
62 normal distribution [18], lognormal distribution [19] or an empirical unimodal distribution [8-10]. However,
63 numerous research literatures have shown that the pore structure of compacted clayey soils or mixed soils consists
64 of interaggregate (macro) and intraaggregate (micro) porosities [20-22], or even more than two sub-porosities [23-
65 25]. A multimodal pore structure might cause a multimodal SWCC, which cannot be accurately described by the
66 conventional unimodal SWCC functions. To take into account the general multimodality of the soils with
67 heterogenous pore structure, a multimodal pore size distribution function $f(r)$ is therefore required in the "direct
68 transformation method".

69 As pointed out by Simms and Yanful [26], the "direct transformation method" oversimplifies the relationship
70 between the PSD and the water retention behaviour of deformable soils, as the pore structure may significantly
71 vary during the SWCC test. That is the reason why the directly transformed SWCC from a PSD data set differs

72 from the measured SWCC for deformable soils [23,27,28]. For example, Simms and Yanful [26] measured the
73 microstructures of four fine-grained soils by means of MIP tests and reported that the pore size distribution curve
74 significantly changed with suction during the SWCC tests. Later, Li and Zhang [29] detected the pore structure of
75 compacted Lean Clay at different degree of saturation and found that intraaggregate pores contracted during drying.
76 Monroy et al. [30] observed the microstructural transformation of the London Clay from an aggregate structure at
77 as-compacted state to a matrix structure at saturation state. More recently, Cai et al. [31] measured different pore
78 size distributions of the compacted Guilin lateritic soil at different suction levels during wetting and drying paths.
79 The evolving microstructure during the SWCC test implies that one obtains different SWCCs for a soil by
80 substituting the pore size distribution curves $f(r)$ into Eq. (2). This means that the water retention property
81 predicted by “direct transformation method” (Eqs. (1) and (2)) without considering the evolving microstructure is
82 far from “characteristic” for deformable soils.

83 To date, very few attempts have been made to predict SWCC directly from PSD measurements. For instance,
84 Simms and Yanful [26] proposed a network approach by modelling the suction induced pore shrinkage and pore
85 trapping from the PSD curves. This approach was later adopted by Zhang and Li [32] to predict the SWCCs of
86 five types of soils varying from gravel to clay. Nevertheless, it seems that the predicted SWCCs do not match well
87 with their measurements. More recently, Hu et al. [33] related the change in pore-size distribution to void ratio
88 and derived a density dependent unimodal SWCC model for deformable soils. Afterwards, Chen et al. [34]
89 extended Hu’s model for bimodal soils by assuming that the overall volume change solely caused the variation in
90 the interaggregate porosity. However, the density-dependent SWCC models of Hu et al. [33] and Chen et al. [34]
91 must be calibrated based on a “reference” SWCC measured at a constant void ratio. That means, these models
92 solely take into account quantitative PSD information in soil water retention behaviour, which are empirical SWCC
93 expressions in nature and incapable of predicting SWCC directly from PSD data. In contrast, Della Vecchia et al.
94 [28] incorporated an empirical correlation between the aggregate porosity and water content to account for the
95 evolutionary fabric in a bimodal pore size distribution expression to modelling the water retention behaviour of
96 compacted soils with different activity of clay fractions. Nonetheless, a closed-form SWCC expression, which
97 facilitates the implementation of the model in particle applications, cannot be derived from this approach.

98 The aim of this paper is to establish a general framework to interpret the relationship between the evolving
99 microstructure and the water retention behaviour. To overcome the limitations of the “direct transformation
100 method”, a general multimodal pore size distribution model is employed, and the dual effects of suction on the
101 pore structure and soil volume during SWCC tests are considered. The proposed model is capable of predicting
102 the multimodal water retention curves directly from PSD measurements, which is validated against experimental
103 data of four different soils with complex pore structure.

104

105 2. Theory

106 2.1. A multimodal PSD model based on probability theory

107 In this subsection, the multimodal PSD model developed by Yan and Cudmani [35] based on probability theory is
108 briefly described. Following Scheidegger [36] and Juang and Holtz [3], the pore radius denoted to a point in the
109 void space is defined as the radius of the largest sphere containing this point within the void space (i.e., the sphere
110 cannot touch soil particle). Under this framework, the pore radius is a continuous random variable depending on
111 the position of the denoted point. According to probability theory, we have

$$\int_0^{+\infty} f(r) dr = 1. \quad (3)$$

112 Herein, $f(r)$ is the pore size density function, and the term $f(r)dr$ represents the probability of the occurrence of
113 a sphere with a radius $r \rightarrow r + dr$ in the void space.

114 For a general case (i.e., a multimodal soil), the overall soil microstructure might be regarded as an assembly of
115 N individual monomodal sub-porosities [17,37,38]. The overall pore size density function $f(r)$ is acquired by a
116 linear superposition of the PSD functions of sub-porosities $f_i(r)$:

$$f(r) = \sum_{i=1}^N R_i f_i(r). \quad (4)$$

117 Herein, R_i represents the volumetric fraction of each sub-porosity, which fulfils the condition

$$\sum_{i=1}^N R_i = 1. \quad (5)$$

118 In addition, the function $f_i(r)$ must fulfil the condition

$$\int_0^{+\infty} f_i(r) dr = 1. \quad (6)$$

119 Considering the requirement in Eq. (6), a proper monomodal pore size density function derived from van-
120 Genuchten model [9] is employed

$$f_i(r) = \frac{m_i (r_i^f / r)^{\frac{1}{1-m_i}}}{r(1-m_i) \left[1 + (r_i^f / r)^{\frac{1}{1-m_i}} \right]^{m_i+1}} \quad (7)$$

121 where m_i is the pore size spectrum number ($0 < m_i < 1$), and r_i^f is a reference pore radius corresponding to the
122 air entry suction and proportional to the maximum and mean (or dominant) pore size of the i -th sub-porosity.
123 Substituting Eq. (7) in Eq. (4), a general multimodal pore size density function gives

$$f(r) = \sum_{i=1}^N R_i \frac{m_i (r_i^f / r)^{\frac{1}{1-m_i}}}{r(1-m_i) \left[1 + (r_i^f / r)^{\frac{1}{1-m_i}} \right]^{m_i+1}} \quad (8)$$

124 which fulfils the condition in Eq. (3).

125 The cumulative pore size distribution curve yields

$$F(r) = \int_0^r f(r) dr = \sum_{i=1}^N R_i \left[1 + \left(\frac{r_i^f}{r} \right)^{\frac{1}{1-m_i}} \right]^{-m_i} \quad (9)$$

126 Particularly, the cumulative pore size distribution curve measured by mercury intrusion porosimetry (MIP) tests
127 can be expressed as [35]:

$$V_{cum}(r) = \frac{e_{MIP}}{G_s} \int_r^{+\infty} f(r) dr = \frac{e_{MIP}}{G_s} \left\{ 1 - \sum_{i=1}^N R_i \left[1 + \left(\frac{r_i^f}{r} \right)^{\frac{1}{1-m_i}} \right]^{-m_i} \right\} \quad (10)$$

128 Here, $V_{cum}(r)$ is the mercury intrusion volume in [cm³/g], e_{MIP} represents the total intruded void ratio and G_s is
129 the specific gravity of soil.

130

131 2.2. Microstructural state variable for soil pore structure

132 A complete picture of soil pore structure consists of two independent aspects: the overall void volume and the
133 microstructure (i.e., the pore size distribution). In conventional soil mechanics, the change in the pore space is
134 characterized by void ratio e , defined as the ratio of the void volume to the soil particle volume, while the changes
135 in microstructure or pore size distribution are rarely considered. A new microstructural state variable Ω is proposed
136 in this study to quantitatively characterize the soil pore size distribution.

137 Considering the proposed general multimodal pore size distribution model [Eq. (8)], a proper microstructural
138 state variable Ω is defined as:

$$\Omega = \Omega_k = \{R_1, r_1^f, m_1, \dots, R_N, r_N^f, m_N\} \quad (11)$$

139 Here, the microstructural state variable Ω (or Ω_k with $1 \leq k \leq 3N$) is a vector with $3N$ entries characterizing a
140 general N-modal microstructure. Then, the multimodal pore size density function in Eq. (8) can be rewritten as

$$f(r) = f(\Omega_k, r). \quad (12)$$

141 Under this framework, the pore structure is completely described by two independent state variables e (for overall
142 void volume) and Ω (for pore size distribution).

143

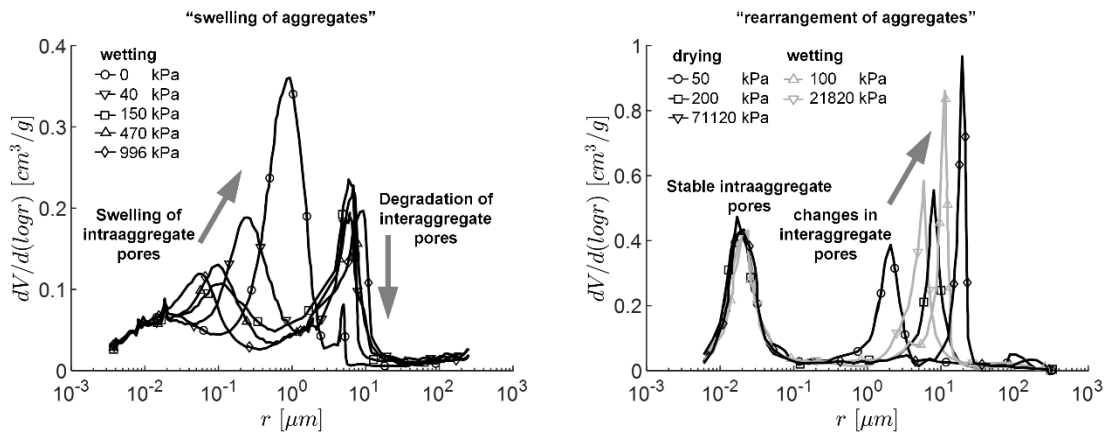


Fig. 1. Microstructural evolution in deformable soils (a) swelling of aggregates in London Clay (data from Monroy et al. [30]) (b) rearrangement of aggregates in Guilin lateritic soil (data from Cai et al. [31])

145 Soil microstructure is affected by various aspects, for example, sample preparation method (e.g., compaction
 146 energy and water content, initial dry density) [39-41], mechanical loading (e.g., pre-consolidation pressure and
 147 current stress state)[20,21], hydraulic loading (e.g., wetting-drying cycles) [42,30,31] and even chemical (e.g.,
 148 salinity of pore water) [43] and thermal loading [44,45]. In this study, only the microstructural evolution along
 149 hydro-mechanical loading paths is taken into account.

150 Delage and Lefebvre [20] observed that the interaggregate pore volume in Champlain clay were significantly
 151 reduced with increasing pre-consolidation pressure, while the intraaggregate pores remained unchanged. Similar
 152 findings have also been reported for other deformable soils under proctor compaction [23,29], isotropic
 153 compression [21] and oedometric compression [46]. In unimodal soils, the mean pores size was suggested to be
 154 proportional to mean net stress [33,47,48]. These experimental studies imply that soil microstructure strongly
 155 depends on the current stress state and the loading history.

156 Soil microstructure also alters with suction in wetting and drying cycles. Fig. 1 shows the microstructural
 157 evolution of the compacted London Clay during wetting (Fig. 1a), and that of the compacted Guilin lateritic soil
 158 during wetting and drying (Fig. 1b). On the one hand, these experimental results reveal the fact that the pore
 159 structure is suction-dependent during the SWCC test. On the other hand, the microstructural behaviour in the two
 160 soils are dominated by different mechanisms. London Clay (Fig. 1a) demonstrates distinguished bimodal
 161 characteristic at high suction level. As suction decreases along the wetting path, intraaggregate pores swell, and
 162 the interaggregate pores progressively degrade and vanish at saturation. This phenomenon can be interpreted by
 163 the "swelling of aggregates" during wetting. In contrast, the intraaggregate pores in Guilin lateritic soil (Fig. 1b)
 164 remain constant, and the interaggregate pores increase with suction, which might be attributed to the
 165 "rearrangement of the aggregates" during the SWCC test.

166 Hydration on the unsaturated soil subjected to high external loading might cause macro collapse (referred to
 167 as "wetting collapse" according to Alonso et al. [49]), leading to irreversible deformation and microstructural
 168 evolution. For example, Della Vecchia [50] reported significant reduction of macro pores of a compacted Boom
 169 Clay sample saturated at a high vertical stress of 600 kPa.

170 Based on the experimental evidence and the multimodal pore size distribution model, a general constitutive
 171 law is proposed to parameterize the microstructural evolution under hydro-mechanical loading paths:

$$\mathbf{\Omega} = \mathbf{\Omega}_k(\sigma_{ij}^{net}, p_0^*, s) \quad (13)$$

172 Here, σ_{ij}^{net} is the net stress tensor, and p_0^* is the pre-consolidation stress at saturated state representing the loading
 173 history associated with the irreversible volumetric deformation of the unsaturated soil [49]. Eq. (13) means that all
 174 the entries in $\mathbf{\Omega}$ depend on the current net stress, loading history and suction level. For an arbitrary set of $\mathbf{\Omega}_k$ at a
 175 given stress state and suction level, following condition is hold:

$$\int_0^{+\infty} f(\mathbf{\Omega}_k, r) dr = 1, \forall \mathbf{\Omega}_k \quad (14)$$

176 2.4. mechanical and hydraulic wetting

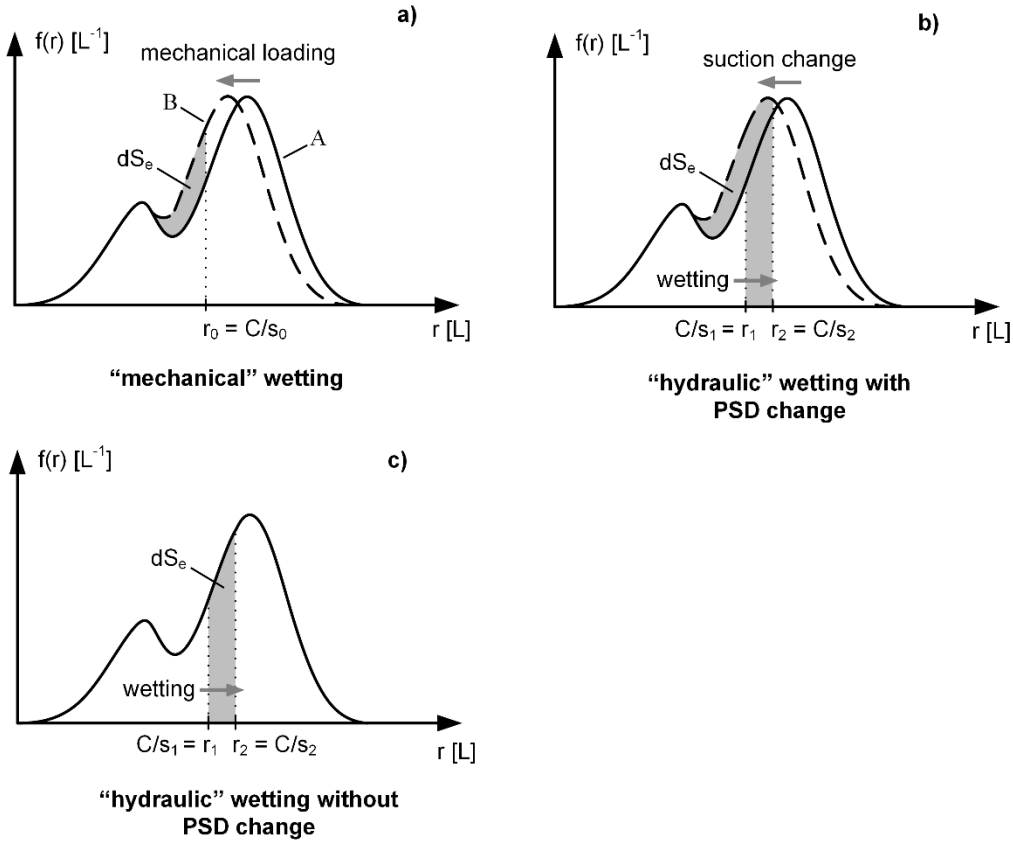


Fig. 2. Schematic for the interpretation of (a) mechanical wetting (b) hydraulic wetting with evolving pore structure (c) hydraulic wetting with stable pore structure

177 Tarantino 2009 pointed out that the increase in the degree of saturation of a soil could originate from two aspects:
 178 (i) increase in the water volume (e.g., by decreasing the suction level) which is referred to as “hydraulic wetting”;
 179 (ii) decrease in the void ratio (e.g., by increasing the mean net stress) which is referred to as “mechanical wetting”.
 180 This essential feature of the water retention behaviour can be interpreted by the proposed framework regarding the
 181 microstructural evolution along hydro-mechanical loading path.

182 Substituting Eq. (13) into Eq. (2), we obtain

$$S_e = \int_0^{C/s} f(\mathbf{\Omega}_k(\sigma_{ij}^{net}, p_0^*, s), r) dr = F\left(\mathbf{\Omega}_k(\sigma_{ij}^{net}, p_0^*, s), \frac{C}{s}\right) \quad (15)$$

183 Eq. (15) describes a general relationship between the effective degree of saturation and soil suction based on a
 184 probabilistic multimodal pore size distribution concept. The model indicates that soil water content is not only

185 dominated by suction but also the current stress state and the loading history. From Eq. (15), the infinitesimal
 186 change of effective degree of saturation can be expressed by

$$\begin{aligned}
 dS_e = & \underbrace{-\frac{C}{s^2} f\left(\Omega_k(\sigma_{ij}^{net}, \sigma_0^*, s), \frac{C}{s}\right) ds}_{T^1} + \underbrace{\sum_{k=1}^{3N} \frac{\partial F}{\partial \Omega_k} \frac{\partial \Omega_k}{\partial s} ds}_{T^2} + \underbrace{\sum_{k=1}^{3N} \sum_{i,j=1}^3 \frac{\partial F}{\partial \Omega_k} \frac{\partial \Omega_k}{\partial \sigma_{ij}^{net}} d\sigma_{ij}^{net}}_{T^3} \\
 & + \underbrace{\sum_{k=1}^{3N} \frac{\partial F}{\partial \Omega_k} \frac{\partial \Omega_k}{\partial p_0^*} dp_0^*}_{T^4}
 \end{aligned} \tag{16}$$

187 In Eq. (16), the term T^1 represents the change of S_e induced by a suction increment with the assumption of a
 188 constant microstructure during the SWCC test; the term T^2 describes the change of S_e due to the suction-induced
 189 microstructural variation; the terms T^3 and T^4 are the infinitesimal change of S_e resulting from the change in
 190 current stress state and the loading history of the soil, respectively.

191 Let us consider a soil sample subjected to mechanical loading at a constant suction level, Eq. (16) degrades to

$$dS_e = \underbrace{\sum_{k=1}^{3N} \sum_{i,j=1}^3 \frac{\partial F}{\partial \Omega_k} \frac{\partial \Omega_k}{\partial \sigma_{ij}^{net}} d\sigma_{ij}^{net}}_{T^3} + \underbrace{\sum_{k=1}^{3N} \frac{\partial F}{\partial \Omega_k} \frac{\partial \Omega_k}{\partial p_0^*} dp_0^*}_{T^4} \tag{17}$$

192 which quantitatively describes the “mechanical wetting” according to Tarantino [51]. Fig. 2a schematically
 193 demonstrates an infinitesimal increase of degree of saturation in a bimodal soil subjected to a mechanical loading.
 194 At a constant suction level s_0 , the upper integration bound r_0 in Eq. (2) is determined by Kelvin’s capillary law.
 195 Assuming that the mechanical loading leads to the horizontal shifting of the interaggregate sub-curve from state
 196 A to state B, the infinitesimal increase of the effective degree of saturation can be represented by the shadowed
 197 area, as shown in Fig. 2a.

198 Then, let us consider an unsaturated deformable soil subjected to a hydraulic loading (change of suction level)
 199 at a constant net stress state. Eq. (16) degrades to

$$dS_e = \underbrace{-\frac{C}{s^2} f\left(\Omega_k(p_0^*, s), \frac{C}{s}\right) ds}_{T^1} + \underbrace{\sum_{k=1}^{3N} \frac{\partial F}{\partial \Omega_k} \frac{\partial \Omega_k}{\partial s} ds}_{T^2} + \underbrace{\sum_{k=1}^{3N} \frac{\partial F}{\partial \Omega_k} \frac{\partial \Omega_k}{\partial p_0^*} dp_0^*}_{T^4} \tag{18}$$

200 Here, dp_0^* in term T^4 represents the suction-induced variation in pre-consolidation pressure [e.g., in the wetting –
 201 collapse process [49]]. For instance, experimental evidence for the irreversible pore structure variation occurring
 202 in the interaggregate porosity associated with wetting – collapse in a compacted loess has been recently reported
 203 by Ge et al. [52].

204 Since SWCCs are conventionally measured under zero or very small net stress (e.g., Pressure Plate, Tempe
 205 Pressure Cells and Chilled-Mirror Hygrometers [14,15]), it is reasonable to assume that the pre-consolidation
 206 pressure p_0^* is not affected by suction during SWCC tests (i.e., no wetting – collapse). Then, the term T^4 in Eq.
 207 (18) vanishes, and the change in effective degree of saturation induced by suction change in a deformable soil
 208 during SWCC tests gives

$$dS_e = \underbrace{-\frac{C}{s^2} f\left(\Omega_k(s), \frac{C}{s}\right) ds}_{T^1} + \underbrace{\sum_{k=1}^{3N} \frac{\partial F}{\partial \Omega_k} \frac{\partial \Omega_k}{\partial s} ds}_{T^2} \quad (19)$$

209 The closed form expression of Eq. (19) gives

$$S_e = \int_0^{C/s} f(\Omega_k(s), r) dr = F\left(\Omega_k(s), \frac{C}{s}\right) \quad (20)$$

210 Eq.(20) describes the SWCC derived from suction-dependent pore size distribution curves of a deformable soil.

211 As the effective degree of saturation increases during drying ($ds > 0; dS_e \leq 0$) and decreases during wetting

212 ($ds < 0; dS_e \geq 0$), following condition must be hold

$$-\frac{C}{s^2} f\left(\Omega_k(s), \frac{C}{s}\right) + \sum_{k=1}^{3N} \frac{\partial F}{\partial \Omega_k} \frac{\partial \Omega_k}{\partial s} \leq 0 \quad (21)$$

213 From Eq.(20), it is not hard to see that suction affects the degree of saturation twofold: on the one hand, suction

214 directly influences the pore size distribution function (see Fig. 2b, the horizontal shifting of the sub-curve); On the

215 other hand, suction changes the upper bound of the integration (see Fig. 2b, r_1 increases to r_2). In Fig. 2b, the

216 shadowed area represents the infinitesimal increase in the effective degree of saturation under the dual effect of

217 suction during wetting, which is defined as “hydraulic wetting” according to Tarantino [51].

218 For granular soils (e.g., sand and gravel), of which the pore structure remains unchanged, and hence the

219 microstructural parameter Ω is constant during SWCC tests, Eq. (19) degrades to

$$dS_e = \underbrace{-\frac{C}{s^2} f\left(\Omega_k, \frac{C}{s}\right) ds}_{T^1} \quad (22)$$

220 The increase in the effective degree of saturation during “hydraulic wetting” is solely attributed to the increase of

221 the upper integration bound (i.e., decrease in suction), as schematically shown in Fig. 2c.

222

223 **2.5. Determine water retention curve from pores size distribution data**

224 **2.5.1. PSD-surface in the $r - s - F(= S_e)$ space**

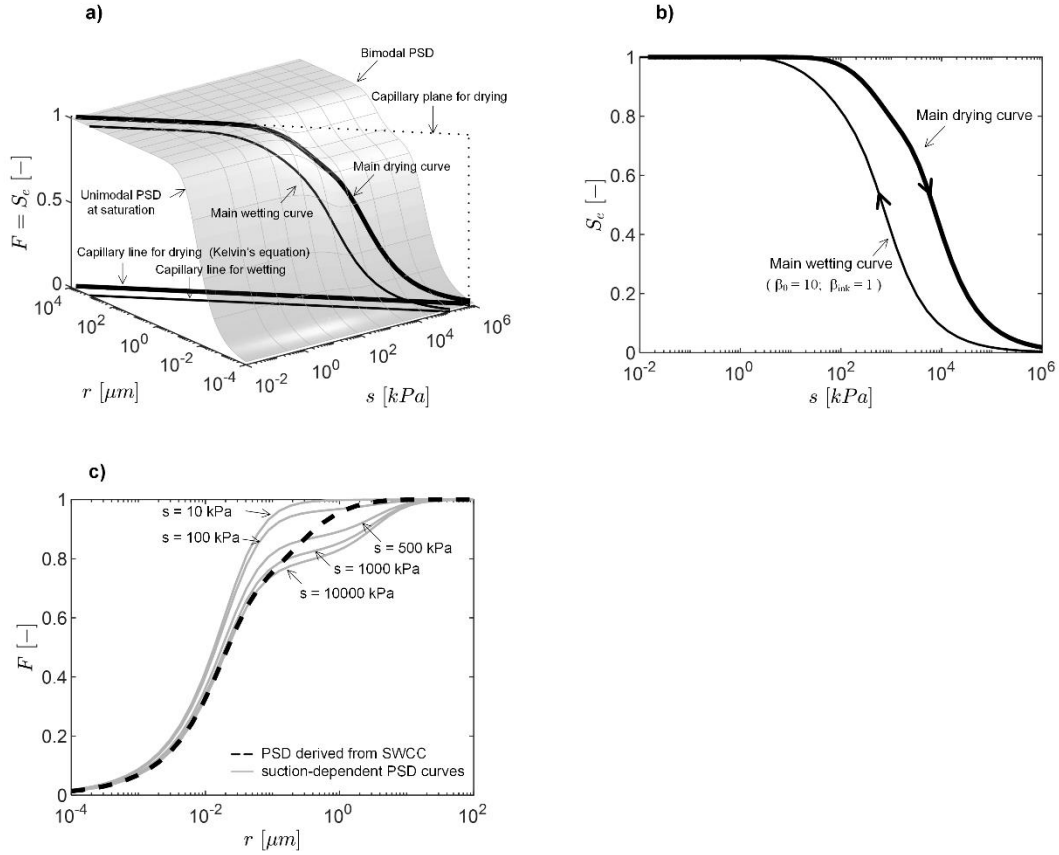


Fig. 3. (a) water retention curves and PSD curves on a unique surface in the $r - s - F(= S_e)$ space (b) water retention curves in the conventional $\log s - S_e$ plane (c) PSD curves in the $\log r - F$ plane

225 Based on the proposed framework (Eq. (20)), water retention behaviour of deformable soils can be directly derived
 226 from suction-dependent PSD curves associated with microstructural evolution during SWCC tests (i.e.,
 227 characterized by $\Omega_k(s)$). The main drying curve gives

$$S_e^d(s) = \int_0^{2T \cos \theta_d / s} f(\Omega_k(s), r) dr = F\left(\Omega_k(s), \frac{C_d}{s}\right) \quad (23)$$

228 Here, C_d is a constant equal to $2T \cos \theta_d$, θ_d is the contact angle between soil and water during drying ($\theta_d \approx 0^\circ$)
 229 and $\Omega_k(s)$ represents the suction-dependent microstructural parameter fulfilling the condition of Eq. (21).

230 For a better interpretation of Eq. (23), the transformation from PSD measurements to SWCC for deformable
 231 soils is visualised in the $r - s - F(= S_e)$ space (see Fig. 3a). The PSD-surface consisting of the cumulative PSD
 232 curves at different suction levels is expressed as:

$$S_e^d(r, s) = F(\Omega_k(s), r) \quad (24)$$

233 Comparing Eq. (23) and (24), the main drying curve can be equivalently expressed by

$$S_e^d(s) = F(\Omega_k(s), r)|_{r=C_d/s} \quad (25)$$

234 Eq. (25) indicates that the main drying curve can be visualized as the cross-section between the PSD-surface and
 235 the capillary plane (i.e., $r = C_d/s$) in the $r - s - F(= S_e)$ space (see Fig. 3a).

236 Fig. 3a shows an example of a PSD-surface (adopted entries in Ω : $m_1 = 0.47$; $m_2 = 0.41$; $r_1^f = 5.0 \mu m$;
 237 $r_2^f = 0.03 \mu m$; $R_1 = 0.22 \times [1 - \exp(-0.002s)]$; $R_2 = 1 - R_1$). As can be seen, the soil pore structure is
 238 unimodal at saturation state and exhibits a distinguished bimodal characteristic at the high suction range. On the
 239 one hand, we obtain the main drying curve by projecting the cross-section between the PSD-surface and the
 240 capillary plane (the bold solid curve in Fig. 3a) on the conventional $\log s - S_e$ plane (see Fig. 3b). It is noted that
 241 the derived main drying curve is almost unimodal. Thus, an apparent “unimodal” SWCC of a deformable soil,
 242 which is “inferred” by naked eye based on the experimental data, is not representative of a unimodal pore size
 243 distribution. On the other hand, projecting the cross section on the $\log r - F$ plane yields the cumulative pore size
 244 distribution curve derived from SWCC (the bold dashed curve in in Fig. 3c), which differs from the true PSD curve
 245 at any suction level, as shown in Fig. 3c. In the past decades, a constant PSD curve derived from SWCC data has
 246 been incorporated into permeability models for unsaturated soils [1,9,53]. The phenomenon observed from the
 247 example in Fig. 3 may explain the discrepancy between the measured and predicted unsaturated permeability at a
 248 certain suction level of deformable soils.

249 2.5.2. Hysteresis effect

250 According to Eq. (20), the microstructural evolution is solely dominated by suction, irrespective of wetting or
 251 drying. This means that a reversible microstructural behaviour during the SWCC tests and hence a unique PSD-
 252 surface for wetting and drying is assumed in the proposed approach. Then, the “hysteresis effect” of SWCC can
 253 be attributed to different contact angles during wetting and drying. The main wetting curve is visualized as the
 254 cross section between the PSD-surface and the capillary plane for wetting, which is shown in Fig. 3a. A
 255 conventional main wetting curve is obtained by projecting the cross section on the $\log s - S_e$ plane (see Fig. 3b).

256 Another factor causes the hysteresis is the “ink bottle” effect [15,14,54], which means that a part of pore air is
 257 entrapped in soil during wetting, resulting in a partial saturation even at zero suction.

258 Considering the change of contact angel and the “ink bottle” effect, the main wetting curve can be expressed
 259 as

$$260 S_e^w = \beta_{ink} \int_0^{2T \cos \theta_w / s} f(\Omega_k(s), r) dr = \beta_{ink} F\left(\Omega_k(s), \frac{\beta_\theta C_d}{s}\right) \quad (26)$$

261 Here, β_θ and β_{ink} are two additional parameters to describe the hysteresis effect, and the parameter β_θ is defined
 as

$$262 \beta_\theta = \frac{\cos \theta_d}{\cos \theta_w} \geq 1 \quad (27)$$

263 where θ_w is the contact angle between soil and water during wetting. The parameter β_{ink} ($0 < \beta_{ink} \leq 1$) is a
 264 scaling factor to take into account the ink bottle effect, which can be approximated by the value of the effective
 265 degree of saturation at zero suction of a wetting curve. An example of a main wetting curve with $\beta_\theta = 10$ and β_{ink}
 266 $= 1$ is schematically shown in Fig. 3a (visualised in the $r - s - F(= S_e)$ space) and 3b (in the conventional $\log s$
 $- S_e$ plane).

267 2.5.3. Adsorptive water and the complete water retention model

268 The water retained in an unsaturated soil consists of two components: the capillary and adsorptive water [55]. The
 269 capillary water dominated by soil pore size distribution has been described by Eq.(20). The adsorptive water,

270 governed by soil specific surface and mineralogy, is tightly bonded on the soil particle surface as a thin film by
 271 attractive forces (i.e., van der Waals forces and hydrogen bonds) between the soil particles and pore water. Revil
 272 and Lu [56] pointed out that the volume of adsorptive water decreases with decreasing concentration of the water
 273 vapor. However, for the aim of simplicity, adsorptive water volume is assumed as a constant (defined as the
 274 residual degree of saturation S_r^{res}) in this study. Then, the effective degree of saturation S_e can be expressed as

$$S_e = \frac{S_r - S_r^{res}}{1 - S_r^{res}}. \quad (28)$$

275 Considering the residual state of the soil (i.e., $S_r \rightarrow S_r^{res}$ as $s \rightarrow +\infty$) and assuming an identical residual water
 276 content for wetting and drying, a complete water retention model in terms of degree of saturation gives:

$$S_r(s) = \begin{cases} (1 - S_r^{res})F\left(\Omega_k(s), \frac{C_d}{s}\right) + S_r^{res}, & \text{for drying} \\ (1 - S_r^{res})\beta_{ink}F\left(\Omega_k(s), \frac{\beta_\theta C_d}{s}\right) + S_r^{res}, & \text{for wetting} \end{cases} \quad (29)$$

277

278 2.5.4. Gravity water content

279 For the SWCC in terms of gravity water content w , both pore structure state variables, i.e., void ratio e and the
 280 microstructural variable Ω , must be taken into account. Denoting the suction-dependent void ratio in the drying
 281 and wetting process as $e_d(s)$ and $e_w(s)$, respectively, the $w - s$ curve yields

$$w(s) = \begin{cases} \frac{e_d(s)}{G_s} \left[(1 - S_r^{res})F\left(\Omega_k(s), \frac{C_d}{s}\right) + S_r^{res} \right], & \text{for drying} \\ \frac{e_w(s)}{G_s} \left[(1 - S_r^{res})\beta_{ink}F\left(\Omega_k(s), \frac{\beta_\theta C_d}{s}\right) + S_r^{res} \right], & \text{for wetting} \end{cases} \quad (30)$$

282 Eq. (30) describes the general relationship between the gravity water content and soil suction based on a complete
 283 picture of pore structure evolution during water retention curve tests. Soil suction dominates not only the overall
 284 void volume $e_d(s)$ and $e_w(s)$, but also the microstructure $\Omega_k(s)$.

285

286 **3. Applications**

287 In this section, the proposed model is validated by predicting water retention curves based on PSD data for different
 288 types of soils. For the aim of simplicity, the residual water content is assumed to be zero (i.e., $S_r^{res} = 0$). It is found
 289 that the simplification does not significantly influence the prediction accuracy for the presented applications. In
 290 general, 3N suction-dependent entries in the microstructural parameter Ω are required, which may lead to difficulty
 291 in the practical applications. Nevertheless, it will be shown that one or two suction-dependent entries are adequate
 292 to describe the microstructural evolution during SWCC tests and predict the water retention curve accurately in
 293 the presented applications.

294 **3.1. Silty Sand**

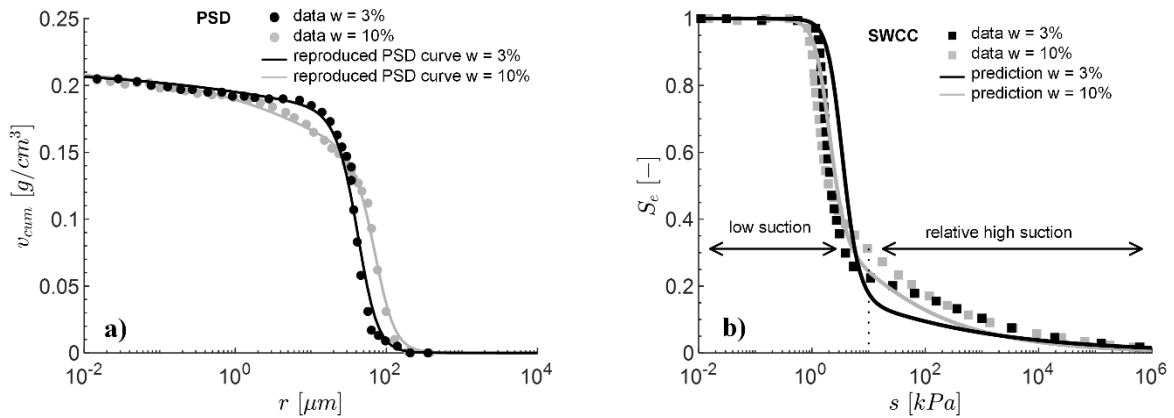


Fig. 4. (a) measured and reproduced cumulative pore size distribution curves (b) measured and predicted main drying curves of a silty sand (data from [57])

295 Angerer [57] prepared two statically compacted low plasticity silty sand (90.5% sand + 8.5% silt + 1% Clay, e_{min}
 296 = 0.47, $e_{max} = 0.76$, $G_s = 2.68$) samples at the same relative density ($I_d = 0.69$) with different initial water contents
 297 ($w = 3\%$ and 10%). The cumulative pore size distribution curves of both samples were measured by MIP tests at
 298 the as-compacted state (see Fig. 4a). Afterwards, the samples were saturated and then desiccated from the
 299 saturation state to measure the main drying curves, as presented in Fig. 4b.

300 For granular soils, the rigid pore structure (including the void ratio and the microstructure) remains unchanged
 301 during the SWCC tests. All the entries in the microstructural parameter Ω are constants. Considering the distinct
 302 bimodality of the pore structure (aggregates formed by the fine contents during compaction), the multimodal PSD
 303 expression [Eq. (8)] with $N = 2$ is substituted into Eq. (23) to predict the main drying curve. The parameters of the
 304 PSD model for each sample are calibrated based on their PSD data (mercury intrusion curves in Fig. 4a), which
 305 are shown in Table 1. A convenient parameter calibration procedure for the proposed multimodal PSD model [Eq.
 306 (8)] has been described in detail by Yan and Cudmani [35].

307 In Fig. 4b, the predicted SWCCs show a good agreement with the SWCC measurements. In the low suction
 308 range (i.e., $s < 10$ kPa), capillary water is almost completely desiccated from interaggregate pores in a narrow
 309 suction range. In addition, an identical air entry suction (about 1 kPa) of both samples is accurately predicted. In
 310 the relatively high suction range (i.e., $10 \text{ kPa} < s < 1 \times 10^6$ kPa), the predicted main drying curves are slightly
 311 underneath the measurements, which might be attributed to the changes in the intraaggregate pores, although the
 312 fine content (= 9.5%) of the silty sand is low.

Reference	Soil/Sample	Microstructural state parameter Ω							Hysteresis	
		R_1 [-]	r_1^f [μm]	m_1 [-]	R_2 [-]	r_2^f [μm]	m_2 [-]	suction dependent entries in Ω	β_θ [-]	β_{ink} [-]
Angerer [57]	Silty Sand ($w = 3\%$)	0.85	47	0.71	0.15	14	0.17	-	-	-
	Silty Sand ($w = 10\%$)	0.70	79	0.71	0.30	24	0.23	-	-	-
Cai et al. [31]	lateritic soil CS1.3	-	-	0.60	-	0.014	0.50	$R_2 = 0.85/e_d$ $R_1 = 1 - R_2$ $r_1^f = 4.1 \times [1 - \exp(-0.015s)]$	1.1	0.80
	lateritic soil CS1.5	-	-	0.60	-	0.014	0.50	$R_2 = 0.85/e_d$ $R_1 = 1 - R_2$ $r_1^f = 8.0 \times [1 - \exp(-0.005s)]$	1.1	0.80
	lateritic soil CS1.7	-	-	0.60	-	0.014	0.50	$R_2 = 0.85/e_d$ $R_1 = 1 - R_2$ $r_1^f = 10.5 \times [1 - \exp(-0.004s)]$	1.1	0.80
Cuisinier and Laloui [58]	Sandy loam	0.25	20.7	0.60	0.75	-	0.33	$r_2^f = 1.16 + 2.1 \exp(-0.008s)$	-	-
Monroy et al. [30]	London Clay	-	19.0	0.78	-	-	0.23	$R_2 = 0.11 + 0.053 \log s$ $R_1 = 1 - R_2$ $r_2^f = \frac{1}{0.5 + 5 \times [1 - \exp(-0.009s)]}$		

313 Table 1: parameters of the proposed model for different types of soils

314 3.2. Lateritic soil

315 Cai et al. [31] conducted a comprehensive investigation on the water retention behaviour of the statically
316 compacted Guilin lateritic soil ($w_L = 67.3\%$, $w_p = 38.1\%$, $G_s = 2.74$) for a wide suction range from 0 to 287.6 MPa,
317 including the main drying and wetting curves as well as the associated volumetric deformation and microstructural
318 evolution. The pore size distribution curves at five suction levels (50, 200 and 71120 kPa from drying, 100 and
319 21820 kPa from wetting) were detected by MIP tests. The series of experiments were performed on the samples
320 with different initial void ratios, 1.3, 1.5 and 1.7 (denoted with CS 1.3, CS1.5 and CS1.7, respectively).

321 In this section, the proposed model is validated by predicting the water retention curves in terms of degree of
322 saturation and gravity water content for the sample CS1.5, by which the volumetric deformation (characterized by
323 void ratio e) and microstructural evolution (characterized by the microstructural variable Ω) during the SWCC
324 tests are taken into account. The model validation for the samples CS1.3 and CS1.7 will be shown in Appendix.

325

326 **3.2.1. Volumetric deformation**

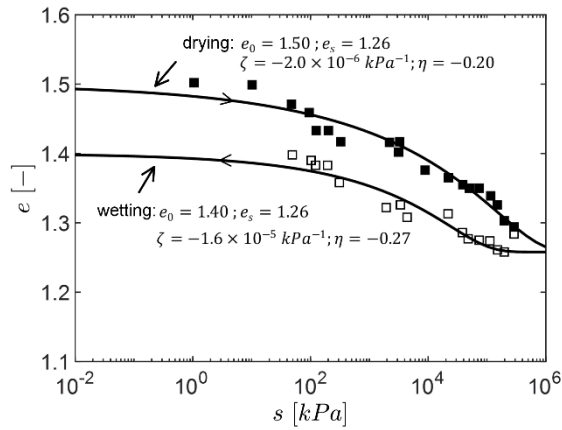


Fig. 5. volumetric deformation of the sample CS1.5 during drying and wetting (data from Cai et al. [31])

327 Fig. 5 demonstrates the volumetric deformation of the sample CS1.5 during the SWCC test. The soil was first
 328 desiccated from a saturated state to a high suction level of 287.6 MPa, and then wetted to a low suction level of 50
 329 kPa. In general, the suction induced volume change can be described in a differential equation [49,59] or
 330 continuous closed-form expression [60-62]. In this study, following continuous curvilinear equation is proposed
 331 to simulate the volumetric deformation during the SWCC test:

$$e(s) = e_0 - \frac{e_0 - e_s}{[1 - \exp(\zeta s)]^\eta} \quad (31)$$

332 Here, e_s and e_0 represent the void ratio at the shrinkage limit and saturation state, respectively; $\zeta < 0$ and $\eta < 0$
 333 are two fitting parameters determining the shape and curvature of the shrinkage and swelling curves.

334 For the CS1.5 sample, the parameter e_0 is approximated by the maximum void ratio of the measured $e - s$
 335 curve ($e_0 = 1.50$ for drying and $e_0 = 1.40$ for wetting). A common e_s for both shrinkage and swelling curve is
 336 approximated by the minimum void ratio at the highest suction level of 287.6 MPa (i.e., $e_s = 1.26$, see Fig. 5).
 337 The reproduced $e - s$ curves for drying and wetting are demonstrated in Fig. 5, which match well with the
 338 measurements.

339

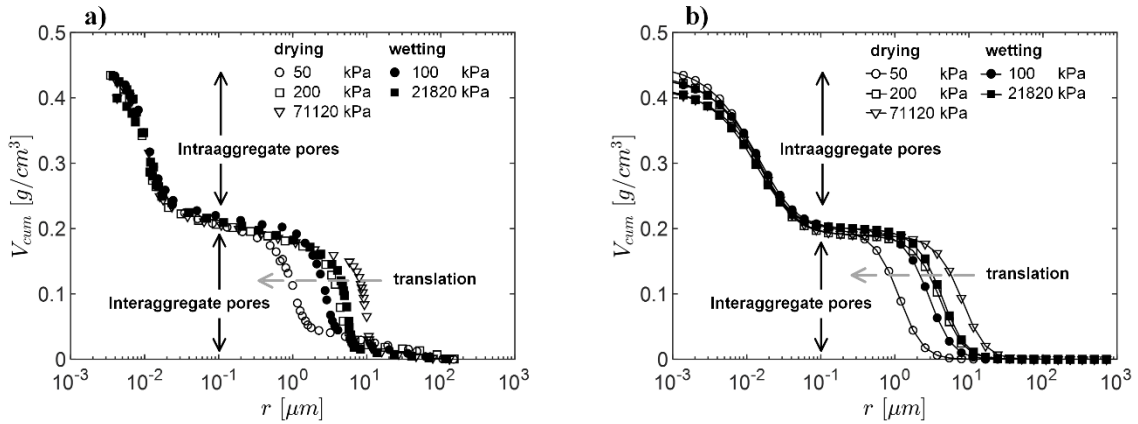


Fig. 6. Compacted Guilin lateritic soil (a) measured mercury intrusion curves (b) parameterized mercury intrusion curves by Eq. (10) with $N = 2$ (data from Cai et al. [31])

341

Reference/soil	Suction/ e_{MIP}	r_1^f	m_1	R_1	r_2^f	m_2	R_2
		$[\mu\text{m}]$	$[-]$	$[-]$	$[\mu\text{m}]$	$[-]$	$[-]$
Cai et al. [31] / lateritic soil	50 kPa / 1.24	1.35	0.67	0.44	0.02	0.50	0.56
	100 kPa / 1.19	3.42	0.67	0.46	0.02	0.50	0.54
	200 kPa / 1.20	4.86	0.67	0.43	0.02	0.50	0.57
	21820 kPa / 1.15	5.11	0.67	0.48	0.02	0.50	0.52
	71120 kPa / 1.14	9.60	0.67	0.46	0.02	0.50	0.54

342 Table 2: parameters of the bimodal PSD model (Eq. (10) with $N = 2$)

343 Fig. 6a presents the cumulative PSD curves during drying and wetting attained by numerical integration of pore
 344 size density data published in Cai et al. [31], which show distinct bimodal characteristic. Therefore, a bimodal
 345 expression (Eq. (10) with $N = 2$) is adopted to parameterize the pore structure. The model parameters for the
 346 mercury intrusion curve at each suction level as well as the total intrusion volume e_{MIP} are listed in Table 2. The
 347 reproduced cumulative pore size distribution curves are demonstrated in Fig. 6b, which are in good agreement
 348 with the PSD measurements.

349 As mentioned in section 2.3, the microstructural behaviour of the compacted lateritic soil might be understood
 350 as the “rearrangement of aggregates”: the intraaggregate pores remain essentially unchanged, while the
 351 interaggregate pores increase with increasing suction (e.g., formation of fissures in soil). This essential feature in
 352 the microstructural behaviour is characterized by the variation of the entries in the microstructural parameter Ω .
 353 As shown in Table 2, the constant parameters r_2^f and m_2 imply the constant intraaggregate porosity, and the
 354 increasing parameter r_1^f indicates the increase of maximum and mean pore size in interaggregate region, leading
 355 to a horizontal translation of the interaggregate sub-curve (see Fig. 6a). Moreover, one sees that the translation of
 356 interaggregate sub curve solely depends on suction, irrespective of drying or wetting process, which supports the
 357 assumption of the reversible microstructural behaviour during the SWCC tests (i.e., a unique PSD-surface for
 358 wetting and drying).

359

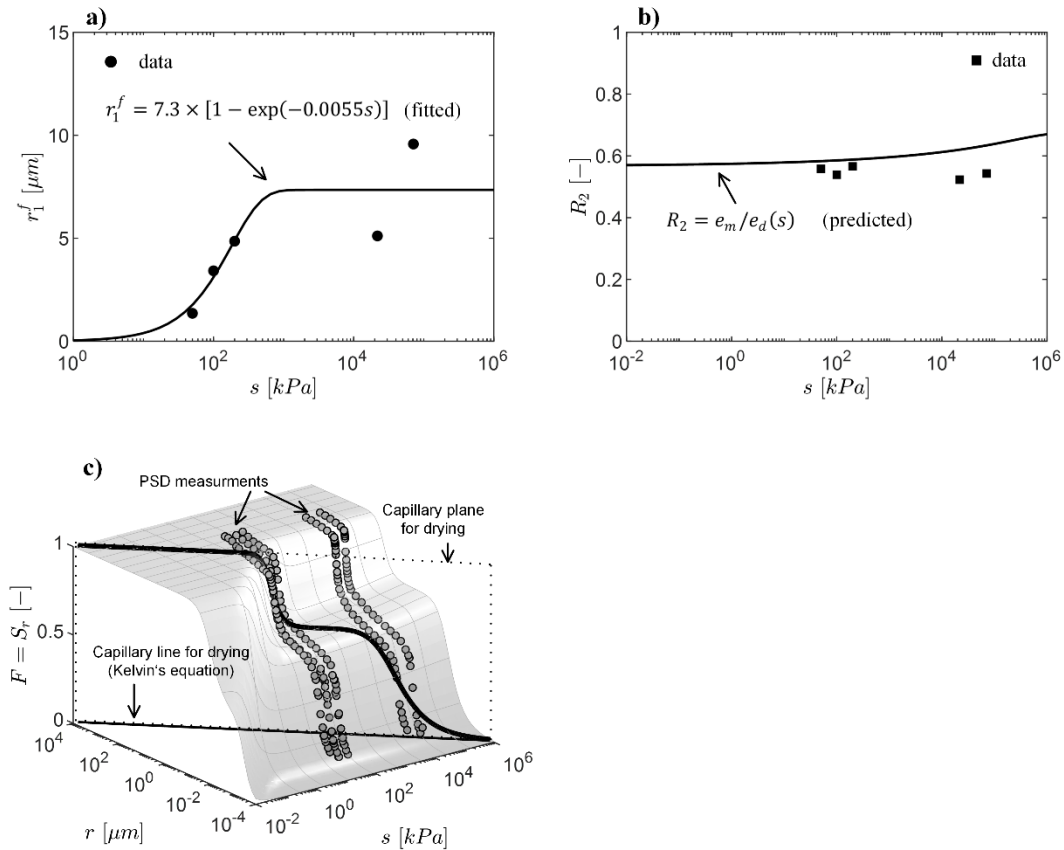


Fig. 7. (a) evolution of the reference pore radius r_1^f in interaggregate porosity (b) evolution of the interaggregate volumetric fraction R_1 (c) the unique PSD-surface in the $r - s - F(= S_e)$ space (data from Cai et al. [31])

361 To determine the PSD-surface of the sample CS1.5, suction-dependent microstructural parameter Ω is attained
 362 based on the analysis of the parameters listed in Table 2. Three parameters r_1^f , R_1 and R_2 vary with suction. Fig.
 363 7a shows the nonlinear fitting equation characterizing the evolution of r_1^f with suction, for which a plateau of r_1^f
 364 is assumed at the high suction range. Since the intraaggregate porosity remains unchanged, the volumetric fraction
 365 R_2 equals the ratio of the intraaggregate pore volume e_m to the overall pore volume $e_d(s)$. The constant value of
 366 e_m can be calculated from the MIP test data, which corresponds to the area under the intraaggregate pore size
 367 density curve (see Fig. 1b). A value of 0.85 is approximated for e_m . Fig. 7b shows the predicted evolution of R_2 ,
 368 which appears slightly higher than the data points. Nevertheless, such an estimation is proved to be adequate to
 369 predict the SWCC accurately, which will be shown in the subsequent sections. Eventually, the interaggregate
 370 volumetric fraction R_1 is solved from Eq. (5) with known R_2 . The constant and suction-dependent entries in Ω for
 371 the CS1.5 sample are listed in Table 1.

372 Fig. 7c demonstrates the PSD-surface in the $r - s - F(= S_e)$ space. The model predicts a quasi-unimodal pore
 373 structure at the saturation state. With increasing suction, the interaggregate pore size progressively increases until
 374 a stable bimodal pore structure is formed at the high suction range. The main drying curve is predicted by
 375 substituting the $\Omega(s)$ in Eq. (23) and visualized as the cross-section of the PSD surface and the capillary plane for
 376 drying in the $r - s - F(= S_e)$ space (see Fig. 7c).

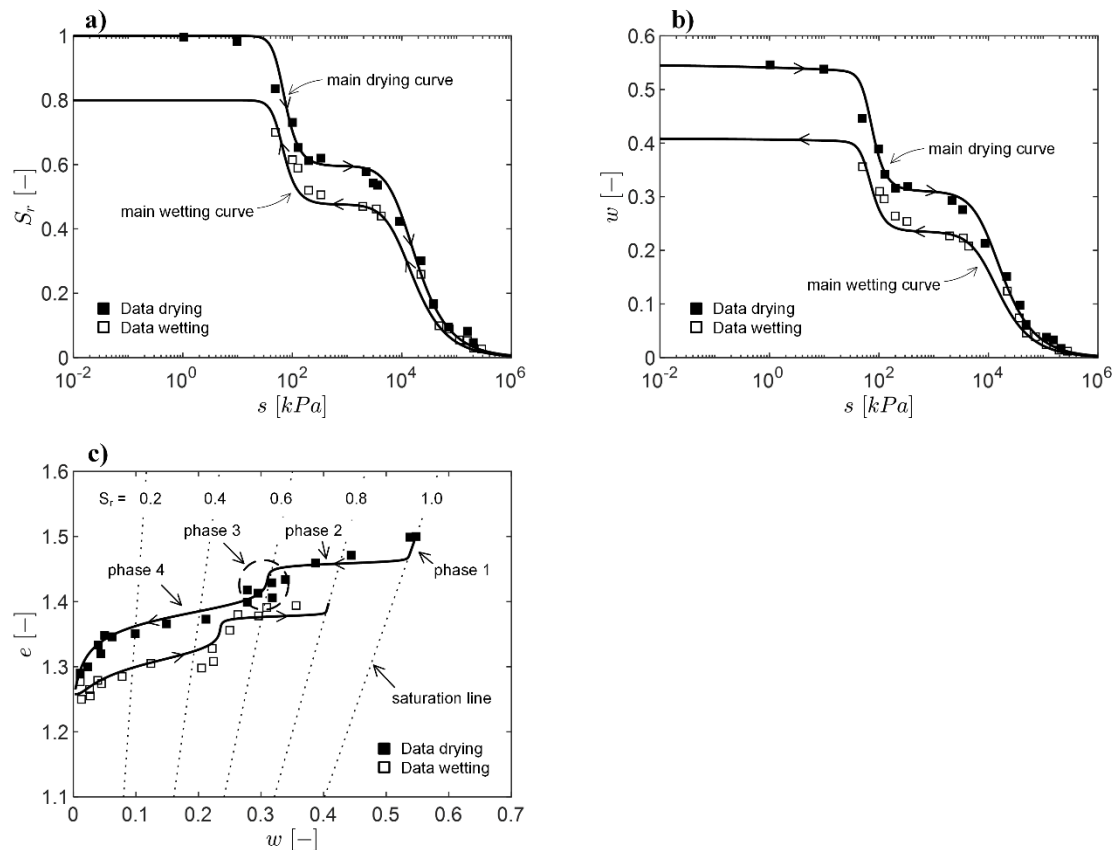


Fig. 8. Sample CS1.5 of compacted Guilin lateritic soil (a) measured and predicted water retention curves in terms of degree of saturation b) measured and predicted water retention curves in terms of gravity water content c) measured and predicted shrinkage and swelling curves (data from Cai et al. [31])

378 Assuming a reversible microstructural behaviour during wetting and drying, Eq. (29) predicts water retention
 379 curves in the conventional $\log s - S_r$ plane (see Fig. 8a), showing a strong consistency with the measurements and
 380 a distinguishing bimodal characteristic. For the main wetting curve, the hysteresis parameters ($\beta_\theta = 1.1$ and
 381 $\beta_{ink} = 0.8$) are approximated based on the experimental data.

382 The water retention curves in terms of gravity water content are attained by substituting $\Omega(s)$, the shrinkage
 383 curve $e_d(s)$ and the swelling curve $e_w(s)$ in Eq. (30), as shown in Fig. 8b. It is noted that the model predicts an
 384 inclined line at the beginning of desiccation, which coincides with the findings of previous studies (e.g., Pasha et
 385 al. [63], Wijaya and Leong [64]). At the suction level lower than the air entry suction, the soil retains saturated,
 386 whilst the increase in the effective stress (due to the increasing suction and Bishop's effective stress parameter is
 387 equal to one [65]) causes the reduction of the overall volume. The pore water is hence compressed out from the
 388 soil in the very beginning of the desiccation process.

389 The predicted shrinkage and swelling curves in the conventional $w - e$ plane are illustrated in Fig. 8c. It is
 390 interesting to note that the curves show “double S-shape” characterization, resulting from the bimodal pore
 391 structure of the soil. The proposed model captures this essential feature and indicates four phases of the desiccation:
 392 Phase 1. Water is drained at the saturation state as suction lower than air entry suction (the part along the saturation
 393 line); Phase 2. As the air entry suction is surpassed, the soil water is rapidly drained from macro pores with slight
 394 reduction in volume; Phase 3. The macro pores are almost fully drained, and the micro porosity remains saturated
 395 (the air entry suction of aggregates has not been reached). The overall soil volume is further reduced due to the

396 increase in the effective stress. Thus, we observe an apparent “collapse” phenomenon in the $w - e$ plane at this
397 transition stage (i.e., a remarkable reduction in void ratio while water content is almost unchanged); Phase 4. When
398 the subjected suction surpasses the air entry suction of aggregates, the water retained in the intraaggregate porosity
399 is drained associated with a dramatic volume reduction. Similarly, the swelling curve also shows the “double S-
400 shape” characteristic along a wetting path.

401 It is worth to point out that most existing shrinkage curve models are unable to describe the complex “double
402 S-shape” $w - e$ curves for bimodal soils. Recently, Leong and Wijaya [66] advanced an expression to reproduce
403 different types of shrinkage curves. However, in contrast to the proposed model in this study, the empirical
404 expression of Leong and Wijaya [66] is in a complex mathematical form and involves a large number of fitting
405 parameters without a clear physical meaning.

406 For the samples compacted to different initial densities CS 1.3 and CS 1.7, the predicted the water retention
407 curves as well as the shrinkage and swelling curves are demonstrated in Appendix. The adopted parameters and
408 the suction dependent entries in Ω are listed in Table 1. A good agreement between the predictions and the
409 measurements can be observed.

410

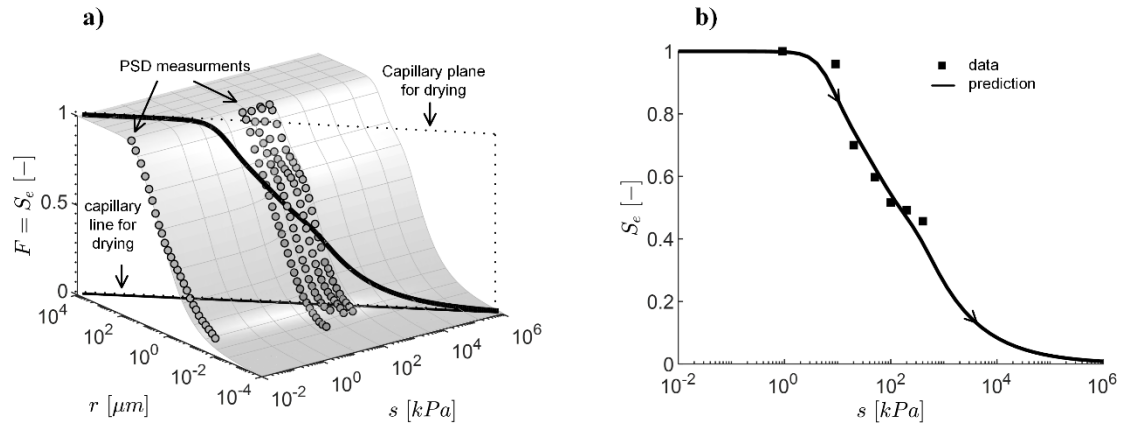


Fig. 9. (a) the PSD surface of a sandy loam in the $r - s - S_e$ space (b) measured and predicted main drying curve (data from Cuisinier and Laloui [58])

412 Cuisinier and Laloui [58] investigated the pore structure evolution of a sandy loam ($w_L = 30\%$, $w_p = 18\%$, $G_s =$
 413 2.66) along a drying path. The pore structure at different suction levels ($s = 0, 50, 100, 200$ and 400 kPa) were
 414 detected by MIP tests. Again, the cumulative PSD curves (attained by numerical integration of pore size density
 415 data from Cuisinier and Laloui [58]) are simulated by the proposed multimodal PSD model with $N = 2$ (bimodal
 416 microstructure). It is found that solely the parameter r_2^f decreases with increasing suction, implying the contraction
 417 of aggregates along the drying path. The constant entries and the suction-dependent r_2^f in the microstructural
 418 parameter Ω are given in Table 1. Fig. 9a shows the PSD-surface of the soil characterized by Ω in the $r - s -$
 419 $F(= S_e)$ space (The PSD data at zero suction is plotted on the plane of $s = 10^{-2}$ kPa).

420 The main drying curve is visualized as the cross section of the PSD-surface and the capillary plane for drying.
 421 In Fig. 9b, the predicted main drying curve is compared with the SWCC measurement in the $\log s - S_e$ plane. The
 422 SWCC data in terms of effective degree of saturation S_e is approximated from a set of gravimetric water content
 423 based SWCC data by assuming $S_e = (w_{sat} - w)/(w_{sat} - w_{res})$, as the volumetric deformation during the SWCC
 424 test is not given in Cuisinier and Laloui [58]. Here, $w_{sat} (= 0.37)$ and $w_{res} (= 0)$ represents the gravity water
 425 content at saturation and residual state, respectively. As can be seen, the prediction shows strong consistency with
 426 the measurement. The air entry suction is precisely predicted, and a slight bimodality of the main drying curve is
 427 also replicated by the proposed model.

428

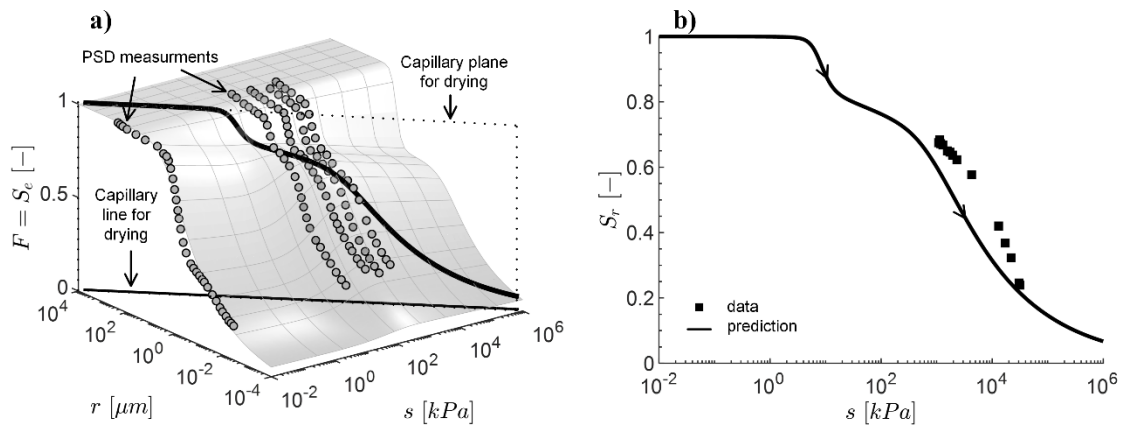


Fig. 10. Compacted London Clay (a) the PSD-surfaces in the $r - s - F(= S_e)$ space (b) measured and predicted main drying curve (data from Monroy [67] and Monroy et al. [30])

430 Monroy et al. [30] investigated the microstructural evolution of compacted London Clay ($w_L = 83\%$, $w_p = 29\%$,
 431 $G_s = 2.70$) along a wetting path. The pore size distribution curves at different suction levels ($s = 0, 40, 150, 470$
 432 and 996 kPa) were measured by MIP tests, as demonstrated in Fig. 10a (The PSD data at zero suction is plotted
 433 on the plane of $s = 10^{-2}$ kPa). As mentioned in section 2.3, the microstructural behaviour of the compacted London
 434 Clay might be understood as the “swelling of aggregates”, leading to the increase of the parameter r_2^f and the
 435 intraaggregate volumetric fraction R_2 . The constant entries and the suction-dependent r_2^f and R_2 in the
 436 microstructural parameter Ω are given in in Table 1, and the corresponding PSD-surface is illustrated in Fig. 10a.
 437 We see that the interaggregate porosity contracts during the wetting path and vanishes at the saturation state, which
 438 means that the modality number N decreases from two to one (bimodal pore structure to unimodal pore structure).

439 The main drying curve is acquired by the cross section of the PSD-surface and the capillary plane for drying
 440 (see Fig. 10a). The model predicts a distinct bimodal main drying curve and a relative low air entry suction (ca. 5
 441 kPa), which might be attributed to the formation of the clay aggregates at low suction level (see the distinct bimodal
 442 PSD at $s = 40$ kPa). The predicted main drying curve is compared with the SWCC data published in Monroy [67]
 443 for the compacted London Clay in the $\log s - S_r$ plane, as shown in Fig. 10b. The predicted water content is
 444 slightly lower than the measurements. Nevertheless, the quality of the prediction is regarded as sufficient, as it is
 445 directly derived from the PSD measurements during wetting.

447 **4. Discussion – inter- and intraaggregate air entry suction**

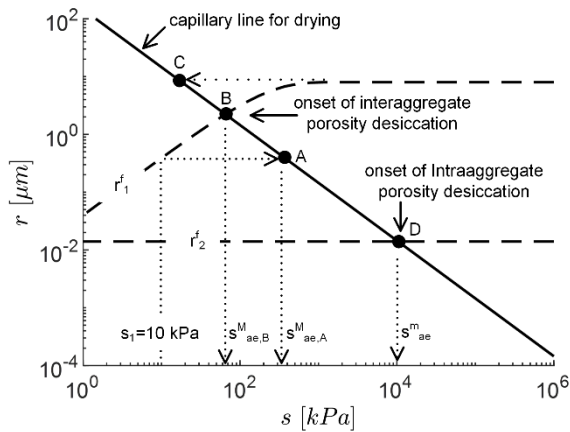


Fig. 11. interpretation of the onset of inter- and intraaggregate-porosity desiccation

448 The proposed framework offers new understanding of the air entry suction (s_{ae}) for deformable soils. Fig. 11
 449 demonstrates the evolving inter- and intraaggregate reference pore radius (r_1^f and r_2^f) of Guilin lateritic soil (see
 450 section 3.2) in $r - s$ plane and interprets the different types of the desiccation onset of inter- and intraaggregate
 451 porosity. At low suction level (e.g., $s_1 = 10$ kPa in Fig. 11), the imposed suction s_1 is much lower than the
 452 interaggregate air entry suction ($s_{ae,A}^M$) governed by the current r_1^f via Kelvin's equation (Eq. (1)), and the soil
 453 remains saturated. As suction increases, the rearrangement of aggregates leads to the increase of r_1^f and hence the
 454 reduction of interaggregate air entry suction. When the equilibrium point (point B, imposed suction equals
 455 interaggregate air entry suction) is reached, one observes the onset of the interaggregate porosity desiccation.
 456 Afterwards, the interaggregate pores further increases with suction until a stable r_1^f is reached (point C). That
 457 means, the "air entry suction" is in fact a variable dominated by the varying interaggregate porosity along the path
 458 A – B – C, and the "air entry suction" conventionally determined from a SWCC is the suction value at the
 459 equilibrium point B. In addition, the intraaggregate reference pore radius r_2^f of Guilin lateritic soil remains
 460 unchanged, resulting in a constant intraaggregate "air entry suction" s_{ae}^m (point D).

461

462 **5. Conclusion**

463 A novel framework is advanced to predict the water retention curve directly from the pore size distribution data
464 for deformable soils. The change of soil pore structure consists of two individual aspects: the volumetric
465 deformation characterized by the void ratio e and the microstructural evolution characterized by the parameter Ω ,
466 which is stress-, loading history- and suction-dependent. “Hydraulic” and “mechanical” wetting of deformable
467 soils can be quantitatively interpreted under the proposed framework.

468 The relationship between the microstructural evolution and the water retention behaviour is interpreted by a
469 unique PSD-surface in the $r - s - F(= S_e)$ space. A reversible microstructural behaviour is assumed during
470 drying and wetting. The main drying and wetting curves are visualized as the cross-sections of the capillary planes
471 (i.e., Kelvin’s equation) and the PSD-surface. The closed-form SWCC expression obtained directly from PSD
472 measurements can be further incorporated into other unsaturated soil property formulations (e.g., unsaturated
473 hydraulic conductivity and effective stress parameter) and facilitate the implementation of the model in particle
474 applications. The model validation relies on the water retention data of four different types of soils, including silty
475 sand, lateritic soil, sandy loam and clay. The predicted water retention curves, based on their PSD data at different
476 suction levels, show strong consistency with the measurements.

477 The proposed framework also provides new insights into the water retention behaviour and microstructural
478 evolution for deformable soils. Following conclusions are drawn: (I) Soil suction has threefold effects on the water
479 retention behaviour: it dominates the overall volume, the current pore size distribution and the maximum size of
480 the pores filled with water via capillary law. (II) The “pore size distribution” derived from a SWCC, which is
481 conventionally incorporated into unsaturated permeability models, differs from the actual pore structure governed
482 by the current suction state. (III) The air entry suction observed in the conventional SWCC test is dominated by
483 both microstructural evolution and the capillary law, which is not representative of a constant maximum pore
484 radius in the soil. (IV) The modality number of the water retention curve may differ from that of the pore size
485 distribution at a certain suction level. That means, a unimodal SWCC measurement does not ensure a unimodal
486 pore size distribution for deformable soils.

487

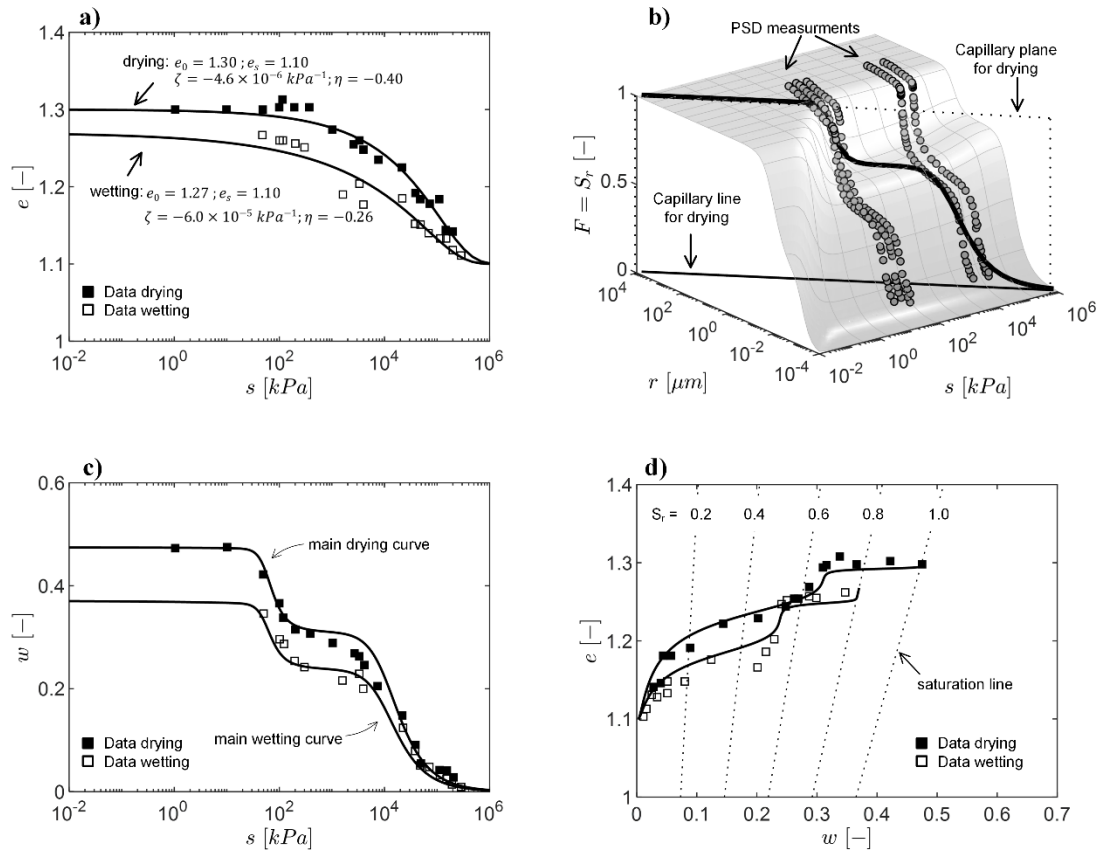


Fig. 12. Sample CS1.3 of compacted Guilin lateritic soil (a) volumetric evolution during the SWCC tests (b) PSD surface in the $r - s - F (= S_e)$ space (c) predicted water retention curves in terms of gravity water content (d) predicted shrinkage and swelling curves (data from Cai et al. [31])

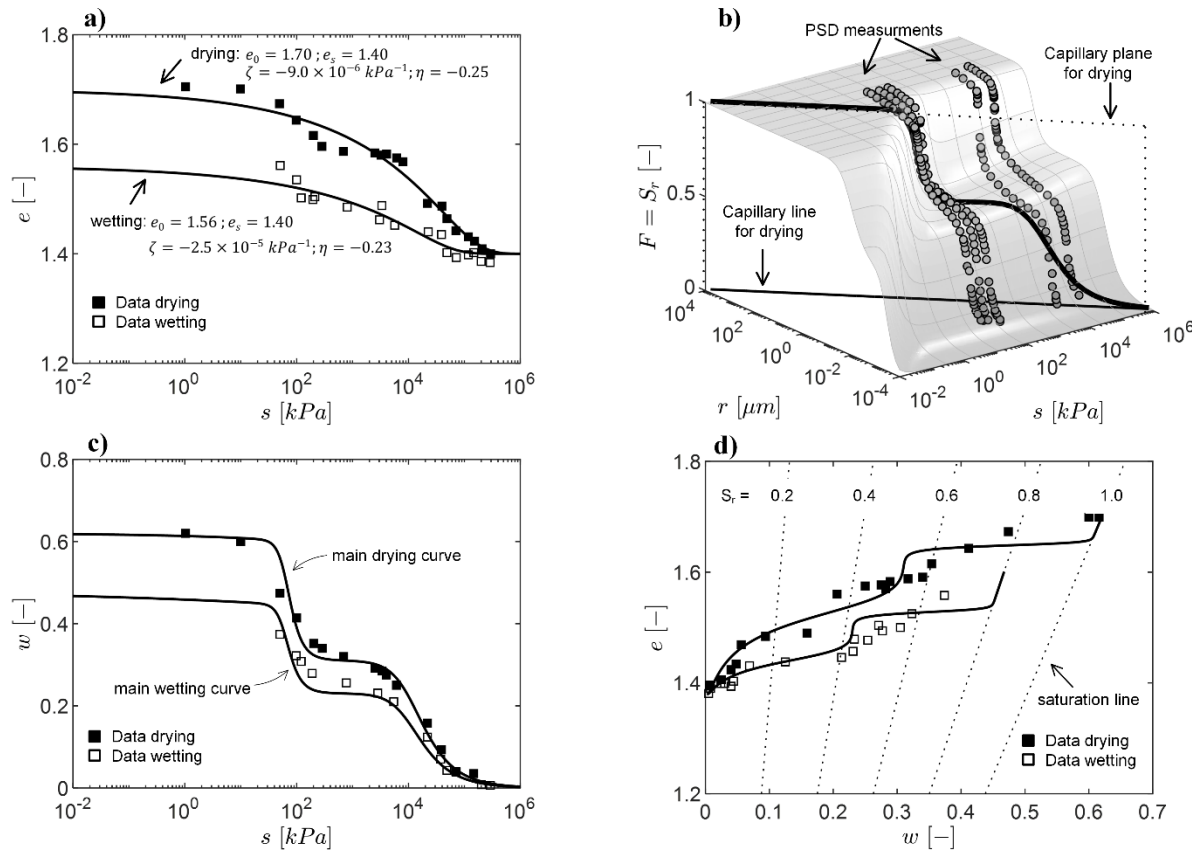


Fig. 13. Sample CS1.7 of compacted Guilin lateritic soil (a) volumetric evolution during the SWCC tests (b) PSD surface in the $r - s - F (= S_r)$ space (c) predicted water retention curves in terms of gravity water content (d) predicted shrinkage and swelling curves (data from Cai et al. [31])

490

491 Acknowledgement

492 The support of the China Scholarship Council (number 201608080128) is greatly acknowledged by the first
493 Author.

494 **Funding:** The research leading to these results received funding from China Scholarship Council under Grant
495 Agreement Number 201608080128.

496

497 **Conflicts of interest:** The authors have no conflicts of interest to declare that are relevant to the content of this
498 article.

499

500 **Availability of data and material:** The data used to support the findings of this study are available from the
501 corresponding author upon request.

502

503 **Code availability:** The code used to support the findings of this study are available from the corresponding
504 author upon request

505

- 507 1. Mualem Y (1976) A new model for predicting the hydraulic conductivity of unsaturated porous media. *Water*
- 508 *resources research* 12 (3):513-522
- 509 2. Leong EC, Rahardjo H (1997) Permeability functions for unsaturated soils. *J GEOTECH GEOENVIRON* 123
- 510 (12):1118-1126
- 511 3. Juang C, Holtz R (1986) A probabilistic permeability model and the pore size density function. *INT J*
- 512 *NUMER ANAL MET* 10 (5):543-553
- 513 4. Khalili N, Khabbaz M (1998) A unique relationship for χ for the determination of the shear strength of
- 514 unsaturated soils. *GEOTECHNIQUE* 48 (5):681-687
- 515 5. Alonso EE, Pereira J-M, Vaunat J, Olivella S (2010) A microstructurally based effective stress for unsaturated
- 516 soils. *GEOTECHNIQUE* 60 (12):913-925
- 517 6. Schnellmann R, Rahardjo H, Schneider HR (2013) Unsaturated shear strength of a silty sand. *ENG GEOL*
- 518 162:88-96
- 519 7. Mun W, McCartney JS (2015) Compression mechanisms of unsaturated clay under high stresses. *CAN*
- 520 *GEOTECH J* 52 (12):2099-2112
- 521 8. Brooks R, Corey T (1964) HYDRAUC properties of porous media. *Hydrology Papers*, Colorado State
- 522 University 24:37
- 523 9. Van Genuchten MT (1980) A closed-form equation for predicting the hydraulic conductivity of unsaturated
- 524 soils. *SOIL SCI SOC AM J* 44 (5):892-898
- 525 10. Fredlund DG, Xing A (1994) Equations for the soil-water characteristic curve. *CAN GEOTECH J* 31
- 526 (4):521-532
- 527 11. Tinjum JM, Benson CH, Blotz LR (1997) Soil-water characteristic curves for compacted clays. *J GEOTECH*
- 528 *GEOENVIRON* 123 (11):1060-1069
- 529 12. Gupta S, Larson W (1979) Estimating soil water retention characteristics from particle size distribution,
- 530 organic matter percent, and bulk density. *Water resources research* 15 (6):1633-1635
- 531 13. Scheinost A, Sinowski W, Auerswald K (1997) Regionalization of soil water retention curves in a highly
- 532 variable soilscape, I. Developing a new pedotransfer function. *Geoderma* 78 (3):129-143
- 533 14. Fredlund DG, Rahardjo H (1993) *Soil mechanics for unsaturated soils*. John Wiley & Sons,
- 534 15. Lu N, Likos WJ (2004) *Unsaturated soil mechanics*. Wiley,
- 535 16. Yan W, Birle E, Cudmani R A simple approach for predicting soil water characteristic curve of clayey soils
- 536 using pore size distribution data. In: *MATEC Web of Conferences*, 2021. EDP Sciences, p 02012
- 537 17. Ross PJ, Smettem KR (1993) Describing soil hydraulic properties with sums of simple functions. *SOIL SCI*
- 538 *SOC AM J* 57 (1):26-29
- 539 18. Milligan W, Adams C (1954) An analytical expression for cumulative pore volumes and pore size
- 540 distributions. *The Journal of Physical Chemistry* 58 (10):891-893
- 541 19. Kosugi Ki (1994) Three-parameter lognormal distribution model for soil water retention. *Water Resources*
- 542 *Research* 30 (4):891-901
- 543 20. Delage P, Lefebvre G (1984) Study of the structure of a sensitive Champlain clay and of its evolution during
- 544 consolidation. *CAN GEOTECH J* 21 (1):21-35
- 545 21. Griffiths F, Joshi R (1989) Change in pore size distribution due to consolidation of clays. *GEOTECHNIQUE*
- 546 39 (1):159-167
- 547 22. Juang C, Holtz RD (1986) Fabric, pore size distribution, and permeability of sandy soils. *Journal of*
- 548 *geotechnical engineering* 112 (9):855-868
- 549 23. Romero E, Gens A, Lloret A (1999) Water permeability, water retention and microstructure of unsaturated
- 550 compacted Boom clay. *ENG GEOL* 54 (1-2):117-127
- 551 24. Wang Q, Cui Y-J, Minh Tang A, Xiang-Ling L, Wei-Min Y (2014) Time- and density-dependent
- 552 microstructure features of compacted bentonite. *SOILS FOUND* 54 (4):657-666.
- 553 doi:10.1016/j.sandf.2014.06.021
- 554 25. Příkryl R, Weishauptová Z (2010) Hierarchical porosity of bentonite-based buffer and its modification due to
- 555 increased temperature and hydration. *Applied clay science* 47 (1-2):163-170
- 556 26. Simms P, Yanful E (2002) Predicting soil—Water characteristic curves of compacted plastic soils from
- 557 measured pore-size distributions. *GEOTECHNIQUE* 52 (4):269-278
- 558 27. Birle E (2011) Geohydraulische Eigenschaften verdichteter Tone unter besonderer Berücksichtigung des
- 559 ungesättigten Zustandes. Technische Universität München,
- 560 28. Della Vecchia G, Dieudonné A-C, Jommi C, Charlier R (2015) Accounting for evolving pore size
- 561 distribution in water retention models for compacted clays. *INT J NUMER ANAL MET* 39 (7):702-723.
- 562 doi:10.1002/nag.2326
- 563 29. Li X, Zhang LM (2009) Characterization of dual-structure pore-size distribution of soil. *CAN GEOTECH J*
- 564 46 (2):129-141. doi:10.1139/t08-110
- 565 30. Monroy R, Zdravkovic L, Ridley A (2010) Evolution of microstructure in compacted London Clay during
- 566 wetting and loading. *GEOTECHNIQUE* 60 (2):105-119. doi:10.1680/geot.8.P.125

- 567 31. Cai G, Zhou A, Liu Y, Xu R, Zhao C (2020) Soil water retention behavior and microstructure evolution of
568 lateritic soil in the suction range of 0–286.7 MPa. *ACTA GEOTECH* 15 (12):3327-3341
- 569 32. Zhang L, Li X (2010) Microporosity structure of coarse granular soils. *J GEOTECH GEOENVIRON* 136
570 (10):1425-1436
- 571 33. Hu R, Chen Y-F, Liu H-H, Zhou C-B (2013) A water retention curve and unsaturated hydraulic conductivity
572 model for deformable soils: consideration of the change in pore-size distribution. *GEOTECHNIQUE* 63
573 (16):1389-1405
- 574 34. Chen R-P, Liu P, Liu X-M, Wang P-F, Kang X (2019) Pore-scale model for estimating the bimodal soil–
575 water characteristic curve and hydraulic conductivity of compacted soils with different initial densities. *ENG*
576 *GEOL* 260:105199
- 577 35. Yan W, Cudmani R (2022) A general analytical expression for pore size distribution based on probability
578 theory. *ENG GEOL* 297. doi:10.1016/j.enggeo.2021.106501
- 579 36. Scheidegger AE (1958) The physics of flow through porous media. *SOIL SCI* 86 (6):355
- 580 37. Durner W (1994) Hydraulic conductivity estimation for soils with heterogeneous pore structure. *Water*
581 *resources research* 30 (2):211-223
- 582 38. Yan W, Birle E, Cudmani R (2021) A new framework to determine general multimodal soil water
583 characteristic curves. *ACTA GEOTECH*:1-22
- 584 39. Delage P, Audiguier M, Cui Y-J, Howat MD (1996) Microstructure of a compacted silt. *CAN GEOTECH J*
585 33 (1):150-158
- 586 40. Wang Q, Minh Tang A, Cui Y-J, Delage P, Barnichon J-D, Ye W-M (2013) The effects of technological
587 voids on the hydro-mechanical behaviour of compacted bentonite–sand mixture. *SOILS FOUND* 53 (2):232-
588 245. doi:10.1016/j.sandf.2013.02.004
- 589 41. Lloret A, Villar MV (2007) Advances on the knowledge of the thermo-hydro-mechanical behaviour of
590 heavily compacted “FEBEX” bentonite. *Physics and Chemistry of the Earth, Parts A/B/C* 32 (8-14):701-715.
591 doi:10.1016/j.pce.2006.03.002
- 592 42. Cui Y, Loiseau C, Delage P Microstructure changes of a confined swelling soil due to suction controlled
593 hydration. In: *Unsaturated soils: proceedings of the Third International Conference on Unsaturated Soils, 2002.*
594 *UNSAT Recife, Brazil*, pp 10-13
- 595 43. Manca D, Ferrari A, Laloui L (2016) Fabric evolution and the related swelling behaviour of a sand/bentonite
596 mixture upon hydro-chemo-mechanical loadings. *GEOTECHNIQUE* 66 (1):41-57. doi:10.1680/jgeot.15.P.073
- 597 44. Houhou R, Sutman M, Sadek S, Laloui L (2021) Microstructure observations in compacted clays subjected
598 to thermal loading. *ENG GEOL* 287:105928. doi:<https://doi.org/10.1016/j.enggeo.2020.105928>
- 599 45. Delage P, Sultan N, Cui YJ (2000) On the thermal consolidation of Boom clay. *CAN GEOTECH J* 37
600 (2):343-354. doi:10.1139/t99-105
- 601 46. Oualmakran M, Mercatoris B, François B (2016) Pore-size distribution of a compacted silty soil after
602 compaction, saturation, and loading. *CAN GEOTECH J* 53 (12):1902-1909
- 603 47. Tanaka H, Shiwakoti DR, Omukai N, Rito F, Locat J, Tanaka M (2003) Pore size distribution of clayey soils
604 measured by mercury intrusion porosimetry and its relation to hydraulic conductivity. *SOILS FOUND* 43 (6):63-
605 73
- 606 48. Ninjarav E, Chung S-G, Jang W-Y, Ryu C-K (2007) Pore size distribution of Pusan clay measured by
607 mercury intrusion porosimetry. *KSCE Journal of Civil Engineering* 11 (3):133-139
- 608 49. Alonso EE, Gens A, Josa A (1990) A constitutive model for partially saturated soils. *GEOTECHNIQUE* 40
609 (3):405-430
- 610 50. Della Vecchia G (2009) Coupled hydro-mechanical behaviour of compacted clayey soils. Ph. D. thesis,
611 Politecnico di Milano,
- 612 51. Tarantino A (2009) A water retention model for deformable soils. *GEOTECHNIQUE* 59 (9):751-762
- 613 52. Ge M, Pineda JA, Sheng D, Burton GJ, Li N (2021) Microstructural effects on the wetting-induced collapse
614 in compacted loess. *Computers and Geotechnics* 138:104359
- 615 53. Fredlund D, Xing A, Huang S (1994) Predicting the permeability function for unsaturated soils using the
616 soil-water characteristic curve. *CAN GEOTECH J* 31 (4):533-546
- 617 54. Abed AA, Sołowski WT (2021) Estimation of water retention behaviour of bentonite based on mineralogy
618 and mercury intrusion porosimetry tests. *GEOTECHNIQUE* 71 (6):494-508
- 619 55. Lu N (2016) Generalized soil water retention equation for adsorption and capillarity. *J GEOTECH*
620 *GEOENVIRON* 142 (10):04016051
- 621 56. Revil A, Lu N (2013) Unified water isotherms for clayey porous materials. *Water Resources Research* 49
622 (9):5685-5699
- 623 57. Angerer L (2020) Experimental evaluation of the suction-induced effective stress and the shear strength of
624 as-compacted silty sands. Technische Universität München,
- 625 58. Cuisinier O, Laloui L (2004) Fabric evolution during hydromechanical loading of a compacted silt. *INT J*
626 *NUMER ANAL MET* 28 (6):483-499
- 627 59. Sheng D, Fredlund DG, Gens A (2008) A new modelling approach for unsaturated soils using independent
628 stress variables. *CAN GEOTECH J* 45 (4):511-534

- 629 60. Lloret A, Alonso E State surface for partially saturated soils. In: International conference on soil mechanics
630 and foundation engineering. 11, 1985. pp 557-562
- 631 61. Mbonimpa M, Aubertin M, Maqsoud A, Bussièrè B (2006) Predictive model for the water retention curve of
632 deformable clayey soils. J GEOTECH GEOENVIRON 132 (9):1121-1132
- 633 62. Stange CF, Horn R (2005) Modeling the soil water retention curve for conditions of variable porosity.
634 Vadose Zone Journal 4 (3):602-613
- 635 63. Pasha AY, Khoshghalb A, Khalili N (2016) Pitfalls in interpretation of gravimetric water content–based soil-
636 water characteristic curve for deformable porous media. International Journal of Geomechanics 16 (6):D4015004
- 637 64. Wijaya M, Leong EC (2017) Modelling the effect of density on the unimodal soil-water characteristic curve.
638 GEOTECHNIQUE 67 (7):637-645
- 639 65. Bishop AW (1959) The principle of effective stress. Teknisk ukeblad 39:859-863
- 640 66. Leong E, Wijaya M (2015) Universal soil shrinkage curve equation. Geoderma 237:78-87
- 641 67. Monroy R (2006) The influence of load and suction changes on the volumetric behaviour of compacted
642 London Clay. Imperial College London (University of London),

643